THE UNIVERSITY *of* EDINBURGH

Computational Modelling of Cellular Blood Flow in Complex Vascular Networks

QI ZHOU

THE UNIVERSITY
of EDINBURGH

School of Engineering
Institute for Multiscale Thermofluids

Thesis submitted for the degree of
Doctor of Philosophy

July 2020

To be, or not be, you ought to finish your PhD.

— Qi Zhou (Charles)

Supervisors:

Dr. Timm Krüger (School of Engineering, University of Edinburgh)

Dr. Miguel O. Bernabeu (Centre for Medical Informatics, University of Edinburgh)

Prof. Peter R. Hoskins (Centre for Cardiovascular Science, University of Edinburgh)

DECLARATION

I declare that this thesis is an original report of my research, has been written by myself and has not been submitted for any previous degree. The computational work contained herein is entirely my own unless stated otherwise; contributions by my experimental collaborators have been clearly indicated and acknowledged. Appropriate credit has been given within the thesis where references are made to the work of others.

Qi Zhou

July 2020

Edinburgh, Scotland, UK

Lay summary

One's earliest impression of blood probably comes from their first blood tests in childhood, either for health assessment or infection screening. Anomalies in the blood are associated with many prevailing diseases in modern society, such as cardiovascular disease, diabetes and malaria, threatening millions of lives globally each year. As the primary blood component occupying 40%-50% of the blood volume, red blood cells (RBCs) are well-known for their indispensable role in transporting oxygen to organs and tissues across the whole human body. This is not a trivial task at all. During each circulation cycle, RBCs need to travel through complex microvascular networks consisting of small vessels that are sometimes narrower than the cells themselves.

To accomplish their grand venture throughout the human body, both the structural characteristics (*e.g.,* cell deformability and shape memory) and spatial organisation (*e.g.,* lateral migration and radial dispersion) of RBCs within blood vessels matter, which will directly affect the perfusion of RBCs in microvascular networks surrounding organs and tissues. These RBC properties and thereby blood flow behaviour may drastically change under pathological conditions. Uncovering the underlying mechanisms, especially at the microvessel level, are crucial for a better understanding of blood flow in health and disease, thus potentially informing innovative biomedical applications. However, direct investigation of RBCs in humans or animals is usually expensive and technically difficult because of complicated regulatory responses.

This PhD sets out to investigate the dynamics of RBCs under microcirculatory conditions using a powerful simulation tool, supported by high-performance computing facilities and cross-validation data provided by experimental collaborators. With a focus on microcirculatory and microfluidic blood flow, the present work reveals some unknown secrets of RBCs, *e.g.,* their association with vascular development at early stage of life such as angiogenesis. The findings of this thesis will further our understanding of the intricate blood flow at the microscale. Furthermore, they provides insights for the design of useful microfluidic devices and the conception of new strategies aimed at improving the diagnosis and treatment of diseases arising from microcirculatory disorders.

Keywords: RBCs, Blood flow, Microcirculation, Microfluidics, Haemodynamics, Angiogenesis

Abstract

Microcirculatory disorders are associated with some of the most prevailing medical conditions in modern society, *e.g.,* cancer and cardiovascular disease (CVD). Early detection and effective treatment of these diseases require an in-depth knowledge of the changes in the haemodynamic environment preceding fatal deteriorating conditions. However, such a knowledge is difficult to obtain merely relying on experiments, on account of the overwhelming complexity of blood flow at the microscale that is sometimes beyond the capability of contemporary experimental techniques. Alternatively, computational modelling provides a potent tool to uncover the missing details of haemodynamics at the microcirculation level.

Thanks to the advent of information era which fosters growingly powerful computing facilities and architectures, the progress that has been made on blood flow modelling over recent years is unprecedented. Notwithstanding, exhaustive modelling of blood flow at the microcirculation level incorporating all blood constituents remains daunting. Existing studies employing a range of models are only possible *via* invoking simplifications justified under different assumptions. However, one important assumption for many modelling studies, namely that blood in the microcirculation can be approximated by a homogeneous non-Newtonian fluid, has been increasingly challenged. The reason is that the microscopic behaviour of red blood cells (RBCs) as the primary blood constituent is found to non-trivially modify key rheological properties of blood flow at the microscale, such as its effective viscosity, cell-free layer (CFL) and wall shear stress (WSS). To ultimately facilitate the translation of scientific investigations to real medical applications, the cellular character of microcirculatory blood flow has to be properly considered by computational models.

Bearing the above challenges in mind, the present PhD embarks on a venture to research the complex behaviour of cellular blood flow under microcirculatory conditions, capitalising on a recently developed computational tool equipped with high-level parallelisation. This computational thesis sets out to answer several important questions, ranging from the rich dynamics of individual RBCs to the collective phenomena of RBC suspensions in either microvascular networks or microfluidic mimicries. The current three-dimensional (3D) computational model is based on the lattice Boltzmann method (LBM) coupled with the immersed boundary method (IBM) for high-level resolution of discrete RBCs, which are modelled as Lagrangian membranes using the finite-element method (FEM). In the thesis, an concise introduction of the computational model is given in Chapter 4. Before applied to research projects, the model has been systematically validated against existing numerical or experimental observations. Three benchmark tests of close relevance to the scope of microscale blood flow are selected for demonstration and discussion in Chapter 5.

The main body of this thesis (Chapters 6–8) reports several novel aspects of blood flow at the microscale including, but not limited to, the non-inertial focusing of RBCs under low Reynolds number as revealed in Chapter 6, the excessive haemodilution induced by CFL asymmetry as

revealed in Chapter 7, and the strong association between RBC perfusion and vascular patterning as revealed in Chapter 8. Some confusion about or misinterpretation of well-known effects in the community has also been clarified, such as the spatial scaling of hydrodynamic lift in non-circular channels, the development length of CFL in typical microfluidic flows, and the existence of high-/low-flow attraction near bifurcating geometries. Quantitative or qualitative agreement has been achieved through elaborated comparison with supplementary experiments from my collaborators or with established empirical models in the literature.

Starting from blood flow in a single microchannel, Chapter 6 highlights an exceedingly large CFL development length even under low inertia, which is greater than 28 times channel hydraulic diameter (D_h) in simulation and $46D_h$ in experiment (*experimental data from my collaborator in Glasgow, UK*). This finding suggests that microfluidic designs need to be longer if their purpose is to investigate localised microscopic behaviour of a dilute suspension without interference from entrance effects or upstream disturbances. On a network level where the RBCs flow through bifurcating microchannels arranged biomimetically following Murray's law, Chapter 7 identifies ideal partitioning of RBCs at symmetric bifurcations (agreeing with predictions of a classic empirical model derived from *in vivo* data), but biased partitioning when significant CFL asymmetry arises in inter-bifurcation branches. Furthermore, the breakdown of CFL symmetry leads to severe haemo-dilution/concentration in the bifurcating network. In Chapter 8, the computational framework is applied to model blood flow in realistic microvasculatures of developmental mouse retina and demonstrates an unreported highly heterogeneous distribution of RBCs in the post-sprouting vascular network. Remarkably, a strong association between vessel regression and RBC depletion is uncovered, driven by the effect of plasma skimming. The association is further confirmed by *in vivo* observation of simultaneous vascular remodelling alongside blood perfusion using a developmental zebrafish model (*experimental data from my collaborator in Berlin, Germany*).

In summary, this thesis provides insights for the design of improved microfluidic devices and the conception of haemodynamic mechanisms governing the onset and progression of microcirculatory disorders. Additionally, the computational model successfully applied to various biological or biomimetic scenarios in this thesis justifies itself as a feasible and reliable tool for practical simulation of microcirculatory blood flows and may seek wider applications of its own accord.

Acknowledgements

My original idea of doing a PhD was deeply rooted in the obsession of having *"Dr."* as salutation to myself. At this very moment of submitting the final dissertation, I am glad that there are way more earned from my PhD than the title itself, for example, a free whisky at the *Doctors* (a pub near the University of Edinburgh) where members of my research group gathered to celebrate me passing the *viva voce*. Doing a PhD can be stressful sometimes, and one can seldom survive it all alone. There are many people I would like to thank, who either generously supported me or positively influenced me during my four years of PhD research.

First of all, I must convey sincere gratitude to my principal supervisor Dr. Timm Krüger, for his insightful guidance, thoughtful supervision and constructive discussions throughout my PhD. Time and time again, Timm has impressed me with his magic ability of coming up with great ideas from seemingly random conversations. In addition, his scientific rigour as a physicist constantly inspires me to think critically and research meticulously. I must also thank my co-supervisor Dr. Miguel Bernabeu, who has profoundly widened the horizons of my PhD research and introduced me to the highly interdisciplinary subject of computational biology. I'm indebted to Prof. Peter Hoskins too, also my co-supervisor, who has taught me the importance of always knowing and refreshing your research aims to avoid losing the focus and working aimlessly.

Special thanks go to Dr. Filippo Menolascina and Prof. Christian Wagner for their time examining my thesis and providing valuable comments on improving this work. Filippo also served on the annual review panel of my PhD progression, through which he offered many useful suggestions.

My experimental collaborators should not be forgotten here as well, without whom my simulations would appear pale and less convincing. I would like to thank Joana Fidalgo and Dr. Mónica Oliveira at the University of Strathclyde (Glasgow, UK) for their corroborative microfluidic experiments and scientific discussions. Also, I need to thank Tijana Perovic, Ines Fechner and Prof. Holger Gerhardt at Max-Delbrück-Center for Molecular Medicine in the Helmholtz Association (Berlin, Germany) for their wonderful animal experiments on the the microvasculatures of mouse retina and zebrafish, which greatly add to the value of my PhD research.

My fellow colleagues in the Krüger group and Bernabeu group are also important people to me, who fully supported me in my endeavours to develop a genuine sense of humour. Rohan, Aruun, Yunzhou, Greg, Emmanouil, Konstantinos, Romain, Ylenia, Ana, Xin, David and Lowell, thanks for standing me! The other friends of mine (okay, too many to name here one by one!) from the Institute of Multiscale Thermofluids should also be acknowledged for many relaxing lunch and coffee breaks. They are all interesting souls in different ways and I hope life treats them well.

Last but not least, the most important persons have to be my wife Xun and our parents, for their unconditional support and immense love, without whom this PhD could not have been done.

This PhD is sponsored by the University of Edinburgh with the award of a Principal's Career Development Scholarship and an Edinburgh Global Research Scholarship to Qi Zhou. Supercomputing time on the ARCHER UK National Supercomputing Service (http://www.archer.ac.uk) was provided by the "UK Consortium on Mesoscale Engineering Sciences (UKCOMES)" under the EPSRC Grant No. EP/R029598/1.

Contents

List of figures

List of tables

Abbreviations

BFL	Bouzidi-Firdaouss-Lallemand
BGK	Bhatnagar-Gross-Krook
BOI	Bifurcation of Interest
CB	Child Branch
CFD	Computational Fluid Dynamics
CFL	Cell-Free Layer
CVP	Caudal Vein Plexus
FEM	Finite Element Method
FSI	Fluid-Structure Interaction
HPC	High-Performance Computing
IBM	Immersed Boundary Method
LBM	Lattice Boltzmann Method
MPI	Message Passing Interface
NNCY	Non-Newtonian Carreau-Yasuda
NSE	Navier Stokes Equations
OCTP	Off-Centre Two-Peak
PB	Parent Branch
PDD	Probability Density Distribution
PSM	Phase Separation Model
RBC	Red Blood Cell
ROI	Region of Interest
WSS	Wall Shear Stress

Part I

INTRODUCTION

Reality is merely an illusion, albeit a very persistent one.

— Albert Einstein

Chapter 1
About this thesis

1.1 Motivation, aim and objectives

Motivation The microcirculation is a vital system sustaining the normal function of the human body and has been at the heart of blood flow research ever since its discovery. Historically, observations in the microcirculation have inspired the inception of fundamental laws or principles that serve as cornerstones of the study of haemodynamics nowadays. The most well-known example is probably the Poiseuille law describing the general pressure-flow relationship in blood flow, the establishment of which was attributed to a series of exceptionally designed experiments by Poiseuille following his observation of blood flowing through arterioles and venules of the frog in the 1830s.

From a practical perspective, microcirculatory disorders are associated with many widespread health threats in modern society, *e.g.,* cancer and cardiovascular disease (CVD). Extraordinary interest has been attracted to this subject in the last two decades, owing to an imperative need of understanding the haemodynamics in the microcirculation during the onset and progression of cancer or CVD. Early detection and predictive medicine of these diseases require an in-depth knowledge of cautioning changes in the haemodynamic environment preceding fatal deteriorating conditions. However, such a knowledge is difficult to obtain merely relying on experiments on account of the overwhelming complexity of microcirculatory blood flows. Such complexity poses critical challenges even for the state of the art of experimental techniques, despite recent breakthroughs made in the development of animal models and microfluidic platforms.

Alternatively, blood flow modelling based on mathematical formulation and computational simulation allows the investigation of physiological or pathological processes beyond the capabilities of current experimental approaches. It provides a potent tool to uncover the missing details of haemodynamics at the microcirculation level. Nevertheless, constrained by the computational

power available in our time, full modelling of microcirculatory blood flow involving all biophysical/biochemical elements is still impossible. As a consequence, various simplifications have been made to existing models, the most common two of which are arguably dimensionality reduction and rheology homogenisation. The former refers to the application of two-dimensional (2D) models to describe three-dimensional (3D) effects observed *in vivo* or *in vitro*. The latter means the utilisation of empirical or constitutive laws to simply the inherent heterogeneity of blood arising from the non-continuum existence of RBCs, *e.g.,* approximating blood flow as a homogeneous non-Newtonian fluid.

The above simplifications in blood flow modelling are sometimes necessary to rule out numerical artefacts and pinpoint potential mechanisms for phenomenological observations, especially for investigation of large-scale systems such as a whole vascular plexus. However, they leave quantitative description of the microcirculatory blood flow difficult despite decades of extensive research and a plethora of established theories. Indeed, there has been increasing evidence over recent years that the cellular character of blood at the microscale would challenge the predictions made by simplified theoretical models considering RBCs as 2D or directly assuming blood as a homogeneous fluid. For instance, by modelling 2D blood flow where RBC are treated as 2D particles, the in-plane shear elasticity of its membrane cannot be accounted for, whereas experiments have clearly demonstrated the crucial role of membrane shear elasticity in modulating blood rheology *via* its effect on RBC morphology and dynamics.

Therefore, characterisation of the cellular character embedded in blood and subsequent investigations of its haemodynamic implications for the microcirculatory blood flow necessitate 3D simulations with finely resolved RBCs in physiologically relevant geometries (*e.g.,* microvascular bifurcations or capillary networks). Such computational studies will not only elucidate haemodynamics at the microscale, but also provide insights into the onset and progression of microcirculatory disorders. Furthermore, with accumulated high-quality simulation data on the microscopic details of cellular blood flow, it may become possible to inform robust reduced-order models or extended constitutive models that can produce convincing predictions while minimising the need for computing power. These considerations motivate the present thesis.

Aim and hypothesis Capitalising on a recently developed computational framework which enables highly-parallel simulation of cellular blood flow in sparse and complex geometries, the present thesis aims to provide an in-depth understanding of the signatures of blood flow under microcirculatory conditions, and in particular, investigate the biophysical implications of its cellular character for vascular patterning in the course of cardiovascular development. Throughout the thesis, the blood flow is modelled as a suspension of RBCs that deform in response to fluid shear and solid boundaries. Given the high relevance of microfluidic devices in the field of blood flow studies, both microvascular and microfluidic geometries are considered by the present work.

The central hypothesis of this thesis is:

The cellular character of blood, featuring the individual motion and collective transport of red blood cells (RBCs), non-trivially alters the haemodynamics at the microscale and plays an important role in the process of vascular development.

Objectives To verify the aforementioned hypothesis, this thesis is dedicated to three objectives:

(I) *To investigate the spatio-temporal dynamics of RBC suspensions in individual microchannels.* The research aligned with this objective is reported in Chapter 6, where novel RBC distribution and unexpected cell-free layer development length under common conditions of microfluidic experiments are identified and analysed.

(II) *To investigate the distribution of RBCs across artificial vascular networks.* The research aligned with this objective is reported in Chapter 7, where complex RBC flux pattern and excessive haemo-dilution/concentration within successively bifurcating microchannels are presented and interpreted.

(III) *To investigate the association between the microscopic behaviour of RBCs and vascular patterning events in developmental microvasculatures.* The research aligned with this objective is reported in Chapter 8, where a remarkable association between RBC dynamics and vascular patterning in realistic developmental microvasculature is uncovered *via* image-based simulation followed by experimental corroboration.

1.2 Thesis outline

This thesis is organised as follows. Chapter 1 states the motivation, aim, hypothesis and objectives of this thesis. Chapters 2–3 present an introduction to the biophysical aspects and modelling aspects of microcirculatory blood flow, respectively. Chapter 4 provides an overview of the three-dimensional computational model employed by this thesis, together with general numerical and experimental methods involved in associated research projects. Chapter 5 demonstrates three benchmark tests of the computational model as validation of its performance under representative biological or biomimetic conditions that RBCs would encounter . Following the validation chapter, Chapters 6–8 report three primary research projects initiated and completed during this PhD, which correspond to the three objectives listed above. For all three projects, experimental data are provided by my collaborators to corroborate the computer simulations. Chapter 9 summarises the main findings and concludes the thesis with outlook for future research.

Chapter 2
Microcirculation and haemodynamics

2.1 Microcirculation: vascular structure and function

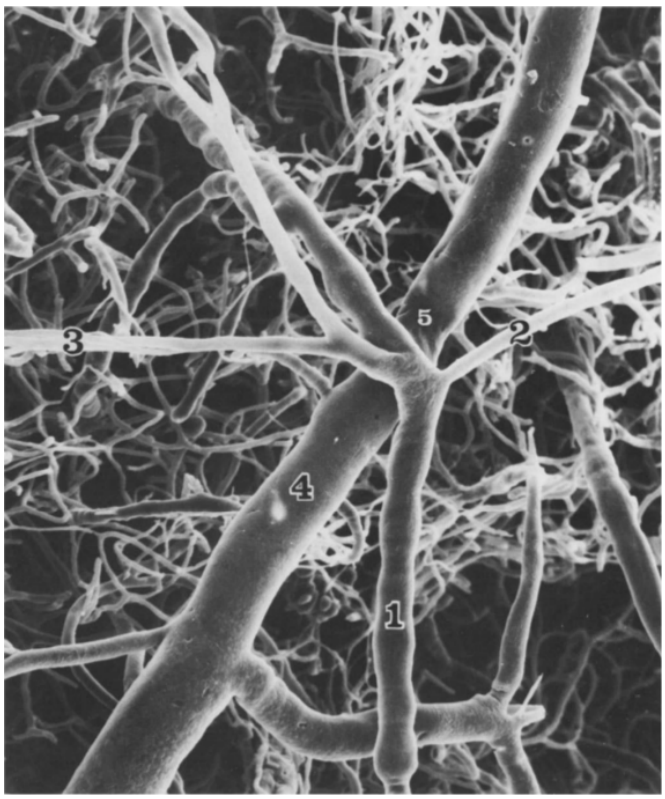

Figure 2.1: *Scanning electron microscope (SEM) image of the blood-vessel cast (obtained via resin injection) in the cerebral cortex of a human brain. (Image from [77])*

The microcirculation is an extensive system of small vessels which accounts for around 80% of the pressure drop occurring between the aorta and the vena cava [234]. These vessels are embedded in organs and directly participate in crucial exchange processes between the blood and tissues. The vasculature in the microcirculatory system typically contains three types of vessels: arterioles, equipped with vascular smooth muscle and typically ranging between 10–100 μm in diameter, are

in charge of delivering blood into the capillary network; venules, organised in parallel with arterioles and typically ranging between 10–200 μm in diameter, are in charge of draining blood from the capillary network; capillaries, the smallest vessels in the cardiovascular system (consisting of a monolayer of endothelial cells) ranging between 4–10 μm in diameter, form the capillary network serving as the exchange site of indispensable substances, *e.g.,* oxygen, carbon dioxide, nutrients and metabolic or signalling molecules [134]. See an example of the microvasculature from the cerebral cortex of a human brain (Figure 2.1).

Apart from transporting nutrients and removing waste products, the microcirculation is also responsible for regulating blood flow (mainly relying on the arterioles) and intravascular pressure through sophisticated mechanisms of information transfer [246]. Furthermore, it is of paramount importance to defend the human body against the invasion of pathogens [173]. All these essential roles render the microcirculation vital for sustaining the normal functions of the human body. Abundant prevailing medical conditions in modern society, such as cancer, malaria, sickle cell disease (SCD), diabetic retinopathy (DR) and various cardiovascular disease (CVD), are associate with microcirculatory disorders. Up to date, mechanisms governing different microcirculatory disorders are still not entirely clear, hindering the development of effective therapies and predictive treatment of some of the most fatal diseases threatening the health and lives of human beings [6].

2.2 Blood and red blood cells (RBCs)

2.2.1 Blood: constituents and rheology

The microcirculation will not function without the blood, which carries vital substances to tissue cells. A typical adult has about 5 litres of blood circulating within the body [87]. It is a complex fluid that behaves distinctively as the vessel size scales down from the aorta to a capillary. A unique term is dedicated to studies of the flow behaviour of blood, *i.e.,* haemorheology [255]. To interpret haemorheology, we need to understand the constituents of blood first. Blood is essentially a suspension of blood cells and biomacromolecules immersed in a fluidic phase known as the plasma (see a vivid cartoon in Figure 2.2a). The plasma occupies nearly 55% of blood in volume and is commonly regarded as a Newtonian fluid containing water, glucose, proteins, hormones, etc. What endows blood with its complex rheology is the presence of blood cells, including red

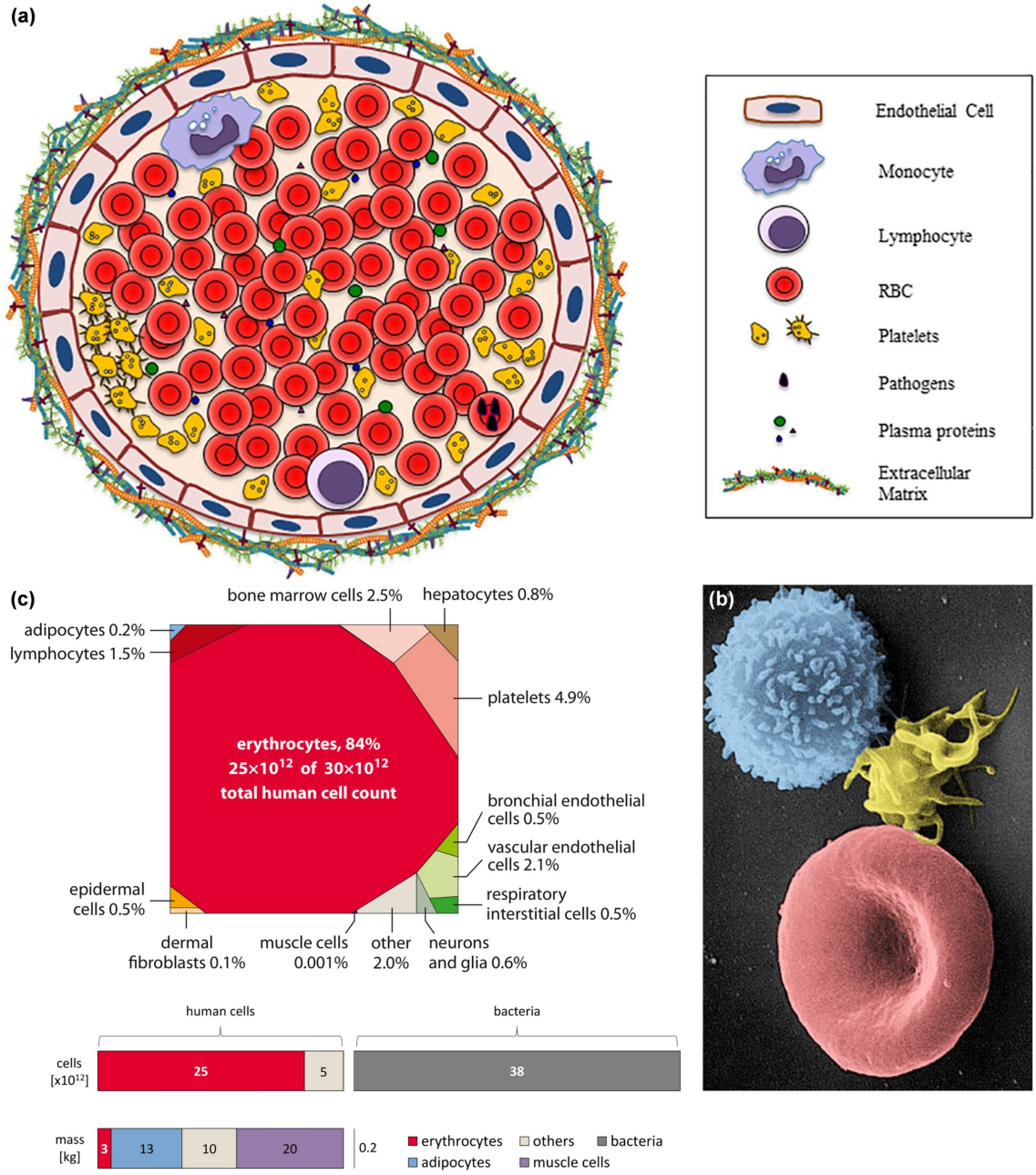

Figure 2.2: *(a) Cross-sectional view of a blood vessel showing common cells and other substances in the blood (Image from [240]). (b) SEM image of blood cells (artificially coloured), including an RBC at rest (in red), an activated platelet (in yellow) and an inactivated WBC (in blue) (Image from* `https://en.wikipedia.org/wiki/Blood`*). (c) Cell count in human body based on a back-of-the-envelope approach (Image from [275]).*

blood cells (RBCs or erythrocytes, about 45% in volume), white blood cells (WBCs or leukocytes, less than 1% in volume) and platelets (PLTs or thrombocytes, less than 1% in volume).

RBCs (Figure 2.2b) account for the majority of the particulate phase and predominantly determine the rheological properties of blood [295]. On this account, a comprehensive look into RBCs will be provided separately in the following Sec. 2.2.2. In the remaining part of the present section, the structural and functional features of WBCs and PLTs are briefly introduced.

WBCs are immune cells circulating in vascular or lymphatic systems. Their responsibility is to protect the human body against infections and injuries. Several types of WBCs exist, *e.g.,* Monocytes, Neutrophils, Eosinophils, Basophils and Lymphocytes, responsible for different pathogens [135]. In inactivated state, they typically present a spherical shape and the diameter is between 10–30 μm (Figure 2.2b). When infections or injuries occur, they are activated and would adhere to the endothelial surface of the vessel lumen and subsequently exit the blood vessel. Normally, WBCs are stiffer than RBCs because of their much higher cytoplasm viscosity and would migrate towards the vessel wall during circulation in the blood stream, the process of which is termed margination [96].

PLTs are technically not blood cells, but rather cell fragments of larger precursor cells named megakaryocytes. The main responsibility of PLTs is for blood clotting and wound healing. In inactivated state, they present a plate-like shape measuring 2–3 μm in diameter and 0.5 μm in thickness [135]. When the endothelium is damaged, the PLTs become activated and would develop a spiky morphology with multiple pseudopods (Figure 2.2b). Because of their small size, they have negligible effect on the hydrodynamics or rheology of blood and behave similarly to nanoparticles. The motion of PLTs in blood vessels also presents the margination effect observed for WBCs owing to hydrodynamic interactions with RBCs [166].

2.2.2 RBC: biomechanics and dynamics

As mentioned in Sec. 2.2.1, RBCs are the most abundant cells in blood. In fact, they are also by far the most populous cell type in the whole human body, occupying a prominent 84% of total cell count in a 70 kg "reference man", albeit their overall weight amounts to 2.5% only ([275], Figure 2.2c). RBCs play a crucial role in maintaining the normal function of tissues and organs in

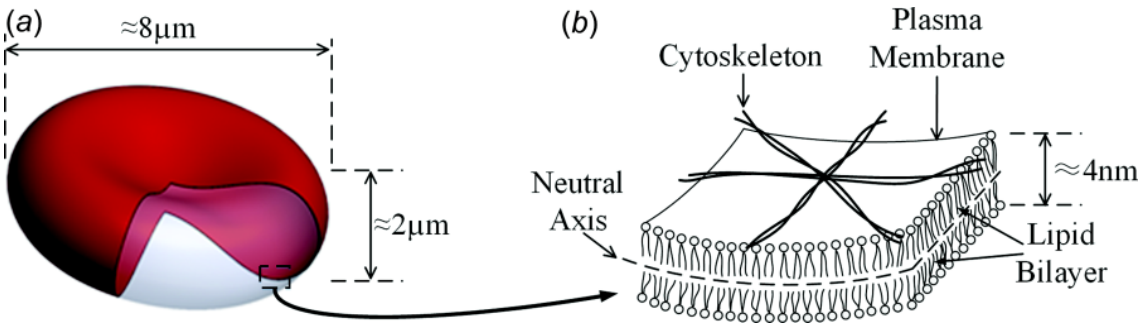

Figure 2.3: *Illustration of (a) a biconcave RBC at rest and (b) the biological composition of the RBC membrane. (Image from [47])*

humans and animals through a series of vital processes, such as transporting oxygen and carbon dioxide, regulating blood viscosity, and affecting the circulation of nutrients and immune cells. To appreciate their relevance to the microcirculatory blood flow, this section will introduce the biological composition, mechanical properties and shear-dependent dynamics of RBCs.

Biological composition and mechanical properties An RBC at rest presents a biconcave shape, featuring two dimples on opposite sides of a nearly flat disc (Figure 2.3a). The typical diameter of a human RBC is about 8 μm and the thickness is about 2 μm, which has a volume of roughly 90 fL and a surface area of 135 μm^2, indicating a large surface-to-volume ratio compared with a sphere of equal volume (90 fL, 97 μm^2) [299]. This "excess area" (around 40 %) of the membrane allows the RBC to deform substantially subject to external stresses. Despite its remarkable deformability, however, the volume and surface area of an RBC is nearly constant. Under excessive forces, an increase of 3% to 4% in its surface area is sufficient to cause cell lysis [206].

The RBC is essentially an outer membrane enclosing an inner cytoplasm, which contains no nucleus or organelles and is primarily a homogeneous solution of haemoglobin (responsible for binding and releasing oxygen). This solution is termed cytosol and has a viscosity five times ($ca.$ 6 mPa s) that of the suspending plasma ($ca.$ 1.2 mPa s) under physiological states, leading to a viscosity ratio of $\lambda = 5$. The RBC membrane consists of a thin lipid bilayer (about 4 nm thick) coupled with an interconnected cytoskeleton, which is network of cross-linked spectrin proteins (Figure 2.3b). The lipid bilayer behaves like a incompressible Newtonian fluid (therefore viscous) and can only resist off-plane bending (characterised by a bending modulus). The cytoskeleton as

a spectrin network endows the membrane with in-plane shearing resistance (characterised by a strain modulus), although it also bears a small part of the bending resistance. The measured bending and strain moduli of the RBC membrane through various experimental techniques are 5.5±3.3 μN/m and 1.15±0.9 Nm, respectively [299]. The hyper-elastic nature of membrane adds to the extraordinary deformability of RBCs and enables them to squeeze through the narrowest vessels (*e.g.,* capillaries, 4–10 μm) or passages (*e.g.,* spleen slit, 1-2 μm) one can find in the human body.

Shear-dependent dynamics and impact on blood rheology Pioneered by Chien and Skalak in the 1960s–1980s [51, 53, 284], extensive studies have been carried out experimentally, theoretically and numerically to elucidate the role of RBCs in the rheological properties of blood (see recent reviews [5, 95, 106, 306, 319]). How the RBCs behave individually and collectively has a profound influence on the blood behaviour. For instance, The shear-dependent dynamics of RBCs predominantly determine the fundamental characteristic of blood, *i.e.,* viscosity. Back to 1970, Chien [50] evidently demonstrated the shear-thinning rheology of blood using RBC suspensions exposed to a wide range of shear rates $\dot{\gamma}$ (Figure 2.4A). The shear-dependence was ascribed to the interplay between RBC aggregation (which also contributes to increased sedimentation of RBCs in blood [103]) and RBC deformation in response to the shear environment. Indeed, blocking either aggregation or deformation of the RBCs was found to have significant effect on the viscosity, either weakening or removing the shear-thinning tendency of blood (Figure 2.4A).

Under relatively low shear rates, RBCs assume a tumbling motion (TB, like flipping a coin) and would form aggregates known as rouleaux in the presence of fibrinogen from the plasma [203], resulting in a high viscosity of the blood. This process is reversible and can be counteracted by increasing the shear rate till the rouleaux disaggregates and the local stress relaxes, thus recovering the normal viscosity. If the shear rate is increased to a level where the RBC substantially deforms and its membrane starts to tank-tread (TT, see a schematic illustration in Figure 2.4B, a status when the RBC's orientation is nearly fixed while accompanied by steady rotation of the membrane, discovered by [91, 110] in the 1970s), the viscosity will further drop. The reason is that the RBCs are now well-aligned with the flow and considerably reduces the hydrodynamic resistance. Furthermore, because the close-wall tank-treading RBCs will migrate away under hydrodynamic forces (leading to axial drift) [3, 219, 220, 223, 274], a cell-free layer (CFL) will develop. This CFL

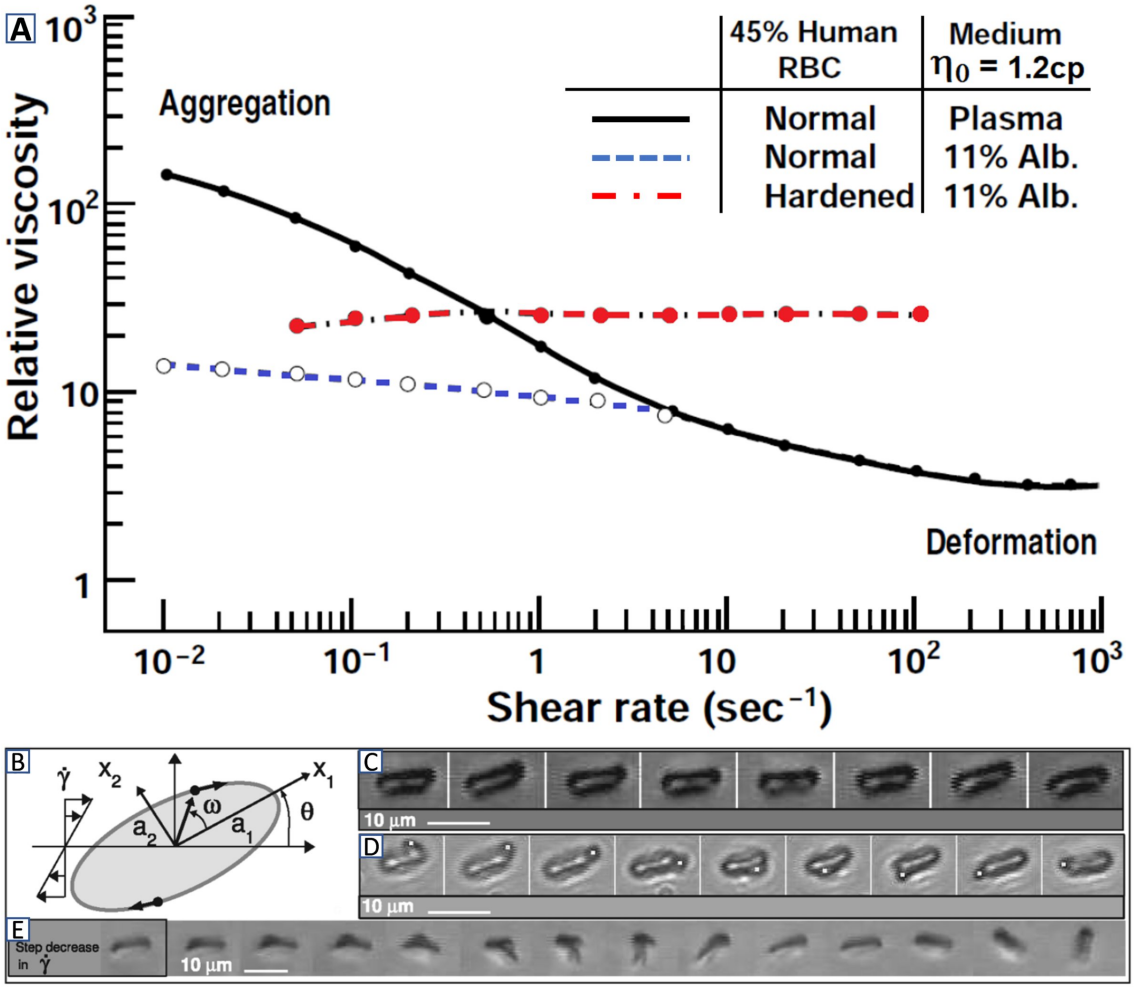

Figure 2.4: *(A) Viscosity-shear relation in three types of RBC suspensions, where the blood viscosity is measured relative to the plasma viscosity (thus called "relative viscosity", Image from [50]). All samples containing 45% human RBCs (by volume). The 11% albumin-Ringer solution (Alb.) has the same viscosity (1.2 centipoises) as plasma but does not allow RBCs to aggregate. The hardened RBCs are prevented from deformation. (B-E) Different motion regimes of a single RBC observed under different shear rates (Image from [4]). Herein, panel (B) shows schematic illustration of a tank-treading ellipsoidal in simple shear flow; panel (C) shows a "swinging" RBC with the suspending medium viscosity $\eta_0 = 47$ mPa s and the shear rate $\dot{\gamma} = 1.33\,s^{-1}$; panel (D) shows a tank-treading RBC with a bead (diameter 1 μm) stuck on the membrane and rotating along the rim ($\lambda = 1/47$, $\dot{\gamma} = 6\,s^{-1}$)); and panel (E) shows a tumbling RBC ($\lambda = 1/47$, $\dot{\gamma} = 2.66\,s^{-1}$).*

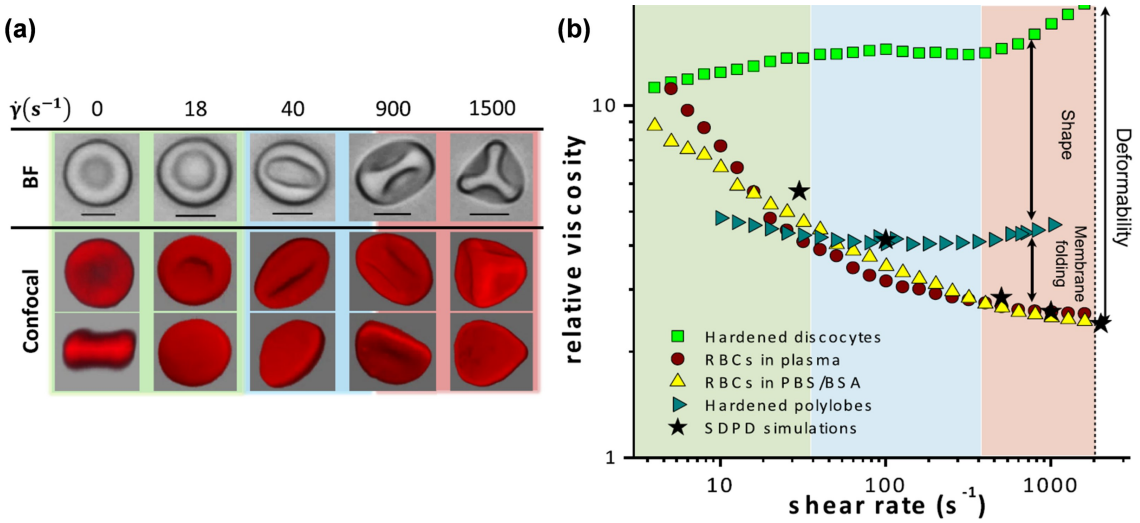

Figure 2.5: *(a) ($\lambda \geq 5$) Optical and confocal microscopy images of hardened RBCs from different shear rates (the cells were instantly hardened while still flowing). (b) Relative viscosity of RBC suspensions with either deformable or hardened RBCs (of different shapes) under varying shear rates. (Image from [169])*

serves as a lubricant film that brings down the apparent viscosity and has important implications for microcirculatory blood flow (to be detailed in Sec. 2.3.1).

The RBC dynamics in a shear flow are incredibly richer than TB and TT. Under moderate shear rates, a swinging motion (SW) of the RBC was discovered in experiments, characterised by an oscillating inclination angle on top of the classic tank-treading motion [2] (see Figure 2.4C-E). Even for apparently rigid RBCs (at low shear rates), they were experimentally observed to assume various motions other than tumbling, *e.g.,* wheel-like rolling or Frisbee-like spinning [76]. Meanwhile, complex RBC shapes other than the commonly reported ones (*e.g.,* biconcave, ellipsoidal, parachute-like, slipper-like, bullet-like, etc.) are also revealed in recent experiments mimicking physiological conditions of microcirculatory blood flow [183, 234], featuring polylobed cell membrane with trilobe or hexalobe patterns (Figure 2.5a). These morphological changes of RBCs are found to substantially alter the relative viscosity of blood (Figure 2.5b).

Until today, an astonishingly rich body of studies (experimentally [2, 63, 69, 145, 146], theoretically [67, 81, 205, 222] or numerically [107, 147, 159, 197, 214, 216, 224, 286], just to name a few here) have been dedicated to the research of RBCs or their biomimetic counterparts (*i.e.,* capsules

and vesicles), aimed at a fundamental knowledge of the principles and mechanisms underlying the complex dynamics of such a simple cell. Nevertheless, the understanding of an RBC's full dynamics in shear flows (liner or quadratic, unbounded or bounded) is still incomplete, owing to the intertwined interaction between myriads of effects, *e.g.,* flow parameters, cell properties, boundary conditions or initial conditions. A extended discussion on this topic will be given in Sec. 2.3.2.

2.3 Microcirculatory blood flow: a literature review

2.3.1 The prominence of cell-free layer (CFL) and associated effects

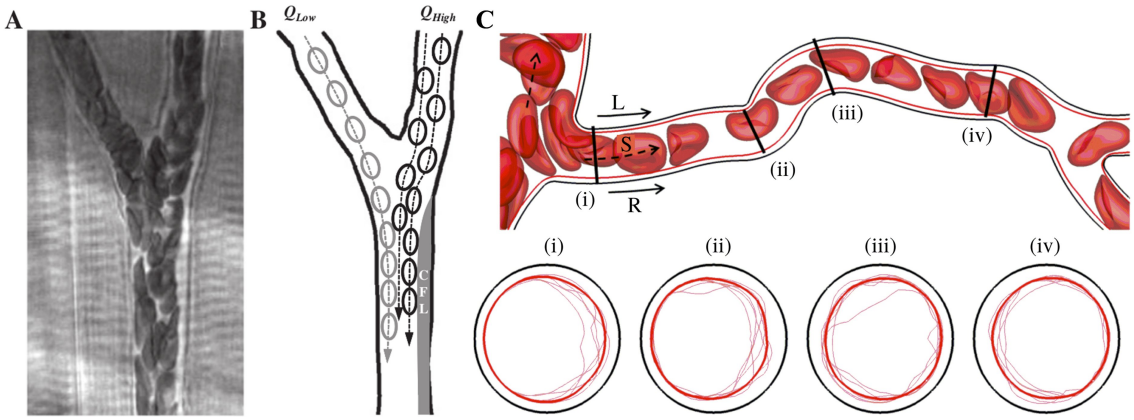

Figure 2.6: *Cell-free layer observed from (A-B) mouse experiments (image from [208]) and (C) computer simulations (image from [20]).*

In the microcirculation, RBCs frequently encounter vessels with comparable or even smaller diameters than their own size and a range of effects absent in large arteries or venules emerge. A prominent phenomenon is the development of a CFL due to the interaction between RBCs and the vessel wall as previously mentioned in Sec. 2.2.2. It has been evidently observed in experiments (either *in vivo* or *in vitro*) and reproduced in numerical simulations (see Figure 2.6).

The CFL commonly comes into being when the diameter of the channel falls below 300 μm and it arises from the lateral migration of RBCs under complex hydrodynamic forces within the blood (to be detailed in Sec. 2.3.2). Owing to this CFL, the blood stream is essentially divided into two phases: a cell core at the vessel centre and a fluid layer around the periphery, presenting a non-uniform radial concentration of RBCs. As a result, the velocity profile is distorted into a blunted

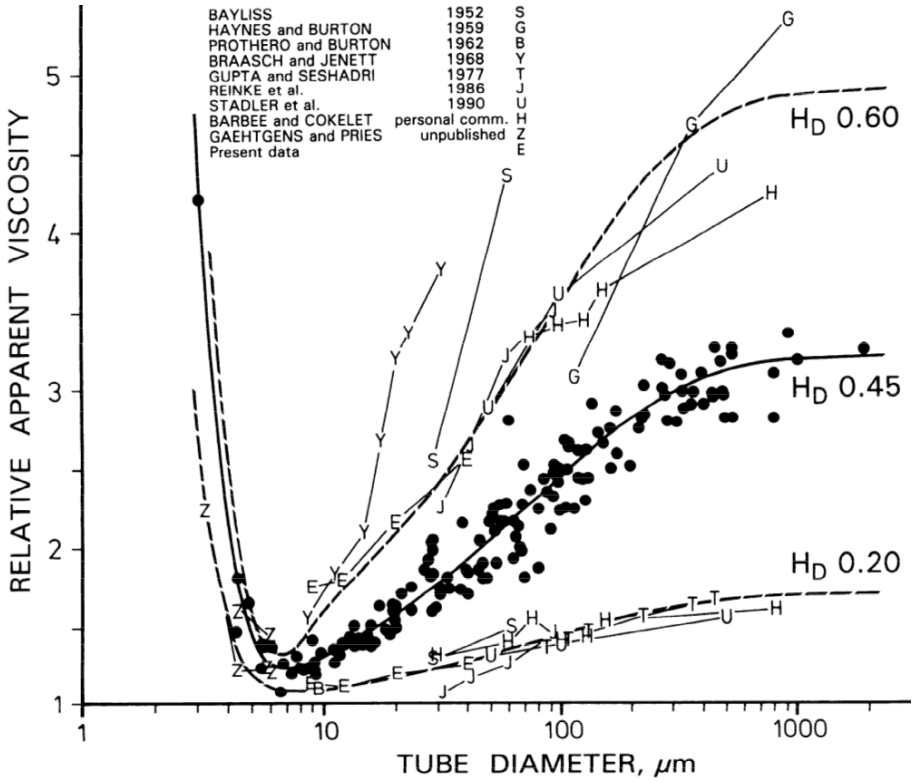

Figure 2.7: *Fåhræus-Lindqvist effect. The apparent viscosity of RBC suspensions η_{app} at different concentrations ($H_d = 0.20, 0.45, 0.60$) is calculated relative to viscosity of the suspending medium η_0 and therefore named "relative apparent viscosity". The continuous line fitting the $H_d = 0.45$ data and two broken lines fitting the $H_d = 0.20, 0.60$ data are predictions of the empirical law derived by Pries* et al. *[243], where this image is extracted from.*

one, deviating from the classic parabola as in large vessels where Poiseuille flow prevails. Furthermore, because the central regions is of higher velocity, the cells would travel faster on average than the overall blood, which causes the measured concentration of RBCs (termed haematocrit) within the channel to be smaller compared to the actual concentration of cells entering and leaving. In literature, the former is usually referred to as the tube haematocrit (H_t) and the latter the discharge haematocrit (H_d). This dynamic reduction between H_t and H_d is termed Fåhræus effect and was found most prominent in glass tubes of 10 μm in diameter [9, 103].

The CFL is also associated with another important effect called Fåhræus-Lindqvist effect [104], which describes the counterintuitive decrease of blood apparent viscosity η_{app} (calculated by treat-

ing blood as an equivalent Newtonian fluid) in capillary glass tubes of decreasing diameter (Figure 2.7). The minimum η_{app} was unanimously observed for blood of various concentration in glass tubes with a diameter of 5–7 μm. The drop in the blood viscosity is attributed to the increasing importance of the lubrication effect of the CFL as the vessel diameter decreases. Over time, Fåhræus-Lindqvist effect has been extensively validated by researchers [21, 109, 243, 248].

If the aforementioned Fåhræus effect and Fåhræus-Lindqvist effect are more or less concerning single vessels/channels, there is another effect that arises from the CFL playing a crucial role on the network level: the Zweifach-Fung effect. The microcirculation is characterised by the non-uniform distribution of haematocrit in the vascular network. This heterogeneity results from the disproportionate partitioning of RBCs (relative to the flow split) upon bifurcations with the presence of a CFL and the underlying mechanism is termed the Zweifach-Fung effect [102, 297]. Under extreme circumstances, some child branches may receive only plasma from the upstream CFL of their parent branches and become completely deprived of RBCs. This phenomenon was coined by Krogh as plasma skimming [160]. Based on the concept of plasma skimming, Pries *et al.* [242] examined data from arteriolar bifurcations in rat mesentery and developed an empirical model that provides quantitative description of the phase-separation process [244, 245, 247, 252]. This empirical model has been widely applied to analyse the partitioning of RBCs at divergent bifurcations (to be detailed in Sec. 2.3.3).

2.3.2 RBC migration and collective transport: a prelude to Chapter 6

After the general introduction of microcirculatory blood flow in Sec. 2.2.2 and Sec. 2.3.1, it should be clear now that the dynamics of RBCs is essential for haemorheology. To date, various factors affecting the RBC dynamics have been determined by theoretical/numerical models of RBCs or biomimetic capsules/vesicles, including (but not limited to): (i) viscosity contrast (between internal and external fluids to the membrane) [66], deformability [162], orientation [59] and initial position [117] of the cell; (ii) shear component (distinct in linear/quadratic flows) [223], suspending viscosity [334], flowline curvature [107] and wall confinement [148] of the flow; (iii) two-body or multi-body hydrodynamic interactions between cells [13]. Most studies focus on the individual dynamics/pairwise interaction of cells or the characteristic signatures of the overall suspension system, *e.g.,* effective viscosity and normal stress differences.

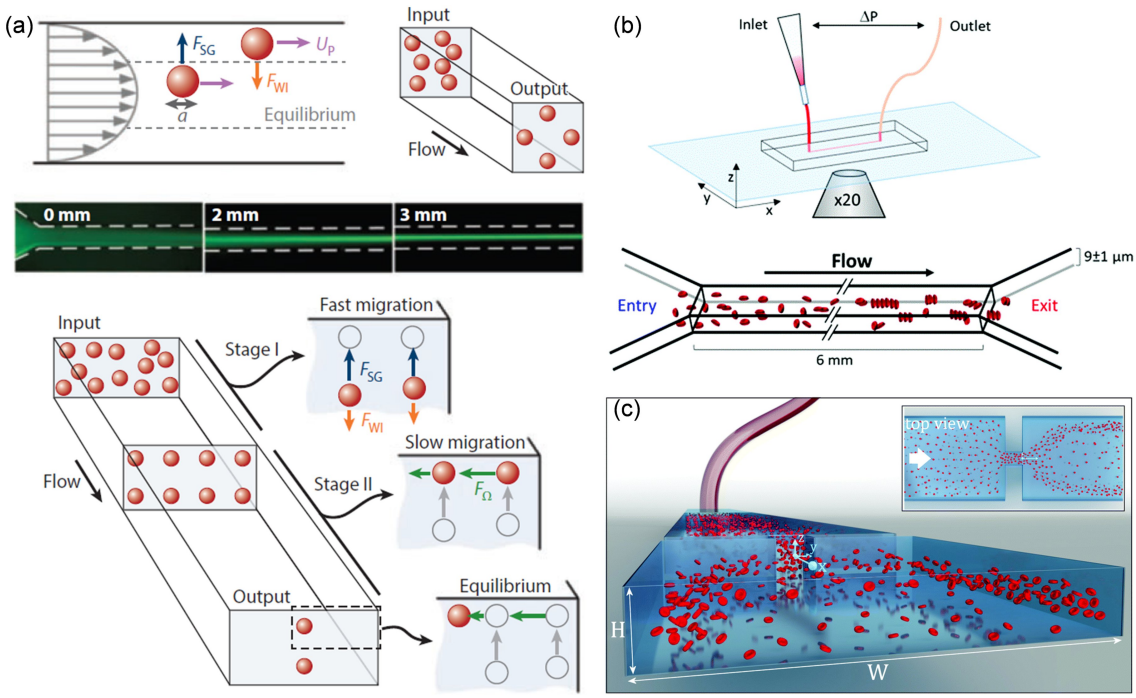

Figure 2.8: *(a) Segré-Silberberg effect of rigid particles in microfluidics (image from [338]). (b) Self-organisation of deformable RBCs in a highly confined channel (image from [139]). (c) Cross-sectional focusing of deformable RBCs in post-constriction channel segment (image from [1]).*

Much less attention has been paid to the collective behaviour of RBCs, *e.g.,* their spatio-temporal organisation or emergent orders, at a realistic length scale in three-dimensional space. Common reasons for avoiding such studies include their complexity of analytical modelling or prohibitiveness of computational cost. In fact, the transport phenomena of RBCs at sub-suspension level plays a key role in bridging the RBC dynamics and haemorheology. A mechanistic understanding of it would help elucidate the onset and progression of blood disorders affecting the RBC deformability and other mechanical properties (such as malaria, diabetes and sickle cell anaemia), and potentially inspire perspectives for new therapies.

From an experimental perspective, the maturing of microfluidic technologies over the last two decades has provided a powerful tool to investigate the otherwise inaccessible behaviour of complex biofluids at the microscale. They are now widely employed for blood flow experiments aimed at various applications [266, 299, 301]. More importantly, microfluidic experiments have inspired

the development of theories for physical interpretation of important phenomena in fluid mechanics such as the Segré-Silberberg effect discovered in the 1960s [271, 272] (also known as "tubular pinch" effect, see Figure 2.8a for a manifestation of this effect in regular microfluidic channels of rectangular cross-section), which describes the migration and accumulation of particles into an annular region within a tube. The origin of the intriguing migration of particles is now commonly accepted to have been caused by inertial forces [106, 196] and the equilibrium position of the particles within the channel is predominantly determined by wall-repulsion (towards channel centre) and shear-gradient lift (towards channel wall) [15, 129, 338]. These theories are fundamental to understand the dynamics of RBCs within microchannels, where finite inertia does exist and can be significant sometimes, depending on the geometry design as well as flow conditions.

For practical reasons in microfluidics, dilute (the concentration $\phi < 10\%$) or semi-dilute (say $\phi =$ 10–20%) RBC suspensions are commonly used, where the clogging of samples is minimal and the measurements of individual cells are quantitatively accurate [182, 256, 315]. Experimented with dilute/semi-dilute RBCs in polydimethylsiloxane (PDMS) microchannels, multiple intriguing properties of blood flow at the microscale have been demonstrated, such as uneven cell-plasma partitioning [316], long-range hydrodynamic interaction [144], tumbling-induced RBC drift [114], cytoplasmic viscosity-promoted membrane polylobes [169] and diffusion-governed cell spreading [55]. Using experiments with semi-dilute RBC suspensions ($\phi = 16\%$), Sherwood *et al.* [278] revealed strongly heterogeneous distribution of cells, which presented a locally skewed haematocrit profile with significant asymmetry. With much lower RBC concentration ($\phi \leq 5\%$), Shen *et al.* [276] found a more pronounce heterogeneity in the RBC distribution featuring a two-file ordering that led to inversion of the classic Zweifach-Fung effect at the downstream bifurcation.

More recently, Iss *et al.* [139] (Figure 2.8b) and Abay *et al.* [1] (Figure 2.8c) discovered emergent self-organisation or focusing behaviour of cells in dilute RBC suspensions arising from geometric features of the microfluidic channel, such as confinement and constriction, rather than inertial forces (the Reynolds number was too low to effectively evoke inertial lift of particles). These studies imply that the spatial arrangement of RBCs in microchannels can be highly dynamical and varies from one location to another, even under low inertia. Such local characteristics, if ignored, may give rise to inaccurate estimation of the haemodynamics in the microfluidic channels, and affect the physiological relevance of the *in vitro* experiments designed to imitate *in vivo* systems.

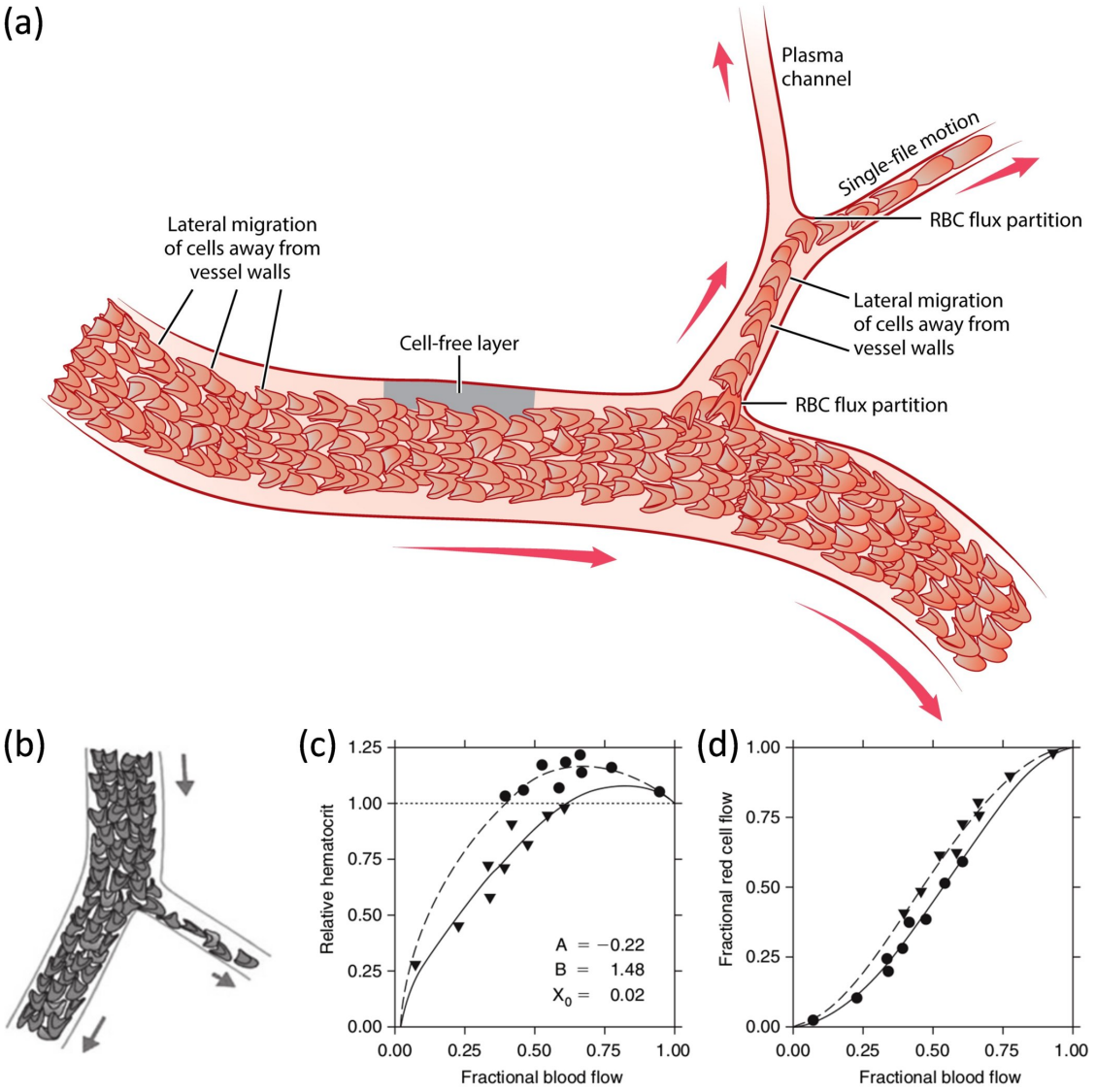

Figure 2.9: *(a) Illustration showing the occurrence of plasma skimming downstream of microvascular bifurcations (image from [268]). (b–d) An empirical model [242] describing RBC distribution at microvascular bifurcations (image from [246]). (b) Schematic of RBCs at a microvascular bifurcation. (c) Haematocrit and (d) RBC flux relative to the feeding vessel for both child branches against the fractional blood flow in the respective branch. The triangles and circles are experimental data while the solid and dotted lines are predictions given by the empirical model.*

2.3.3 RBC partitioning and bifurcation law: a prelude to Chapter 7

As introduced in Sec. 2.1, the microcirculation in humans and animals is a network of microvessels (including arterioles, venules and capillaries) exhaustively perfused by blood to maintain the normal function of organs and tissues [234]. A hallmark of the microcirculatory blood flow is the highly heterogeneous haematocrit (Ht, volume fraction of RBCs). This heterogeneity is a direct consequence of disproportionate partitioning of RBCs (relative to the flow split) at successive bifurcations, which is commonly known as the Zweifach-Fung effect arising from the prevalence of CFLs in microvessels [102, 297]. Under extreme circumstances, some child branches may only receive the plasma from the CFL of the feeding branch and are completely deprived of RBCs (see illustration in Figure 2.9a), coined by Krogh as plasma skimming [160].

Extensive studies have been carried out *in vivo* [155, 199, 242, 265] and *in vitro* [44, 88, 256, 276, 278, 316] to investigate factors that could potentially affect the partitioning of RBCs at a bifurcation. Using bioplastic bifurcating channels ranging from 20–100 μm in diameter, Fenton *et al.* [88] determined three key variables: the feeding haematocrit, the vessels diameter and the fractional flow rate in the child branches. Pries *et al.* [242] further confirmed the dominance of the above variables via examining multiple arteriolar bifurcations from rat mesentery. Based on the *in vivo* data, Pries *et al.* developed an empirical model that can provide quantitative description of the phase-separation process at microvascular bifurcations (hereafter referred to as PSM, see Figure 2.9b–d). Over time, the PSM was improved with modified parametric formulation [244, 245, 247, 252] and has been widely applied to validate theoretical or computational models.

For a mechanistic understanding of the disproportionate partitioning, a range of two-dimensional (2D) models have been dedicated to the microscopic behaviour of individual RBCs at a bifurcation [23, 78, 307, 322]. Several effects have been proposed, such as the vessel obstruction effect [22], the unbalanced shear force effect [313], the branching angle effect [310] and the low-flow attraction effect [74]. Recently, three-dimensional (3D) computer simulations considering more realistic interaction between RBCs and the bifurcation [136, 191, 308, 309, 327] emerged to overcome the potential limitations arising from simplified 2D models.

Apart from the interaction between individual RBCs and the bifurcation, the breaking-down or recovery of CFLs in pre-/post-bifurcation branches is also a focus of computational studies [40,

323, 332]. The CFL is usually disturbed downstream of a bifurcation. Due to insufficient inter-bifurcation segment lengths, CFL symmetry may not be restored before reaching the next bifurcation. As a consequence, biased phase separation violating the empirical PSM model can occur. Indeed, a recent study of simulated microvascular network demonstrated highly asymmetric CFLs that vary along vessels segments [20]. The same authors also suggested that the influence of the skewness of the upstream haematocrit profile on the RBC partitioning at bifurcations [19].

2.3.4 RBC perfusion and vascular patterning: a prelude to Chapter 8

Sprouting angiogenesis is an essential vascularisation mechanism governing the formation of new blood vessels [43, 236], which takes place in both health (*e.g.,* embryonic development) and disease (*e.g.,* cancer or diabetic retinopathy). It consists of two well-differentiated stages: sprouting and remodelling. During the sprouting phase, a primitive network of vessels is laid out in response to morphogen gradients via a well-established programme of events [236, 288] (Figure 2.10). The remodelling phase is responsible for overhauling this primitive network into a hierarchical structure that can efficiently implement the nutrient transport and waste removal capabilities of the cardiovascular system.

During the remodelling phase, vessel pruning occurs throughout the vascular network to remove the excess of redundant segments relying on the behaviour of endothelial cells (ECs), whose metabolism and dynamics underpin the ultimate development of a functional vasculature [62, 235]. Figure 2.11a–b shows a premature vasculature of the developmental mouse retina, where abundant vessel pruning can be observed between postnatal day 6 and day 21. It is of fundamental interest to investigate what is driving such pruning processes, *e.g.,* whether they are genetically programmed or merely subject to the perfusion of blood flow.

The mechanobiological nature of ECs has been extensively studied in the literature and it is well established that ECs sense and react to their haemodynamic environment [180]. It has been shown in various animal models (including chick embryo [213], mouse yolk sac [189, 303], mouse aortic arch [317], zebrafish embryo [39, 48, 93, 156] and mouse retina [93] that blood itself serves as haemodynamic cues for vascular remodelling, rather than merely serving as a medium to circulate signalling molecules or deliver oxygen. These studies investigated in detail the haemodynamic

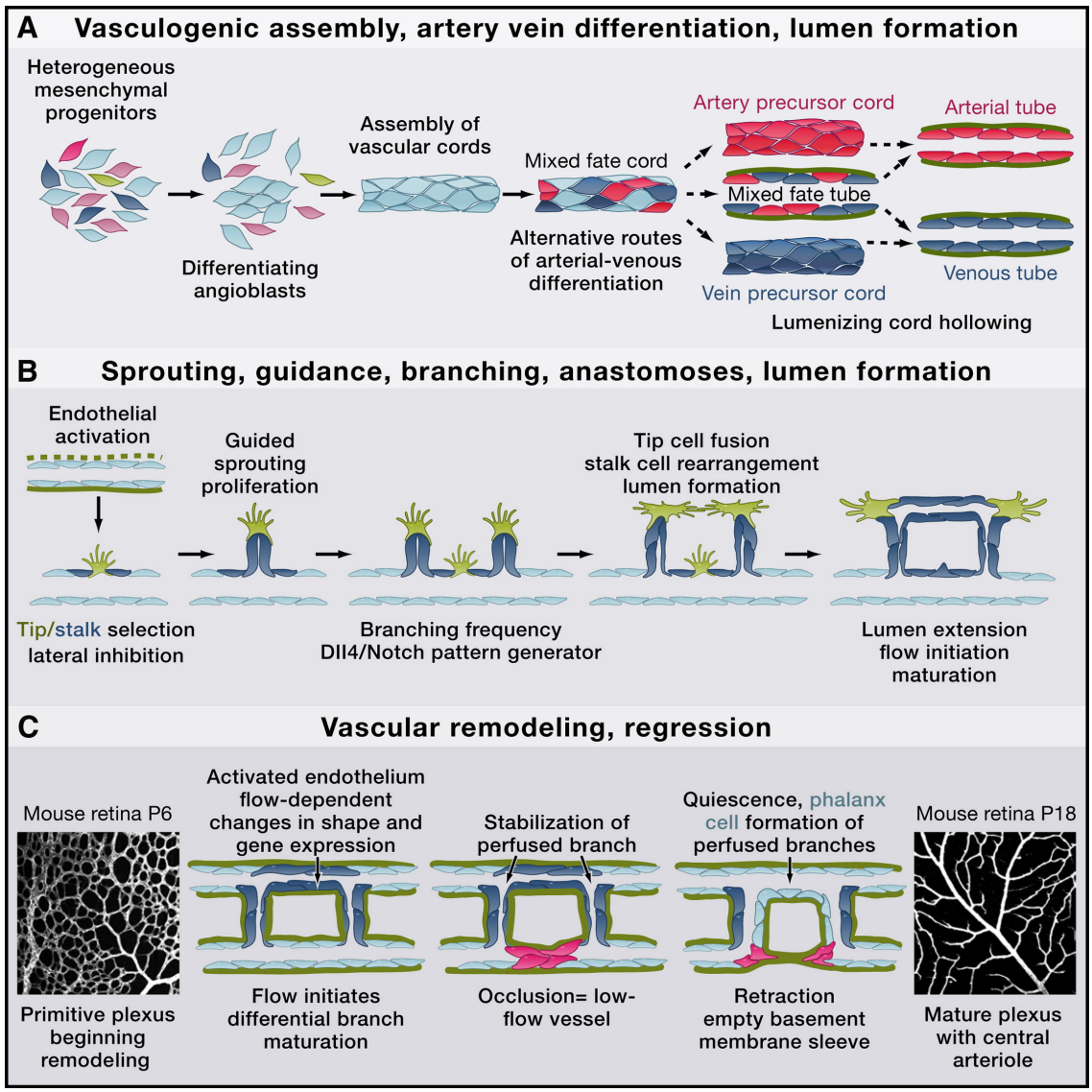

Figure 2.10: *Hallmarks of vessel growth in the embryo. (A) Differentiation of angioblasts into endothelial cells and subsequent formation of vessel cords and lumina. (B) Vessel sprouting, anastomosis and lumen formation. (C) Vascular remodelling from a primitive plexus towards a stabilized and mature network. (image from [236])*

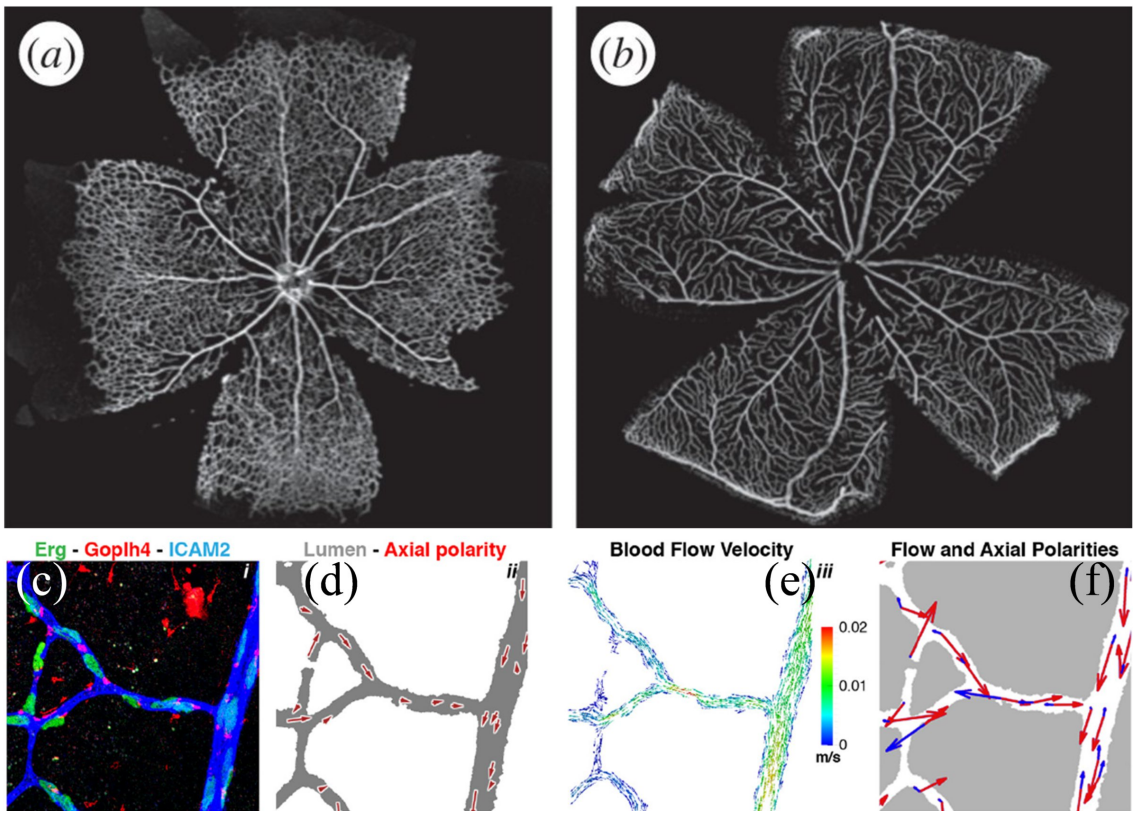

Figure 2.11: *(a-b) Vascular plexuses of mouse retina at postnatal day 6 and 21, respectively (Image from [30]). (c-f) Correlation between vascular remodelling and blood flow in mouse retina (Image from [94]): (c) a vascular plexus labelled for EC nuclei (Erg), vessel lumen (Icam2) and EC Golgi (Golph4); (d) image segmentation of the plexus with axial polarity vectors (pointing nuclei-Golgi direction) marked in red; (e) simulated blood flow pattern within the plexus; (f) correlation between axial polarity and blood flow direction at the endothelial nuclear position.*

links and have inspired the discovery of multiple flow-mediated signalling pathways and molecular modulators that regulate the endothelial activity in response to blood-induced shear stress, such as VEGF [16], Wnt [94], Notch [80, 192], TGFβ/BMP [61, 210, 305], DACH1 [45] and KLF2 [71].

Previous works have established how ECs use the information of fluid shear stresses to coordinate their behaviour throughout the remodelling phase to extensively prune the primitive network [93, 94, 305]. It is found that differences in wall shear stress (WSS) between neighbouring vessel segments led to polarisation and migration of ECs away from vessel segments experiencing low WSS (Figure 2.10c–f). Such a process of cell migration and convergent extension will contribute

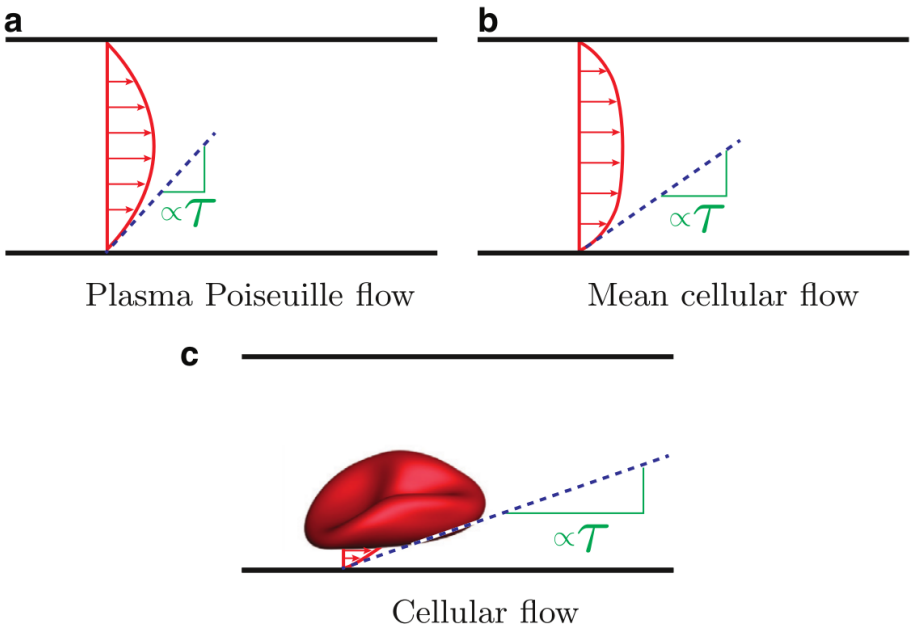

Figure 2.12: *Wall stress τ in (a) plasma-only Poiseuille flow, (b) mean cellular flow, and (c) instantaneous RBC flow. (Image from [100])*

to establishing preferential flow paths that eventually become the main flow axes of the network (*i.e.,* arteries, arterioles, venules, and veins) through a process not yet fully characterised.

Despite the important findings, a potential limitation existed in the quantification of WSS by these studies: the WSS values are estimated using mathematical flow models assuming simplified hemorheology without considering the presence of RBCs, whereas recent studies of WSS in microscale vessels imply that the cellular character of blood flow through the microvasculature cannot be neglected [19, 20, 150, 169, 217]. This is because the RBCs leave transient WSS footprints when travelling in microvessels [100, 131, 227] (see Figure 2.12 for a schematic illustration) and may non-trivially modify the local WSS differences predicted by simplified models without considering RBCs.

Chapter 3
Modelling of cellular blood flow

After the introduction of microcirculatory blood flow in Chapter 2, it should be clear now that the cellular character of blood is of paramount importance at the microscale and cannot be simply neglected if blood in microvessels (with diameters less than 300 μm where the CFL is prominent) or microvascular networks is to be modelled. This may pose critical challenges on the modelling task, as the inclusion of large number of discrete particles would render the simulation process highly non-linear, despite the fact that the flow itself in the microcirculation is typically of low Reynolds number and behaves linearly. The non-linearity comes from the arbitrarily deformed membranes of RBCs dispersed in the flow.

To mimic the dynamical behaviour of RBCs using simulations, their mechanical properties should be carefully considered by the numerical model. In the literature, a range of experimental measurements were dedicated to probe the RBC membrane and useful constitutive models have been formulated to describe the fundamental features of the membrane, *e.g.,* shearing and bending. Meanwhile, various modelling tools have been developed to model blood as particulate flow in recent years, largely benefiting from the fast development of modern computing facilities.

This chapter aims to elaborate on the requirements of modelling cellular blood flow and to provide a brief overview of existing numerical methods that are applied to simulate blood flow at the cell-scale. Furthermore, advantages of the lattice Boltzmann method over other available methods for modelling microcirculatory blood flow are introduced.

3.1 Physical ingredients

3.1.1 Hydrodynamics of blood

From a physical perspective, the motion of an incompressible fluid (including blood) is governed by the general incompressible Navier-Stokes equations (NSE):

$$\rho\left(\frac{\partial \boldsymbol{u}}{\partial t}+(\boldsymbol{u}\cdot\nabla)\boldsymbol{u}\right)=-\nabla p+\nabla\cdot\boldsymbol{\tau}+\boldsymbol{f},\quad\text{(momentum equation)} \tag{3.1}$$

$$\nabla\cdot\boldsymbol{u}=0.\quad\text{(continuity equation)} \tag{3.2}$$

In the NSE, ρ, $\boldsymbol{u}$ and p are the density, velocity and pressure of the fluid, respectively. $\boldsymbol{\tau}$ is the shear stress tensor accounting for the contribution of viscous dissipation, and $\boldsymbol{f}$ represents an external forcing term arising from gravity or other force fields. For a simple Newtonian fluid, $\boldsymbol{\tau}$ is linearly related to the strain tensor $\boldsymbol{\varepsilon}$ and Newton's constitutive law applies [25]:

$$\boldsymbol{\tau}=2\eta\boldsymbol{\varepsilon},\quad \boldsymbol{\varepsilon}=\frac{1}{2}\left(\nabla\boldsymbol{u}+(\nabla\boldsymbol{u})^{\mathrm{T}}\right) \tag{3.3}$$

where η is the dynamic viscosity, a constant for Newtonian fluids.

However, blood is a complex fluid with non-Newtonian behaviour and appears as shear-thinning, meaning that its apparent viscosity drops with increasing shear rates [50]. For blood, the linear strain-stress relation in Eq. (3.3) breaks down and alternative formulations are required to calculate $\boldsymbol{\tau}$ if the wall shear stress (WSS [254]), a flow property with important biological implications for vascular structure and function) is to be studied. An explicit formulation of $\boldsymbol{\tau}$ in this case can be complicated as blood is a soft matter containing manifold microstructures, due to the extraordinary deformability and rich dynamics of RBCs. The deformation of RBCs greatly adds to the complexity of blood by introducing elastic stresses on top of the hydrodynamic stresses, and the relative importance of these two types of stresses in the system should be characterised [161].

3.1.2 Dimensionless numbers

The motion and deformation of individual RBCs in shear flows is primarily determined by two non-dimensional numbers, namely the Reynolds number Re and the capillary number Ca. There

are two different Reynolds numbers involved when considering particle-laden flow at the microscale. The first one is the channel Reynolds number Re_{c}, charactering the ratio of inertial to viscous forces within the fluid. The second is the particle Reynolds number Re_{p}, charactering the ratio of particle inertia to fluid viscous force, is defined based on Re_{c}. Re_{c} and Re_{p} are given by

$$Re_{\mathrm{c}} = \rho_{\mathrm{ex}} \bar{u} D_{\mathrm{h}} / \eta_{\mathrm{ex}}, \quad Re_{\mathrm{p}} = Re_{\mathrm{c}} \left(2 r_{\mathrm{rbc}} / D_{\mathrm{h}}\right)^2 \tag{3.4}$$

where r_{rbc} is the RBC radius and D_{h} is the hydraulic diameter of the channel; $\bar{u}$ is the cross-sectional mean velocity of the unperturbed flow; ρ_{ex} and η_{ex} are the density and dynamic viscosity of the suspending fluid exterior to the RBC membrane, respectively. Ca measures the deformation of RBC membrane when exposed to shear and is defined using the membrane shear elasticity (evaluated by the strain modulus κ_s) as

$$Ca = \tau \dot{\gamma}_{\mathrm{c}}, \quad \tau = \eta_{\mathrm{ex}} r_{\mathrm{rbc}} / \kappa_s, \quad \dot{\gamma}_{\mathrm{c}} = 8\bar{u} / D_{\mathrm{h}} \tag{3.5}$$

where τ is a characteristic time scale for the RBC membrane to relax from a transient state to its equilibrium shape and $\dot{\gamma}_{\mathrm{c}}$ is the characteristic wall shear rate in an equivalent Poiseuille flow.

3.1.3 Modelling considerations

Modelling complex soft matter like blood is in general challenging and expensive, even with state-of-the-art computing facilities, owing to the existence of multiple length and time scales in the system [264]. It is often necessary to identify the key aspects of the research objective and make reasonable simplifications for less important effects. As for the present thesis, which focuses on the haemodynamics under microcirculatory conditions (*e.g.,* in microvessels or capillary beds), the deformation and collective dynamics of RBCs are of paramount importance. Therefore, the RBCs should be sufficiently resolved to reflect their intricate morphologies in potentially sparse and complex geometries. Also, the hydrodynamic interactions between RBCs should be accurately modelled to ensure that collective behaviours are captured as one would observe from experiments. However, advanced biophysical properties of the RBC membrane or biochemical interactions between individual RBCs, albeit desirable for physical realism and broader impact [95], are secondary for this thesis and will not be considered.

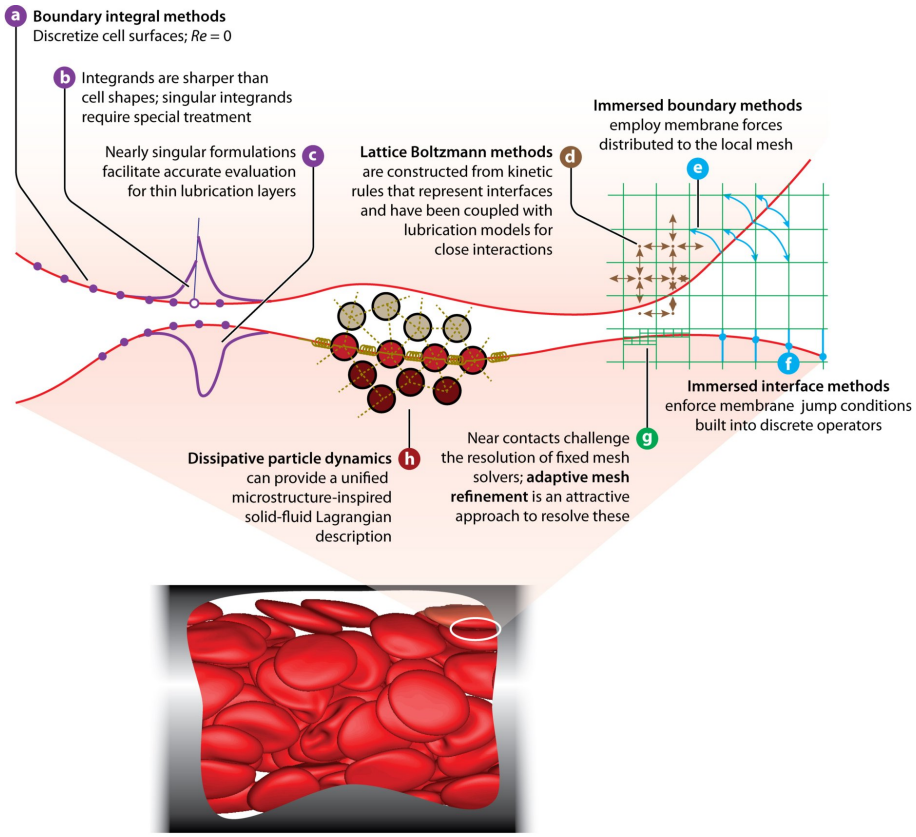

Freund JB. 2014.
Annu. Rev. Fluid Mech. 46:67–95

Figure 3.1: *Illustration of numerical methods simulating cellular blood flow. (Image from [95])*

3.2 Overview of cellular blood flow models

A variety of numerical models have emerged over the past two decades for the simulation of cell-level blood flow (see Figure 3.1 and Table 3.1), which is generally regarded as a suspension of blood cells and particles dispersed in a Newtonian solvent, *i.e.,* the plasma (although it shows bulk viscoelasticity when experiencing strong extension rates [36, 304]). The simulation of cellular blood flow is essentially a multiphase flow problem and any model designed for this purpose has three main components to consider: the fluid phase (plasma), the cell phase (RBCs) and the fluid-structure interaction (FSI) between them. Choosing a flow model is usually the priority, and the RBC model as well as fluid-cell coupling algorithm can be decided accordingly. In many cases, a generic RBC model or FSI scheme can be suited to multiple flow models. Depending

Table 3.1: *Mainstream numerical methods applied for cellular blood flow simulation since 2000.*

Flow model	Length scale	Discretisation	Representative works
FDM/FEM/FVM	macroscale	mesh-based (M)	Liu *et al.* [185], Liu and Liu [184], Bagchi [17], Doddi and Bagchi [72], Jafari *et al.* [140], Ye *et al.* [324], Lan and Khismatullin [168], Tan *et al.* [298], Xu *et al.* [314], Shi *et al.* [280], Balogh and Bagchi [18], Iss *et al.* [139]
DPD	mesoscale	particle-based (P)	Pivkin and Karniadakis [232], Fedosov *et al.* [82], Fedosov *et al.* [84], Pan *et al.* [228], Li *et al.* [179], Lei *et al.* [172], Ye *et al.* [328], Zhang *et al.* [336], Lykov *et al.* [191], Pivkin *et al.* [233], Blumers *et al.* [32], Alexeev *et al.* [11]
SDPD	mesoscale	particle-based (P)	Fedosov *et al.* [86], Katanov *et al.* [150], Lanotte *et al.* [169], Müller *et al.* [207], Ye *et al.* [330], Mauer *et al.* [197], Ye and Peng [325], Ye *et al.* [326], Li *et al.* [174], Li *et al.* [175]
LBM	mesoscale	hybrid (M)-(P)	Dupin *et al.* [75], Zhang *et al.* [335], Sui *et al.* [291], Sun and Munn [294], Melchionna [201], Krüger [161], Yin *et al.* [332], Gross *et al.* [115], Závodszky *et al.* [342], Kotsalos *et al.* [158], Czaja *et al.* [65], Latt *et al.* [170], Zhou *et al.* [339], Guglietta *et al.* [119]
BIM/BEM	macroscale	boundary integral	Pozrikidis [237], Zhao *et al.* [337], Freund and Orescanin [99], Freund and Vermot [100], Salehyar and Zhu [261], Bryngelson *et al.* [38], Lu and Peng [188]

on how the flow is solved (namely the flow solver), existing models employed for cellular blood flow simulation can be classified into four categories: continuum-fluid models, particle-based models, hybrid mesh-particle models and integral-based models (see recent reviews on numerical simulation of cellular blood flow [14, 85, 95, 137, 143, 264, 329]).

The first category, namely continuum models, directly solves the incompressible NSE through a mesh-based discretisation strategy and solutions of the flow (*e.g.,* velocity and pressure) are obtained on discrete nodes of the mesh. Based on how the solutions are discretised and interpolated in the continuous flow filed, there generic methods exist: finite-difference method (FDM), finite-volume method (FVM) and finite-element method (FEM). These methods serve as the cor-

nerstones of conventional computational fluid dynamics (CFD) and have seen wide applications across different realms of fluid mechanics including the simulation of biological flows [218]. However, in the context of blood flow, they are more often used for simulating larger-scale systems where the particulate nature of blood can be neglected (*e.g.,* in arteries or macrocirculatory networks) [137]. For cellular blood flow at the microscale where the continuum assumption breaks down and the intricate RBC dynamics need to resolved and coupled with the flow solutions, the requirement of meshing quality for FDM/FVM/FEM is demanding, especially when complex geometries are involved. Furthermore, solving the implicit pressure terms (governed by a Poisson equation) in the presence of arbitrarily evolving RBC membranes can be an excessively expensive task. Therefore, advanced models incorporating multi-scale algorithms are often required for these conventional CFD methods to simulate microcirculatory blood flow at the cell scale. For recent studies on cellular blood flow falling into this category, please refer to Table 3.1.

The second category, namely particle-based models, adopts a mesoscopic approach (see definition of "mesoscopic" in Figure 3.2) to describe the flow using a collection of particles (each particle representing a group of atoms or molecules) which interact with each other in the computational domain. Rather than directly solving the NSE, these models are of stochastic nature and recovers the hydrodynamics described by NSE at the macroscopic level via averaging. Because of their intrinsic molecular composition (related to molecular dynamics, MD), these models are naturally amenable to the inclusion of microscopic structures in the flow, such as discrete RBCs. Common methods in these category include dissipative particle dynamics (DPD [133]), multiple-particle collision dynamics (MPC [194]), smoothed particle hydrodynamics (SPH [108, 190]) and moving-particle semi-implicit method (MPS [157]). Smoothed dissipative particle dynamics (SDPD [79]), a hybrid method combing the advantages of SPH and DPD, has also been exploit to combine advantages from both methods. Representative studies that have applied the particle-based models to simulate cellular blood flow are listed in Table 3.1. The essence of these mesoscopic models is to "coarse-graining" the microscopic details of a complex system (which may contain too many degrees of freedom to be effectively resolved by MD) and to allow the bridging of multiple time and length scales [264]. When simulating cellular blood flow, a set of particles are applied for the solid boundary, the suspending medium, the cell membrane and the cytoplasm, respectively. External/internal fluids of the RBC are separated through bounce-back reflections at the interface

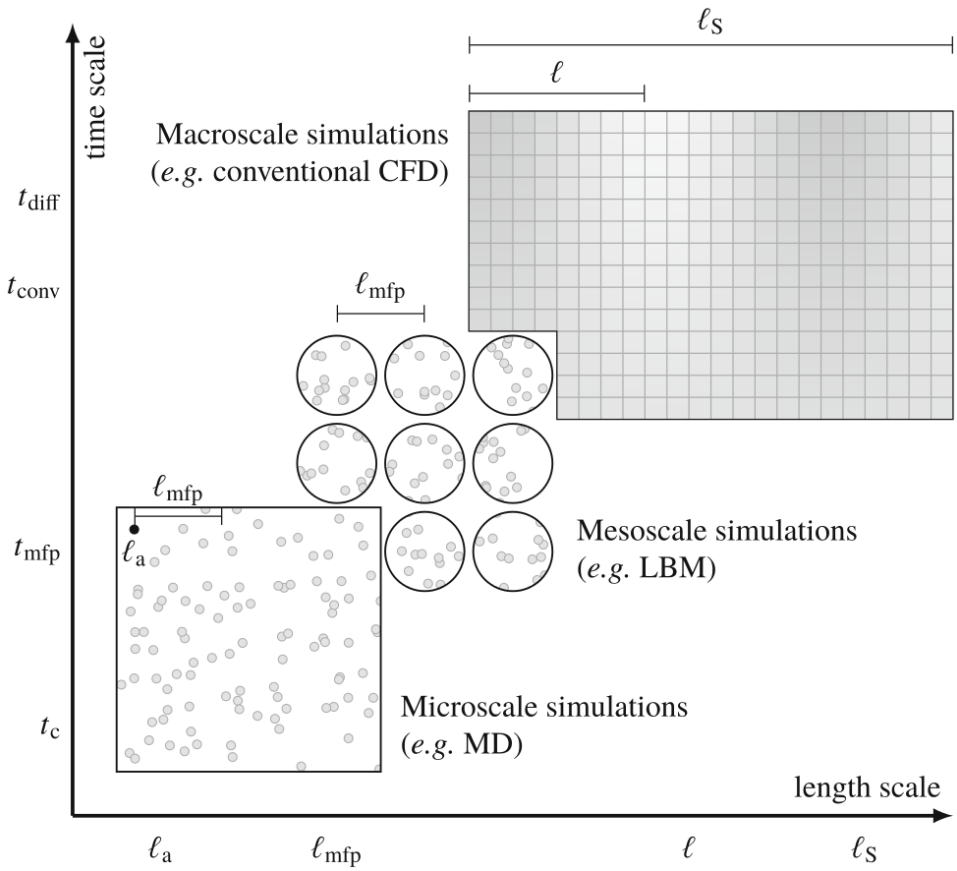

Figure 3.2: *Sketch of length and time scales for microscopic, mesoscopic and macroscopic numerical methods. (Image from [164])*

and no-slip boundary conditions on the membrane are realised through viscous force coupling or collisions [85]. One potential issue for the particle-based methods is their computational overhead when a large number of cells are simulated or complex geometries are involved. Another issue is that the physical interpretation of RBC membrane (ideally of negligible mass against the cytoplasm) may be challenged when the number of membrane particle need to be large (thus violating the mass-free requirement for the membrane) to adequately resolve extreme RBC deformations [329]. Furthermore, for DPD and MPC, their accuracy for hydrodynamics at length scales much larger than the RBC may be questioned despite the highly resolved cell phenomenology [95].

The third category, namely hybrid mesh-particle models, is represented by the growingly popular lattice Boltzmann method (LBM [200, 289]) over recent years, which is also a mesoscopic

method but based on a regular of uniform grids (the so-called "lattice"). Unlike the particle-based models which track the "particles", LBM is formulated to reflect the probability distribution of these particles in accord with kinetic theory. To enable simulation of particle-laden flows, LBM is commonly combined with the immersed-boundary method (IBM [230]), a widely employed FSI technique that can be easily incorporated into various flow solvers. In a typical IB-LBM computational framework involving moving RBCs or other cells, physical quantities such as velocities and forces are interpolated between Eulerian nodes on the fixed fluid mesh and Lagrangian nodes from the membrane mesh of the cells. The membrane mesh does not need to conform to the fluid mesh and can evolve arbitrarily over space and time. Owing to its ease of numerical implementation, flexibility for complex geometry and amenability to parallel computing, IB-LBM has become widely applied for the simulation of complex biological flows in the past decade (see Table 3.1 and recent reviews [8, 28, 218]). Because IB-LBM is the method chosen by the present thesis, the introduction of it will be given in more detail elsewhere (Sec. 3.3 and Sec. 4.1.1).

The last category, namely integral-based models, relies on the boundary integral method (BIM) or boundary element method (BEM) to formulate and couple the Stokes flow onto the cell membrane (see representative works in Table 3.1 and detailed introduction in recent reviews [26, 95]). The cell membrane itself is usually modelled as spectral elements and can be precisely represented [70, 337]. Due to its rigorous mathematical formulation, BIM/BEM methods are arguably the most accurate method for resolution of the cell membrane (approximated by spherical harmonics), especially at close cell-cell distances [98]. However, their strict requirement of Stokes limit may render the model impractical for solving blood flows in realistic vascular networks, as finite inertia exists in relatively larger microvessels. Also, BIM/BEM methods are usually expensive for 3D models, and may not work well with sparse and complex flow geometries encountered in the microcirculatory system.

3.3 Why lattice Boltzmann method (LBM)?

Computational modelling of blood flow is a multidisciplinary subject at the interface of physics, biology and engineering. Choosing a method is problem-specific, depending on the system to be tackled and the research after pursuit. Often, compromises need to be made between accuracy

(*e.g.,* how small is the numerical artefact and how realistic is the cell biology) and capacity (*e.g.,* how large the simulation domain can be extended to and how many cells can be included). Meanwhile, a balance between input and yield needs consideration to avoid unnecessary computational cost. Reviewing the modelling considerations for the present thesis as in Sec. 3.1.3, there are three primary requirements for the model to work: first, sparse and complex flow domains should be allowed, *e.g.,* a microvascular network; second, low Reynolds number flows (but non-zero inertia) need to be solved with accuracy for confidence in the resultant hydrodynamics (*e.g.,* velocity and stress); third, a moderate or large number of deformable RBCs need to be resolved with sufficient details, including their motion, deformation and collective transport. Given all these requirements, the ideal model should be either highly efficient or capable of parallel computing.

LBM is intrinsically localised, naturally parallelisable and can easily accommodate complex or sparse fluid domains. Furthermore, either velocities or stresses solved by standard LBM can preserve 2nd-order accuracy. Combined with the versatile IBM for tracking RBCs, an IB-LBM model conveniently satisfies all the aforementioned requirements provided that a proper RBC model is incorporated. Over recent years, multiple IB-LBM models have been developed for the simulation of cellular blood flow [158, 165, 292, 335, 342].

Part II

METHODS

All models are wrong, but some are useful.

— George E. P. Box

Chapter 4
Computational modelling and experimental corroboration

The present thesis reports on research projects that are highly collaborative in nature, and contain both computational and experimental elements. The computer simulations and pertinent analyses are entirely my own work; the experiments are performed by my collaborators, but the analysis and interpretation of experimental data regarding the research questions is led by myself. To make research results in later chapters of the thesis easier to understand, this chapter is dedicated to introduce the fundamental aspects of all methods involved, either computational or experimental. Contributions from the experimentalists will be explicitly referenced in the text.

Sec. 4.1 covers the computational model, which is made available to this PhD for validation and application in the context of microcirculatory blood flow. The model has been systematically validated by myself before employed to design computer simulations for research projects. Because the primary interest of this thesis is to adapt existing numerical tools (rather than developing new software) for simulating cellular blood flow in complex vascular networks, only key elements of the computational model are covered in this section. More comprehensive details such as mathematical formulation and numerical implementation will be referred elsewhere.

Sec. 4.2 covers the relevant methods for microfluidic experiments in Chapters 6–7, including experimental setup, sample preparation, data acquisition and image analysis. The figures and text in this section are by courtesy of Joana Fidalgo at the University of Strathclyde (Glasgow, UK).

Sec. 4.3 covers the relevant methods for animal experiments in Chapter 8, including the preparation and imaging of microvasculatures in developmental mouse retina/zebrafish caudal vein plexus. Herein, figures and text for mouse experiments are provided by Tijana Perovic at Max-Delbrück-Center for Molecular Medicine in the Helmholtz Association (Berlin, Germany), while those for zebrafish experiments are by courtesy of Ines Fechner at the same institute.

4.1 Model, simulation and numerics

4.1.1 Computational model

4.1.1.1 Overview

In the present thesis, a three-dimensional (3D) immersed-boundary-lattice-Boltzmann model (IB-LBM [161]) parallelised through Message Passing Interface (MPI) is validated and applied to simulate cellular blood flow in a range of biologically relevant geometries. The model is implemented in the open-source lattice-Boltzmann flow simulator *HemeLB* [198] (`http://ccs.chem.ucl.ac.uk/hemelb`) by incorporating a new module for discrete deformable cells. The fluid flow governed by the Navier-Stokes equations is solved by the lattice-Boltzmann method (LBM, [122, 164, 289]) with standard D3Q19 lattice [251], Bhatnagar-Gross-Krook (BGK) collision operator [31], Guo's forcing scheme [123] and the Bouzidi-Firdaouss-Lallemand (BFL) no-slip boundary condition at the walls [33]. For precise control of the flow in complex geometry with multiple inlets/outlets, inflow/outflow open boundaries are implemented with the Ladd velocity boundary condition [167]. The RBCs are modelled as Lagrangian membranes using finite element method (FEM). The fluid flow and RBC membrane are coupled through the immersed-boundary method (IBM, [231]), which tackles the interpolation of velocities and the spreading of forces. The following sections will give a concise introduction to the three pillars of the computational model, namely the flow solver, the RBC model and the fluid-cell coupling.

4.1.1.2 Flow solver

First applied to overcome statistical noises of the Lattice Gas Automata (LGA, [101, 125]), LBM was invented in the late 1980s [128, 200] and has seen growing applications in the simulation of complex fluid flows over recent decades [8, 49]. It is based on the kinetic theory and numerically solves the Boltzmann equation using a mesoscopic approach, from which the macroscopic Navier-Stokes equations can be recovered by invoking the Chapman-Enskog analysis [46].

At the heart of LBM is the probability density function $f(\boldsymbol{x}, \boldsymbol{c}, t)$, which represents the probability of having particles with velocity $\boldsymbol{c}$ at position $\boldsymbol{x}$ and time t. In LBM, the Boltzmann equation is discretised not only for space and time (Δx and Δt), but also for the microscopic particle velocity,

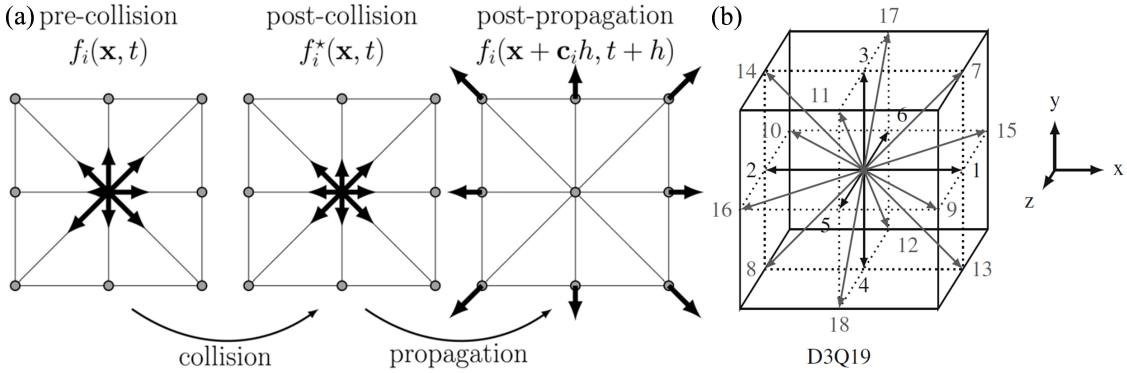

Figure 4.1: *(a) Schematic of population collision and propagation on a D2Q9 lattice (Image from [264]). (b) Schematic of the D3Q19 lattice for 3D simulation (Images from [164]).*

leading to the lattice Boltzmann equation (LBE)

$$f_i(\boldsymbol{x}+\boldsymbol{c_i}\Delta t, t+\Delta t) = f_i^*(\boldsymbol{x},t) = f_i(\boldsymbol{x},t) + \Omega_i(\boldsymbol{x},t), \tag{4.1}$$

where $\boldsymbol{c_i}$ $(i = 0, ..., q-1)$ is a designated set of velocity vectors at each node (based on velocity discretisation) of a d-dimensional regular lattice. Common choices of the velocity set to recover accurate hydrodynamics at the macroscale include D2Q9 for 2D simulation and D3Q19 for 3D simulation (Figure 4.1). $\Omega_i(\boldsymbol{x},t)$ is the collision operator that allows all q particle populations to evolve towards a local equilibrium f_i^{eq}, which observes the Maxwell-Boltzmann distribution (MBD).

A widely applied collision operator is the Bhatnagar-Gross-Krook collision operator (BGK, [31]), which relaxes the populations at a constant rate of $1/\tau$ towards f_i^{eq} (τ being the dimensionless relaxation time):

$$\Omega_i(\boldsymbol{x},t) = -\frac{1}{\tau}\left(f_i(\boldsymbol{x},t) - f_i^{\mathrm{eq}}(\boldsymbol{x},t)\right) + f_i^F(\boldsymbol{x},t)\Delta t, \tag{4.2}$$

where

$$f_i^F = \left(1-\frac{1}{2\tau}\right) w_i \left(\frac{\boldsymbol{c_i}-\boldsymbol{u}}{c_s^2} + \frac{\boldsymbol{c_i}\cdot\boldsymbol{u}}{c_s^4}\boldsymbol{c_i}\right)\cdot\boldsymbol{f} \tag{4.3}$$

is a forcing term added to reflect the effect of external forces, *e.g.,* a body force density $\boldsymbol{f}$ [123]. Herein, w_i represent specific weights assigned to the velocity set $\boldsymbol{c_i}$ and the values vary for different choices of lattice. c_s is the lattice speed of sound ($c_\mathrm{s} = \Delta x/\sqrt{3}\Delta t$ for both D2Q9 and D3Q19 lattices) which relates the microscopic relaxation time τ of the populations to the macroscopic

kinematic viscosity ν of the fluid

$$v = c_{\mathrm{s}}^2 \left(\tau - \frac{1}{2}\right) \Delta t. \tag{4.4}$$

Each time step of the LBE Eq. (4.1) contains two successive processes: local collision (also termed relaxation) of populations at present node towards the equilibrium distribution and non-local propagation of post-collision populations (also termed streaming) along the discretised velocities of the present node to neighbouring nodes (see an illustrative schematic in Figure 4.1). The post-collision and post-propagation populations are denoted $f_i^*(\boldsymbol{x}, t)$ and $f_i(\boldsymbol{x} + \boldsymbol{c_i}\Delta t, t + \Delta t)$ in Eq. (4.1), respectively. The local equilibrium distribution derived from the MBD is given by

$$f_i^{\mathrm{eq}}(\boldsymbol{x}, t) = w_i \rho \left(1 + \frac{\boldsymbol{u} \cdot \boldsymbol{c_i}}{c_{\mathrm{s}}^2} + \frac{(\boldsymbol{u} \cdot \boldsymbol{c_i})^2}{2c_{\mathrm{s}}^4} - \frac{\boldsymbol{u} \cdot \boldsymbol{u}}{2c_{\mathrm{s}}^2}\right), \tag{4.5}$$

wherein ρ the mass density and $\boldsymbol{u}$ the flow velocity are macroscopic properties of the fluid readily to be obtained from the zeroth and first moments of the local populations

$$\rho(\boldsymbol{x}, t) = \sum_i f_i(\boldsymbol{x}, t), \quad \boldsymbol{u}(\boldsymbol{x}, t) = \frac{1}{\rho} \sum_i \boldsymbol{c_i} f_i(\boldsymbol{x}, t) + \frac{\Delta t}{2\rho} \boldsymbol{f}. \tag{4.6}$$

The pressure p is obtained via the equation of state

$$p = c_{\mathrm{s}}^2 \rho, \tag{4.7}$$

which is needed for solving a incompressible fluid (with constant ρ) as the LBE itself is weakly compressible and the system of equations are not closed without an equation of state.

One notable feature of LBM is that the shear stress tensor $\boldsymbol{\tau}$ (needed for wall shear stress calculation) can be obtain from the local populations with ease:

$$\boldsymbol{\tau} = -\left(1 - \frac{1}{2\tau}\right) \sum_i (f_i - f_i^{\mathrm{eq}}) \boldsymbol{c_i} \boldsymbol{c_i} + \boldsymbol{\Gamma_c}, \tag{4.8}$$

where

$$\boldsymbol{\Gamma_c} = -\frac{\Delta t}{2}\left(1 - \frac{1}{2\tau}\right)(\boldsymbol{u}\boldsymbol{f} + \boldsymbol{f}\boldsymbol{u}) \tag{4.9}$$

is a lattice correction term accounting for the external forces [123].

4.1.1.3 RBC model

As introduced in Sec. 2.2.2, an RBC is primarily a given volume of haemoglobin solution encapsulated by a membrane that deforms in response to fluid forces and vessel confinement. There are in general two categories of RBC models employed by researchers in the community of cellular blood flow: continuum-level models relying on constitutive laws and network-based models utilising spectrin-link representation (see the review [85]). Ideally, the following conditions need to be satisfied by an RBC model to accurately reflect both the mechanics and dynamics of a real RBC:

- An equilibrium state of the cell should be properly defined, from which the cell deforms when exposed to external stresses. To date, the cell shape for the equilibrium state is not conclusively determined in literature and several options have been reported, including biconcave, spherical or oblate spheroidal [89, 116, 197, 282]. Once the external stresses are removed, the cell shape should recover to the equilibrium state after some relaxation time, featuring a "shape memory" [60, 90].

- The surface and volume of the cell are strictly incompressible [181, 206] and therefore should keep conserved as the cell deforms.

- The membrane of the cell should be able to resist both in-plane shearing (contributed by the cytoskeleton) and off-plane bending (mainly contributed by the lipid bilayer), manifested as shearing elasticity and bending rigidity, respectively [18, 82, 86, 158, 161, 177, 281].

- The viscous dissipation of the lipid bilayer, represented by membrane viscosity, should also be taken into account [52, 130]. The membrane viscosity has been reported to be important for the frequencies of RBC's TB and TT motion as well as the transition between the two regimes [318, 320, 321]. It also affects the relaxation time of the RBC membrane [119, 239].

- The cytoplasmic viscosity should be considered different from that of the plasma if the RBC morphology and blood viscosity are to be accurately characterised [169, 197], the effect of which has been demonstrated by Figure 2.5 in Sec. 2.2.2.

In reality, satisfying all criteria above is challenging for modelling of cellular blood flow at realistic length/time scales, both in terms of numerical complexity and computational cost. Depending

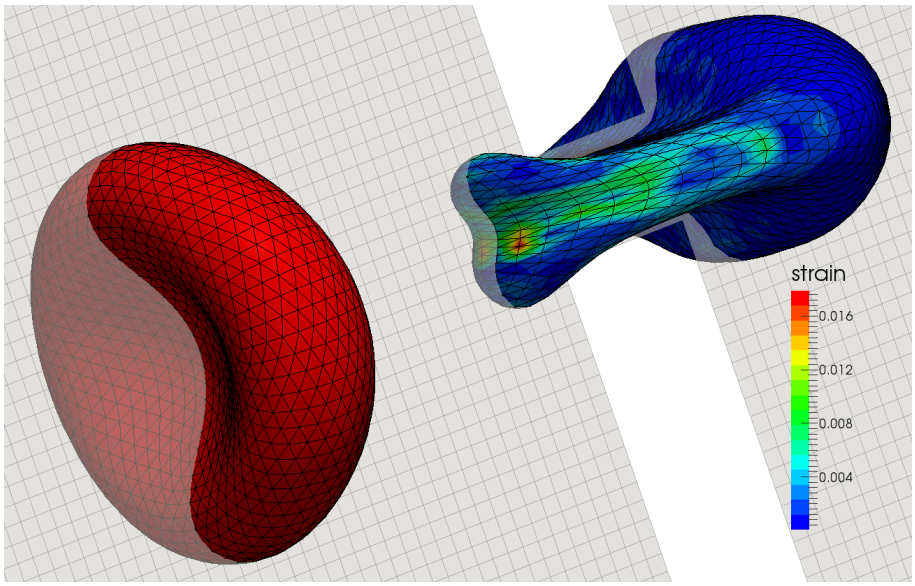

Figure 4.2: *Deformation of shape and distribution of strain on the membrane as a deformable RBC approaches a narrow passage (imitating the spleen slit) and squeezes itself through. A slice of the flow domain is shown in the background with grey lattices.*

on the research question, it is often necessary to make justified simplifications. For instance, the membrane viscosity is usually ignored when in-plane shearing of the RBC membrane insignificant [169, 197]. Assuming identical viscosity for the cytoplasm to the suspending fluid is another simplification commonly made for studies aiming at macroscopic flow properties rather than single cell rheology, *e.g.,* the collective behaviour of RBC suspensions within microchannels and the development of CFL near the wall [40, 150, 239, 277, 343]. Recent numerical studies evidently demonstrate that the influence of cytoplasmic viscosity (therefore viscosity contrast) is weak regarding flow resistance and CFL thickness [54, 68, 260]. Furthermore, it has been reported that the effect of a higher viscosity contrast can be well approximated with decreased RBC deformability [7], which can be tuned via modifying the membrane elasticity or flow shear rates.

For simulations included in the present thesis, each RBC is modelled as a liquid-filled hyperelastic membrane that is homogeneous and isotropic (RBC model validated in [161]). Because this thesis does not aim at characterising the morphological variation or regime transition of individual RBCs, the membrane viscosity is assumed of secondary effect and therefore not considered in the current model. Also given the focus of this thesis, namely the transport phenomena of RBCs in

microcirculatory blood flow, the viscosity contrast between the RBC internal fluid (*i.e.,* cytoplasm) and external fluid (*i.e.,* plasma) is considered as unit for computational efficiency. A recent study similarly employing IB-LBM combined with a novel FEM model for the RBC has also made the same simplification provided that collective transport rather than cell rheology is concerned [158].

Using a finite element approach, the RBC membrane is evenly discretised into N triangular facets (Figure 4.2), with the meshing resolution matching the grid size of the LBM lattice constant Δx for numerical stability and accuracy [165]. A general rule of thumb is $N = 20(r_{\mathrm{rbc}}/\Delta x)^2$ such that the average edge length of the membrane mesh $\tilde{l}$ roughly equals the lattice size Δx. The unstressed shape of the RBC is assumed as a biconcave discoid and the mechanical properties of the RBC are controlled by five moduli which govern different energy contributions. They are the strain modulus κ_{s}, the dilation modulus κ_α, the bending modulus κ_{b}, the surface modulus κ_{A} and the volume modulus κ_{V}. To begin with, κ_{s} and κ_α are from Skalak's constitutive model governing RBC deformation [285]:

$$E_{\mathrm{S}} = \int dA\, \epsilon_S, \quad \epsilon_S = \frac{\kappa_{\mathrm{s}}}{12}(I_1^2 + 2I_1 - 2I_2)) + \frac{\kappa_\alpha}{12} I_2^2 \tag{4.10}$$

where E_{S} is the in-plane strain energy and ϵ_S is the area density of it. I_1 and I_2 are strain invariants describing the local shear deformation and area dilation of the RBC membrane, respectively. κ_{b} is derived from the Helfrich bending energy E_{B} [116]:

$$E_{\mathrm{B}} = \frac{\kappa_b}{2} \oint \mathrm{d}A (H - H_{(0)})^2 \tag{4.11}$$

where H is trace of the surface curvature tensor and $H_{(0)}$ is the spontaneous curvature, a local invariant property of the RBC membrane (see a detailed discussion of "spontaneous curvature" in [116]). κ_A and κ_V are numerical penalties for surface and volume deviations and are defined following [273]:

$$E_{\mathrm{A}} = \frac{\kappa_A}{2} \frac{(A - A_{(0)})^2}{A_{(0)}} \tag{4.12}$$

$$E_{\mathrm{V}} = \frac{\kappa_V}{2} \frac{(V - V_{(0)})^2}{V_{(0)}} \tag{4.13}$$

where E_{A} and E_{V} are the corresponding energies. $A_{(0)}$ and $V_{(0)}$ are the equilibrium surface area and volume, and A and V stand for the current surface area and volume.

The values of κ_{s} and κ_{b} are determined based on experimental measurements of the RBC membrane, whereas κ_α, κ_A and κ_V are selected in a way to constrain the local area, RBC surface and RBC volume so that the simulation is stable. With these RBC moduli as input, the FEM model discretise and numerically evaluate Eqs. 4.10–4.13 to calculate the total membrane energy E_{rbc}:

$$E_{\mathrm{rbc}} = E_{\mathrm{S}} + E_{\mathrm{B}} + E_{\mathrm{A}} + E_{\mathrm{V}} \tag{4.14}$$

The forces $\boldsymbol{F_i}$ imposed on individual membrane vertices of the RBC membrane i at positions $\boldsymbol{x_i}$ can be computed base on the principle of virtual work as:

$$\boldsymbol{F_i} = -\frac{\partial E_{\mathrm{rbc}}\left(\{\boldsymbol{x_i}\}\right)}{\partial \boldsymbol{x_i}} \tag{4.15}$$

4.1.1.4 Fluid-cell coupling

The flow solver and RBC model should be coupled in a bidirectional manner: the cells move with the ambient fluid flow, whereas the flow responds to the motion of cell membranes that impose additional boundary conditions. One method to realise this coupling is IBM, which was developed in 1972 by Peskin [230] and first combined with LBM for RBC simulations in 2007 [17, 75, 335]. The elegance of IBM lies in its explicitness of implementation and flexibility of coupling. To incorporate IBM into a flow model, there are essentially no modifications needed for the flow solver except the addition of a forcing term. Furthermore, the immersed boundaries in the fluid can have arbitrary shapes without conforming to the fluid mesh. IBM relies on the introduction of two coordinate systems to address the fluid-structure interaction (Figure 4.3): an Eulerian one consisting of regular Cartesian mesh ($\boldsymbol{X}$, stationary over time) to describe the fluid motion and a Lagrangian one to map the cell membranes ($\boldsymbol{x_i}$, evolving over time) on top of the Cartesian mesh. Rather than directly imposing solid boundaries that arise from the fluid-cell interfaces, IBM enforces boundary conditions via body forces to mimic the presence of "imaginary" and massless cell membranes immersed in the fluid.

There are two essential steps for the IBM scheme to work smoothly: the flow velocities are locally interpolated to update the positions of membrane vertices, which is called velocity interpolation; the forces acting on the membrane vertices are spread back to the Eulerian mesh to update the

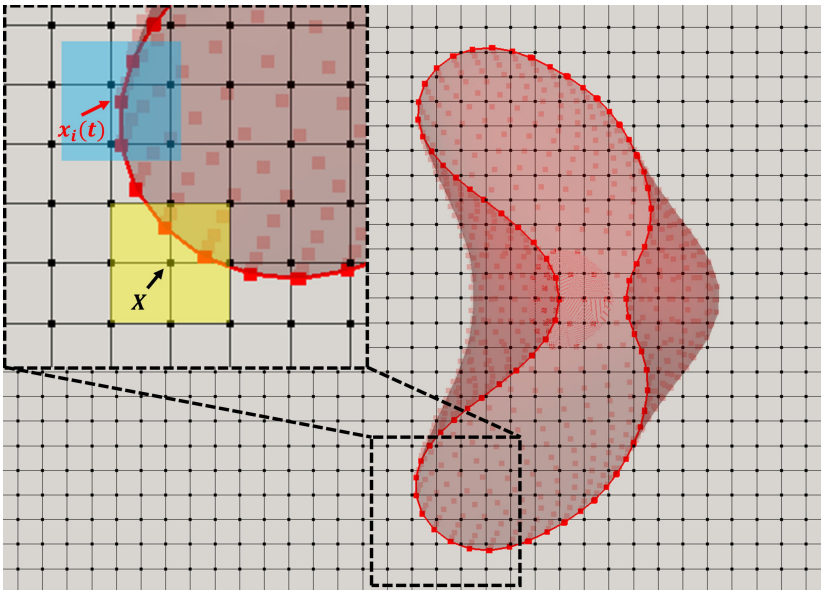

Figure 4.3: *Illustration of the fluid-cell coupling. The inset demonstrates velocity interpolation within the blue patch and force spreading within the yellow patch. The range over which (*i.e., *number of nodes covered by the coloured patch) the interpolation is implemented depends on the choice of interpolation stencil for the Dirac delta function.*

flow field (via solving the NSE), which is called force spreading. These two steps are realised via transformations using the discretised Dirac delta function $\Delta\left(\boldsymbol{x_i}(t)-\boldsymbol{X}\right)$ that serves as the interpolation function [231] (also known as interpolation kernel):

$$\dot{\boldsymbol{x_i}}(t+1)=\sum_{\boldsymbol{X}}\boldsymbol{u}(\boldsymbol{X},t+1)\Delta\left(\boldsymbol{x_i}(t)-\boldsymbol{X}\right) \tag{4.16}$$

$$\boldsymbol{f}(\boldsymbol{X},t)=\sum_{i}\boldsymbol{F_i}(t)\Delta\left(\boldsymbol{x_i}(t)-\boldsymbol{X}\right) \tag{4.17}$$

For numerical implementation, the interpolation function $\Delta\left(\boldsymbol{x}\right)$ is factorised as the product of interpolation stencils for each lattice direction

$$\Delta\left(\boldsymbol{x}(x,y,z)\right)=\phi(x)\phi(y)\phi(z) \tag{4.18}$$

Unless otherwise specified, the 3-point interpolation stencil $\phi_3(x)$ is applied for all simulations in the present thesis, which suits well for LBM in terms of computational efficiency while preserving

accuracy in resultant hydrodynamics:

$$\phi_3(x) = \begin{cases} \frac{1}{3}(1+\sqrt{1-3x^2}) & \text{for} \quad 0 \leq |x| \leq \frac{1}{2} \\ \frac{1}{6}(5-3|x|-\sqrt{-2+6|x|-3x^2}) & \text{for} \quad \frac{1}{2} \leq |x| \leq \frac{3}{2} \\ 0 & \text{for} \quad \frac{3}{2} \leq |x| \end{cases} \tag{4.19}$$

4.1.2 Simulation setup

Depending on the research project included in this thesis, the simulation setup varies. Given the ultimate goal of the present work, namely modelling of cellular blood flow in complex vascular networks, an example procedure will be demonstrated here for the simulation of RBCs flowing through the microvasculature of developmental mouse retina. For details of the retina images, which are provided by my experimental collaborators at Max-Delbrück-Centrum für Molekulare Medizin (Berlin, Germany), please refer to Sec. 4.3.1.

4.1.2.1 Geometry reconstruction

To reconstruct a three-dimensional (3D) flow model capturing the luminal surface (Figure 4.4b), the Col.IV binary mask of mouse retina (Figure 4.4a) is processed using the open-source software *PolNet* developed by Bernabeu *et al.* [29]. There are mainly three steps involved:

- Image segmentation: distinguishing vascular and non-vascular regions in the binary mask of luminal surface;
- Network skeletonisation: calculating interconnected vessel centrelines that depict the skeleton of the vasculature;
- Surface reconstruction: generating vessel segments from the calculated centrelines assuming circular vessel cross-sections.
- Domain discretisation: the flow domain enclosed by the reconstructed surface is then discretised into uniform cubic voxels with a lattice size of Δx, the value of which is determined by the criterion that the flow can be accurately solved throughout the reconstructed network for reliable haemodynamics even in the smallest vessels [30].

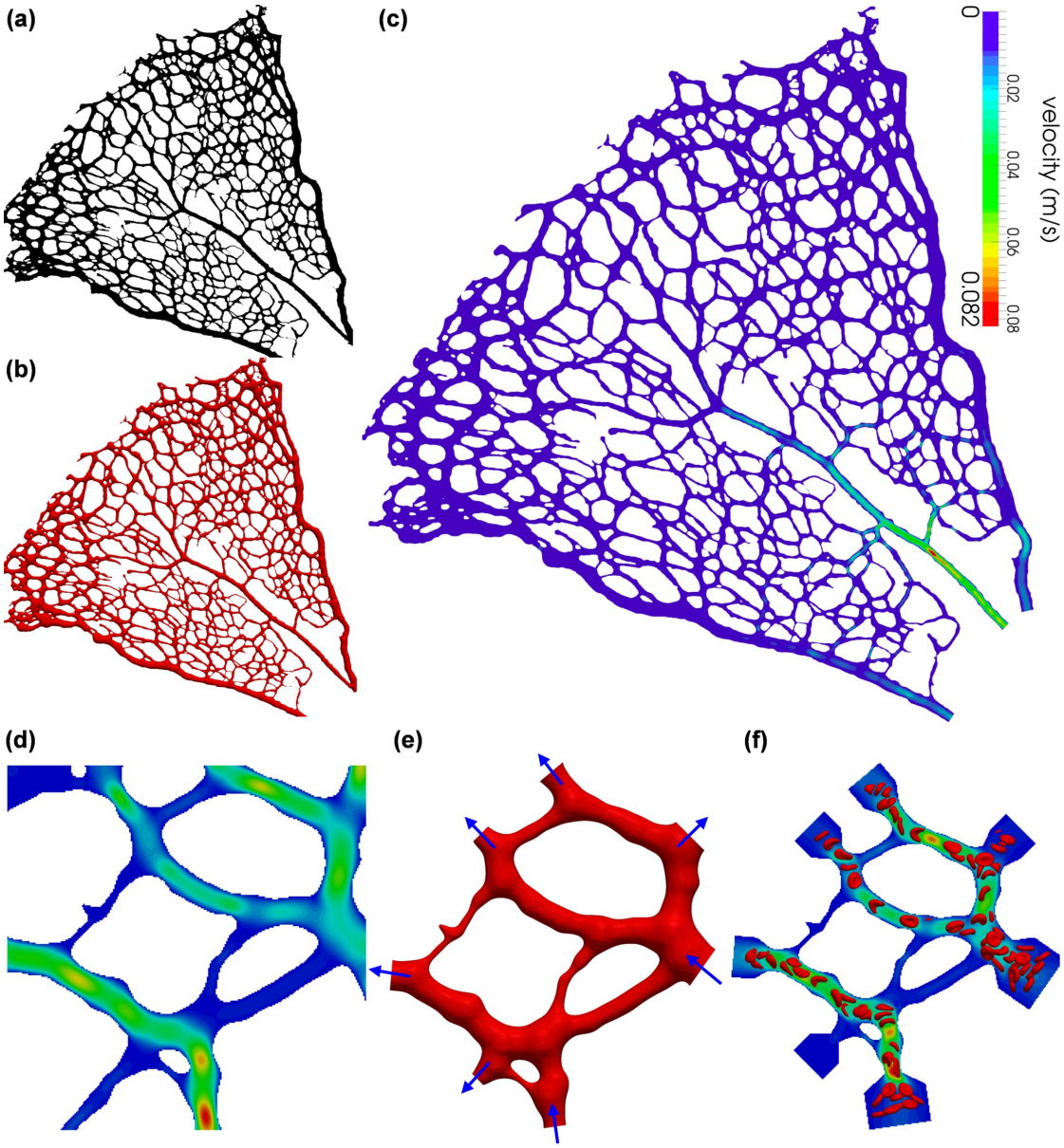

Figure 4.4: *Procedure of model configuration and simulation setup for simulating cellular blood flow in designated regions of interest (ROIs) from the vascular plexus of mouse retina. (a) Binary image of the vascular plexus stained for Col.IV. (b) Reconstructed whole-network geometry of the vessel luminal surface from (a). (c) Velocity field within the retinal network resolved by a flow model applying the non-Newtonian Carreau-Yasuda (NNCY) blood rheology in (b). (d) Zoomed in velocity field for a designated ROI in (c). (e) Clipped ROI subset from the whole-network geometry. (f) Cellular flow simulation in the designated ROI imposing inflow/outflow and pressure conditions extracted from (d).*

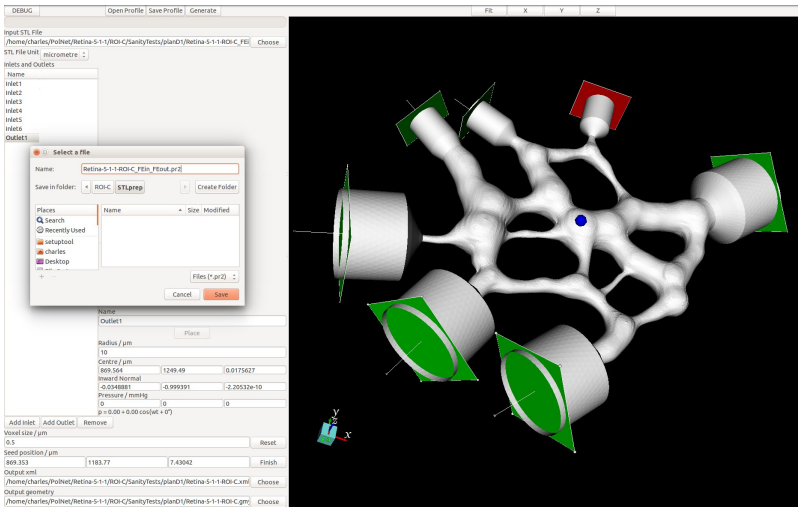

Figure 4.5: *Simulation setup interface in HemeLB. The velocity and pressure boundaries of the flow domain are imposed with green-coloured and red-coloured planes, respectively. The cylindrical regions are flow extensions designed for cell insertion and removal.*

4.1.2.2 Boundary conditions

There are two primary steps for simulating the cellular blood flow in the reconstructed vascular network, starting from a whole-plexus simulation with simplified rheology, followed by localised simulations with highly-resolved RBCs. The whole-plexus simulation adopts a non-Newtonian Carreau-Yasuda (NNCY [30, 34]) rheology model, where the blood is simulated as a generalised Newtonian fluid characterised by shear-thinning behaviour. By imposing a physiological ocular perfusion pressure (OPP) between the arteriole and venules, a steady flow within the vascular plexus is solved (Figure 4.4c) to provide boundary conditions for subsequent RBC simulations in designated regions of interest (ROIs) for on-site investigation. OPP = 55 mmHg is chosen for the present simulations based on a literature survey and sensitivity analysis conducted in [30].

Localised RBC simulations are then carried out for ROIs of the retinal network where evident vessel regression events are observed (*e.g.,* Figure 4.4d). First, the designated ROI is clipped from the whole-plexus as a geometric subset (Figure 4.4e). For a ROI subset with N open boundaries, $(N-1)$ Poiseuille velocity inlets/outlets (with parabolic velocity profiles imposed given a centre-line velocity of $\hat{u}$) and one pressure outlet (with a reference pressure p_{out}) are set up (see Figure 4.5 for an example). Specifically for velocity outlets, they are regarded as "artificial inlets" with

reversed flow directions in the simulation setup tool. These boundary conditions are informed from the NNCY simulation through measuring local flow rates Q in vessel cross-sections and subsequently calculating $\hat{u}$ from Q assuming Poiseuille flow postulated by $\hat{u} = 2\bar{u} = 8Q/(\pi D^2_{vessel})$.

4.1.2.3 Cell initialisation

With all the above boundary conditions set, a plasma flow simulation is initiated in a given ROI with the fluid viscosity equal to that of plasma η_{plasma}. Once steady flow is achieved and the velocity field is verified against the NNCY simulation, the ROI is populated with RBCs which are continuously fed at a fixed haematocrit of 20 % from the flow extension of each inlet of the subset network (Figure 4.4f). A fading function for inserting/removing RBCs is applied at all inlets/outlets to minimise the disturbance to the bulk flow.

4.1.3 Numerical analysis

In the present thesis, three primary research projects are reported (Chapters 6–8), and RBC simulations are conducted both in microfluidic devices and microvascular networks. Because the numerical analysis depends much on the specific research project, this section named "numerical analysis" is not intended for an exhaustive coverage of all data processing involved. Rather, it aims to introduce some fundamental aspects of blood flow at the microscale. In the light of this spirit, most examples of numerical analysis demonstrated herein are surrounding the simplest geometry of a single microchannel with rectangular cross-section as will be researched in Chapter 6.

4.1.3.1 Calculation of RBC velocities

The axial and lateral velocities for RBCs in a horizontally or vertically aligned channel can be calculated as their unit displacement along the respective direction over a unit time step:

$$V_{\mathrm{x}} = \Delta L_x/\Delta t, \quad V_{\mathrm{l},y} = \Delta L_y/\Delta t, \quad V_{\mathrm{l},z} = \Delta L_z/\Delta t \tag{4.20}$$

Based on the trajectories of individual RBCs, it is handy to group cells according to the location of their centre of mass and conduct statistical analysis of RBC hydrodynamic lift within the channel.

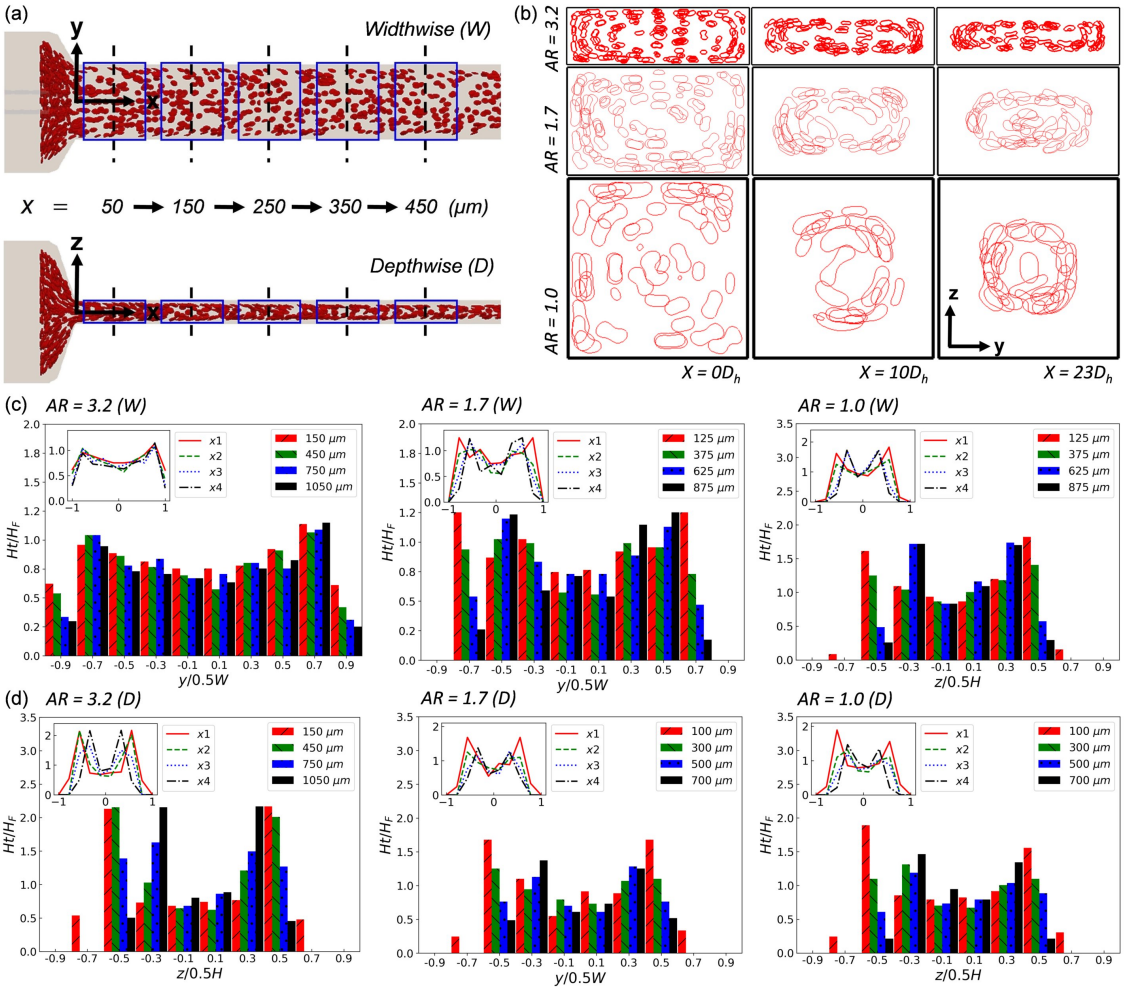

Figure 4.6: *(a) Example of the haematocrit (Ht) analysis showing superimposed RBCs from multiple simulation snapshots (at designated time intervals) in sequential sampling boxes (blue) measuring* 50 *μm long each at target locations (ROIs) downstream of the channel entrance. Cells within each sampling box are projected and allocated into 10 bins across the width (W) and depth (H) directions for counting, respectively, with their position determined by centre of mass. (b) Cross-sectional slices showing the accumulative transverse pattern of RBCs at* $x = 0D_h, 10D_h, 23D_h$ *away from the entrance, combining snapshots from 50 consecutive time steps. The 1st, 2nd and 3rd row represent snapshots of the* $H_F = 1\%$ *RBC suspension in a straight rectangular channel with aspect ratios* $AR = 3.2, 1.7, 1.0$ *(varying* $W = 96, 50.5, 30\,\mu m$ *while keeping* $H = 30\,\mu m$ *fixed), respectively. The calculated histograms (bars) at* $x = 3.3D_h$, $10D_h$, $16.5D_h$, $23D_h$ *downstream of the channel, showing (c) the widthwise and (d) the depthwise distribution of RBCs. The inset in each panel shows the approximate Ht profiles enveloping the calculated histograms for visual clarity.*

4.1.3.2 Calculation of haematocrit profile

Once the RBCs are fully perfused inside a vessel/channel and the number of cells within becomes stable, snapshots of the simulation are extracted at given time intervals, which are then assembled to count the cells for the calculation of time-averaged haematocrit profiles. The number of time steps is set as n_{t}, the value of which should ensure sufficient cells existing in the sampling pool.

Next, various ROIs alongside the channel length are selected to count cells locally (Figure 4.6a). Taking a rectangular channel for example (width W and depth H), at each target position, cells contained in a $W \times H \times \Delta L$ (ΔL determined based on volume flow rate to ensure statistical accuracy) sampling box are considered. All cells within this box are counted based on their centre of mass and allocated into a number of subdivisions either across the widthwise (W) direction or the depthwise (H) direction. The local haematocrits $Ht_{(i)}$ in each subdivision are then calculated

$$Ht_{(i)} = \frac{n_{\mathrm{rbc}(i)} Vol_{\mathrm{rbc}}}{n_{\mathrm{t}} Vol_{\mathrm{bin}}}, \quad Vol_{\mathrm{bin}} = \frac{Vol_{\mathrm{box}}}{N_{\mathrm{bin}}}, \quad (i = 1, 2, \ldots, N_{\mathrm{bin}}) \tag{4.21}$$

where $n_{\mathrm{rbc}(i)}$ is the number of cells detected in a given subdivision, $Vol_{\mathrm{rbc}} = 100$ fL is the standard volume of an RBC (fixed for all simulations), Vol_{bin} is the volume of each subdivision, $Vol_{\mathrm{box}} = W \times H \times \Delta L$ is the volume of the sampling box, and N_{bin} is the number of subdivisions in Vol_{box}. With the local haematocrit values calculated as above, haematocrit profiles can be plotted (Figure 4.6c-d). Furthermore, the cross-sectional RBC pattern is also readily to be found (Figure 4.6b).

4.1.3.3 Calculation of RBC fluxes

Based on the tube haematocrits $Ht_{(i)}$ (subdivided into N_{bin} bins as in Eq. 4.21) at a distance x downstream of the flow inlet, the corresponding cross-sectional RBC fluxes $Q_{\mathrm{rbc}(i)}$ can be calculated via the discharge haematocrit $H_{D(i)}$ and blood volume flow rate $Q_{\mathrm{B}(i)}$:

$$Q_{\mathrm{rbc}(i)} = H_{\mathrm{D}(i)} Q_{\mathrm{B}(i)}, \quad (i = 1, 2, \ldots N_{\mathrm{bin}}) \tag{4.22}$$

$$H_{\mathrm{D}(i)} = Ht_{(i)} \left(\bar{V}_{\mathrm{x}(i)} / \bar{U}_{\mathrm{B}(i)} \right), \quad Q_{\mathrm{B}(i)} = \bar{U}_{\mathrm{B}(i)} A_{\mathrm{bin}} \tag{4.23}$$

where $A_{\text{bin}} = W \times H/N_{\text{bin}}$ is the cross-sectional area of each bin, and $\bar{V}_{\text{x}(i)}$ and $\bar{U}_{\text{B}(i)}$ are the spatial-average RBC velocity and blood flow velocity within each bin, respectively. Combining Eqs. (4.22) and (4.23), the following equation is derived for RBC flux calculation:

$$Q_{\text{rbc}(i)} = Ht_{(i)}\bar{V}_{\text{x}(i)}A_{\text{bin}} \tag{4.24}$$

A similar process can be applied to vessels with circular cross-section for the calculation of haematocrit profile and RBC fluxes through proper division of the cross-section (*e.g.,* dividing the circle into N proportions by evenly splitting the diameter). When the vessels are not horizontally or vertically aligned, the centreline vector of each selected ROI is re-oriented based on a specific rotation matrix to enable cell counting using regular divisions (Figure 4.7).

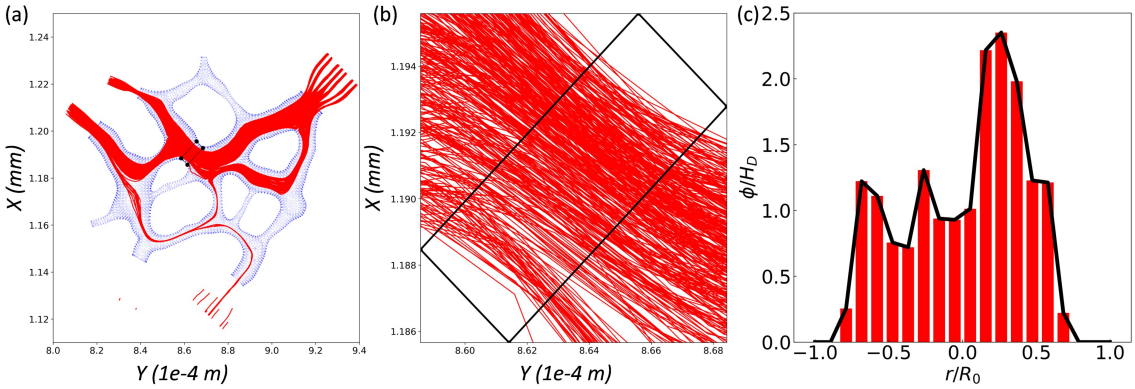

Figure 4.7: *(a-b) RBC trajectories (shown in red solid lines) within a vascular network. (c) Calculated haematocrit profile based on local haematocrits for an extracted ROI from the vascular network in (a) (marked by rectangular black box), for which an enlarged view is shown in (b).*

4.1.3.4 Calculation of cell-free layer

For a rectangular channel width W and depth H, to characterise the CFLs within, a cross-section at a distance x downstream of the flow inlet is divided into four triangles by the diagonals and the wall edges. The heights of the four triangles, each perpendicular to a channel wall, are located at $\theta = 0, \pi/2, \pi, 3\pi/2$, respectively (see illustration in Figure 4.8a). Using a Monte Carlo approach, a large set of random points are dropped within each triangle and the RBC density $\phi(h, \theta', x, t)$ at a point $p(x, h, \theta')$ of longitudinal coordinate x, height coordinate h and angular coordinate θ'

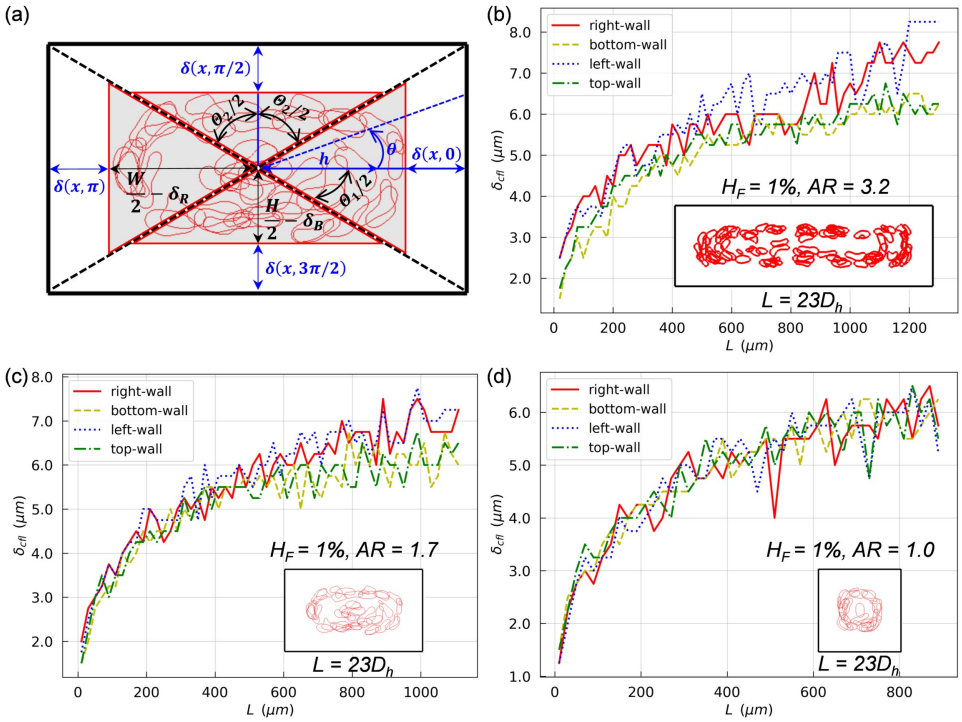

Figure 4.8: *(a) Illustration of the CFL analysis for an example channel cross-section (the same with that in (c)). (b–c) CFLs calculated along each wall of the channel (Right/Bottom/Left/Top-walls) from different simulations. (b) $H_F = 1\%$, AR = 3.2; (c) $H_F = 1\%$, AR = 1.7; (d) $H_F = 1\%$, AR = 1.0. The inset in each panel shows a cross-sectional view of the RBC pattern at $L = 23D_h$ away from the entrance, combining snapshots from 50 consecutive time steps from the corresponding simulation.*

within a given triangle for a certain time instant t is as 1 if that point is enclosed by at least one RBC membrane; otherwise, $\phi(h, \theta', x, t) = 0$. The time-mean RBC density within any of the fours triangles can then be obtained via integration over (h, θ') and average over t:

$$\bar{\phi}(x, \theta) = \frac{1}{N} \sum_{i=1}^{N} \int_0^{L_\mathrm{h}} \int_{\theta-\Theta/2}^{\theta+\Theta/2} \phi(h, \theta', x, t_i) h \tan|\theta' - \theta| \mathrm{d}\theta' \mathrm{d}h \tag{4.25}$$

wherein N is the number of time steps extracted from the simulation, L_h is the height of the triangle and Θ is its tip angle centred in the cross-section. For the left and right triangles:

$$L_{\mathrm{h}1} = W/2, \quad \Theta_1 = 2\arctan(H/W) \tag{4.26}$$

and for the top and bottom triangles:

$$L_{\mathrm{h}2} = H/2, \quad \Theta_2 = 2\arctan(W/H) \tag{4.27}$$

If the CFL is defined as a thin layer in proximity to a given wall (base of the triangle) which contains only a negligible fraction of RBC density ε, *e.g.,* $\varepsilon = 1e-6$, then the thickness of this layer $\delta(x,\theta)$ can be determined using numerical iterations:

$$\varepsilon \leq \frac{1}{\bar{\phi}(x,\theta)N}\sum_{i=1}^{N}\int_{L_{\mathrm{h}}-\delta(x,\theta)}^{L_{\mathrm{h}}}\int_{\theta-\Theta/2}^{\theta+\Theta/2}\phi(h,\theta',x,t_i)h\tan|\theta'-\theta|\mathrm{d}\theta'\mathrm{d}h \tag{4.28}$$

By calculating $\delta(x,\theta)$ for each θ at consecutive x locations, the CFL thickness for each wall (left/right/top/bottom) can be obtained along the channel axis direction (Figure 4.8b-d).

4.2 Microfluidic experiments

(Disclaimer for this section.[1])

The experimental setup used an inverted microscope (Olympus IX71) for flow visualisation and a syringe pump (Nemesys, Cetoni) for fluid control. The microfluidic device was illuminated using a halogen lamp. Videos were acquired by a sensitive monochrome CCD camera (Olympus, XM10) using a $10\times$ magnification objective with numerical aperture of 0.25 to guarantee that the depth of field and image depth are large enough to observe cell trajectories across the entire channel height.

An algorithm was developed *in-house* (by Joana Fidalgo) based on ImageJ software to detect and count the cells automatically. The RBC probability density distribution (PDD) along the width direction of a given region of interest (ROI) is then calculated using a minimum of 300 frames, containing more than 8,000 cells. The cell-free layer (CFL) is determined as half the difference between the overall channel width and the RBC-core width, using composite images generated via the Z-projection method.

[1] All figures and text in Sec 4.2 are provided by Joana Fidalgo at the University of Strathclyde (Glasgow, UK) through a collaborative project.

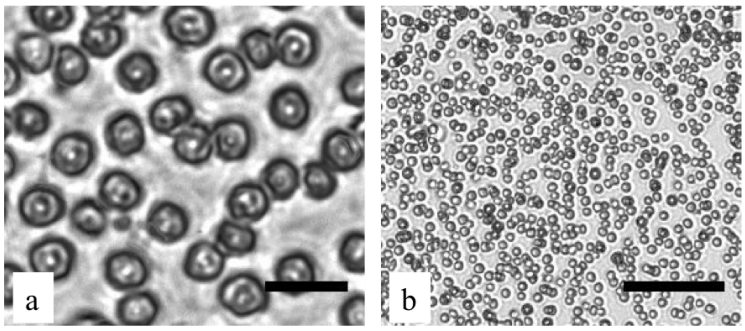

Figure 4.9: *Photomicrograph of the RBC suspension in PS (NaCl 0.9% w/v) at different magnifications. (a) 40x, scale bar 10 μm; (b) 10x, scale bar 50 μm. (image from [339])*

4.2.1 Preparation of RBC suspensions

The RBC suspensions were prepared using horse blood (Fig. 4.9) instead of human blood due to laboratory restrictions. The blood sample was provided by TCS Biosciences (UK), in anticoagulant ethylenediaminetetraacetic acid (EDTA) 1.5 mg/mL, and stored at 4 °C until further use. Sample processing and disposal were performed following the Ethics Committee for Animal Experimentation at University of Strathclyde. Since the blood was provided from different animals in distinct periods, the packed cell volume (PCV) or haematocrit could range from 30 to 50%, according to the blood provider. This variability is overcome by producing cell suspensions from the cell sediment after washing and centrifugation. The haematocrit (Ht), defined by the cell volume fraction, is controlled to be $Ht \leq 1\%$.

Fig. 4.10 shows the steps involved in sample processing. First, an Eppendorf with 1.5 mL of whole blood (WB) was centrifuged at 6000 rpm for 1 min (miniFUGE), after which the supernatant containing the yellow plasma and buffy coat (mainly white blood cells and platelets) was discarded. Second, the RBCs were washed twice with physiological saline PS (NaCl 0.9% w/v), with the transparent supernatant discarded. Third, the final sample was prepared by suspending the desired volume of RBC in Dextran40 solution (Dx40 M_w = 40000 g/mol, 0.1 g/mL in isotonic medium). This suspending medium will avoid the phenomenon of cell sedimentation during experiments, which is a common problem for suspensions prepared in PS or in original blood plasma. The steady shear rheology of Dextran 40 was determined by a rotational rheometer (DHR2, TA Instruments, with minimum resolvable torque 0.1 nNm) using a cone-plate geometry of 60 mm diameter and angle θ = 1° (CP60/1), 30 μm truncation gap.

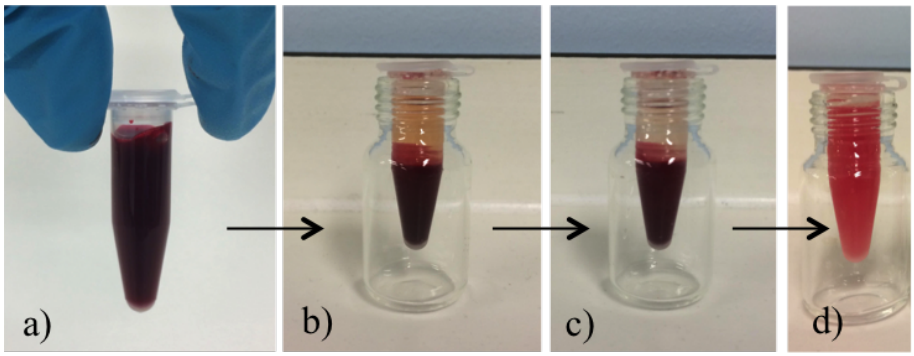

Figure 4.10: *Steps for the preparation of RBC suspensions. (a) Eppendorf with whole blood; (b) separation (by centrifugation) of the supernatant plasma and buffy coat from the RBCs sediment; (c) transparent supernatant after RBC washing and centrifugation with PS; (d) RBC suspension in Dx40 solution ($Ht \leq 1\%$). (image from [339])*

4.2.2 Data acquisition and image analysis

An inverted microscope (Olympus, IX71) was used to observe the device with bright field, employing a small magnification objective (10x/0.25 NA) in order to inspect cells across the entire channel depth and throughout a relatively large section of the channel length. For each flow condition tested, the system was allowed to stabilize for a few minutes before image acquisition by a sensitive monochrome CCD camera (Olympus, XM10) at a frame rate of 15 Hz. The exposure time was set to 100 μs allowing well-defined images of the cell boundaries. Videos of at least 300 frames each, corresponding to approximately 20 seconds of experiment, were acquired for four ROIs. All the images were obtained at the channel centreplane ($z = 0$). The images acquired need post-processing for image enhancement and cell detection. For this purpose, we applied an automatic cell counting routine developed *in-house* on ImageJ software.

Background correction The bright field images obtained from experiments usually present an unbalanced intensity distribution, in particular close to the channel inlets and outlets, where the fittings are connected to the device. To enhance the images, they were first corrected by subtracting the background. For this purpose, the Rolling ball radius filter was used, applying a radius of 10 pixels, which corresponds to an approximate diameter of a horse RBC ($D_{\text{rbc}} \approx 6\,\mu$m). This procedure allowed obtaining a clear and balanced image without losing information of the RBC (Fig. 4.11), especially for those cells located far away from the focal plane.

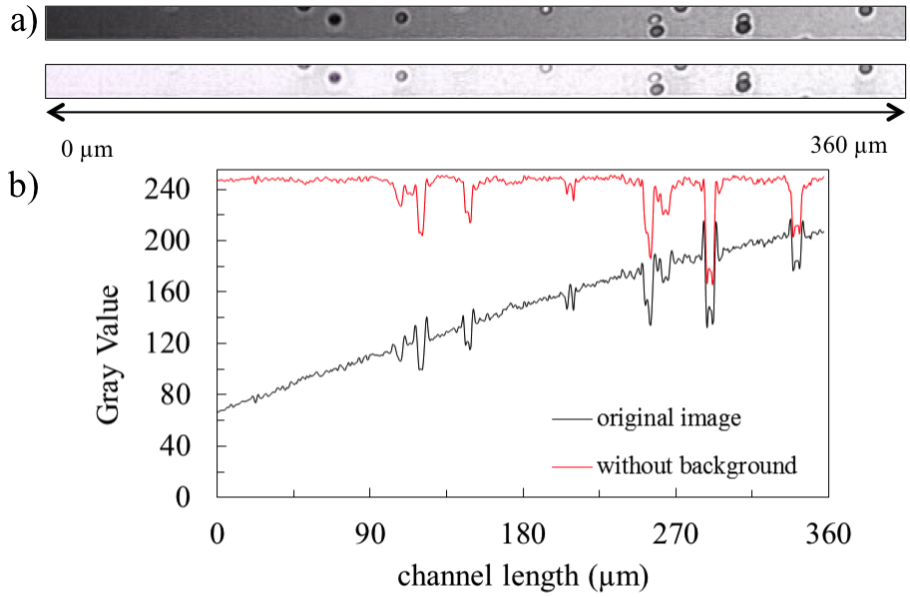

Figure 4.11: *Background correction using Rolling Ball Radius function in ImageJ. (a) Image sections before and after background subtraction; (b) Corresponding intensity profiles to the image sections in (a). (image from [339])*

Cell detection The RBCs in images with corrected background are detected and counted using an automatic routine developed on ImageJ software. Fig. 4.12 describes the intermediate steps for further image enhancement and cell detection, based on the image with corrected background.

First, a binary image (Fig. 4.12b) is generated from the image with corrected background (Fig. 4.12a), followed by function Dilate (Fig. 4.12c) and function Fill holes (Fig. 4.12d). This procedure allows recovering the cell contour for brighter cells that are located away from the focal plane. Subsequently, function Watershed is applied to generate separation among slightly overlapped cells (Fig. 4.12e). Then, function Outline allows delimiting each foreground object in the binary image, by generating a one-pixel wide outline (Fig. 4.12f). Based on this image, function Analyse Particles provides information of each delimited object, following which the Circularity filter is applied to detect objects whose circularity is in the range of 0.5–1.0, defined by $4\pi A/P^2$ (where A is the cell area and P the cell perimeter). The output is the image presented in Fig. 4.12g, providing numbered cells together with a list of values including the centre of mass (X_{CoM}, Y_{CoM}) and perimeter of each cell. A second filter is applied to the perimeter of the automatic detected object, in order to delete the ones presenting even smaller sizes than an undersized cell ($D_{\mathrm{rbc}} \approx 4\,\mu$m).

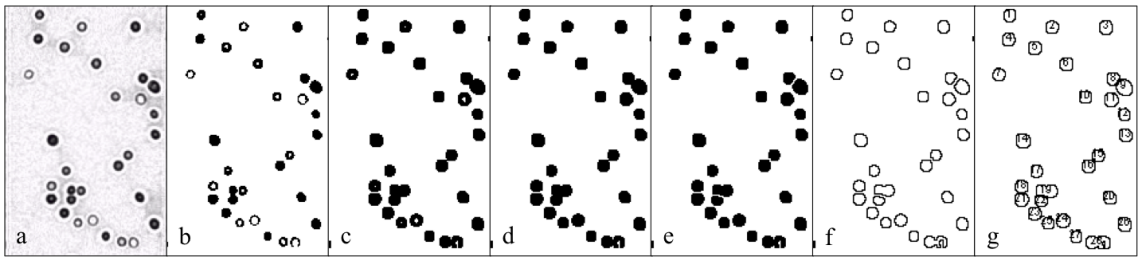

Figure 4.12: *Procedures of detecting cells from the experimental images. (a) Image with corrected background; (b) The corresponding binary image; (c) function Dilate; (d) function Fill Holes; (e) function Watershed; (f) function Outline; (g) detected cells after function Analyse Particles on applying the Circularity filter. (image from [339])*

4.2.3 Probability density distribution (PDD)

Calculation of local RBC fractions Local RBC fractions in experiments are determined using the centre of mass information from detected cells within each ROI. We first divide the whole width of the channel into N bins ($N \geq 26$) and apply a frequency function to count the cells that fall into each bin. The RBC fraction for each bin is then calculated as its cell percentage (%) relative to the total number of cells detected in the whole ROI. The above calculation of relative RBC fractions is to counterbalance the cell counting error arising from the automatic detection method, which does not allow accurate recording of absolute cell numbers because of the interference from cell overlapping in experimental images. By plotting the RBC fractions on the cross-section of the designated ROI, the Probability density distribution (PDD) of RBCs is obtained, which can be regarded as an approximate representation of the haematocrit profile.

Accuracy of the PDD profile To verify the accuracy of PDD profiles depicting RBC distribution obtained from the automatic counting method, two validation tests were performed. First, we examined the minimum number of frames needed to ensure a converged distribution. For a given ROI, the RBC distribution was determined using four different image stacks, containing 50, 100, 200 and 300 image frames, respectively. The PDD profiles resulting from a relatively small stack, *e.g.,* 50 and 100 frames, were found to present significant noises and differ much from each other (Fig. 4.13a). In contrast, the distributions obtained from a larger stack, namely 200 and 300 frames, were much smoother and appeared similar to each other (Fig. 4.13a). Therefore, we conclude that a stack with 300 frames is enough to generate a converged RBC distribution.

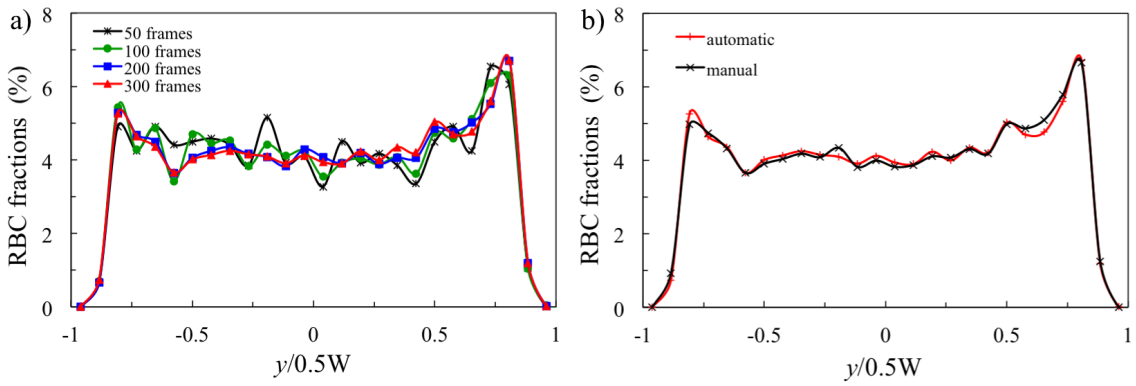

Figure 4.13: *(a) Effect of the number of frames on the RBC distribution calculated by the automatic cell counting method. The PDD profiles are calculated using a stack of 50 frames (black line), 100 frames (green line), 200 frames (blue line) and 300 frames (red line), respectively. (b) PDD profiles (using a stack of 300 images) obtained from automatic cell counting (red line) and manual cell counting (black line), respectively. (image from [339])*

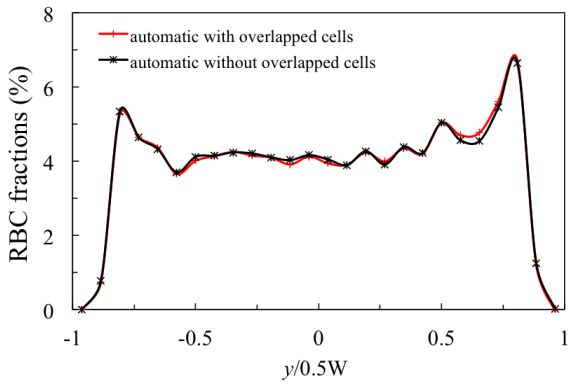

Figure 4.14: *Effect of cell overlapping on the calculated RBC distribution, showing PDD profiles obtained from automatic counting with (red line) and without (black line) overlapped cells in the images, respectively. (image from [339])*

Second, we compared the RBC distribution obtained from our automatic counting using a stack of 300 frames with one based on manual counting. The result showed a high-level similarity between the two distributions (Fig. 4.13b), hence validating the accuracy of our proposed method for the analysis of RBC distribution in experiments using low haematocrit ($Ht \leq 1\%$), where the boundaries of individual cells can be well defined.

Effect of cell overlapping The effect of cell overlapping is also investigated. In Fig. 4.12g, it is possible to observe false "agglomerates" (given the RBC concentration and the type of Dextran used in our experiments, we expect no physical aggregation) caused by the overlapping of cells across the channel depth direction. To study the impact of these "agglomerates" on the calculated RBC distribution, they were identified and excluded in a test case. The resulting RBC distribution was then compared to the original RBC distribution, where the two distributions obtained are found virtually identical (Fig. 4.14). This suggests that the statistical effect of cell overlapping is negligible on the final cell distribution obtained using our automatic counting method.

4.2.4 Cell-free layer

To measure the CFL at a ROI within the channel, a combined image of 300 frames via minimum intensity Z-projection is generated (Fig. 4.15a). Using this method, if a cell is passing through the ROI with lower intensity than the background, it will be registered; with a sufficient number of image frames, the layer depleted of cells (CFL) close to the walls can be distinguished. The binary image of such a projection (Fig. 4.15b) presents a sharp boundary separating the RBC core and the CFL. The average CFL thickness is then defined as half of the averaged difference between the channel width and the RBC core along the ROI.

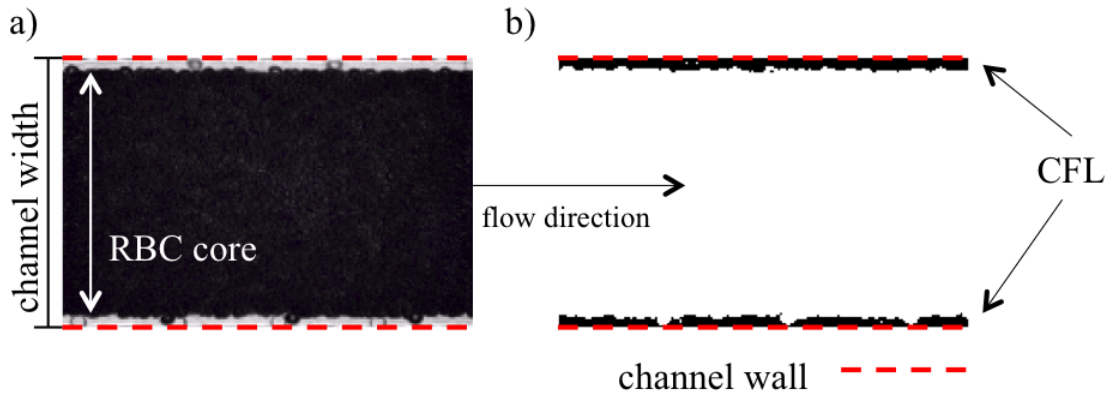

Figure 4.15: *CFL measurement. (a) Minimum intensity Z-projection image using a stack of 300 frames. (b) Binary image of the Z-projection for calculation of the CFL thickness. (image from [339])*

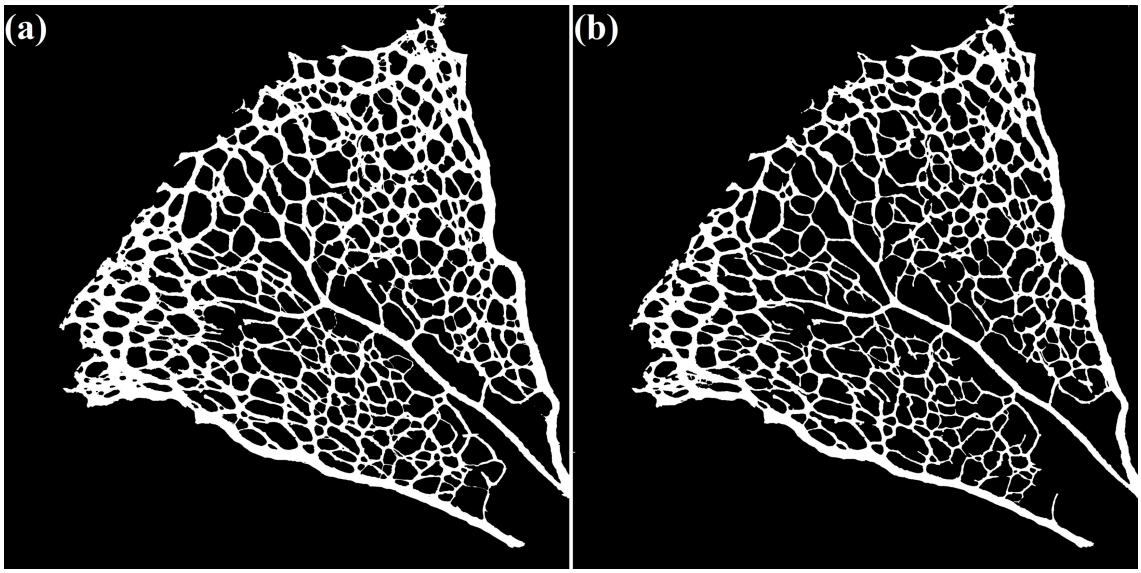

Figure 4.16: *A vascular plexus of postnatal day 5 (P5) mouse retina, with the collagen matrix sleeves and the endothelial luminal surface labelled by (a) Col.IV and (b) ICAM2, respectively. (Image by courtesy of Tijana Perovic)*

4.3 Mouse and zebrafish experiments

4.3.1 Preparation of mouse retina for binary mask acquisition

(Disclaimer for this subsection.[2])

The mouse strain used in the present study was C57/BL6J. Mice were maintained at the Max Delbrück Center for Molecular Medicine under standard husbandry conditions. Animal procedures were performed in accordance with the animal license X9005/15. Mouse eyes were collected at P5 and fixed with 4% PFA in PBS for 1 h at 4°C, and retinas were then dissected in PBS. Blocking/permeabilisation was performed using Claudio's Blocking Buffer (CBB; [92]), consisting of 1% FBS (Gibco), 3% BSA (Sigma-Aldrich), 0.5% Triton X-100 (Sigma-Aldrich), 0.01% sodium deoxycholate (Sigma-Aldrich), and 0.02% sodium azide (Sigma-Aldrich) in PBS at pH 7.4 for 2 h with rocking at 4°C. Primary antibodies were incubated at the desired concentration in 1:1 CBB/PBS with rocking at 4°C overnight and secondary antibodies were incubated at the desired

[2]All figures and text in Sec 4.3.1 are provided by Tijana Perovic at Max-Delbrück-Center for Molecular Medicine in the Helmholtz Association (Berlin, Germany) through a collaborative project.

concentration in 1:1 CBB/PBS for 2 h at room temperature. Retinas were mounted on slides using Vectashield mounting medium (H-1000; Vector Labs).

The following primary and secondary antibodies were used *In vivo*: collagen IV (ref 2150-1470, rabbit; 1:400; AbD Serotec) and ICAM2 (ref 553326, rat; 1:200; BD Biosciences), anti-Rat Alexa 488 (ref A21208, donkey 1:400, Invitrogen), anti-Rabbit Alexa 568 (ref A10042, donkey 1:400, Invitrogen). Complete high-resolution three-dimensional (3-D) rendering of whole mount retinas were taken using a LSM 780 inverted microscope (Zeiss) equipped with a Plan-Apochromat 63×/1.4 NA DIC objective. Images were taken at room temperature using Zen 2.3 software (Zeiss). Tiled scans of whole retinas were analysed with ImageJ to generate binary masks of ICAM2 (Figure 4.16a) and Collagen IV (Figure 4.16b).

4.3.2 Morpholino oligomers, zebrafish husbandry and imaging

(Disclaimer for this subsection.[3])

Morpholino oligomer (MO) against gata1 morpholino (gata1 MO, Figure 4.17b) as described in [12] (sequence 5'-CTGCAAGTGTAGTATTGAAGATGTC-3') was injected at 8 ng/embryo following [132]. A control MO (ctl MO, Figure 4.17a) served the standard control Morpholino targeting a human beta-globin intron mutation (sequence 5'- CCTCTTACCTCAGTTACAATTTATA-3'). The control was injected at similar amount of 8 ng/embryo. Zebrafish (*Danio rerio*) were raised and staged as previously described in [154]. For growing and breeding of transgenic lines, we complied with regulations of the animal ethics committee at the MDC Berlin [10].

Embryos were anaesthetised in 0.014% tricaine (Tricaine Pharmaq 1000mg/g, PHARMAQ Limited), mounted in plastic petri dishes (94x16 mm - Sarstedt Ref#82.1473) containing 0.014% tricaine, and bathed in E3 media containing 0.007 (0.5x) tricaine and 0.003% PTU. Imaging was performed on an upright 3i spinning-disc confocal microscope using Zeiss Plan-Apochromat 20x/1.0 NA water-dipping objectives. Screening of embryos was performed using a Leica M205 FA stereomicroscope with filter set ET GFP M205FA/M165FC.

[3] All figures and text in Sec 4.3.2 are provided by Ines Fechner at Max-Delbrück-Center for Molecular Medicine in the Helmholtz Association (Berlin, Germany) through a collaborative project.

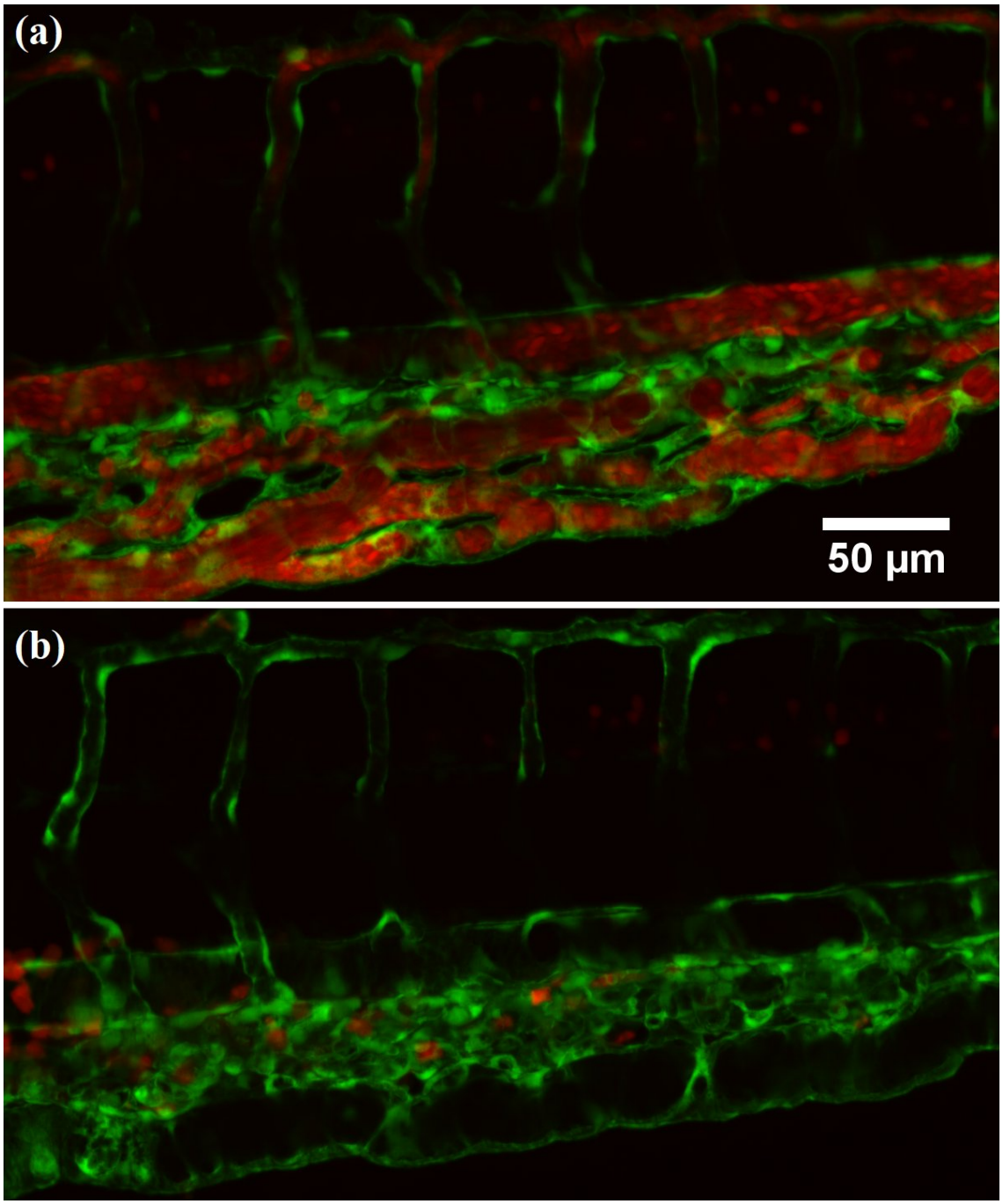

Figure 4.17: *Two exemplar CVPs from (a) a ctl MO embryo (with RBC perfusion) and (b) a gata1 MO embryo (without RBC perfusion). Note that the RBC precursors in (b) are located outside the vasculature and therefore not circulating with the blood flow. (Image by courtesy of Ines Fechner)*

Part III

RESEARCH

If you thought that science was certain - well, that is just an error on your part.

— Richard P. Feynman

Chapter 5
Benchmark tests of a single RBC in typical channel flows

In recent decades, we have witnessed the application of various numerical methods as introduced in Sec. 3.2 to model blood flow. A majority of existing studies are two-dimensional (2D) in nature. They have greatly enhanced our understanding of blood by providing invaluable insights into the underlying principles or mechanisms governing RBC dynamics and suspension rheology. Notwithstanding, a quantitative description of the microscopic behaviour of RBCs at the cellular level is difficult to achieve with 2D models. To overcome this limitation, three-dimensional (3D) models emerged over recent years, such as the immersed-boundary-lattice-Boltzmann model (IB-LBM) as introduced in Sec. 4.1.1.

Before employed to conduct research projects, the present IB-LBM was validated against numerical results of existing 3D models as well as experimental observations. In this chapter, three typical benchmark tests are selected for demonstration on account of their relevance to central research projects to be covered later in this thesis, namely Chapters 6–8. In brief, the benchmark tests cover the behaviour of an individual RBC in geometries typical of biological passages (*e.g.,* vessels, slits) or microfluidic channels, including its common shape and wall shear stress (WSS) footprint in Sec. 5.1, membrane deformation and transit regime in Sec. 5.2, and cross-streamline migration in Sec. 5.3. Characterisation of a 3D RBC's microscopic behaviour under these conditions will not only help validate the present model, but also contribute to the understanding of RBC dynamics as they flow through microscale vessels or channels.

5.1 RBC in a small cylindrical tube

5.1.1 Background

One challenge of modelling cellular blood flow is to accurately capture the dynamical variation of RBC shape in response to fluid shear. Since its first observation in the 1670s, RBCs have been extensively characterised *in vivo* and *in vitro*. A range of distinct shapes are found simply by varying the flow that the cell is exposed to, from the most well-known biconcave disc [299] to the recently reported polylobed morphology [169, 197]. In the microcirculation, the capillaries where the RBCs travel in are usually highly confined, where the RBC shape heavily deviates from its undeformed biconcave state and turns into a parachute-like or bullet-like morphology, either symmetrically or asymmetrically (depending on capillary diameter, flow conditions and cell property). This shape transition has been widely investigated [105, 121, 300] and is commonly used to validate computational models [73, 82, 215, 232, 337, 343]. The parachute-like RBCs are mostly observed at the centre of small vessels or tubes, with a thin layer of fluid (known as the cell-free-layer, CFL) existing between the cell and channel wall. Subject to the variation of CFL, distinct patterns of the wall shear stress (WSS) can form on the channel wall [100, 209, 312, 333].

5.1.2 Model and parameters

To examine the shape evolution of RBCs in small vessels/channels, cylindrical tubes with $D_{tube} =$ 5–10 μm in diameter are modelled. The flow is driven from left to right, with a parabolic velocity profile (assuming Poiseuille flow) imposed at the inlet and a reference pressure assigned at the outlet. After the flow converges, an undeformed RBC with biconcave shape is inserted near the inlet with its initial position on the tube axis. Given the RBC diameter $D_{rbc} = 8\,\mu$m, cylindrical tubes with $D_{tube} < 8\,\mu$m need some special treatment to enable the initialisation of RBCs in a flow-facing manner. To this end, another cylindrical segment of larger size ($10\,\mu$m in diameter) preceding the target tube of designated diameter is arranged (Figure 5.1). Between this segment and the investigated tube, there exists a tapper region where the RBC gradually deforms to enter the tube of investigation. To allow enough number of fluid nodes to solve the film flow in the small gap between the cell body and the wall, the lattice size in $D_{tube} = 10\,\mu$m is $\Delta_x = 1/3\,\mu$m; the lattice size in $D_{tube} = 5,\ 6,\ 7,\ 8\,\mu$m is $\Delta_x = 1/6\,\mu$m.

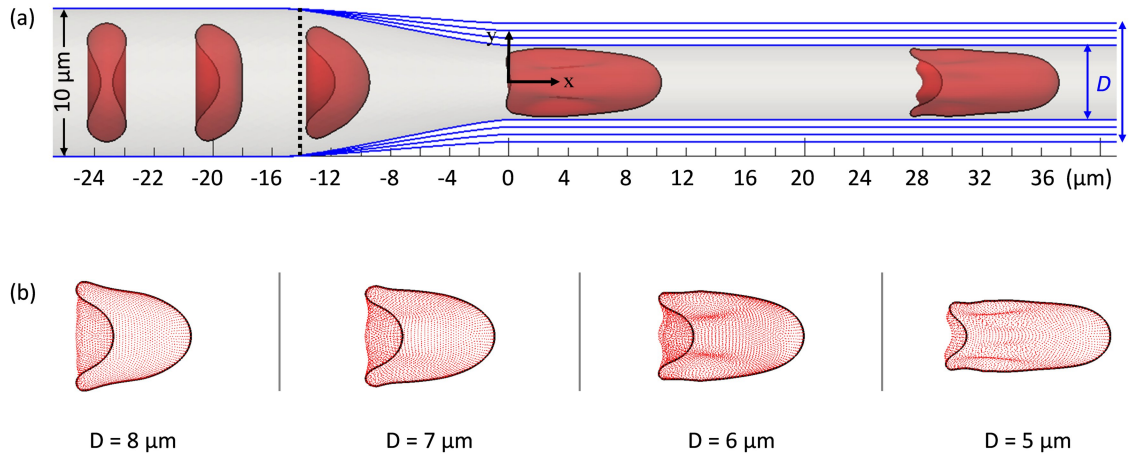

Figure 5.1: *(a) Schematic of flow models for the simulation of an RBC in cylindrical tubes of diameter $D_{tube} = 5, 6, 7, 8\,\mu m$, respectively. (b) Snapshots of the respective RBC shape with $D_{tube} = 5, 6, 7, 8\,\mu m$. Following the practice of [269], the mean flow velocity in all tubes is kept constant. The respective Reynolds numbers are $Re = 0.25, 0.3, 0.35, 0.4$, and the respective capillary numbers are $Ca = 0.76, 0.63, 0.54, 0.48$.*

The RBC is modelled as a closed finite-element membrane with N triangular facets (meshing resolution matching the lattice size Δx for numerical stability and accuracy [165]). For $D_{tube} = 10\,\mu$m, $N = 2880$; for $D_{tube} = 5, 6, 7, 8\,\mu$m, $N = 11520$. More details of the RBC model can be found in Chapter 4. The behaviour of RBCs in flow is determined by two non-dimensional numbers: the Reynolds number Re and the capillary number Ca. Re represents the ratio of fluid inertia to viscous force and is defined based on the channel diameter:

$$Re = \rho_{\text{ex}} \bar{u} D_{\text{tube}} / \eta_{\text{ex}} \tag{5.1}$$

where $\bar{u} = 0.25$ mm/s is the mean velocity of the unperturbed flow (without the cell); ρ_{ex} and η_{ex} are the density and dynamic viscosity of the suspending fluid, respectively. Ca represents shear-induced deformation of the RBC membrane and is defined using its shear elasticity:

$$Ca = \tau \dot{\gamma}_{\text{w}}, \quad \tau = \eta_{\text{ex}} r_{\text{rbc}} / \kappa_s, \quad \dot{\gamma}_{\text{w}} = 8\bar{u} / D_{\text{tube}} \tag{5.2}$$

where τ is a characteristic time scale of the RBC membrane to relax to equilibrium shape from a transient state; $\dot{\gamma}_{\text{w}}$ is the wall shear rate; r_{rbc} is the RBC radius; κ_s is the membrane strain modulus.

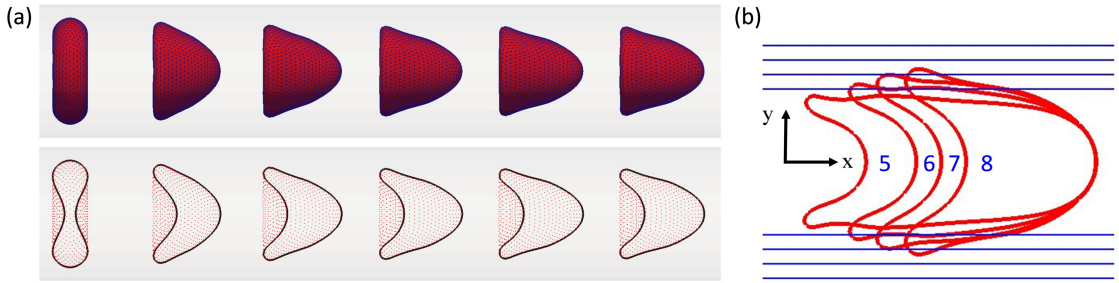

Figure 5.2: *(a) Shape evolution of the RBC flowing in the cylindrical tube of diameter* $D = 10\,\mu m$*,* $Ca = 1$*. (b) Comparison of RBCs from the simulations in cylindrical tube of diameter* $D_{tube} = 5,\ 6,\ 7,\ 8\,\mu m$*, respectively.*

5.1.3 Results and discussion

RBC shape At $D = 10\,\mu$m, the RBC gradually evolved into a parachute shape in response to the flow (Figure 5.2a). The time-sequence cross-sectional views of the cell membrane demonstrate the development of a round nose in the front and two bulging rim tips at the rear end under the combined effect of strain and bending forces. Decreasing the tube diameter down to $D = 5\,\mu$m (high degree of confinement) gives rise to an elongated cell with bullet shape, featuring increased cell length but reduced cell width (Figure 5.2b). These findings agree well with earlier experimental observations [105, 121] and theoretical derivations [267, 269] under comparable flow conditions.

WSS footprint The RBC-induced disturbance on the WSS is found dramatic. Far from the cell, the WSS remains unperturbed with a steady value of τ_0 (proportional to the tube diameter and the pressure drop). In the vicinity of the RBC, the WSS presents a "peak-valley-peak" pattern featuring three transitions, namely τ_1 a primary peak (near the fore-end), τ_2 a valley (near the rear-end) and τ_3 a secondary peak (right behind the cell). This variation of WSS is in line with a previous 2D IB-LBM study [312]. However, $\tau_2 < \tau_0$ was concluded for all cases investigated by the authors, whereas in the present 3D simulations, τ_1, τ_2, τ_3 can all be higher than τ_0 (Figure 5.3). This implies that the amplification effect of instantaneous WSS induced by the RBC may be underestimated by the 2D model. When the tube becomes exceedingly small and the cell rim gets much closer to the wall, the "peak-valley-peak" pattern is replaced by a single-peak profile, with a pronounced τ_1 (several fold higher than τ_0) emerging around the RBC rear (Figure 5.4).

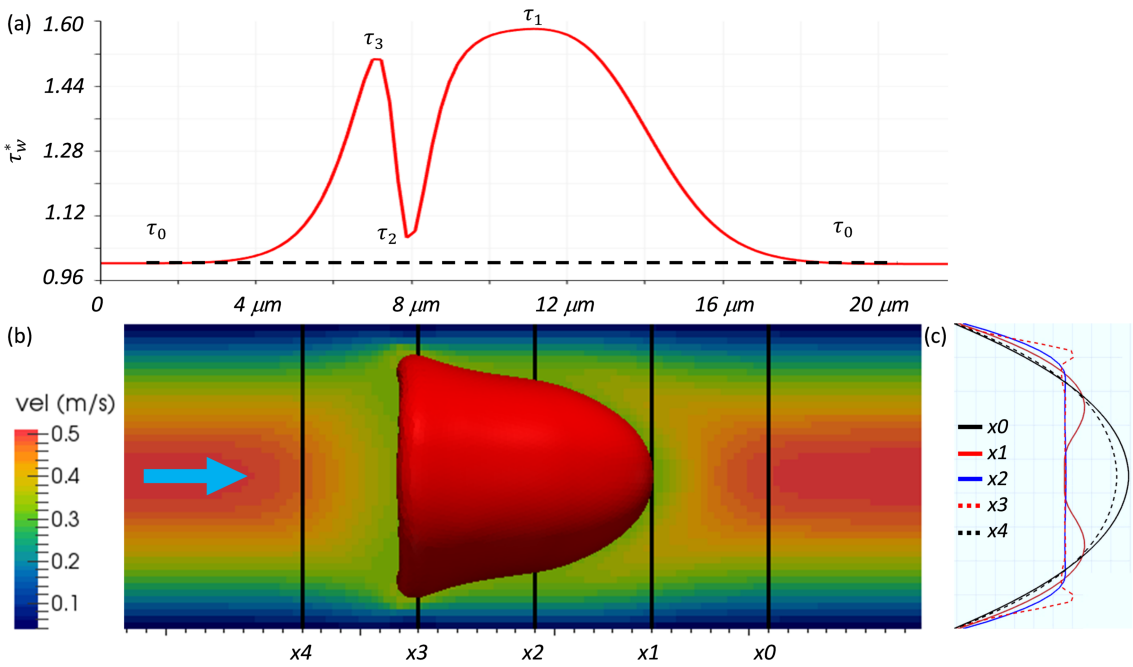

Figure 5.3: *(a) WSS footprint of the RBC flowing through a cylindrical tube of* 8 μm *in diameter. All WSS values are normalised by* τ_0*, the mean WSS at a position far away from the cell. (b) shows the disturbance of the RBC to the velocity field, and (c) plots the velocity profiles at positions marked in (b) by black solid lines.*

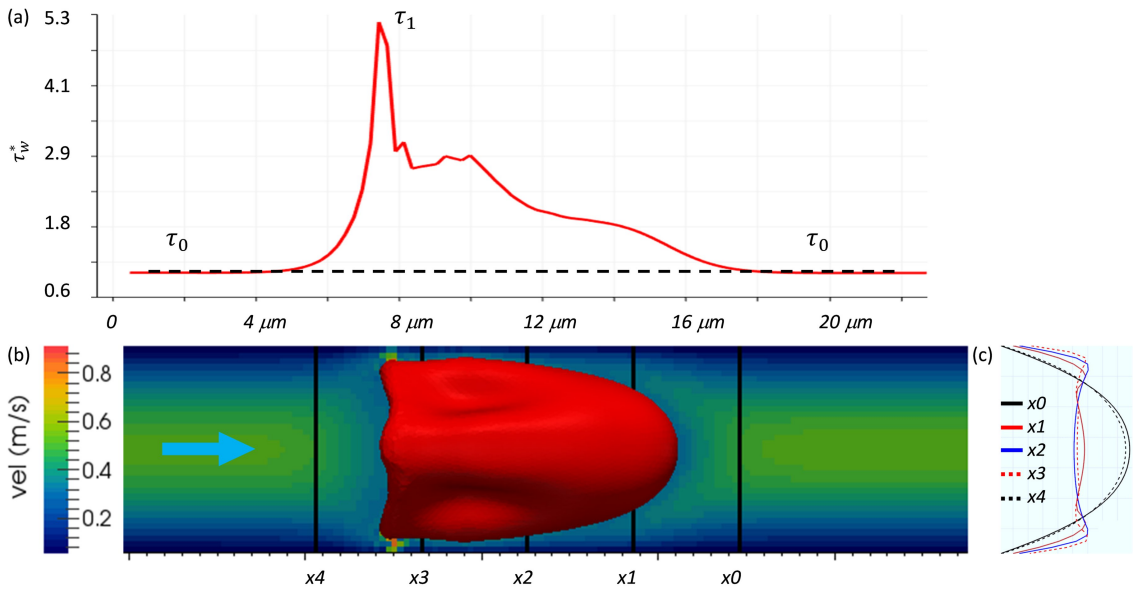

Figure 5.4: *Same caption as Figure 5.3, except for a cylindrical tube of* 6 μm *in diameter.*

5.2 RBC through a narrow splenic slit

5.2.1 Background

Healthy RBCs are extraordinarily deformable and can squeeze through vessels much smaller than their own size [178]. The narrowest passages in the human body probably exist in the spleen, where aged or diseased cells are challenged owing to impaired deformability and removed either through phagocytosis or mechanical dissociation [176]. This process serves to filter unhealthy RBCs from our blood. The modelling of RBC transit through a spleen slit is challenging given the excessively small size of the passage, which is typically 1–2 μm wide or even narrower. Recent studies successfully simulating this process employed boundary integral/element methods (BIM/BEM) [97, 188, 261, 262] or (smoothed) dissipative particle dynamics (DPD) methods [233, 311, 331]. Additionally, a coarse-grain molecular dynamics (CGMD) model was applied and verified for reliable results[176]. To the best knowledge of the author, no such simulations have been performed using the lattice-Boltzmann method. Therefore, the present study aims to test our IB-LBM model with this problem and compare the results from other models.

5.2.2 Model and parameters

Figure 5.5 shows the computational model built to simulate a single RBC squeezing through a splenic slit. The slit has the same dimensions as the one studied by [97], which is 1 μm in depth and 2.82 μm in length. The channels upstream and downstream the slit have a square cross-section with the same width and depth ($W = H$). A cylindrical flow entry region, whose diameter D_e equals to the width/depth of the square channel, is added at the inlet to impose a parabolic velocity profile (assuming Poiseuille flow). The whole domain is 18 μm wide/deep and 44.8 μm long, including 2,884,668 lattice sites. The lattice size is ΔX = 1/6 μm. The inlet, the outlet and the flow direction (from left to right) are labelled in Figure 5.5.

An RBC of biconcave shape is inserted from the cylindrical flow entry region (at the centre) once steady flow converges in the domain. The RBC will then be driven towards the spleen slit. The same as in Sec. 5.1.2, the RBC is modelled as a closed finite-element membrane with N triangular facets ($N = 8000$ here). The RBC's deformability is manipulated via the capillary number Ca,

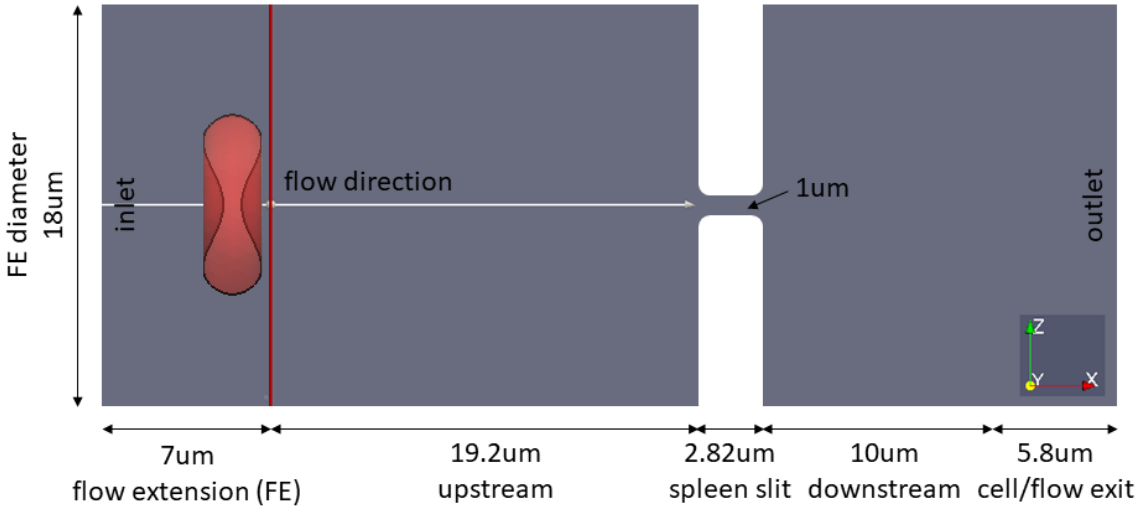

Figure 5.5: *Model configuration of a single cell squeezing through a narrow slit.*

which is defined based on the cylindrical flow entry region with a diameter of $D_e = 18\,\mu$m:

$$Ca = \eta_{ex}\dot{\gamma}_w r_{rbc}/\kappa_s, \quad \dot{\gamma} = 8\bar{u}/D_e \tag{5.3}$$

wherein $\eta_{ex} = 1$ mPa s is the dynamic viscosity of the suspending fluid, $\dot{\gamma}$ is the wall shear rate and $r_{rbc} = 4\,\mu$m is the radius of the RBC. κ_s is the strain modulus of the RBC membrane, which is varied in different simulations to achieve a designated Ca number. $\bar{u} = 5.6$ mm/s is the mean velocity of the flow imposed at the inlet (kept constant for all simulations).

5.2.3 Results and discussion

Regimes of cell transit A parametric study $Ca = 0.001,\ 0.01,\ 0.059,\ 0.1$ (increasing cell deformability by varying the membrane strain modulus while keeping the ambient flow velocity fixed) at low Reynolds number ($Re = 0.2$ as calculated following Eq. 5.1) reveals that the cell travels faster towards the slit with a larger Ca value. This is easy to understand as a softer cell would experience less flow resistance as it deforms more substantially. Three different regimes can be defined when a cell of different deformability encounters the narrow slit: a rigid cell getting stuck ($Ca = 0.001,\ 0.01$); a soft cell passing through ($Ca = 0.059$); and an even softer cell becoming jammed with severe membrane infolding ($Ca = 0.1$) (see Figure 5.6).

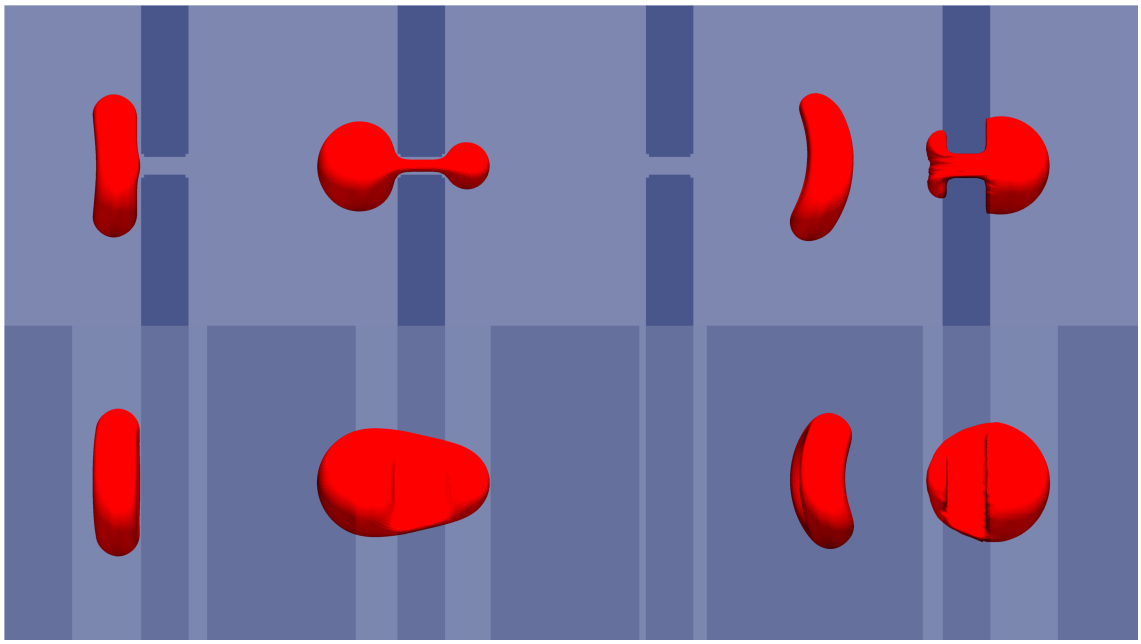

Figure 5.6: *(λ = 1) Regimes of the cell transit (four cells). From left to right: Ca = 0.001 (stuck), Ca = 0.01 (stuck), Ca = 0.059 (pass), Ca = 0.1 (infold). The first row of the figure panel shows the side view of the cell, and the second row shows the top view.*

The three regimes are similar to those reported in [97] by varying flow velocities $\bar{u}$ and viscosity contrasts λ (ratio of cytosol viscosity to plasma viscosity). However, because the present simulations consider no viscosity contrast (namely $\lambda = 1$) whereas [97] only included $\lambda > 1$ cases in the velocity-viscosity phase diagram, a quantitative comparison of regime transition cannot be made. A notable difference from [97] is that, the threshold Ca number for the transition between the passing-through and infolding-jammed regimes to occur in the present study is much lower. Furthermore, the fore-end of the infolding cell here escapes the splenic slit and presents a spherical head, with two tails left behind (which resembles the "two-tongue" shape reported in [261]), instead of being trapped by the slit as in [97]. This shape difference may be attributed to the possibly under-resolved infolding cell limited by numerical stability with current resolution.

Transit time of cell Case $Ca = 0.059$ has been designed to reproduce one simulation in Freund [97] to enable quantitative comparison of the transit time, where Ca' was defined as:

$$Ca' = \eta_p \bar{u} / \kappa_s \tag{5.4}$$

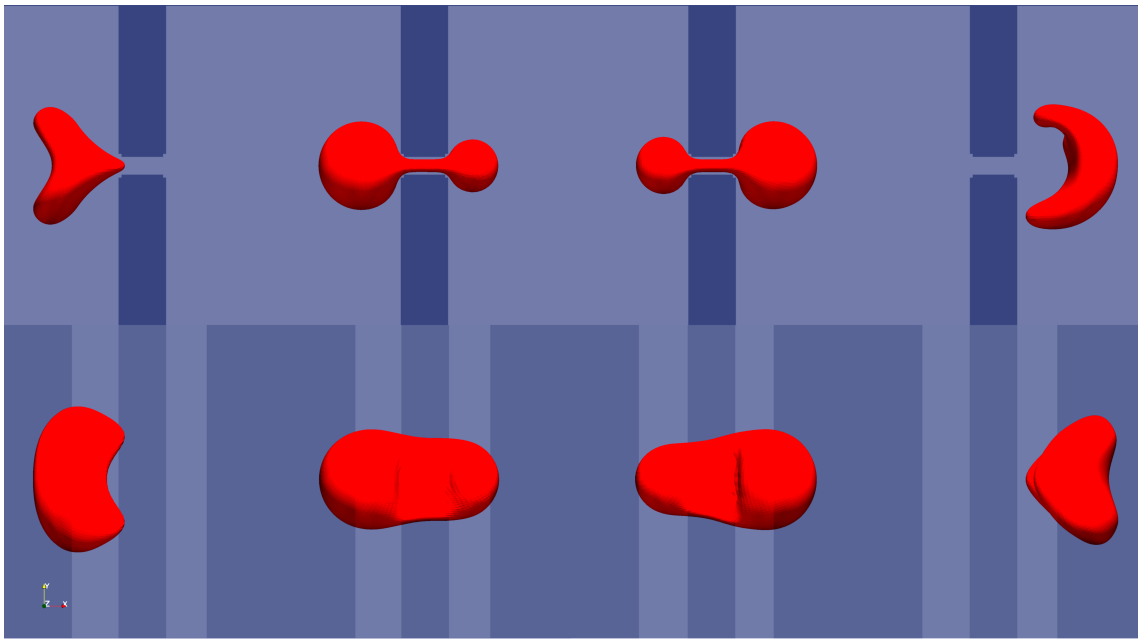

Figure 5.7: *(Ca = 0.059, λ = 1) One single cell passing through the Spleen Slit. From left to right: t_1 = 80 ms, t_2 = 87 ms, t_3 = 100 ms, t_4 = 111 ms. The first row of the figure panel shows the side view of the cell, and the second row shows the top view.*

where $\eta_p = 1.2$ mPa s is the viscosity of blood plasma; $\bar{u} = 141\ \mu$m/s is the flow mean velocity; $\kappa_s = 4.2\times10^{-6}$ N/m is the membrane modulus. By comparing Eq. 5.3 and Eq. 5.4, the conversion relations between the two capillary numbers can be found as $Ca' = 0.675Ca$. Accordingly, the $Ca = 0.059$ simulation here is equivalent to $Ca' = 0.04$ in Freund's model, where the cell falls well into the "passing through" regime.

Figure 5.7 demonstrates a time-lapse sequence of the $Ca = 0.059$ cell with its centroid approaching (t = 80 ms), entering (t = 87 ms), escaping (t = 100 ms) and leaving (t = 111 ms) the slit, respectively. The total transit time is calculated to be 13 ms. This value is comparable to reported transit time for equivalent flow conditions, for example, 22 ms and 37 ms as reported by [97] and [262], respectively. The slightly slower cell transit in the above works may be due to their setup of a 0.1 μm exclusion zone to avoid singularity (given the adverse effect of potentially strong lubrication on the BIM/BEM methods they use when the cell is in close contact with the slit walls). On the other hand, the LBM method does not accurately resolve the film flow in the narrow cell-wall gap with current resolution, which may also contribute to this discrepancy in transit time.

5.3 RBC in a rectangular channel

5.3.1 Background

Abundant theoretical and experimental studies have excluded the possibility of cross-streamline motion for axisymmetric rigid bodies (*e.g.,* spheres, discs, rods) in the absence of inertia. Some most well-known works include [35, 112, 124, 141, 151]. Notwithstanding, when it comes to stiff RBCs in microfluidic flows, uncertainties arise. One argument for the migration-free viewpoint is that, a rigid RBC in inertia-free shear flows cannot tank-tread and would instead assume a flipping-like or tumbling motion [286]. In such motion mode, the orientation orbit of the RBC presents repeated reversals that would recover the spherical symmetry in a periodic manner [35]. In other words, despite its non-spherical shape, the rigid cell still behaves as if being spherical and consequently no symmetry-breaking motion will be generated to trigger cross-streamline drift in purely viscous flow [193].

However, RBCs are strongly non-spherical objects with a biconcave shape featuring two dimples. Also, even rigid RBCs are not perfectly solid because they have viscous fluid inside [202]. Therefore, it is still subject to scrutiny whether the theories largely derived based on solid spheres or ellipsoids in the literature are applicable to predict the motion of RBCs at low Reynolds (Re) number, especially for channel flows where multiple solid boundaries exist. Furthermore, despite their typical low Re number, microfluidic flows are definitely not inertia-free. It is still a debatable issue for realistic geometries under which Re number the inertia is decisively low so that Stokes flow can be safely invoked, albeit many numerical studies assume $Re = 1$ as the critical threshold.

The present single-RBC simulations in a rectangular microchannel (commonly for microfluidic devices) show clear lateral migration of rigid RBCs occurring at small Re number ($Re < 1$), causing the cell to move away from walls and approach the channel centre. This finding is contrary to existing understanding of the motion of rigid objects in low-Re shear flow (Newtonian fluid). The behaviour of the RBC is found to show complex dynamics that can introduce unsteady momentum which in turn gives rise to a net drift in the shear plane. Key theoretical and numerical works that may help elaborate the problem include [56, 221, 223, 290] and [59, 163, 238, 263]. Recent studies by Rosén [257, 258, 259] are also important by providing invaluable insights on the potentially chaotic angular dynamics of non-spherical bodies in shear flows with vanishing inertia.

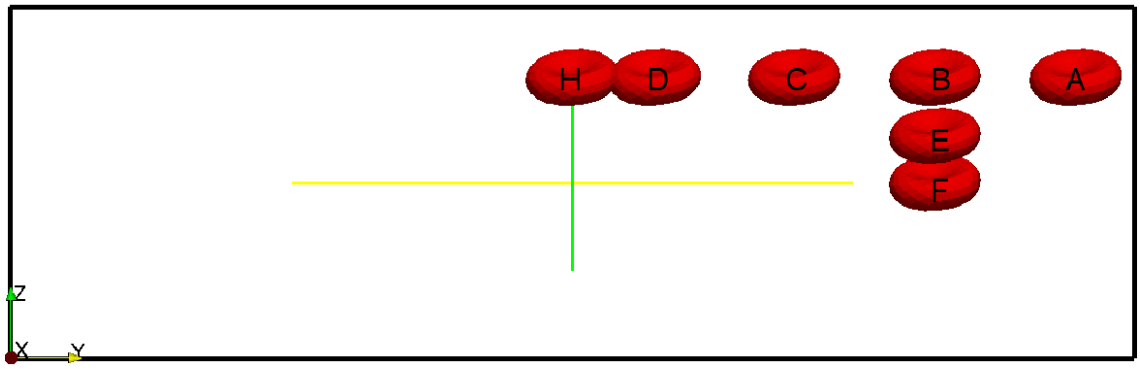

Figure 5.8: *Schematic of the channel cross-section and cell A, B, C, D, E, F, H initialised at seven different positions. The centre is located at (X, Y, Z) = (10, 49, 16).*

5.3.2 Model and parameters

The computational domain has a size of $80\Delta X \times 98\Delta X \times 32\Delta X$ ($L \times W \times H$), centred at $(X, Y, Z) = (40, 49, 16)$. The lattice size for all simulations is set as ΔX = 1 μm unless stated otherwise. The left, right, top, bottom wall is located at $Y = 1$, $Y = 98$, $Z = 32$ and $Z = 1$, respectively. Periodic boundary conditions are imposed in the $x-$direction, along which the flow is driven with a body force. The RBC model is the same as introduced in Sec. 5.1.2 and Sec. 5.2.2, but with a coarser mesh of $N = 500$. Definitions of the Reynolds number (Re) and the capillary number (Ca) are also similar to Sec. 5.1.2, except that the cylindrical tube diameter D_{tube} is replaced by the hydraulic diameter D_h of the present rectangular channel, which is calculated as:

$$D_h = \frac{2WH}{W+H} \approx 45.7\Delta X \tag{5.5}$$

To investigate the interaction between the RBC and different channel walls, seven initial positions A-H are designed so that the RBC is placed close to either one or two of the walls (Figure 5.8). All cells are initialised at an inclination angle of 40 degrees about the vector $\vec{R} = (1, 2, 3)$ (unless otherwise specified), which is intended to generate a random orientation in the three-dimensional space without losing generality. Unless otherwise specified, all simulations in this study are run for 2 million time steps (so that $L > 10000\Delta X$, typically costing 2 days each) with Reynolds number $Re = 1$, $Ca = 0.001$ and relaxation time $\tau = 1$. Parametric simulations shown in Figure 5.11 with varying Re number ($Re = 0.1,\ 0.3,\ 0.5,\ 0.7,\ 1.0$) are run with $Ca = 0.01$ and $\tau = 2$.

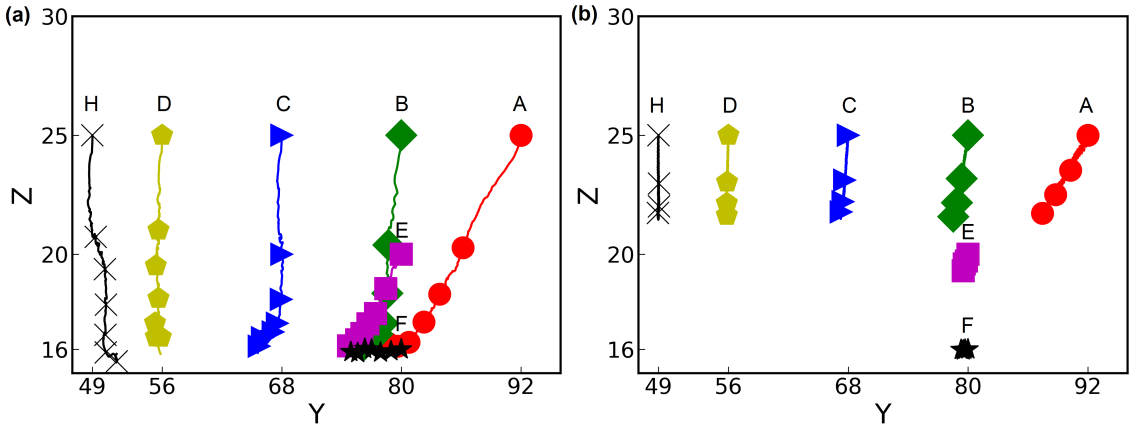

Figure 5.9: *Trajectory projection of cell A, B, C, D, E, F, H on a cross-sectional plane of the channel. (a)* $Ca = 1$ *and (b)* $Ca = 0.001$*. The cell position is determined by its centre of mass.* $Re = 1$ *for all simulations.*

5.3.3 Results and discussion

5.3.3.1 Effect of initial position and cell deformability

In this section, both soft and rigid RBCs are studied to investigate the effect of cell deformability on the RBC's lateral migration, which is observed from the transverse plane normal to flow direction.

Cell trajectory At $Re = 1$, the initial position of the RBC is found to have a profound effect on its lateral migration (reflected by the transverse projection of its trajectory), whether it is soft or rigid (Figure 5.9). Overall, the lateral migration of cells initially placed near walls (*e.g.,* cells A, B, E) are much stronger than those initialised near channel axes (*e.g.,* cells D, F, H).

Specifically, when a soft RBC ($Ca = 1$) is initially placed on or close to one of the channel axes (*e.g.,* cell D, cell F and cell H), it would largely migrate along the respective axis with only slight side drift, leaving a nearly straight transverse path behind (Figure 5.9a). As the initial position moves away from the axis, a curved path comes into being with a trend of marching towards the channel centre. All these signs seemingly suggest that the channel centre is an equilibrium position for lateral migration of the soft cells.

The paths of rigid RBCs ($Ca = 0.001$) on the transverse plane are qualitatively similar, but

with substantially reduced displacement (Figure 5.9b). To quantify the difference in displacement between soft and rigid RBCs, the changes of cell position along the widthwise and depthwise directions are examined independently (Figure 5.10). For off-axis RBCs (*e.g.,* cells A, B, C, E), decreasing $Ca = 1$ to $Ca = 0.001$ is found to cut the lateral displacement in the respective direction by more than half. This is particular obvious for cells placed near the corner, *e.g.,* cell A (compare Figure 5.10a–b) and cell B (compare Figure 5.10d–e). In addition, the reduction in streamwise translation for rigid cells is also significant, again most prominently for cells initialised in the low-velocity region near the corner of the channel.

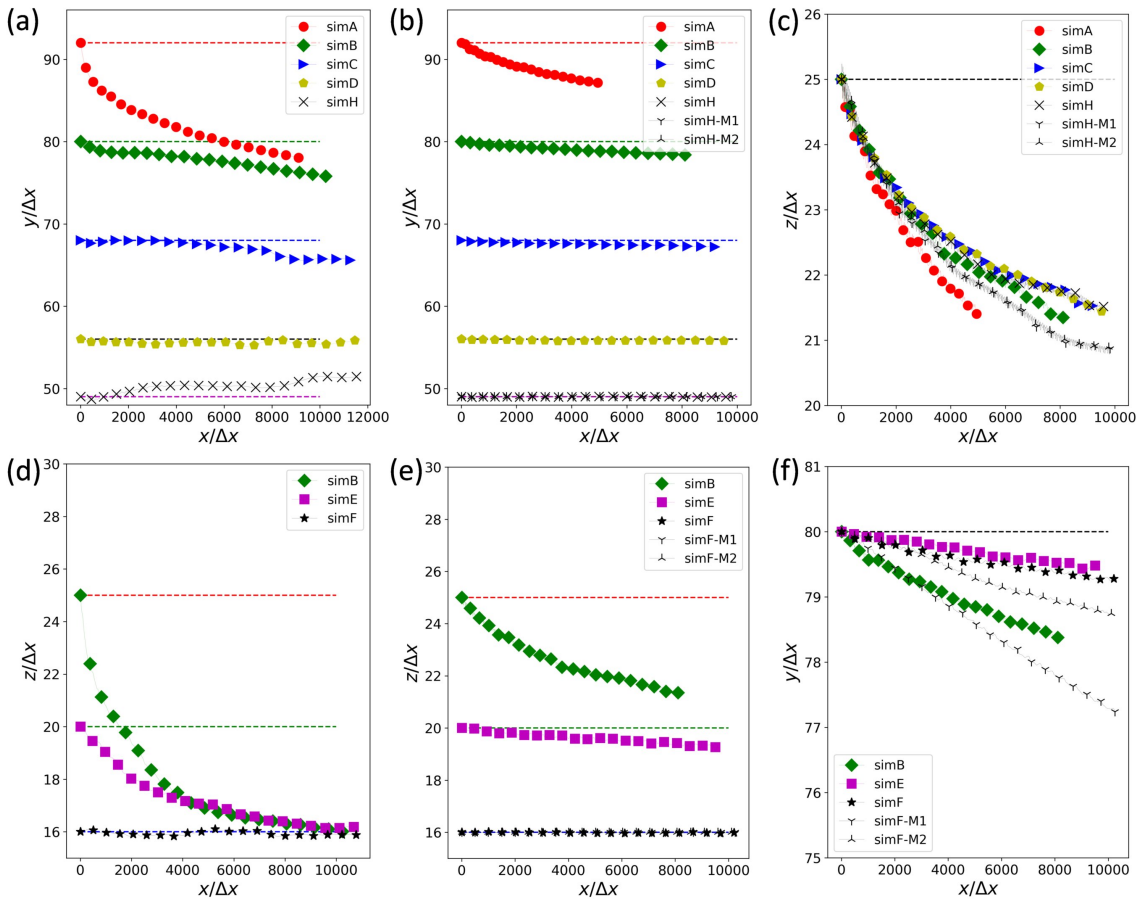

Figure 5.10: *Trajectories of (a–c) cell A, B, C, D, H and (d–f) cell B, E, F. For (a) and (d), $Ca = 1$; for (b–c) and (e–f), $Ca = 0.001$. (a–b) and (f) show the migration of cells in the widthwise direction; (c) and (d–e) show that in the depthwise direction. For all simulations in (a–f), $Re = 1$. M1 (meaning "Mode 1") and M2 (meaning "Mode 2") for cell F and cell H represent two other initial orientation angels for the cells, which are discussed in Sec. 5.3.3.2.*

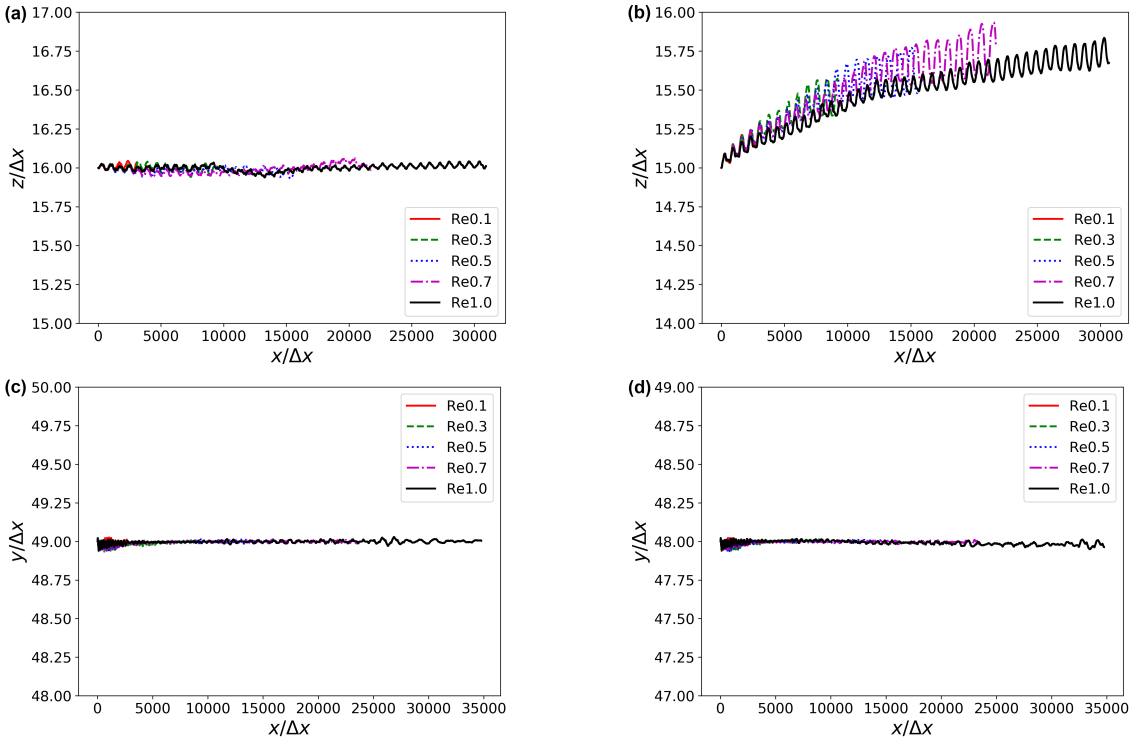

Figure 5.11: *Stability test of the equilibrium position. (a) Cell F placed exactly at the middle of channel depth,* i.e., *Z = 16. (b) Cell F' placed at Z = 15. (c) Cell H placed exactly at the middle of channel width,* i.e., *Y = 49. (d) Cell H' placed at Y = 48.*

Stability of equilibrium position The results above suggest the channel geometric centre as the equilibrium position, particularly for rigid cells that are initially placed on the channel axes (*i.e.,* cell F and cell H). Besides the $Re = 1$ cases, a range of Re numbers below 1 are investigated, which all present the same trend (Figure 5.11a and Figure 5.11c). To determine whether the channel centre is perfectly stable or only marginally stable, two cells (hereafter referred to as cell F' and cell H') are arranged slightly off the respective axes. Cell F' clearly migrates back to $Z = 16$ (Figure5.11b), whereas cell H' remains at the new position and no sign of migration towards $Y = 49$ can be observed even over $660D_h$ (Figure5.11d). In this respect, the central equilibrium does appear stable for the depthwise migration but is only quasi-stable for the widthwise migration. The multiple equilibria in the width direction of the rectangular channel are presumably due to a finite zero-shear-rate range arising from the flattened velocity profile, which is in sharp contrast with the depth direction where a parabolic velocity profile prevails.

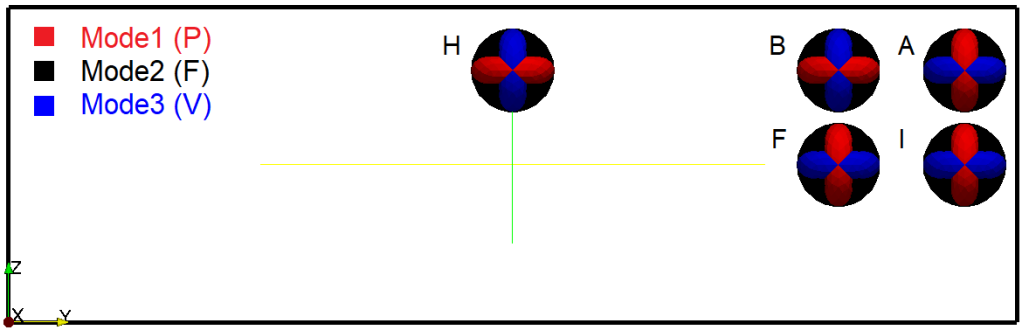

Figure 5.12: *Schematic of the channel cross-section and cell A, B, F, H, I initialised at three principal directions. Each cell has three orientations, namely parallel to wall (Mode 1, or M1), facing the flow (Mode 2, or M2) and vertical to wall (Mode 3, or M3).*

5.3.3.2 Rigid cell migration: effect of initial orientation

In this section, further investigation of rigid RBCs initialised at selected positions (including A, B, F, H, I) is conducted to understand the potential effect of initial orientation on their lateral migration (Figure 5.12). For the RBC at a given position, three orientation modes are considered, corresponding to the principal directions of the rigid body. In the Mode 1 (P), the cell is parallel to the closest wall; in the Mode 2 (F), the cell is facing the flow; in the Mode 3 (V), the cell is vertical to the closest wall. Through comparison, the dynamics of cell H, cell I and cell A is found representative of other cells and the following presentation will focus on these three cells.

Cell trajectory For cell H and cell I (initialised on channel axes), their lateral migration in all three modes are aligned with the respective axes with negligible drift in the sidewise direction. This axis-exclusive motion agrees with what was found in Sec. 5.3.3.2 for cells H, F initialised through a 40-degree rotation about $\vec{R}(1, 2, 3)$, therefore suggesting its independence of cell orientation angle. Nevertheless, the orientation does have an effect on the cell trajectory. For both cells H and I, a surprising "phase-jumping" pattern is observed under the V mode, featuring stepwise changes of lateral position followed by static phases of zero displacement (Figure 5.13a–b). The simulation animations (not shown here) reveal that both cells in V mode assume a forward "wheel-rolling" motion aligned with the axes. Meanwhile, the P and F modes for cell H show identical trajectories, and those for cell I show similar trajectories with a minor difference in net displacement. Both cells in P or F modes demonstrate the classic tumbling motion.

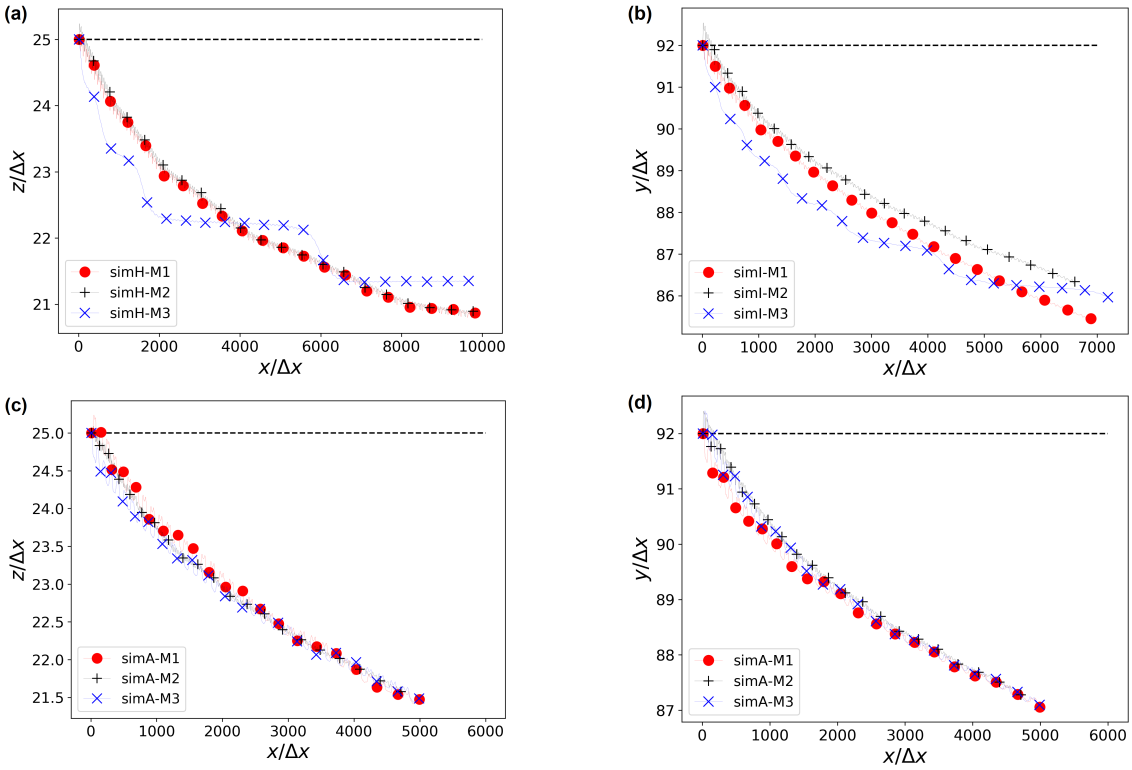

Figure 5.13: *Trajectories of cell H, I, A in three modes. (a) Lateral migration of cell H in the depthwise direction (there is negligible widthwise direction for cell H). (b) Lateral migration of cell I in the widthwise direction (there is negligible depthwise direction for cell I). (c) Lateral migration of cell A in the depthwise direction. (c) Lateral migration of cell A in the widthwise direction*

The "phase-jumping" behaviour vanishes for cell A, where the three modes show similar trajectories that present more or less steady increase of lateral displacement in both the depth and width directions (Figure 5.13c–d). The simulation animations of A (not shown here) present complex wobbling motions without a fixed rotation axis under all three modes (as if trembling or oscillating), but all cells do follow the same path in the transverse plane as already suggested by their trajectory projections in Figure 5.13c–d.

Angular dynamics To understand the origin of the net migration (laterally) observed for rigid RBCs presented above, the patterns of their angular velocities Ω in all principal directions are investigated, *i.e.*, Ω_x, Ω_y, Ω_z (Figure 5.14). The main findings are as below. First, for cells which

are initialised on channel axes (*i.e.,* cell H and cell I), the P and F modes are virtually equivalent, with only a phase difference in their waveforms of angular velocity (compare waveforms of M1 and M2 in the figures). Furthermore, for the P/F modes of these cells (again cell H and cell I), the only unstable waveform of angular velocities (*i.e.,* with a non-zero mean over time) is found in the vorticity direction, which is perpendicular to the respective shear plane. Then, for all cells, the V mode (*i.e.,* M3 in the figures) appears unstable or at best quasi-stable in all directions, albeit in some directions the angular velocities are one to two orders lower in magnitude than the primary direction and should be considered as numerical noises. Specifically for cell A, which is placed at the corner and near to two walls, the pattern of its angular velocities is the compromised result of wall-induced effects from both directions, seemingly integrating the angular dynamics of cell H and cell I in corresponding principal directions.

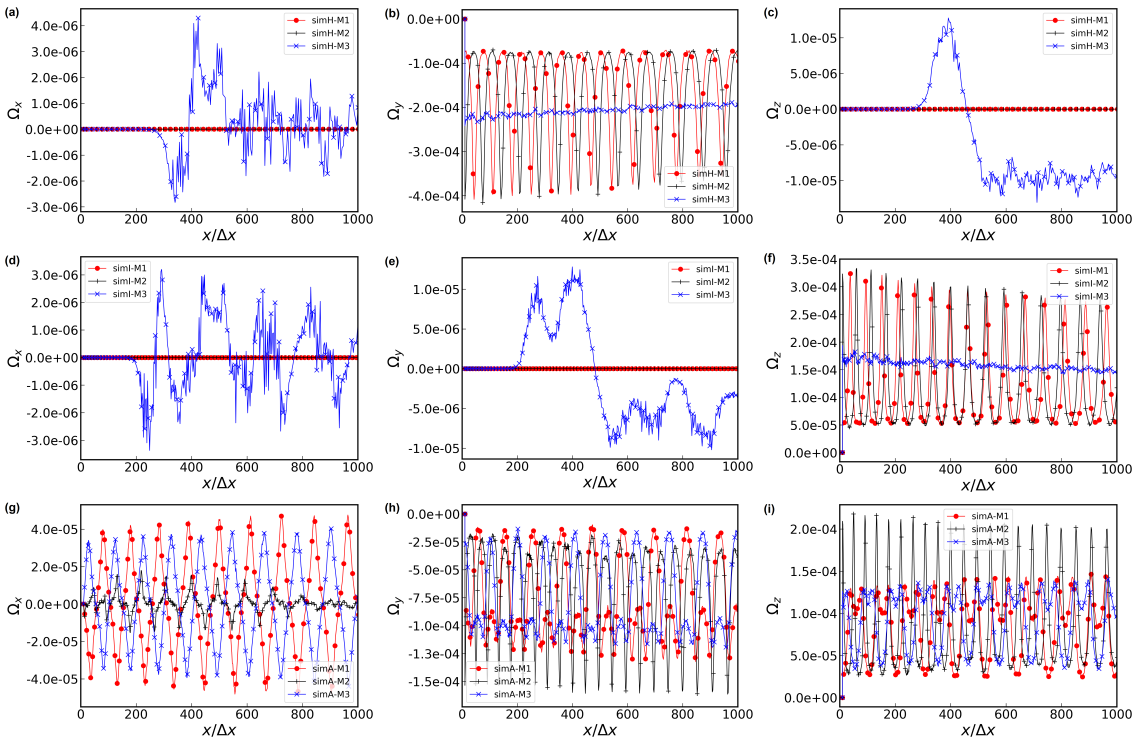

Figure 5.14: *Angular dynamics of cell H, I, A. (a-c) show the angular velocities of cell H in the $x-$, $y-$ and $z-$ directions, respectively. For cell H, $y-$axis indicates the direction of vorticity. (d-f) show the angular velocities of cell I in the $x-$, $y-$ and $z-$ directions, respectively. For cell I, $y-$axis indicates the direction of vorticity. (g-i) show the angular velocities of cell A in the $x-$, $y-$ and $z-$ directions, respectively.*

Importantly, for the tumbling cases including cell H and cell I under either P or F modes, clear symmetry-breaking of the waveform between the first and second halves of one tumbling cycle (featuring alternating round-peaks/sharp-troughs or sharp-peaks/round-troughs) can be observed in the vorticity direction, which is along $y-$axis for cell H and along $z-$axis for cell I (see Figure 5.14b and Figure 5.14f). This symmetry-breaking also occurs to the wobbling cases, namely cell A under all three modes, and in both $y-$axis and $z-$axis directions (for cell A it is difficult to define the shear plane and vorticity direction). This symmetry-breaking observed here may be the reason behind the lateral migration of the rigid RBCs (which cannot be treated as solid objects due to the fluid interior to the cell membrane) even under low inertia (small but non-zero Reynolds number, therefore residual deformation may still arise). The occurrence of such symmetry-breaking is presumably associated with the biconcave shape and fluid-filled nature of the seemingly "solid" RBC, which interacts with the channel wall in a more complex way than commonly expected.

5.4 Concluding remarks

RBCs or their biomimetic counterparts (*e.g.,* capsules and vesicles) in shear flow have been exhaustively studied over the past decade, mainly because of their prominent role in the microcirculatory system and related biomedical applications. Major breakthroughs have been made to deepen our understanding of their dynamics. However, a holistic view of the principles and laws governing their complex behaviour under different scenarios is still lacking, which is partially caused by insufficient "cross-talk" between experimental observations, theoretical modelling and computational simulations regarding some fundamental phenomena or processes of RBCs. Using the present IB-LBM model, this chapter has been dedicated to revisit relevant problems (to this thesis) that have been considered by other researches using different methods before. On one hand, this is to validate our model for future application to related problems; on the other, some uncertainties of previous research on these problems are reviewed. As shown by the results in this chapter, the present IB-LBM equipped with message-passing-interface (MPI) parallelisation is capable to solve some of the most computational-challenging cases (*e.g.,* RBCs squeezing through capillary vessels or splenic slits) and show satisfactory agreement with other established models. Furthermore, the finding of the tumbling-induced symmetry-breaking provides new insights into the intriguing lateral migration of apparently rigid RBCs.

Chapter 6
Dynamics of dilute RBC suspensions in a straight microchannel

Microfluidic technologies are commonly used for the manipulation of red blood cell (RBC) suspensions and analyses of flow-mediated biomechanics as previously introduced in Sec. 2.3.2. To enhance the performance of microfluidic devices, understanding the dynamics of the suspensions processed within is crucial. In this chapter, novel aspects of the spatio-temporal dynamics of RBC suspensions flowing through a typical microchannel at low Reynolds number are reported. Originally in experiments with dilute RBC suspensions (by J. Fidalgo), an off-centre two-peak (OCTP) profile of cells contrary to the centralised distribution (commonly reported for low-inertia flows) was found. The OCTP profile was reminiscent of the well-known "tubular pinch effect" which usually arises from inertial effects [271, 272]. However, given the conditions of negligible inertia in the experiments, an alternative explanation was needed for the profile. To uncover the underlying mechanism, massively-parallel simulations of RBC flow in real-size microfluidic dimensions are performed using the IB-LBM model and confirm the experimental findings. Further by analysing the RBC migration and cell-free layer (CFL) development within a high-aspect-ratio channel, it is demonstrated that such a distribution is co-determined by the spatial decay of hydrodynamic lift and the global deficiency of cell dispersion in dilute suspensions. A CFL development length exceedingly longer than typical lengths of microfluidic designs for localised measurements is reported. This work highlights the key role of transient cell distribution in dilute suspensions, which may negatively affect the reliability of experimental results if not taken into account.

This chapter springs from a collaborative project with my experimental collaborators at the University of Strathclyde (Glasgow, UK). The experimental schematic/data in Figures 6.1, 6.4, 6.8a, 6.13a are provided by J. Fidalgo. Except the above, all contents contained in this chapter are my own work. A peer-reviewed journal paper [339] has been published [1].

[1] *Zhou, Q* et al., *Spatiotemporal dynamics of dilute red blood cell suspensions in low-inertia microchannel flow, Biophysical Journal (2020), 118(10):2561-2573*

6.1 Overview

The present chapter aims to elucidate the spatio-temporal distribution of RBCs in a dilute suspension flowing through a typical microfluidic channel of rectangular cross-section. For a dilute suspension ($Ht \leq 1\%$) of horse RBCs in the microchannel, cell density profiles are obtained by a direct cell-counting routine developed *in-house* (see experimental details in Sec. 4.2.2). Consequently, a counterintuitive cell distribution with off-centre two-peak ordering rather than a single peak near the centreline is found, even in the negligible inertia regime. Large-scale simulations performed for an equivalent system confirm the experimental finding and provide insight into the underlying mechanisms. The chapter is organised as follows: the experimental and numerical methods are briefly reviewed in Sec. 6.2. In Sec. 6.3.1, cell density profiles from experiments and simulations are presented. Sec. 6.3.2 provides analysis of the observed cross-streamline migration and investigates the mechanism behind the density profiles. Sec. 6.4 compares the present study with existing works and states the key implications of the findings. Sec. 6.5 concludes the chapter.

6.2 Model configuration and parameters

The materials and methods used for the experiments and the simulations involved in this study are outlined in Secs. 6.2.1 and 6.2.2, respectively.

6.2.1 Microfluidic design

General experimental equipment and sample preparation methods are detailed in Sec. 4.2 already and therefore not repeated here. The microfluidic device for the present study was manufactured by soft-lithography using an SU8 mould produced by photo-lithography (microLIQUID). The microfluidic channel was made in PDMS (polydimethylsiloxane, Sylgard 184, Dow Corning) and bonded to a glass slide substrate with oxygen plasma (Zepto, Diener). The channel has a rectangular cross-section, with the width and depth dimensions ($W = 87\,\mu$m, $H = 31\,\mu$m) determined by optical microscopy, giving a hydraulic diameter of $D_\mathrm{h} = 45.7\,\mu$m. The density and shear viscosity values used to calculate dimensionless numbers (*e.g.,* Reynolds number Re and Capillary number Ca) for experiments are 1.07 g/mL and 5.0 mPa s, respectively.

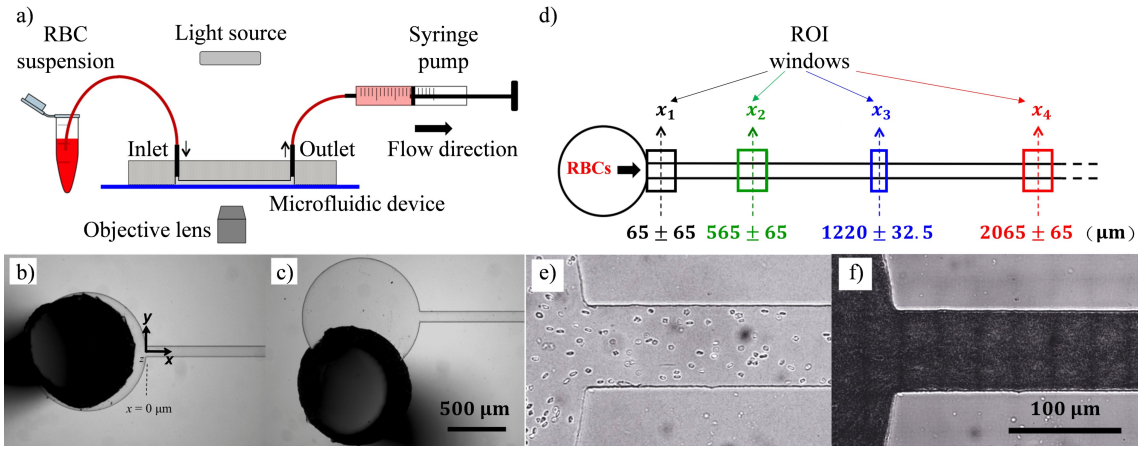

Figure 6.1: *(a) Schematic of the experimental setup. (b–c) Inlet configuration of the microfluidic device, showing optical images of the flow entry region where the inlet port is (b) aligned and (c) misaligned relative to the channel centreline. In (b), the coordinate axes are shown. (b–c) share the same scale bar of 500 μm. (d) Schematic showing designated regions of interest (ROIs) for the measurement of probability density distribution (PDD) of RBCs in the suspension. (e) An individual frame of RBCs flowing in the microchannel and (f) a composite image combining 300 frames of the same region, obtained using the Z-projection method based on minimum intensity. In (e–f), $Q = 0.2\,\mu L/min$, and they share the same scale bar of 100 μm.*

Fig. 6.1a shows a schematic of the experimental setup, where the sample is infused into the inlet of the microdevice using the withdraw function of the syringe pump located at the outlet. With this proposed system, the sample-containing Eppendorf can be gently stirred at regular time intervals to minimise cell sedimentation, which typically limits the duration of experiments. To test the effect of inlet conditions, inlet ports are manually punched onto the PDMS, so that the tubing connection can be either aligned (Fig. 6.1b) or misaligned (Fig. 6.1c) with the centreline of the microdevice. All results are for the aligned case unless otherwise stated.

6.2.2 Numerical simulation

Most numerical methods are covered in Sec. 4.2 already. Here, only the model configuration (Fig. 6.2) and simulation setup (Fig. 6.3) specific to the present study are introduced. The simulations have identical capillary number Ca and viscosity contrast λ (between RBC interior/exterior) to experiments to ensure comparability (see Table 6.1 for key simulation parameters).

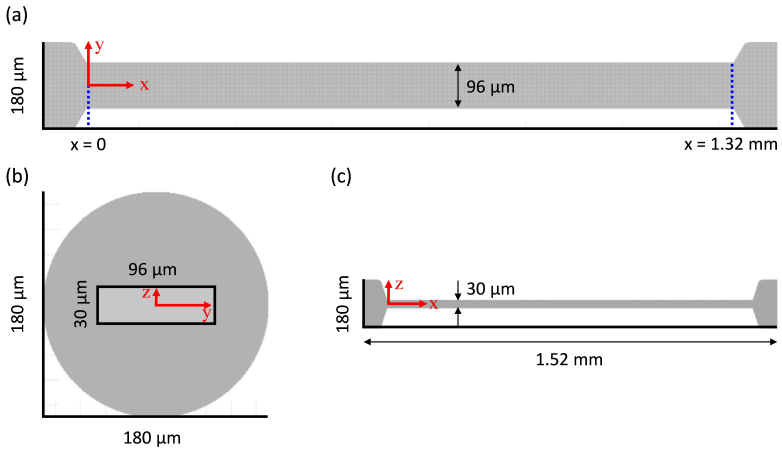

Figure 6.2: *Geometry of the computational model (CTRAC-L, larger contraction). (a) is the top view of the geometry, showing the widthwise span of the channel. In (a), the main channel (rectangular) is marked with two blue dotted lines. (b) shows cross-sectional views of the front-end and rear-end of the tapered entry region, the latter of which coincides with the channel entrance ($x = 0$). (c) is the side view of the geometry, showing the depthwise span of the channel.*

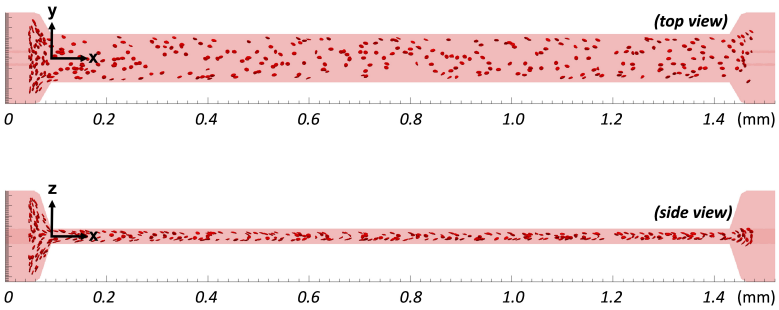

Figure 6.3: *A snapshot of the simulation at t = 0.37s, showing distribution of the 1% RBC suspension in the width and depth directions of the microchannel. Once arriving at the end of the channel, the cells are removed from the system.*

Model configuration Fig. 6.2 shows the 3D computational model for simulation of the RBC flow through a rectangular microchannel. Two geometries have been designed in the simulation to account for potential entrance effects that exist in experiments due to inlet configuration, which primarily arise from the inflow contraction between the entry region and the main channel. The main channel part in both geometries is the same, which is 96 μm wide, 30 μm deep and 1.32 mm long. The only difference is the front-end diameter of the tapered entry region (100 μm long).

Table 6.1: *Key simulation parameters. The symbol "∼" represents simulation units.*

Parameter	Symbol	Value
channel geometry		
width	W	96 μm
depth	H	30 μm
length	L	1320 μm
hydraulic diameter	D_{h}	45.7 μm
entry region diameter	D_{entry}	180 or 96 μm
RBC model		
cell radius	r_{rbc}	4 μm
viscosity contrast	λ	1.0
feeding haematocrit	H_{F}	1%
local haematocrit	Ht	variable
simulation setup		
particle Reynolds number	Re_{p}	0.03
capillary number	Ca	0.6
LB relaxation parameter	$\widetilde{\tau}_{\mathrm{BGK}}$	1.0
voxel size	Δx	0.6667 μm
time step	Δt	7.41 $\times 10^{-8} s$
shear modulus	$\widetilde{\kappa}_s$	5.00 $\times 10^{-4}$
bending modulus	$\widetilde{\kappa}_b$	4.50 $\times 10^{-5}$
reduced bending modulus	$\widetilde{\kappa}_b \Delta x^2 / (\widetilde{\kappa}_s r_{\mathrm{rbc}}^2)$	1/400

The entry region for the first geometry has a front-end diameter of 96 μm (hereafter referred to as CTRAC-S, meaning "smaller inflow contraction"), and the one for the second geometry has a front-end diameter of 180 μm (hereafter referred to as CTRAC-L, meaning "larger inflow contraction". All simulation data and plots presented in this chapter are for CTRAC-L, unless otherwise specified). An identical entry region is also added to the channel outlet for removing cells from the simulation. The whole domain measures 1.52 mm in length, with a total of 26,201,764 lattice voxels (each Δx = 2/3 μm. All dimensions of the domain are labelled in Fig. 6.2, shown from three camera views.

Simulation setup Initially, a plasma flow (no cells) is driven from left to right along the x-axis direction with a fixed volume flow rate (Fig. 6.3). The flow is controlled by imposing a parabolic velocity profile (assuming Poiseuille flow) at the inlet and a reference pressure at the outlet. The no-slip condition on walls is implemented with the Bouzidi-Firdaouss-Lallemand

method (BFL [33]). Because it is computationally prohibitive to simulate the realistic experimental condition where the particle Reynolds number approaches zero, the fluid flow in the simulation is numerically accelerated to a state where the particle Reynolds number equals 0.03 (still within the low-inertia regime). After the plasma flow is converged, RBCs are randomly inserted from the cylindrical entry region in a continuous manner with fixed haematocrit (H_{F} = 1%). To make the experiments and simulations comparable, the similitude is established using the capillary number Ca. For the target $Ca = 0.6$, the RBCs are fairly deformable in the channel assuming tank-treading motion, where the cell membrane is fluidized and rolls around the cell interior.

6.3 Results

The experimental and simulation results on the RBC distribution in the channel are shown in Sec. 6.3.1. Additional data of the RBC flow and analysis of underlying mechanisms leading to the observed cell distribution is provided in Sec. 6.3.2.

6.3.1 Counterintuitive RBC distribution

The main results are reported here, focusing on the dynamical distribution of RBCs in a dilute suspension. Experimentally, by continuously feeding RBCs at fixed haematocrit ($H_{\mathrm{F}} \leq 1\%$) into the microfluidic device, the transverse motion of cells can be evaluated by monitoring the probability density distribution (PDD) of RBCs at sequential locations along the channel axis. This process is also replicated numerically to corroborate the experimental observations and provide further insights into the 3D motion of cells in a microchannel of rectangular cross-section.

Experiments Under negligible inertia ($Re_{\mathrm{p}} < 2 \cdot 10^{-4}$), an evident increase of cell concentration is observed in the close-wall region, manifested by the augmentation of two off-centre peaks in the PDD profile depicting RBC fractions across the channel (Fig. 6.4a, $Ca = 0.6$). Locations of the two peaks are approximately symmetric about the channel centreline and keep moving inwards until a certain distance about 0.2–0.25 times the half channel width $W/2$ to the wall is reached (*i.e.,* $y/(0.5W) = 0.75 \sim 0.8$). Beyond this distance, the inward migration of cells ceases (compare $x = 1220,\ 2065\,\mu$m) and eventually causes an off-centre two-peak (OCTP) profile, sug-

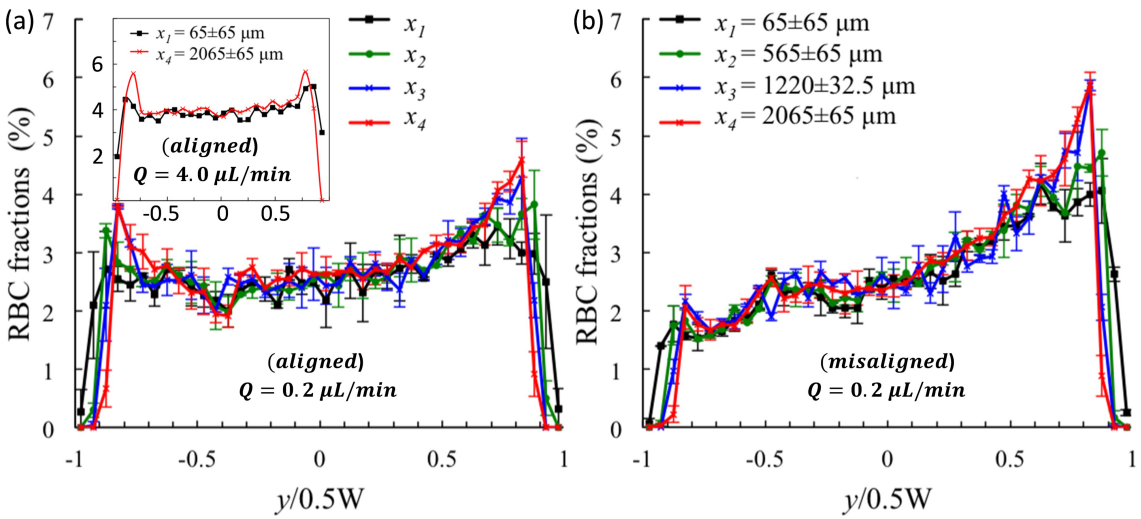

Figure 6.4: *(Experiment) Probability density distribution (PDD, see Chapter 4) of RBCs at* $x =$ 65, 565, 1220, 2065 μm *away from the entrance, under a volume flow rate of* $Q =$ $0.2\,\mu L/min$*. The inlet ports are (a) aligned and (b) misaligned relative to the channel centreline, respectively. The inset of (a) shows the PDD profiles at* $x = 65$, 2065 μm *under a volume flow rate of* $Q = 4.0\,\mu L/min$ *for the aligned configuration.*

gesting the inertial "tubular pinch effect" (or Segré-Silberberg effect [271, 272]). Contrarily, in the central region, the cell concentration remains nearly unchanged. By comparing the PDD profiles along the channel length, a cell population originally close to each wall is found to cross streamlines and progressively shift inwards (see $x = 65,\ 565,\ 1220\,\mu$m). For an initial cell distribution with significant left-right asymmetry induced by misaligned flow inlet (see experimental image in Fig. 6.1c), the same inward motion of cells near the wall occurs (Fig. 6.4b).

The observed quasi-steady OCTP distribution of RBCs does not agree with the commonly reported cell distribution (or haematocrit profile) in microscale channels, which typically exhibits a core of cells near the channel centre accompanied by a cell-depleted layer near the channel wall [58, 83]. To rule out the possibility that such an OCTP distribution is exclusive to the volume flow rate $Q = 0.2\,\mu$L/min ($Ca = 0.6$), Q is also varied up to 4.0 μL/min ($Ca = 12.1$) for the aligned configuration (inset of Fig. 6.4a). Clearly, the volume flow rate does impact the initial PDD profile at $x = 65\,\mu$m: a low Q (*e.g.*, $Q = 0.2\,\mu$L/min) yields a virtually flat density profile, whereas a high Q (*e.g.*, $Q = 4.0\,\mu$L/min) gives rise to appreciable density peaks near the walls. Despite the dependence of initial RBC distribution on Q (presumably within a range where the cell deforma-

tion is sensitive to Ca), qualitatively similar evolution (up to $x = 2065\,\mu$m) of the PDD profile is identified for all cases, featuring the development/enhancement of density peaks at two symmetric locations near the lateral channel walls.

Simulations To understand the peculiar cell distribution observed in experiments, numerical simulations for a 1% RBC suspension flowing at low Reynolds number (Re_{p} = 0.03) are performed in a long straight microchannel of identical hydraulic diameter ($D_h = 45.7\mu$m) and similar aspect ratio ($W/H = 3.2$). In simulations, access to the three-dimensional distribution of RBCs within the channel is available and the RBC pattern in individual cross-sections can be investigated, which are unobservable from common experimental set-ups. In line with what the experiments suggested, the gradual formation of a RBC loop reminiscent of the "tubular pinch effect" by visual inspection of the cross-sectional snapshots is observed in the simulation (Fig. 6.5a).

To quantify the RBC distribution, further analysis of the time-averaged haematocrit (Ht) profiles is performed across respective directions of the channel (Fig. 6.5b). While results from the width direction W can be directly compared with experimental data, complementary results from the depth direction H provide additional insight into the RBC dynamics. From the calculated histogram of local haematocrits at a position near the entrance ($x = 150\,\mu\mathrm{m} \approx 3.3D_{\mathrm{h}}$), distinct initial states of the suspension can be found in the width and depth directions upon the entry of RBCs into the rectangular channel. While the widthwise distribution of cells presents a more or less centralised pattern, the depthwise distribution features two primary density peaks (Fig. 6.5c). Subsequent Ht profiles monitored at downstream locations ($x = 450,\ 750,\ 1050\,\mu$m) bear a general resemblance to the corresponding initial distribution at $x = 150\,\mu$m, indicating the suspension's persisting memory of the initial state even after a development length $> 20D_{\mathrm{h}}$ (Fig. 6.5d–e). Specifically, in the W direction, the Ht profiles gradually develops into a two-peak profile with the near-wall cells progressively shifting inwards (Fig. 6.5d). Conversely, cell densities in the central area only change in a minor way, despite the continuous enrichment of concentration within the neighbouring peaks. This overall trend is in line with the experimental findings of the PDD profile. Note how the "pseudo-equilibrium" position of the peaks agrees with that found in experiments, being about 0.3 times of half channel width away from the wall (*i.e.,* $y/(0.5W) = 0.7$).

In the H direction (Fig. 6.5e), a distinct pattern for the haematocrit profile is the evolution of a

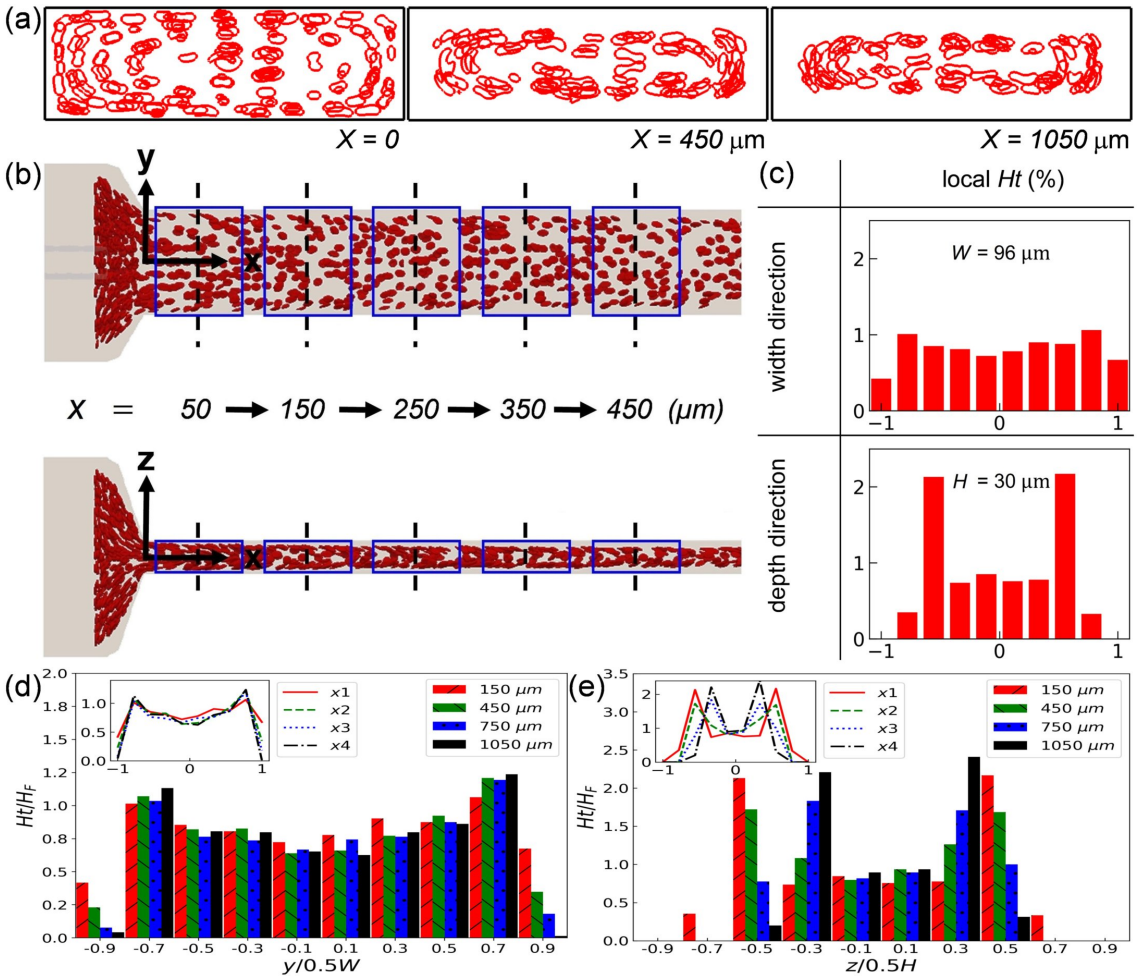

Figure 6.5: *(Simulation) (a) Cross-sectional slices showing RBCs at $x = 0, 450, 1050\,\mu m$ away from the entrance, combining snapshots from 50 consecutive time steps. (b) Example of the haematocrit (Ht) analysis showing superimposed RBCs from multiple simulation snapshots (at designated time intervals) in sequential sampling boxes (blue) measuring $50\,\mu m$ long each at target locations (ROIs) downstream of the channel entrance. Cells within each sampling box are projected and allocated into 10 bins across the width or depth directions for counting, with their position determined by centre of mass. (c) Histograms of time-averaged local Ht measured at $x = 150\,\mu m$ in the width and depth directions. (d–e) Evolution of the Ht histogram across the channel in (c) the width direction and (d) the depth direction at $x = 150, 450, 750, 1050\,\mu m$, respectively. All Ht values in (d–e) are normalised by the feeding haematocrit $H_F = 1\%$. The insets within (d–e) depict Ht profiles corresponding to the histograms.*

five-layered ordering, featuring a cell-depletion layer next to each wall, two cell-enrichment layers neighbouring the centre, and one cell-depression layer right at the centre. Far downstream from the entrance ($x = 1050\,\mu$m), the heterogeneity of cell concentration across the depthwise direction becomes highly pronounced, presenting an arguable equilibrium position for the primary density peaks located at about 0.7 times the half channel depth away from the wall (*i.e.,* $z/(0.5H) = 0.3$). Overall, a substantial inward march of cells towards the channel centreline can be observed, with marked shifts of both density peaks.

6.3.2 Flow properties and RBC dynamics

To reveal the underlying physics behind the intriguing OCTP distribution of RBCs presented in Sec. 6.3.1, several key aspects of the problem need to be understood, including the origin of transverse cell migration, the effect of channel geometry, the distribution of cell velocity, the formation of the cell-depletion layer and the variation of tube haematocrit. Two main questions to be answered are: 1) How do the two density peaks in the PDD profile come into being? 2) Why do the peaks keep building up instead of being dispersed?

Mechanism for cell migration Given its small Reynolds number, the RBC flow considered here falls into the low-inertia regime, where viscous effects dominate. For deformable objects in viscous flow, their lateral drift away from the wall is well-documented, dating back to the 1830s when Poiseuille first observed a plasma layer (or cell-free layer, CFL) in frog arterioles and venules [296]. The origin of such motion of RBCs was later determined to be the non-inertial hydrodynamic lift arising from unbalanced pressure forces on the cell. This lift can drive cells in microscale vessels/channels to cross streamlines and migrate towards the central area, ultimately leading to the formation of a two-phase flow featuring a cell core and a fluid periphery [58, 83]. Following the discovery by Goldsmith and Mason [111], the lateral migration of deformed particles in non-inertial flows has been confirmed by other experimental studies [3, 41, 64, 186] and numerous modelling reports [42, 72, 81, 126, 149, 204, 270, 279, 293]. In principle, there are three mechanisms for the cross-streamline motion of RBCs in low-Reynolds-number shear flows: 1) wall-repulsion-induced lift force on RBCs, 2) shear-gradient-induced asymmetric deformation of RBCs, and 3) hydrodynamic diffusion (or shear-induced diffusion) between RBCs due to cell-

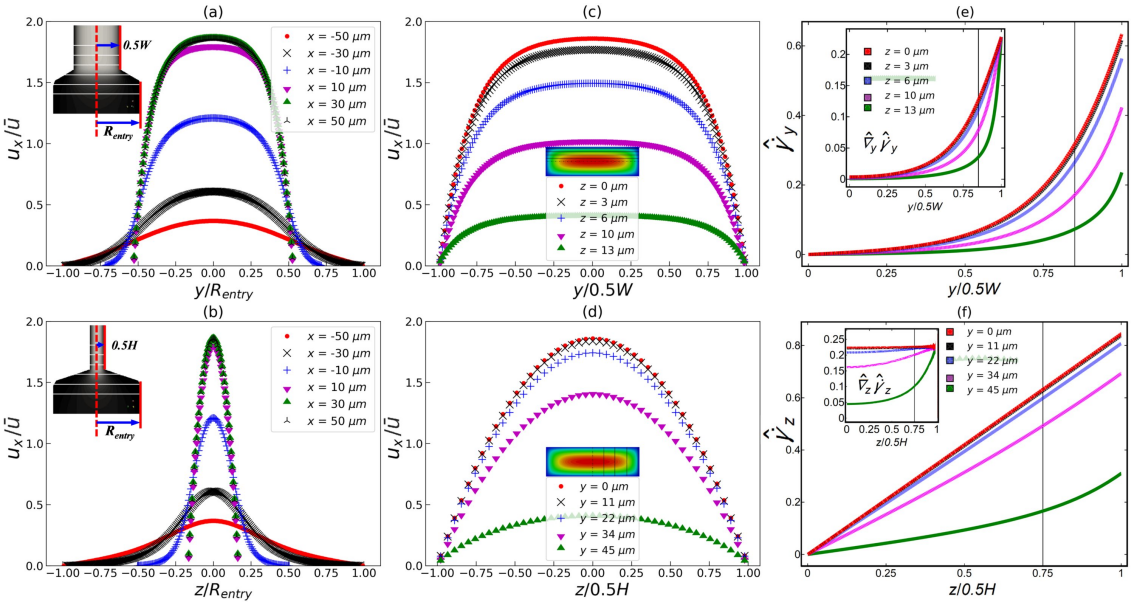

Figure 6.6: *(a–b) (Simulation) Transient mid-plane velocity profiles at six locations near the entrance region of the channel ($x = -50, -30, -10, 10, 30, 50\,\mu m$). The insets in (a–b) mark these locations by white solid lines on the mid-plane of the channel, where $x = 0$ is located at the transition point from the cylindrical flow inlet (gradually tapered) to the rectangular channel. (c–d) (Simulation) Steady velocity profiles at $x = 50\,\mu m$. z and y values in the legends represent positions relative to the mid-plane in each direction, with $z = 0$ and $y = 0$ denoting the widthwise and depthwise mid-planes, respectively. (e–f) (Analytical) Shear rates (main frame) and shear-rate gradients (inset) calculated from asymptotic solutions in [37]. The colours represent z or y values as in (c–d). The black vertical lines in (e–f) indicate the centre of the outmost layer of cells at $x = 50\,\mu m$ detected in the RBC simulation along the (e) y-direction and (f) z-direction, respectively (see Fig. 6.7).*

cell interactions. Depending on the flow properties (*e.g.,* velocity profile, shear distribution and wall confinement) and cell conditions (*e.g.,* position, shape and rigidity), the direction and strength of RBC motion under the combined effect of the above mechanisms can be difficult to determine.

Geometric effect and shear anisotropy In the present problem, where a laminar flow is pressure-driven in a rectangular microchannel of high aspect ratio ($W/H = 3.2$), the flow field is complex because distinct velocity profiles co-exist in the channel cross-section: a typical parabola characteristic of Poiseuille flow in the depth (H) direction and a blunted profile featuring plug-like flow in the width (W) direction [37]. Additionally, the existence of entrance effects further increases

the complexity of the problem. These two aspects contribute to a plethora of scenarios for the velocity profile curvature (reflecting the shear-rate gradient), which on the one hand constitutes a mechanism for cell migration itself (by introducing symmetry-breaking deformation [149]) and on the other hand impacts the wall-induced lift (being a function of the particle shape [219]). The evolution of unperturbed mid-plane velocity profiles (in the absence of cells) are shown near the entrance across both directions, where rich behaviour of the velocity profile can be found as the fluid accelerates through the contracted transition between the entry region and the channel itself (Fig. 6.6a–b). This geometry-induced velocity alteration potentially underpins the distinct initial distribution of RBCs between the W and H directions of the channel observed in Fig. 6.5c.

Fig. 6.6a–b reveal that the flow becomes fully-developed between x = 30–50 μm in the simulations. Fig. 6.6c–d show the converged velocity profiles velocity profiles for different z- and y-planes at $x = 50\,\mu$m, respectively. Using the asymptotic solution of this microfluidic flow [37], the shear-rate profiles and shear-rate-gradient profiles are calculated and plotted. The cross-sectional pattern of shear rates (normalised by the characteristic time scale τ as in Eq. 4.2 of Chapter 4) turns out more intricate than often assumed (Fig. 6.6e–f), even in the narrow dimension (H) where linearity is commonly assumed for such a high aspect ratio ($W/H > 3$) [64]. At close distances to the wall (*e.g.,* $y = 45\,\mu$m in Fig. 6.6d), the H-direction velocity profile deviates significantly from a parabolic one (Fig. 6.6f), resulting in non-linear decrease of shear rate on approaching the channel centreline and varying shear gradients (inset of Fig. 6.6f). In the W direction where blunted velocity profiles prevail (Fig. 6.6c), the shear gradients vary both at close and large distances to the wall (inset of Fig. 6.6e), leaving the hydrodynamic lift even more unpredictable by the classic theory derived on the basis of ideal shear flows [219].

Decay of lift velocity The presence of RBCs at $H_{\mathrm{F}} = 1\%$ (or below) does not significantly disturb the apparent velocity profiles from their unperturbed states (compare Fig. 6.6 and Fig. 6.10), therefore the transverse motion of RBCs can be analysed with respect to the unperturbed flow. Subject to the complex flow pattern in the channel as elaborated by Fig. 6.6, the motion of RBCs within are likely to be affected by both the solid wall and the fluid shear gradients. At low Reynolds number, this motion can be conveniently decomposed into two orthogonal directions, hereby the W and H directions, on assuming negligible inertia and invoking the Stokes equations. Fig. 6.7a–

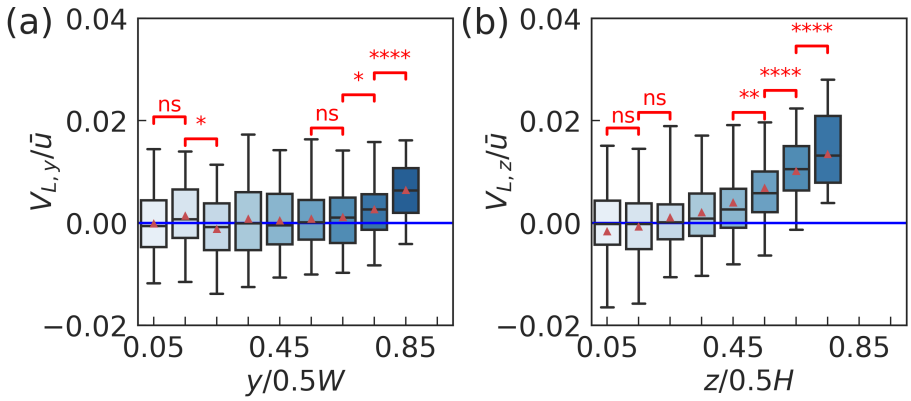

Figure 6.7: *(Simulation) Statistical lift velocities of RBCs within $x = (50 \pm 8)$ μm, characterising the RBC migration along the (a) y-direction (widthwise) and (b) z-direction (depthwise), respectively. For statistical analysis in both (a) and (b), the channel is fictitiously folded along the channel centreline and then divided into 10 bins, followed by the assignment of cells according to the position of their centre of mass. A positive lift velocity here indicates an inward motion of RBCs towards the channel centreline. Statistics note: the black solid line and the red triangle inside each box represent the median and the mean lift velocity within each bin, respectively. The horizontal hats (red) above the boxes show results of Welch's T test between neighbouring cell groups, where *P $<$ 0.05 is considered as statistical significance; **P $<$ 0.01, ****P $<$ 0.0001.*

b show the statistical RBC lift velocities V_l (relative to the unperturbed flow mean velocity $\bar{u}$) in 10 subdivisions of a cross-section, divided either widthwise (W) or depthwise (H). Compared with the depthwise lift, the widthwise lift is found to decay much faster as the cell-wall distance increases. While $V_{l,z}$ vanishes at 0.75 times of $H/2$ away from the wall ($z/(0.5H) = 0.25$), $V_{l,y}$ already becomes negligible at 0.35 times of $W/2$ away from the wall ($y/(0.5W) = 0.65$). The contrast of lift decay between the two directions can be explained by the shear-rate and shear-rate-gradient profiles in the cross-section (Fig. 6.6e–f). As the cells migrate towards the channel centreline, the local shear rate diminishes to zero, with much faster drop in W than in H. Meanwhile, the local shear gradient also quickly vanishes in W direction, whereas that in H direction decreases in a relatively mild way. Consequently, contributions of both the wall-induced lift and shear-gradient-induced lift in the W direction are weakened more quickly.

The distribution of lift velocities in both the width and depth directions coincides with the overall evolution of the Ht profiles presented in Fig. 6.5d–e: while a "pseudo-equilibrium" position close

to the wall exists for the widthwise migration (beyond which the lateral motion of cells ceases), the depthwise cell migration is more substantial and results in a "pseudo-equilibrium" position much closer to the channel centre. Therefore, a correlation between the decaying lift of cells and their spatial distribution in the cross-sectional direction can be inferred.

Growth of cell-free layer Now let us move on to investigate how the transverse motion of RBCs contributes to the spatial development of CFL along the channel axis. Shown in Fig. 6.8a is the growth of CFL thickness over $46D_\mathrm{h}$ in experiments (recording the averaged CFL from the two lateral walls). The data manifests an evident power-law behaviour with a best-fit exponent of 0.39 ($R^2 = 0.93$). The simulation CFLs over $28D_\mathrm{h}$ (recording separate CFLs for individual lateral/vertical walls) present similar trends, also showing a power-law increase. However, further scrutiny of the simulation data reveals a slight discrepancy in the growth rate (Fig. 6.8b-e). Compared to the experimental value of 0.39, the power-law exponents found in the simulation are smaller. In the width direction, the exponents are 0.26 and 0.29 for the right and left walls, respectively; in the depth direction, they are 0.29 and 0.25 for the bottom and top walls, respectively. Further analysis and quantification of this discrepancy between experimental and simulation CFL will be discussed in Sec. 6.4.2, with support from a scaling law derived for the current problem.

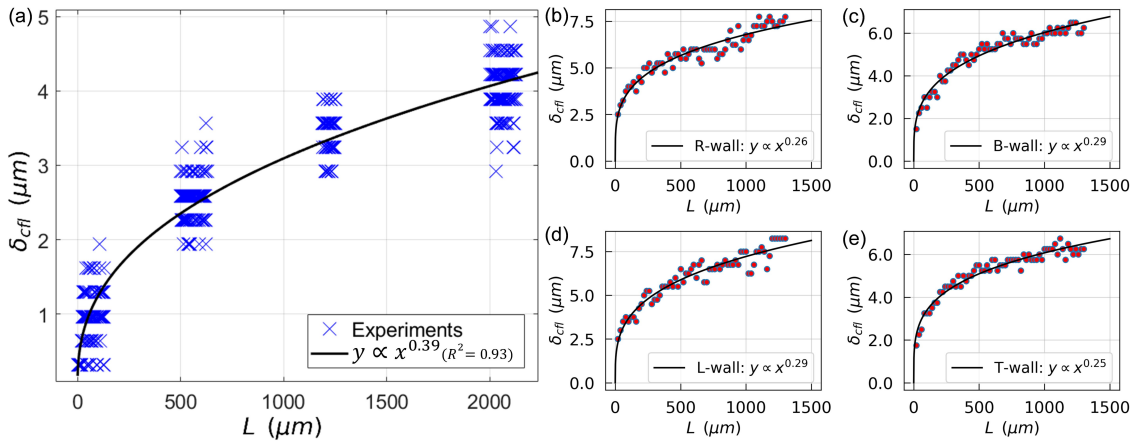

Figure 6.8: *(a) (Experiment) CFL measured in the width direction of the channel (averaged between opposite walls) under $Q = 0.2\,\mu$L/min ($Ca = 0.6$). (b–e) (Simulation) Power-law fitting for numerical CFLs from an equivalent simulation ($Ca = 0.6$) developing along each wall of the channel (right/bottom/left/top walls). The R-square values are 0.91, 0.94, 0.91, 0.95 for the R-/B-/L-/T-walls, respectively.*

Despite quantitative differences in the CFL thickness and growth rate between the experimental and simulation data (to be discussed elsewhere in Sec. 6.4.4), a neutral finding is that no critical saturation of the CFL increase can be identified within the investigated range. This means that the development of CFL in a typical microfluidic channel (rectangular cross-section) for a dilute suspension can take much longer than earlier estimates provided for microvessels or cylindrical tubes [150, 211, 242, 323]. In particular, Katanov *et al.* [150] reported a universal length $L_c \leq 25D$ (independent of flow rate and haematocrit) for full CFL development in channels between D = 10–100 μm, whereas $L_c > 28D_h$ is found in present simulations (only serving as a lower-bound estimate because the flow domain was limited to such length for tractable computation) and $L_c > 46D_h$ in current experiment (channel hydraulic diameter $D_h \approx 45.7\,\mu$m). Based on earlier findings of the "pseudo-equilibrium" positions for the widthwise cell migration (until 0.3 times of half channel width from wall) and depthwise cell migration (until 0.7 times of half channel depth from wall), the CFL thickness in simulations might continue to grow until reaching 10–14 μm, which will be much larger than the 6–8 μm monitored within $L_c \leq 28D_h$ (Fig. 6.8b-e).

Reduction of tube haematocrit The long-range development of CFL will inevitably affect the local rheological properties of the suspension. As shown in Table 6.2, the tube haematocrit Ht measured from either of the simulated geometries (CTRAC-L: large-contraction inlet, all simulation data and plots presented elsewhere in the present chapter are from this geometry; CTRAC-S: small-contraction inlet. See more details of CTRAC-L and CTRAC-S in Sec.6.2.2) drops continuously along the channel axis compared to the feeding haematocrit H_F, even after $1050\,\mu$m ($\approx 23D_h$) away from the entrance.

This reduced volume fraction of blood flow in microchannels versus the discharge haematocrit ($H_D \approx H_F$) is known as the Fåhræus effect, where $Ht/H_D = \bar{U}_B/\bar{V}_x < 1$ ($\bar{U}_B$ and $\bar{V}_x$ are average velocities of the overall blood flow and the cells, respectively) [9, 103]. It stems from the cross-streamline motion of RBCs towards the high-velocity region around channel centreline, which

Table 6.2: *(Simulation) Variation of tube haematocrits along the channel axis.*

Inlet type	H_F	Ht-150 μm	Ht-450 μm	Ht-750 μm	Ht-1050 μm	Ht-1150 μm
CTRAC-L	1%	0.810%	0.749%	0.703%	0.696%	0.685%
CTRAC-S	1%	0.705%	0.661%	0.659%	0.622%	0.619%

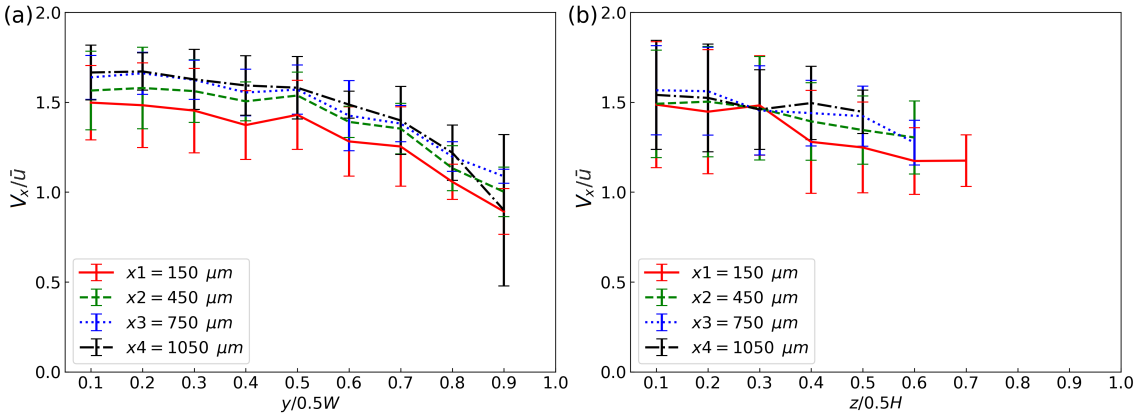

Figure 6.9: *(Simulation) Axial (streamwise) velocity of RBCs V_x in the channel (normalised by mean velocity of the unperturbed flow $\bar{u}$) at $x = 150, 450, 750, 1050\,\mu m$ away from the entrance. (a) and (b) show the width and depth directions of the channel, respectively. For statistical analysis in both (a) and (b), the channel is fictitiously folded along the channel centreline and then divided into 10 bins, followed by the assignment of cells according to the position of their centre of mass. Each error bar here shows the mean and standard deviation of the streamwise velocity.*

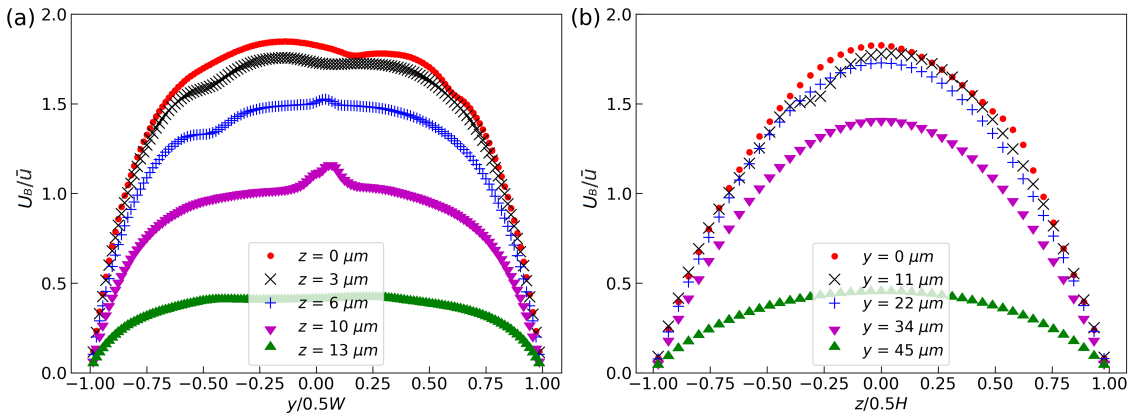

Figure 6.10: *(Simulation) Velocity profiles of the RBC-laden flow at $x = 50\,\mu m$. z and y values in the legends represent positions relative to the mid-plane in each direction, with $z = 0$ and $y = 0$ denoting the widthwise and depthwise mid-planes, respectively. The blood flow velocity U_B is normalised by mean velocity of the unperturbed plasma flow $\bar{u}$.*

empowers the cells within the channel to travel faster on average than the ambient fluid in the streamwise direction. Owing to the fairly long CFL development length ($> 28D_{\mathrm{h}}$ in simulation), the average ratio of cell-to-fluid velocities (Fig. 6.9) continues to change till the very end of the channel (a direct consequence of the varying cross-sectional distribution of RBC fluxes Fig. 6.11), leaving consistent measurement of tube haematocrits within the microchannel difficult.

6.4 Discussion

In the following the findings in Sec. 6.3 will be compared with existing studies and interpretations. Their implications for experimental studies on dilute RBC suspensions will also be discussed.

6.4.1 Velocity profile and RBC flux

Disturbance of RBCs to the plasma flow The velocity profiles from the RBC-laden flow at $H_F = 1\%$ (Fig. 6.10) apparently do not deviate much from the unperturbed flow in the absence of RBCs (Fig. 6.6). This implies that the sparse distribution of RBCs in the dilute limit only affects the flow velocity to a limited amount and causes local disturbances without modifying the overall velocity profile significantly. Therefore, it is reasonable to analyse the migration of RBCs in the 1% suspension using the unperturbed plasma flow.

Cross-sectional RBC flux distribution The Ht profile is co-determined by the lateral migration (towards channel centreline) and the streamwise acceleration (along channel axis) of RBCs, the former of which arises from the hydrodynamic lift effect and the latter is associated with the Fåhræus effect. Both effects have an impact the distribution of local haematocrits and can affect the dynamical evolution of the Ht profile. In this sense, the peaks emerging in the Ht profile (Fig. 6.5d-e) may not be ideal markers of the "pseudo-equilibrium" position for the inward migration of cells. Therefore, to ascertain the "pseudo-equilibrium" positions suggested by Ht peaks, these two effects need to be decoupled. To this end, the RBC fluxes are calculated, the sum of which strictly conserves along the channel axis and examine the cross-sectional distribution of the RBC fluxes. This allows us to exclude the effect of cell acceleration and distinguish the amount of lateral migration of the cells (Fig. 6.11).

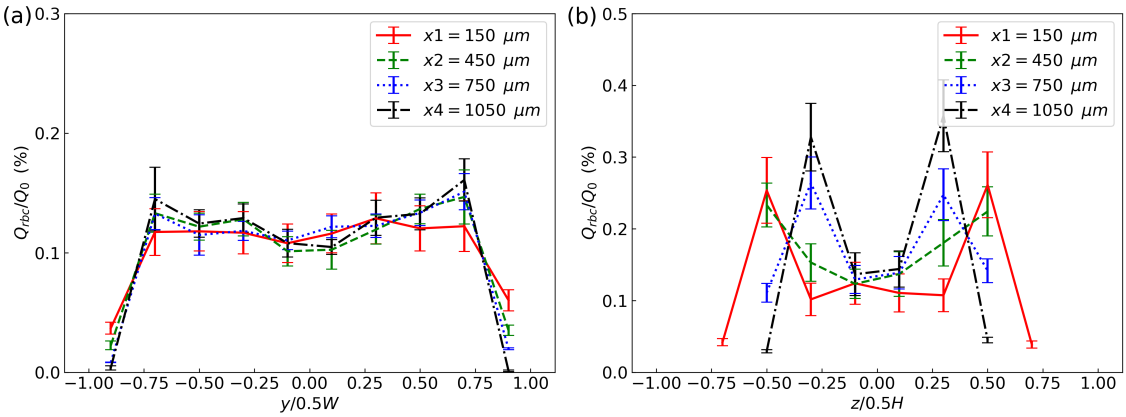

Figure 6.11: *(Simulation) Evolution of the cross-sectional RBC fluxes alongside the channel in (a) the width direction, and (b) the depth direction. The four colours red, green, blue, black indicate a distance of* $x = 150, 450, 750, 1050\,\mu m$ *away from the entrance, respectively. The RBC fluxes* Q_{rbc} *are all normalised by the volume flow rate of the unperturbed flow* Q_0*, and then converted to percentage (%).*

The evolution of RBC-flux distribution turns out qualitatively similar to that of the Ht profiles. It reveals a clear trend of inward RBC migration over time, with near-wall RBC fluxes moving away and subsequently accumulating at a "pseudo-equilibrium" position in both directions of the channel. For the widthwise migration, this equilibrium position is found to be 0.3 times of half channel width away from the wall; for the depthwise migration, it is 0.7 times of half channel away. The inward shift of RBC fluxes is accompanied by the continuous expansion of a zero-flux zone in the vicinity of the wall, which corresponds to the gradually growing CFL.

6.4.2 Hydrodynamic lift and CFL

Hydrodynamic lift The mechanism of hydrodynamic lift for tank-treading particles in shear flows has been analysed theoretically by Olla and Seifert in the 1990s [222, 274]. A simplified scaling law $V_l \sim \dot{\gamma}/h^2$ was derived for the lift velocity V_l under constant shear, as a function of the shear rate $\dot{\gamma}$ and cell-wall distance h [219]. This quadratic scaling has been widely employed in the literature as an approximation to estimate the lateral migration of particles in various flow conditions. However, recent studies show that in pressure-driven channel flows where non-constant shear (or non-zero shear gradient) exists, *e.g.,* Poiseuille flow, the curvature of the velocity profile modifies the scaling law in a non-trivial way and would significantly slow down the spatial decay

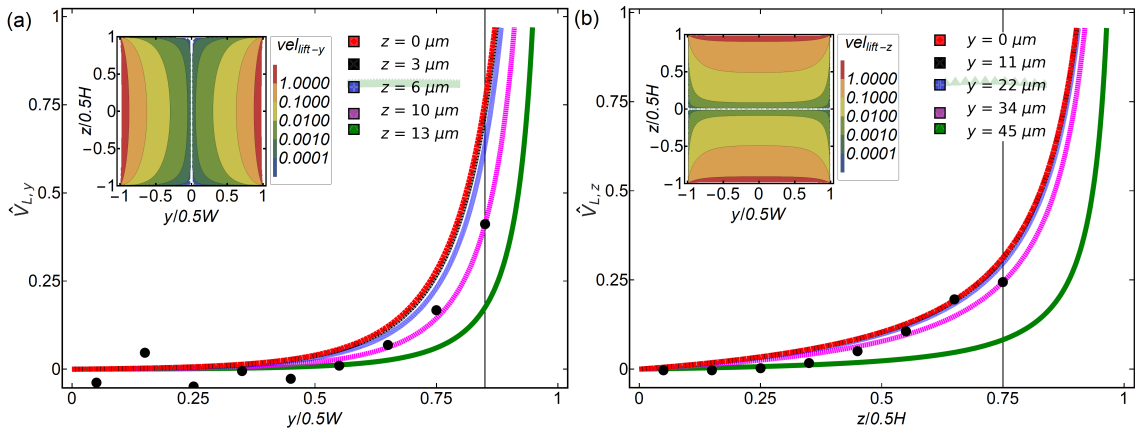

Figure 6.12: *Theoretical prediction of RBC lift velocities (line curves and contour plots) given by $V_l \sim \dot{\gamma}/h$ across (a) the width direction and (b) the depth direction of the channel, respectively. z and y values in the legends represent positions relative to the mid-plane in each direction (see Fig. 6.6c–d), with $z = 0$ and $y = 0$ denoting the widthwise and depthwise mid-planes, respectively. The black dots represent rescaled values of the numerical lift velocities extracted from Fig. 6.7a–b. The black vertical lines in (a–b) indicate the centre of the outmost layer of cells at $x = 50$ μm detected in the RBC simulation (see Fig. 6.7).*

of the lift velocity [67, 81, 149, 212]. Indeed, through systematic measurement of the lateral migration of various vesicles in bounded planar Poiseuille flow under different confinement degrees, Coupier *et al.* revealed that the scaling $V_l \sim \dot{\gamma}/h^2$ would fail to predict the trajectory of the vesicle, while a markedly different empirical law $V_l \sim \dot{\gamma}/h$ held [64]. Losserand *et al.* confirmed the scaling $V_l \sim \dot{\gamma}/h$ using RBC experiments and further refined the empirical law [187].

To examine whether the lateral migration of RBCs in the simulation obeys the lift scaling that Coupier *et al.* [64] and Losserand *et al.* [187] proposed for Poiseuille flow, theoretical shear rates are adopted from the asymptotic solution of pressure-driven flow in rectangular channel [37] and calculate the lift velocities applying $V_l \sim \dot{\gamma}/h$ (abandoning all prefactors for generality). Further with weighted normalisation, the dimensionless theoretical lifts ($\hat{V}_{l,y}$ and $\hat{V}_{l,z}$) are obtained for both W and H directions (Fig. 6.12a–b). For comparison with the theoretical prediction, numerical medians of the numerical lift velocities are extracted from Fig. 6.7a–b. After rescaling and overlapping them onto the theoretical curves, satisfactory data agreement across the H direction is observed, but only partial agreement in the W direction for the near-wall region. Approaching the central region in the W direction, the theoretical prediction breaks down. This is actu-

ally expected since the velocity profile there is abruptly blunted and significantly deviates from a parabolic shape. The simulation data are also examined against the theoretical prediction given by $V_{\mathrm{l}} \sim \dot{\gamma}/h^2$, which would overestimate the spatial decay of the lift in general and failed to yield an agreement with the simulation (results not shown here).

Cell-free layer CFL characterisation is an active research field owing to the prominent role of CFL in regulating blood viscosity and local haemodynamics. Limited by the complexity of in vivo imaging and measurement [153], glass capillaries and PDMS microchannels have been widely used to mimic the micro-circulatory environment for experimental observation of CFLs in vitro under different rheological conditions [302]. Meanwhile, versatile computational tools are developed and plenty of in silico studies on CFL emerge in the literature [83]. However, despite the large number of in vitro/in silico studies, most of them assumed a steady CFL for a given channel segment and hence failed to capture the highly heterogeneous and spatio-temporal nature of realistic CFLs as in the microcirculation [152, 225]; albeit some authors were aware of this problem and proposed a nominal CFL development length denoting the product of the development time and the mean flow velocity [150, 334]. It is only recently that exact analyses of the spatio-temporal heterogeneity of CFL were presented [20, 226, 323], detailing the spatial development/recovery of the CFL alongside microchannels in the presence of upstream disturbances.

In the present problem, having confirmed the spatial decay of lift velocity $V_{\mathrm{l}} \sim \dot{\gamma}/h$ (rather than $V_{\mathrm{l}} \sim \dot{\gamma}/h^2$) against the cell-wall distance h for individual RBCs, estimation can be made for the longitudinal development of δ_{cfl} in the dilute limit using an analytical approach (see Sec.6.4.3 for further details). The derivation shows that considering $a = 1$ in Eq. (6.1) (corresponding to $V_{\mathrm{l}} \sim \dot{\gamma}/h$) yields a power-law scaling for the CFL as expressed in Eq. (6.11): $\delta_{\mathrm{cfl}} \sim \ell^{\beta}$, $\beta = 1/3$, where ℓ is the axial distance along the channel. The exponent of 1/3 here is surprising as it coincides with the power-law scaling for vesicle/RBC motion in simple shear flow with constant shear rate (see Eq. 3 in [41]). Note that because $\delta_{\mathrm{cfl}} \sim \ell^{1/3}$ is derived on the basis of a parabolic velocity profile under the assumption of planar Poiseuille flow (constant shear-rate gradient), whereas the flow patterns in a real microchannel are far more complex (Fig. 6.6), its accuracy for the prediction of spatial CFL development remains to be verified by the numerical and experimental data.

The power-law growth $\delta_{\mathrm{cfl}} \sim \ell^{1/3}$ predicted by the scaling analysis assuming ideal Poiseuille flow

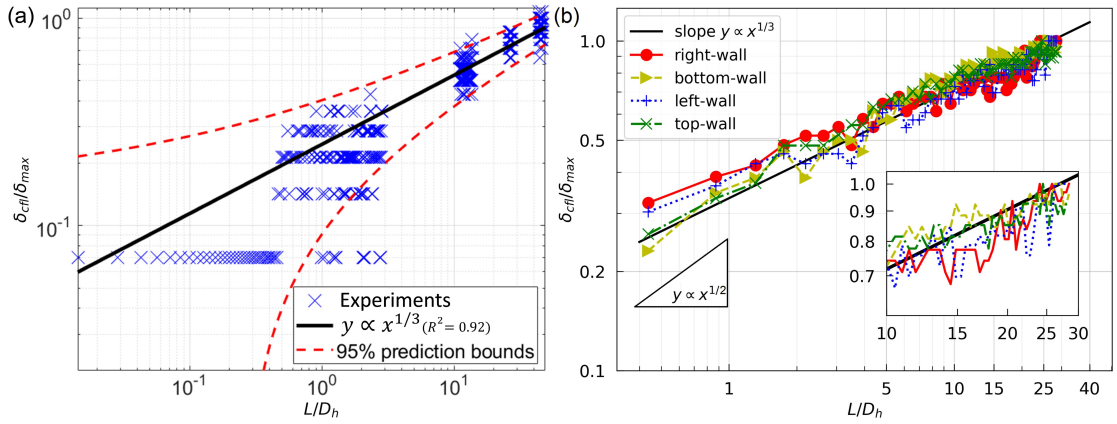

Figure 6.13: *Regression analysis (log-log scale) of the (a) experimental and (b) numerical CFLs as in Fig. 6.8. The CFL values δ_{cfl} are normalised by the maximum CFL thickness δ_{max} detected within the whole investigated range, and the development lengths L are normalised by the channel hydraulic diameter D_h. The inset of (b) shows a zoom-in view of the numerical CFL trends within $L = 10 \sim 28D_h$.*

(Sec.6.4.3) turns out to lie between the experimental and numerical trends, the best-fitted power-law exponents for which are 0.39 and 0.25–0.29, respectively (Fig. 6.8). Through regression analyses of the experimental and numerical data in log-log scales, both data sets are found to compare well with $\delta_{\mathrm{cfl}} \sim \ell^{1/3}$ (Fig. 6.13a–b). Furthermore, for the numerical data, the instantaneous slopes in the log-log graph are found to be nearly independent of ℓ at the early stage of CFL development, presenting a roughly steady increase of 1/3 (Fig. 6.13b). This implies the predominant role of a single mechanism for the transverse motion of cells, which is sensibly the hydrodynamic lift as the scaling analysis suggests. Moving downstream of the channel, a continual increase of the CFL thickness is observed upon approaching $\ell = 28D_{\mathrm{h}}$, but with slower growth indicated by decreasing slopes (noticeably smaller than the original 1/3, see the inset of Fig. 6.13b). This deceleration in CFL growth is expected down to the fact that the lift forces are weakened as the cells migrate further away from the wall and enter the low-shear region with blunted velocity profiles, where the lateral motion of cells will slow down.

In simulations of much denser RBC suspensions (Ht =15%–45%) in cylindrical tubes [150], a similar power-law behaviour was reported for the steep increase of CFL thickness at an initial development stage (before a second time scale induced by relaxation of the RBC core came into play). However, the power-law exponents reflected by the authors under a range of shear rates

were in general smaller than the value of 1/3. The deviation from 1/3 was caused by the cell-cell interactions existing in a dense suspension, which obstructed the initial migration of RBCs and led to slower CFL growth than what could happen in a dilute suspension. Arguably, the authors reasoned for the ideal growth factor of 1/3 by invoking the lift force scaling $F_{\mathrm{l}} \sim V_{\mathrm{l}} \sim 1/h^2$ (where $\dot{\gamma}$ is a constant and does not affect the scaling) derived from simple shear flows [204, 293]. Albeit such reasoning does explain the qualitative trend of their CFL growth, the simple shear flow approximation itself for quadratic flows in a microchannel (where $\dot{\gamma}$ varies) is questionable, which may fail to capture important features of the RBC distribution in the presence of shear rate gradients as recent theories of particle migration at low Reynolds number demonstrate [127, 250].

6.4.3 CFL scaling analysis

6.4.3.1 RBC migration

Consider an RBC whose centre of mass is initially located at a position (x_0, y_0) in close proximity to the wall ($y = 0$) upon entry into a microchannel of hydraulic radius R_{h}. To make the asymptotic analysis tractable, a unidirectional flow is considered along the axial direction of the channel with velocity $u_{\mathrm{x}}(y)$, which is a function of the distance to the channel wall. Driven by the flow, the RBC will gradually migrate towards the channel centreline ($y = R_{\mathrm{h}}$) under hydrodynamic lift while travelling along the streamwise direction (*i.e.,* x-direction), for which the motion can be described by a two-component velocity $v(v_{\mathrm{x}}, v_{\mathrm{y}})$. Note that v is deliberately used here to represent cell velocity while u is reserved for fluid velocity. For leading-order estimation, $v_{\mathrm{x}} := u_{\mathrm{x}}(y)$ is assumed. Based on the empirical law by Losserand *et al.*, an expression for the lift velocity of the RBC v_{y} can be proposed as

$$v_{\mathrm{y}} = \dot{y} = K\dot{\gamma}(y)y^{-a}, \quad \dot{\gamma}(y) = \frac{\partial u_{\mathrm{x}}(y)}{\partial y}, \tag{6.1}$$

where $\dot{\gamma}$ is the shear rate of the unperturbed flow, and K and a are constants depending on flow conditions and cell properties. For a given period of time, *e.g.,* $t \in [0, t']$, the RBC travels to a new position (x', y'), and the axial distance ℓ can be written as

$$\ell = x' - x_0 = \int_0^{t'} v_{\mathrm{x}}\, \mathrm{d}t = \int_{y_0}^{y'} u_{\mathrm{x}}(y)\, \frac{\mathrm{d}t}{\mathrm{d}y}\mathrm{d}y = \int_{y_0}^{y'} \frac{u_{\mathrm{x}}(y)}{\dot{y}}\, \mathrm{d}y. \tag{6.2}$$

Combining Eqs. (6.1) and (6.2), one finds:

$$\ell = \frac{1}{K}\int_{y_0}^{y'} y^a v_{\mathrm{x}}(y)\left(\frac{\partial u_{\mathrm{x}}(y)}{\partial y}\right)^{-1}\,\mathrm{d}y. \tag{6.3}$$

On assuming Poiseuille flow, the form of u_{x} is known and v_{x} may be expressed as

$$v_{\mathrm{x}} = u_{\mathrm{x}}(y) = \hat{u_{\mathrm{x}}}\left(1-\left(\frac{R_h-y}{R_h}\right)^2\right), \quad \hat{u_{\mathrm{x}}} = 2\bar{u}, \tag{6.4}$$

where $\hat{u_{\mathrm{x}}}$ and $\bar{u}$ are the maximum and mean flow velocity, respectively. By replacing v_{x} in Eq. (6.3) with the above, one gets:

$$\ell = \frac{1}{2K}\int_{y_0}^{y'} y^{a+1}\left(2+\frac{y}{R_h-y}\right)\,\mathrm{d}y. \tag{6.5}$$

Given that lateral migration of the RBC away from the wall happens very slowly, $y \ll R_h$ can be assumed over the time scale of the investigation. This means $y/(R_h-y)$ is small, which allows us to arrive at a straightforward expression of the axial distance ℓ that can be integrated over the lateral displacement:

$$\ell \approx \frac{1}{K}\int_{y_0}^{y'} y^{a+1}\,\mathrm{d}y = \left.\frac{y^{a+2}}{(a+2)K}\right|_{y_0}^{y'}. \tag{6.6}$$

After some rearrangement, the equation can be written as

$$y' = \left((a+2)K\ell + y_0^{a+2}\right)^{\frac{1}{a+2}}. \tag{6.7}$$

6.4.3.2 CFL development

Now let us consider an arbitrary RBC cloud in the microchannel flow setting off from the wall. It is actually the outermost cells of the cloud that determine the CFL thickness δ_{cfl}, representing the distance between the RBC membrane and the wall. At high Ca numbers (*e.g.,* $Ca = 0.6$), the RBCs are highly deformable and significantly elongated along the flow, and δ_{cfl} can be approximated by y, namely the distance of the RBC's centre of mass to the wall:

$$\delta_{\mathrm{cfl}}(0) \approx y_0, \quad \delta_{\mathrm{cfl}}(t') \approx y'. \tag{6.8}$$

Combining Eqs. (6.7) and (6.8), an expression describing the growth of δ_{cfl} along the channel axis at sequential positions of ℓ is arrived at:

$$\delta_{\text{cfl}}(t') = \left((a+2)K\ell + \delta_{\text{cfl}}(0)^{a+2}\right)^{\frac{1}{a+2}}. \tag{6.9}$$

Ideally, if the outermost cells are directly in contact with the wall, $\delta_{\text{cfl}}(0) = 0$. This simplification results in a power-law scaling between δ_{cfl} and ℓ, with an exponent of β:

$$\delta_{\text{cfl}} \sim \ell^{\beta}, \quad \beta = \frac{1}{a+2}. \tag{6.10}$$

Specifically, for $a = 1$, corresponding to $V_{\text{l}} \sim \dot{\gamma}/h$, the exponent becomes 1/3 and the below scaling holds:

$$\delta_{\text{cfl}} \sim \ell^{1/3}. \tag{6.11}$$

6.4.4 Implications and limitations

What has been covered not only elucidates the "aberrant" RBC distribution observed in experiments and simulations which contradicts earlier findings, but also has wider implications for experimentalists working on dilute suspensions, especially with high-aspect-ratio microfluidic devices. In brief, microfluidic designs (sometimes local channel features) need to be longer if their purpose is to investigate the microscopic behaviour of a dilute suspension *after* completed lateral migration. Experimentally, it is notoriously difficult to accurately control the inlet distribution of a cell suspension under various *entrance effects*. Therefore, local observations are frequently reported based on the assumption that the suspensions are free of transient effects at the chosen region of interest (ROI) provided that the ROI is adequately far away from the entrance. However, the required length as revealed by this study turns out more demanding than commonly believed [150, 211, 242, 323]. Some key messages are:

(I) For experiments of dilute RBC suspensions in *high-aspect-ratio* channels, the hydrodynamic lift of RBCs are substantially suppressed due to the existence of low-shear-rate and low-shear-gradient zones in the centre. Consequently, the full development of a CFL in these channels may require a much longer length ($L_{\text{c}} > 28D_{\text{h}}$ in simulations and $L_{\text{c}} > 46D_{\text{h}}$ in experiments) than

what is normally expected for cylindrical tubes ($L_c \leq 25D$ according to [150]). Furthermore, the relevance of in vivo measurements of cellular behaviour using such high-aspect-ratio microchannels to the realistic microcirculatory blood flow needs reappraisal. After all, the vessels in the microcirculation are more likely to have circular cross-sections and considerably different velocity profiles, which the radial distribution of RBCs heavily relies on.

(II) When determining the organisation of a dilute suspension (*e.g.,* haematocrit profile) in a typical microchannel of rectangular cross-section, local measurements may be misleading if the channel is short or only moderately long. This is because heterogeneities emerging in the suspension (*e.g.,* density peaks) will persist and hinder the formation of an equilibrium cell distribution due to the lack of RBC dispersion under *weak cell-cell interactions*. In particular, if certain upstream disturbance exists (*e.g.,* geometric constriction or expansion), history effects need to be considered when recording local rheological properties such as the tube haematocrit. Comparing the cases CTRAC-S and CTRAC-L in Table 6.2, with channel geometry, unperturbed flow rate and feeding haematocrit all being the same, yet the tube haematocrits measured at sequential locations constantly differ by more than 6% (relative change). The reason is simply their differently configured flow inlets, causing unequal degrees of disturbance to the initial distribution of cells.

(III) Phenomena violating empirical laws may occur downstream of bifurcations if the upstream RBC suspension is at an intermediate stage of development and has special cell distribution, *e.g.,* the OCTP profile observed in this study. Recently, counterintuitive inversion of haematocrit partition against the classic Zweifach-Fung effect in a bifurcating channel was reported by Shen *et al.*, arising from the formation of consecutive layers of high and low RBC haematocrits in the parent branch [276]. The juxtaposed configuration of RBCs discovered by that study is in line with the five-layered ordering of cells found in the depth direction of the RBC flow here (Fig. 6.5e). Therefore, the phenomenon Shen *et al.* captured might also have been a consequence of insufficient channel length for the suspension to be fully developed in the parent branch.

Some limitations of the present study are:

- While the numerical model simulates human RBCs, horse RBCs are used in experiments due to laboratory restrictions. This may have caused a certain degree of discrepancy between simulation and experimental results, *e.g.,* the absolute values of CFL thickness, par-

tially because horse RBCs are naturally of lower deformability than human RBCs. Ideally, simulations using horse RBCs would provide a more quantitative comparison with the experiments. However, unlike for the extensively explored human RBC, there is currently no validated membrane model for horse RBC, as characterising tests of its shear elastic modulus (an essential parameter governing the deformation and motion of the cell) are lacking given technical difficulties (see [27]). Implementation of a reliable model for horse RBC is well beyond the scope of the present work and may be a topic of future research.

- The effect of inlet configuration on suspension organisation has not been systematically characterised in a quantitative manner, which can potentially provide more specific guidance for experimentalists to improve their microfluidic designs by reducing transient effects. This issue is to be addressed in future studies, involving geometric factors such as constrictions, expansions and bifurcations.

- The experimental data is insufficient for analysis of instantaneous growth rates of the CFL thickness as has been performed for the simulation. More measurements from a denser arrangement of ROIs, though quite challenging, should be made in future experiments in order to enable point-wise local comparison with simulations.

- To make the full-range (channel length > 1 mm) simulation tractable, the parameter space has been largely reduced and a comprehensive investigation of multiple flow scenarios is not conducted (*e.g.,* various volume flow rates with either higher or lower channel aspect ratios) and cell conditions (*e.g.,* pathologically stiffened or sickle-shaped RBCs). A parametric study integrating all these effects will lead to enhanced understanding of the intricate behaviour of dilute suspensions processed in microfluidic devices.

6.5 Concluding remarks

In this work, both microfluidic experiments and numerical simulation of dilute blood suspensions are reported for a low-Reynolds-number channel flow ($Re_{\mathrm{p}} \ll 1$). Surprisingly, an off-centre two-peak (OCTP) ordering of RBCs was found, which is reminiscent of the "tubular pinch effect" typical of the radial distribution of particles in inertial microfluidics [229, 271]. However, the

transverse motion of cells in our case has an entirely different origin: the non-inertial hydrodynamic lift of deformable particles [111].

Back to the two primary questions raised earlier in Sec. 6.3.2: how do the two density peaks in the PDD profile come into being and why do the peaks keep building up instead of being dispersed? The reason behind the persistence of significant density peaks is the deficiency of hydrodynamic interactions among cells in the dilute limit, where shear-induced diffusion remains weak and falls short to smooth out density heterogeneities brought by the lateral migration of cells. Consequently, the evolution of the density profiles is predominantly determined by the decay of hydrodynamic lift within the suspension, which exhibits distinct patterns in the width and depth directions of a high-aspect-ratio microchannel and contributes to a counterintuitive profile of cells in the larger dimension. Additionally, depending on the inflow configuration, the initial distribution of cells upon their entry into the channel varies substantially, which brings extra complexity to the restoration of a converged density profile and the development of an equilibrium cell-free layer.

It is important to note that, the emphasis of the present chapter is to reproduce the experimentally observed phenomena using simulations and to offer physical interpretation of the RBC distribution in dilute suspensions flowing through microfluidic channels. In this context, it has to be mentioned that despite the inevitable difference in deformability between the horse RBCs in experiments and the human RBC model adopted by simulations, the DI-SS (deformation index versus shear stress) curves for both RBCs are qualitatively similar [287]. The sizes of horse RBC and human RBC are also close, being roughly 6μm and 8μm, respectively. As such, the similarity between the two types of cell are sufficient to assess qualitatively the behaviour emerging in dilute RBC suspensions through microfluidic channels, such as the occurrence of off-centre density peaks and the power-law development of CFL.

The comprehensive quantification and analysis of simulation results corroborated by experimental data highlight the local and transient characteristics of RBC suspensions at the dilute limit that are crucial for the interpretation of microfluidic experiments even under low-Reynolds-number conditions. Experimentalists should therefore be cautious when working with dilute suspensions in microfluidics and make judicious assumptions about suspension properties with the presence of upstream disturbance to the flow, especially when the microscopic behaviour of the suspension is the focus of research.

Chapter 7
Behaviours of RBCs in a biomimetic bifurcating network

The microcirculation is a vast network consisting of myriad small vessels up to 100–200 μm in diameter and contains a large number of bifurcations/junctions. It is within this microcirculatory network that crucial exchange of matter occurs for tissues and cells, where the blood transports O_2, CO_2 and important metabolic or signalling substances. Because the partitioning of red blood cells (RBCs) at microvascular bifurcations is often uneven (see earlier introduction in Sec. 2.3.3), either physiological or pathological phenomena can arise in downstream vessels as a consequence, such as plasma skimming, cell screening, haemo-concentration/-dilution, shunt occurrence, and so on. Despite extensive research studying microcirculatory blood flow in recent decades, the behaviour of RBCs as blood flow travels through a vascular network is still not entirely clear.

To investigate RBC dynamics under microcirculatory conditions and elaborate on the associated transport phenomena, the immersed-boundary-lattice-Boltzmann model is employed to simulate cellular blood flow in an artificial vascular network consisting of bifurcating microfluidic channels that are arranged in a biomimetic manner. The present chapter aims to uncover the microscopic behaviour of RBCs at a bifurcation as well as their motion in post-bifurcation vessels, and furthermore, to relate the findings to the development of the cell-free layer, which has important implications for haemodynamics in the microcirculation.

This chapter springs from a collaborative project with my experimental collaborators at the University of Strathclyde (Glasgow, UK). The experimental schematic in Figure 7.1a and experimental data in Figure 7.3 are provided by J. Fidalgo. Except the above, all contents contained in this chapter are my own work. A paper manuscript is in preparation [1].

[1] *Zhou, Q* et al.*, Red blood cell partitioning in a biomimetic bifurcating network, in preparation*

7.1 Overview

The present study aims to study the microscopic behaviour of a dilute RBC suspension encountering consecutive bifurcations, where complicated cell-cell interactions are avoided and the detailed partitioning behaviour of RBCs can be tracked. The computational model is reconstructed from a biomimetic design of artificial vascular network with bifurcating microchannels, for which experiments were conducted to provide comparison data. Three generations of microchannels are involved with two types of bifurcations incorporated: a primary Y-type bifurcation with symmetric geometry and secondary T-type bifurcations with asymmetric geometry. Subject to the ratio of volume flow rates imposed at the outlets of the network, the partitioning of RBCs within the bifurcating network can be tuned to demonstrate specific patterns, which have important implications for the development of useful microfluidic devices handling RBC suspensions.

7.2 Model configuration and parameters

The experimental and numerical methods used in the present study are mostly covered in Sec. 6.2 of Chapter 6 already, except the design of the microfluidic device and the resultant computational domain, which will be described in this section. For general information about the microfluidic experiments (*e.g.,* sample preparation, experimental setup, data acquisition and image analysis) and computational modelling (*e.g.,* flow solver, RBC model, and numerical analysis), please refer to Sec. 4.1 in Chapter 4. The empirical phase-separation model (PSM) first proposed by Pries *et al.* [242] is also briefly reviewed here, as it will be heavily used to evaluate the simulation data.

7.2.1 Microfluidic design

Figure 7.1a shows the bifurcating microfluidic device with volume flow rates controlled at the outlets by 2 syringe pump modules (one for Q_1 and the other for Q_2), each containing two syringes coupled. There are in total 3 generations of microchannels in the device. The 0th generation ($i = 0$) has only one microchannel, which will be hereafter referred to as the parent branch (PB). The PB bifurcates into two child branches (CB) in the 1st generation ($i = 1$), which are denoted CB11 and CB12, respectively. CB11 and CB12 further bifurcate into two child branches each in

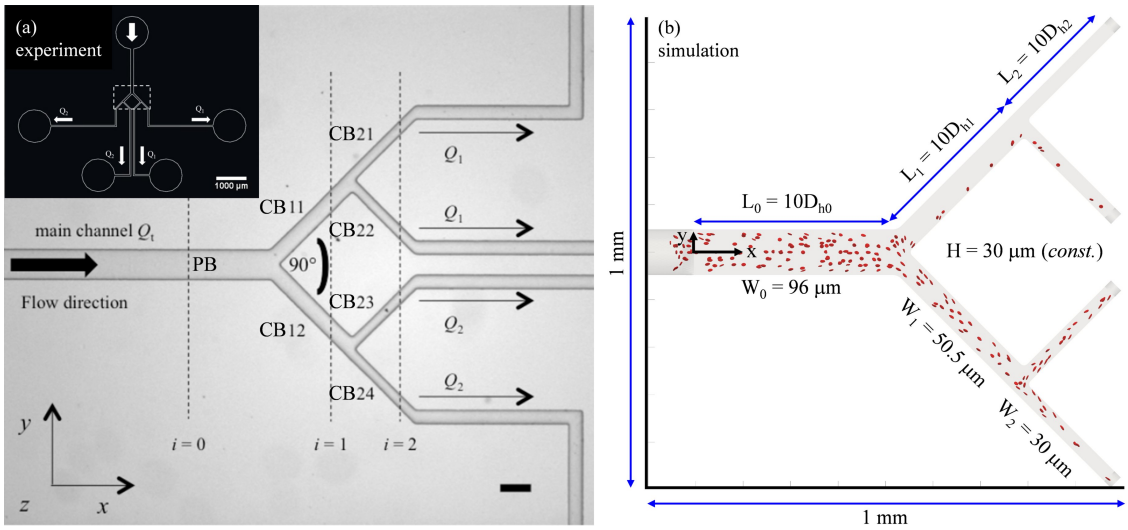

Figure 7.1: *(a) Photomicrograph of the microfluidic device with one inlet and four outlets. Two flow rates Q_1 and Q_2 are imposed in pair at the outlets, and the resulting total volume flow rate in the system is Q_{tot} (at the parent branch); all bifurcation angles are 90 degrees; scale bar 100 μm. The inset (black colour) shows the full design of the device; scale bar 1 mm. (b) A snapshot of the simulation under flow ratio $Q_2/Q_1 = 19$, showing the computational domain and RBCs continuously fed with a fixed volume fraction of 1% at the inlet. Cells arriving at the outlets are automatically removed from the system.*

the 2nd generation ($i = 2$), which are denoted CB21, CB22, CB23 and CB24, respectively. All channels are of constant depth $H = 30\mu$m. The channel width W_i varies following the biomimetic rule proposed by [24, 341] so that Murray's law is observed (*e.g.*, $D^3_{h(0)} = 2D^3_{h(1)}$, where $D_{h(i)}$ is the hydraulic diameter of a given branch). The segment length of a given branch is designed as $L_i = 10D_{h(i)}$. The main difference between the current geometry and that proposed in [24, 341] is the bifurcation angle, which is chosen to be 90 rather than 180 degrees to avoid sharp bends at generation transitions. Another microfluidic device with an angle of 60 degrees at all bifurcations has also been fabricated to test the effect of bifurcation angle.

7.2.2 Numerical simulation

The computational domain is reconstructed using dimensions of the microfluidic device. The flow inlets/outlets are modelled as cylindrical regions with the same geometry as the CTRACT-S configuration ("smaller inflow contraction") of the microchannel simulated in Chapter 6. Such

a design enables an RBC distribution leading to large initial CFLs at the entry region, so much shorter length of the PB ($\approx 10D_{h(0)}$) than its experimental counterpart ($\approx 30D_{h(0)}$) is needed for the CFL to fully develop before reaching the first bifurcation. This treatment is necessary, as an equivalent length of the PB to the experimental design would be prohibitively expensive to simulate. To start the simulation, a plasma flow (without RBCs) is pulled from left to right with a fixed volume flow rate $Q_{tot} = 4\mu$L/min in PB and varying terminal flow ratio $Q1/Q2$. This is realised by imposing a parabolic velocity profile (assuming Poiseuille flow, with no-slip condition on the channel wall) at each outlet. After the steady flow of the plasma is established within the whole network, RBCs are randomly inserted from the cylindrical entry region in a continuous manner with fixed feeding haematocrit (H_{F} = 1%).

7.2.3 Empirical model

To date, several models have been proposed to describe the partitioning of RBCs at microvascular bifurcations. Among others, the most widely-applied one is probably the phase-separation model (PSM as mentioned in the introduction) developed by Pries *et al.* based on *in vivo* experiments and theoretical modelling [241, 242, 244, 245, 247]. In brevity, the PSM derived a set of empirical equations from experimental observation of RBCs at arteriolar bifurcations in rat mesentery, and established a flow-mediated mechanism to quantitatively describe the RBC fluxes received by child branches of diverging bifurcations within a microvascular network.

The PSM correlates the fractional RBC flow FQ_E in a child vessel of a divergent bifurcation with the fractional blood flow FQ_B that it receives:

$$FQ_E = \begin{cases} \frac{1}{1+\mathrm{e}^{-[A+B\ln(\frac{FQ_B-X_0}{1-(FQ_B+X_0)})]}}, & X_0 < FQ_B < 1-X_0 \\ 0, & FQ_B \leq X_0 \\ 1, & FQ_B \geq 1-X_0 \end{cases} \tag{7.1}$$

where A, B and X_0 are fitting parameters obtained *via* linear regression analysis. A reflects the size difference of the two child vessels, B reflects the shape of the haematocrit profile in the parent vessel and X_0 is related to the corresponding thickness of cell-depleted layer (or cell-free layer).

According to the formulation in [244, 245]:

$$A = -13.29[(D_\alpha^2/D_\beta^2 - 1)/(D_\alpha^2/D_\beta^2 + 1)](1 - H_D)/D_F \tag{7.2}$$

$$B = 1 + 6.98(1 - H_D)/D_F \tag{7.3}$$

$$X_0 = 0.964(1 - H_D)/D_F \tag{7.4}$$

wherein D_α, D_β and D_F are diameters (formulated in μm) of the two child branches and the parent branch, respectively. H_D is the discharge haematocrit in the parent branch.

7.3 Results

7.3.1 Deformation of RBCs under varying shear

Table 7.1: *(Simulation) Characteristic capillary number Ca throughout the branching network under different flow conditions ($Q_2/Q_1 = 3, 9, 19, 39$). The Ca here is evaluated at the wall of an equivalent circular channel with the same hydraulic diameter.*

Q_2/Q_1	PB	CB11	CB12	CB21	CB22	CB23	CB24
3	0.6	0.35	1.04	0.37	0.37	1.10	1.10
9	0.6	0.14	1.25	0.15	0.15	1.32	1.32
19	1.0	0.12	2.19	0.12	0.12	2.32	2.32
39	0.6	0.03	1.35	0.04	0.04	1.43	1.43

The bifurcating network creates an environment of varying shear and leads to diverse capillary number Ca (see Table 7.1), which characterises the RBC deformability using the nominal wall shear rate as defined in Eq. (3.5) of Chapter 3.

As an RBC travels the network of microchannels, various shapes are observed with distinct patterns on the cell membrane (Figure 7.2). In response to different levels of fluid shear, the RBC morphology can deviate substantially from the unstressed biconcave shape (Figure 7.2a), and presents either stretched or folded structures (Figure 7.2b–i). Overall speaking, as the magnitude of shear experienced by the RBC increases (reflected by the local Ca number estimated at its centre of mass), highly three-dimensional features such as membrane lobes develop on the surface of the RBC, which are reversible and can be flattened as the membrane relaxes under decreasing shear.

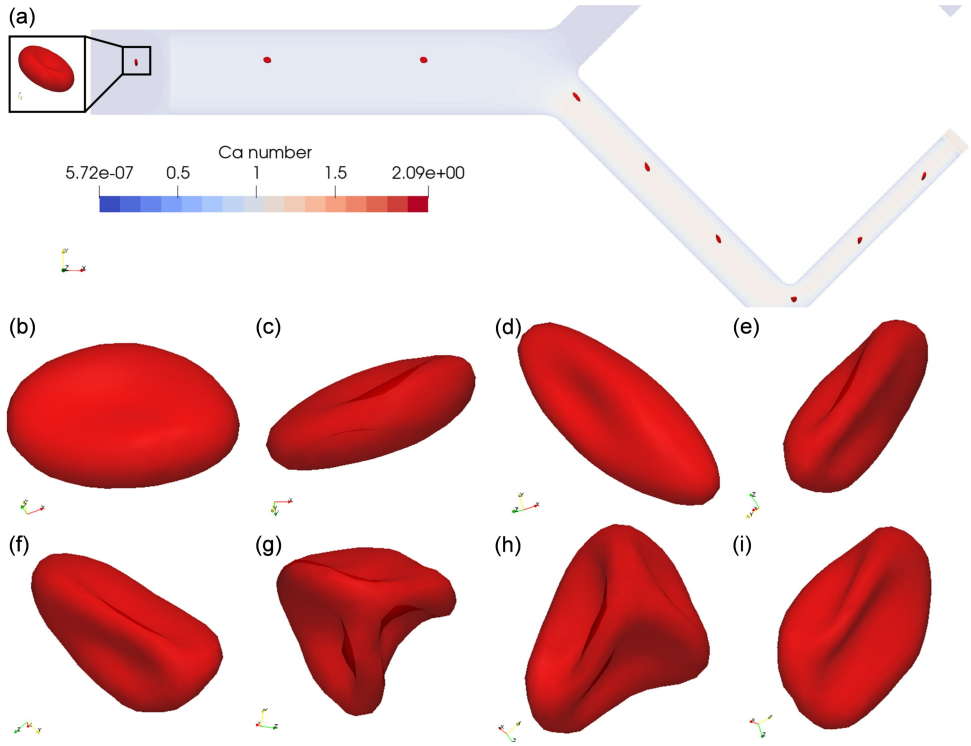

Figure 7.2: *Morphological variation of an RBC responding to varying shear. (a) A snapshot of the simulation (flow ratio $Q_2/Q_1 = 19$, viscosity contrast $\lambda = 1$) with superimposed RBC path (covering PB, CB12 and CB23) from nine time instants. The inset shows an enlarged view of the initial RBC shape, which presents a biconcave discoid. The contour shows the distribution of capillary number Ca in the bifurcating network. (b–i) show the RBC at the other eight locations as in (a). The local Ca numbers estimated at the centre of mass of the RBC are (b) $Ca = 0.01$, (c) $Ca = 0.02$, (d) $Ca = 0.17$, (e) $Ca = 0.17$, (f) $Ca = 0.15$, (g) $Ca = 0.56$, (h) $Ca = 0.15$, (i) $Ca = 0.14$, respectively.*

It is noteworthy that the present simulations successfully reproduce the polylobes experimentally observed for RBCs in microfluidic channels [253], which have not been verified through simulations in a Poiseuille flow setting (instead of assuming unbounded simple shear flow) until now (Figure 7.2g–h).

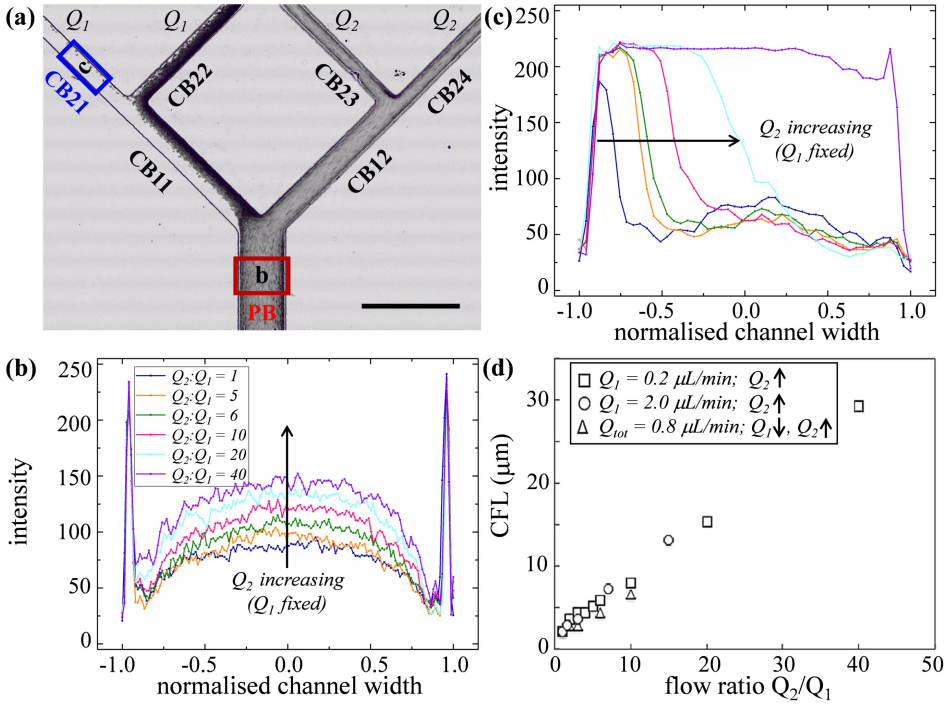

Figure 7.3: *(Experiment) (a) A composed image from the experiment combining 300 video frames using the Z-projection method (minimum intensity). The peak-intensity regions indicate cell-free zones known as CFL. $Q_1 = 0.2\,\mu$L/min and $Q_2 = 8.0\,\mu$L/min; scale bar 200 μm. (b) Intensity profiles (as an indirect measurement of cell distribution) obtained from a region of interest (ROI, marked by red square in (a)) in the parent branch as a function of the flow rate ratio Q_2/Q_1 (with $Q_1 = 0.2\,\mu$L/min fixed). (c) Intensity profiles obtained from a ROI (marked by blue square in (a)) in channel CB21 as a function of the flow rate ratio Q_2/Q_1 (with $Q_1 = 0.2\,\mu$L/min fixed). (d) CFL measured in channel CB21 as a function of the flow rate ratio Q_2/Q_1 under different flow conditions.*

7.3.2 Partitioning of RBCs mediated by terminal flow ratio

7.3.2.1 Experiments

In experiments with RBC suspensions at $H_F = 1\%$, by keeping Q_1 constant ($Q_1 = 0.2\,\mu$L/min) while gradually increasing Q_2 to achieve higher flow ratios ($Q_2/Q_1 = 1-40$), distinct partitioning of cells is observed within the bifurcating network. Figure 7.3 shows a composite image of the RBC distribution in the network for $Q_2/Q_1 = 40$. Strikingly, despite the fact that CB21 and CB22 have the same flow rate (both being Q_1), a marked discrepancy of RBC perfusion exists

between them. Plots of the intensity profiles against flow ratio reveals that the CFLs in the PB remain symmetric regardless of the flow ratio (see the overlapping intensity peaks in Figure 7.3b), whereas in CB21 there exists a sharp asymmetry with virtually no CFL near the inner-wall of the channel (Figure 7.3c). With $Q_2/Q_1 = 20$, the outer-wall CFL in CB21 occupies nearly half of the channel width (see blue curve in Figure 7.3c). Further increasing the flow ratio to $Q_2/Q_1 = 40$ leads to the expanding of the CFL across the whole channel width (see purple curve in Figure 7.3c), corresponding to the complete depletion of cells observed in Figure 7.3a.

Subsequent quantification shows that the trend of CFL expansion against the flow ratio is almost linear (Figure 7.3d). A similar trend for the CFL in CB21 is observed if Q_1 is fixed as $Q_1 = 2.0\,\mu$L/min instead while varying $Q_2/Q_1 =$ 1–40, or having the total volume flow rate in the whole network fixed as $Q_{tot} = 0.8\,\mu$L/min while tuning both Q_1 and Q_2 to designated flow ratios (Figure 7.3d). All experiments mentioned above were also repeated in the second microfluidic device with 60-degree bifurcations, and the same trend was found (results not shown here). This suggests that the bifurcation angle does not play an important role for RBC partitioning within the designed bifurcating network.

7.3.2.2 Simulations

To understand the RBC partitioning behaviour in experiments and provide physical insights, an equivalent system of RBC flow ($H_F = 1\%$) is simulated with fixed Q_{tot} in the parent branch but varying flow ratio Q_2/Q_1 at the outlets. Agreeing with the experimental findings, two CFLs symmetric about the channel axis persist in the PB, both in the widthwise direction and the depthwise direction (the latter of which is not accessible in the experimental setting). The CFL thickness measured close to the Y-bifurcation (at $x = 400\,\mu$m) is nearly independent of the imposed flow ratio, being about 7 μm widthwise and 5 μm depthwise for all flow ratios investigated (Figure 7.4).

By adjusting Q_2/Q_1, a similar trend of the RBC fluxes (represented by cell trajectories over time) is found as in experiments (Figure 7.5). The RBC fluxes in the upper-half child branches of the network (including CB11, CB21 and CB22), where the flow rates are considerably smaller than their counterparts in the lower-half child branches (including CB12, CB24 and CB23), gradually diminish as the flow ratio increases. At $Q_2/Q_1 = 19$, the first exit branch CB21 is completely

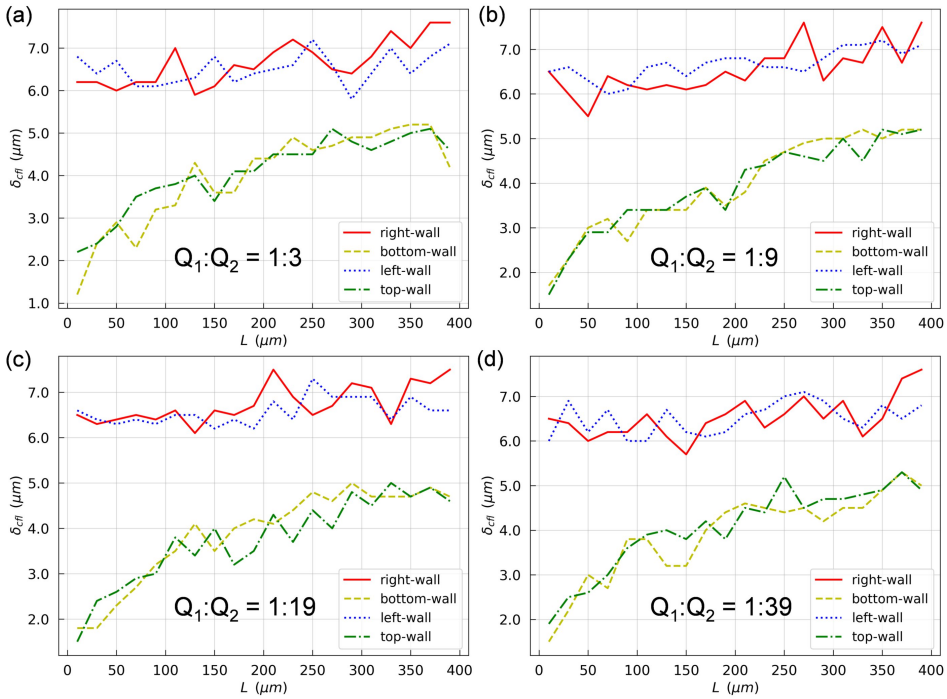

Figure 7.4: *(Simulation) CFLs along the channel axis of PB (at right/bottom/left/top walls) plotted as the CFL thickness δ_{cfl} against the development length L.*

devoid of cells (Figure 7.5c). Further increasing the flow ratio to $Q_2/Q_1 = 39$ leaves both the first and second exit branches (CB21 and CB22) free of cells (Figure 7.5d).

This flow-induced asymmetry of cell partitioning suggests a potential approach for separation of RBCs and the suspending fluid, at least in the dilute/semi-dilute limit without significant cell-cell interactions in the suspension. Whether this method is applicable to denser RBC suspensions or even whole blood (where shear-induced diffusion and RBC dispersion play an important role) remains to be investigated with future experiments and simulations.

Next, the distribution of RBC fluxes is quantified at the primary Y-bifurcation. To this end, the discharge haematocrits (H_D) in the involved three branches (PB, CB11 and CB12) are calculated and evaluated against the established empirical model PSM [242, 244, 247]. Good agreement is found between the simulation data and the empirical predictions, with the relative errors under all tested flow conditions below 2% (Table 7.2). Such quantitative agreement suggests that the RBC partitioning at the Y-bifurcation can be well-predicted by the empirical model. Furthermore, it can

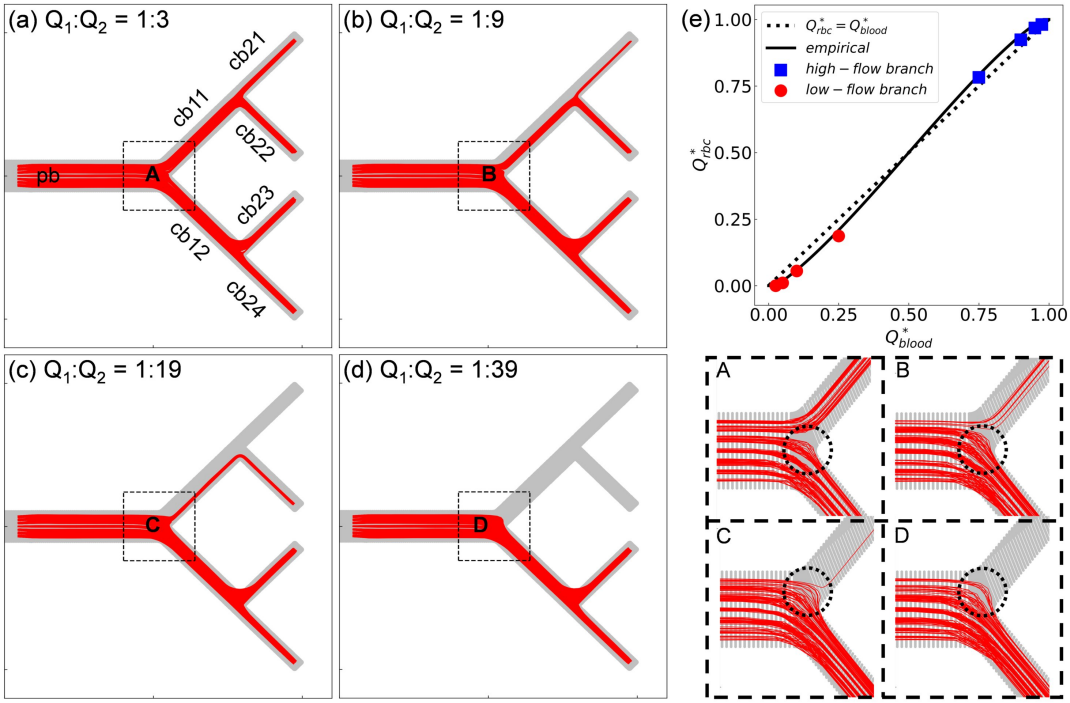

Figure 7.5: *(Simulation) RBC fluxes across the bifurcating network under different flow conditions. (a–d) show the superimposed RBC trajectories under terminal flow ratios $Q_2/Q_1 = 1, 3, 9, 39$, respectively. The accompanied panel labelled with "A"–"D" shows enlarged views of the Y-bifurcation region with reduced number of trajectories (about 150 each). (e) Comparison of the simulated RBC fluxes at "A"–"D" against the empirical model [242, 244]. Q^*_{rbc} and Q^*_{blood} mean the normalised RBC flux and normalised blood flow in a child branch (relative to the parent branch). The circles and squares represent the relatively lower-flow and higher-flow child branches, respectively. The solid line is the empirical prediction, and the dotted line indicates a linear correlation.*

be inferred that with the present channel dimensions ($50 - 100\ \mu m$) where the cells are essentially not confined, the effect of flow on the RBC partitioning dominates over that of channel geometry (non-circular channels in the simulation). In other words, the microfluidic bifurcating network consisting of rectangular channels can reasonably mimic the distribution of RBC flow through microvasculature consisting of circular cross-sections.

One intriguing feature found in the trajectories of RBCs at the geometrically symmetric Y-bifurcation is a protrusion cap into the lower-flow branch (marked with dotted circles in Figure 7.5A–D). This protrusion cap indicates a reversal of RBC fluxes near the bifurcation apex, with cells entering the

Table 7.2: *(Simulation) Relative errors of the simulated RBC fluxes at the primary Y-type bifurcation against predictions made by the empirical model [242, 244].*

Child Branch	A	B	C	D
High-Flow	1.7%	1.4%	1.7%	0.9%
Low-Flow	0.2%	0.7%	0.3%	2.2%

lower-flow branch abruptly pulled away and diverted towards the higher-flow branch instead. The size of this protrusion cap increases as the flow ratio is increased, with complete prevention of RBC fluxes from entering the low-flow branch CB11 achieved at $Q_2/Q_1 = 39$, further leading to the deprivation of cells in the entire upper-half of the network (including CB11, CB21 and CB22).

7.3.3 Reversal of RBC fluxes at the primary Y-bifurcation

To corroborate the occurrence of RBC flux reversal near the primary Y-bifurcation, the embedded flow patterns which underpin the motion of RBCs is investigated. From the flow field in the vicinity of the bifurcation apex (point A in Figure 7.6a), a breakdown of flow symmetry and development of asymmetric streamlines can be clearly observed as Q_2/Q_1 deviates from 1 (Figure 7.6a–c). One notable feature is the existence of a separation point A' (located at L_s away from the apex A), where the stagnation streamline meets the solid wall. All streamlines on the left-hand side of A' will enter the high-flow branch, whereas those on the right end in the low-flow branch. As Q_2/Q_1 increases, A' is found to shift inward the low-flow branch, thus extending the separation distance L_s. Accompanied by the increase of L_s is an enlarged nose tip formed by curved streamlines near the bifurcation region, which matches the protrusion cap observed in the pattern of RBC fluxes (Figure 7.5A-D).

On approaching the bifurcation boundary, the motion of RBCs virtually follows the streamlines and no cross-separation-streamline migration is detected (Figure 7.6d–f). This suggests that the partitioning of RBCs at the Y-bifurcation (where confinement is negligible) would obey the classic Zweifach-Fung effect, which solely arises from the presence of symmetric CFLs in the PB (Figure 7.4). Indeed, the PSM first proposed by Pries *et al.* [242], which is an empirical representation of the Zweifach-Fung effect derived from *in vivo* data, has satisfactorily predicted the simulated distribution of RBC fluxes at the Y-bifurcation (see Figure 7.5e).

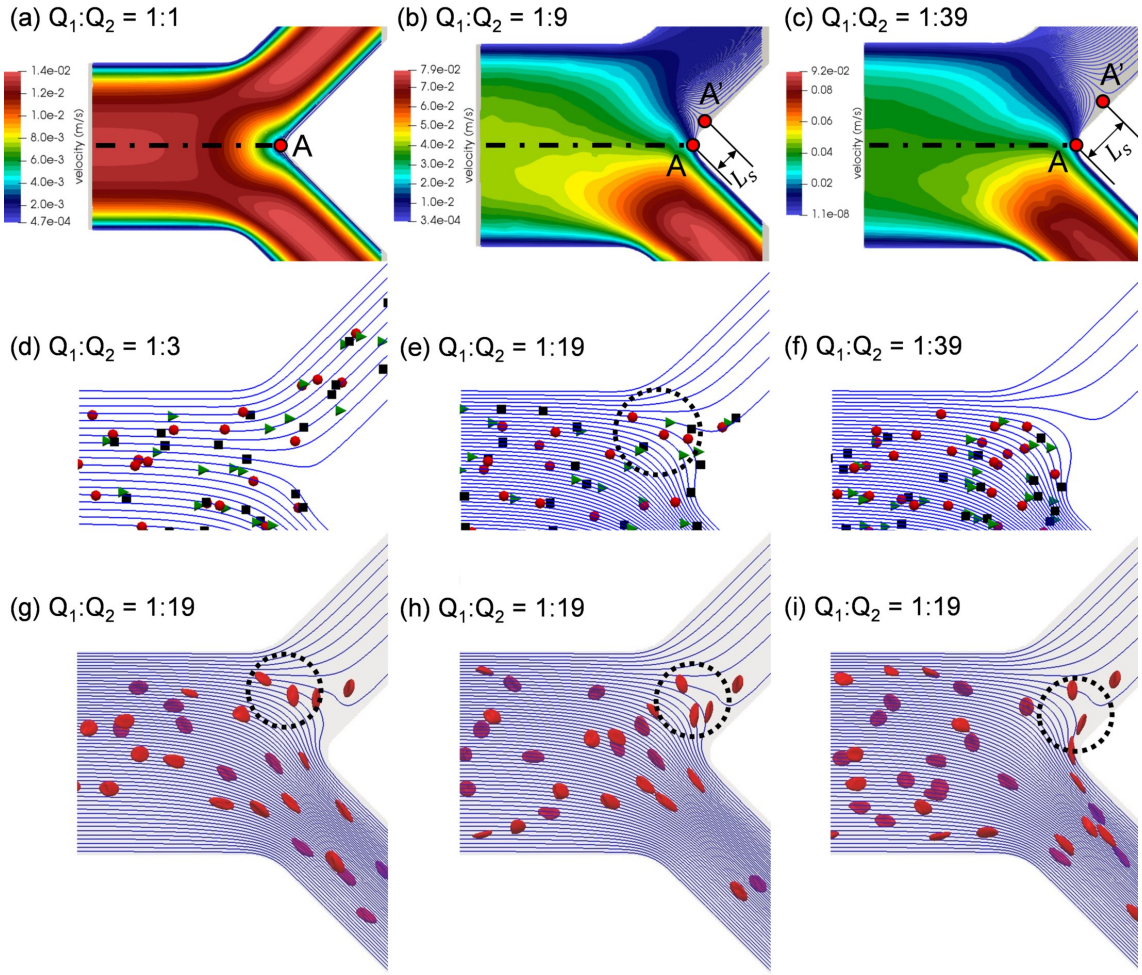

Figure 7.6: *(Simulation) (a–c) Steady flow streamlines (unperturbed) in the Y-bifurcation region of the PB under terminal flow ratios $Q_2/Q_1 = 1, 9, 39$, respectively. The background contour shows magnitude of the velocities. Point A indicates the bifurcation apex; point A' indicates the position where the stagnation streamline (separating streamlines entering the upper and lower branches) meets the solid boundary; L_s is the distance of AA'. (d–f) Temporal RBC motion under $Q_2/Q_1 = 3, 19, 39$, respectively. The red circles, green cones and black squares represent RBCs by centre of mass at sequential time steps with an interval of $\Delta t = 1.48$ ms. (g–i) Time sequence of the RBCs corresponding to (e)* (i.e., $Q_2/Q_1 = 19$) *at t = 114.09 ms, 115.57 ms, 117.05 ms, respectively.*

Under high flow ratios, only a small proportion of streamlines originally close to the PB wall are directed into the low-flow branch CB11, which causes excessive bending of streamlines to satisfy flow continuity (see Figure 7.6g–i for $Q_2/Q_1 = 19$). These streamlines largely originate from the outer-wall CFL region in PB and therefore only carry a few cells with them. As show in Figure 7.6g–i, due to the severely bent streamlines, the single RBC entering lower-flow branch CB11 is laterally transported across the whole channel width and travels along the CB11 inner-wall thereafter. Meanwhile, the protrusion zone is so profound that the other two RBCs already travelling deep into CB11 revert their paths, linger against the bifurcation and eventually proceed towards to the higher-flow branch CB12 (Figure 7.6h–i). As the flow ratio increases to $Q_2/Q_1 = 39$ and the flow rate in the lower-flow branch further drops, all streamlines entering CB11 are exactly from the CFL upstream and carry no cells at all (Figure 7.6f).

7.3.4 Biased phase-separation at secondary T-bifurcations

Different from the primary Y-bifurcation (referred to as PB-BIF hereafter), the partitioning of RBC fluxes at the secondary T-bifurcations (including CB11-BIF and CB12-BIF) disobeys the Zweifach-Fung effect. The violation is particularly apparent at CB11-BIF, where complete depletion of RBCs can occur in one of the downstream child branches although the flow from CB11 is evenly split in to CB21 and CB22 (Figure 7.5c).

Underlying this phenomenon is a severely asymmetric CFL in the feeding branch CB11 (see Figure 7.5C). Recalling the analysis in Sec. 7.3.3, such asymmetry primarily arises from the way how RBCs enter CB11, which behaves sensitively to the flow ratio imposed. At sufficiently high flow ratios, the RBCs entering branch CB11 (if any) will be located much closer to the inner wall, causing a substantial CFL near the outer wall (Figure 7.6g–i). Ideally, one would expect the cells to laterally migrate inward relative to the channel centreline when travelling through CB11 (which is 10 times the hydraulic diameter) under the effect of hydrodynamic lift, therefore gradually recovering the inner-wall CFL and mitigating the CFL asymmetry between opposite walls.

However, one need to be aware that when the flow ratio becomes increasingly high at the outlets, the volume flow rate and the associated shear rate will be progressively lowered in CB11. If the shear rate that RBCs experience becomes exceedingly low, their deformation largely disappears

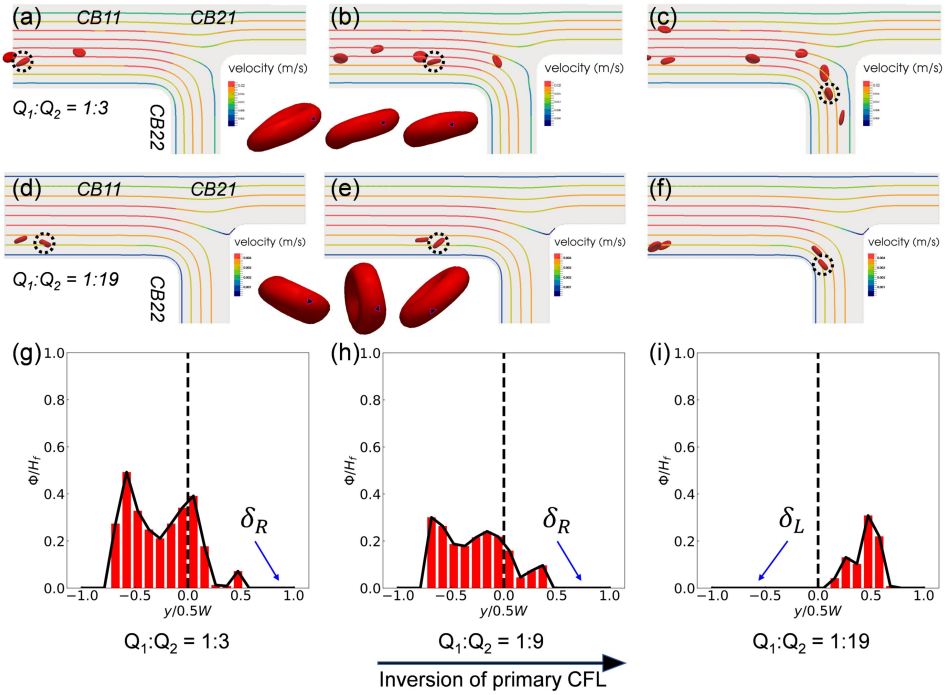

Figure 7.7: *(a–c) RBC motion in CB11 under $Q_2/Q_1 = 3$. The highlighted cell with a dotted circle performs a spinning motion with nearly fixed orientation. (d–f) RBC motion in CB11 under $Q_2/Q_1 = 19$. The highlighted cell with a dotted circle performs a typical tumbling motion similar to rigid-body rotation. The black spot (triangle-shaped) on the highlighted cell in (a–c) and (d–f) marks a fixed mass element on the RBC membrane. (g–i) Histogram of local haematocrits ϕ (normalised by the feeding haematocrit H_F) in channel CB22 under $Q_2/Q_1 = 3$, 9, 19, respectively. The CFL is defined as the region where $\phi/H_F = 0$. The primary CFL labelled as δ_R or δ_L indicates the side with relatively larger CFL measured at opposite walls ("R" and "L" are relative to the flow direction).*

(see the Ca numbers in Table 7.1) and the cells would simply tumble resembling rigid-body rotation rather than tank-tread in fluidised state. Under tumbling mode, the cross-streamline migration of RBCs is greatly suppressed in the rectangular channel.

To examine whether this is the case in the simulation, let us move on to inspect the motion of RBCs under a high flow ratio $Q_2/Q_1 = 19$ in comparison with a mild flow ratio $Q_2/Q_1 = 3$. Before proceeding to the motion regime, a notable difference can already be observed in the initial position of RBCs when they first enter CB11, which predominantly determines the stream layer they are exposed to (Figure 7.7a–f). Under $Q_2/Q_1 = 3$, the cells perform a "Frisbee-like" spinning

motion with nearly fixed orientation (relative to the streamlines), accompanied by a slight increase in cell-wall distance (Figure 7.7a–c). This spinning behaviour has been previously captured in RBC experiments using simple shear flow, and is a transient motion regime towards tank-treading under increasing shear [76]. For $Q_2/Q_1 = 19$, the cells in CB11 are tumbling all the way on their original streamlines and no sign of cross-streamline migration can be observed (Figure 7.7d–f). The above two differences, one about the initial position and one about the motion regime of RBCs in the feeding branch, are both subject to the system flow ratio and co-determine the path selection of RBCs at the T-bifurcation. Notably, an inversion of the primary CFL location in CB22 occurs as the flow ratio is increased from $Q_2/Q_1 = 9$ to $Q_2/Q_1 = 19$ (Figure 7.7h–i). This inversion primarily arises from the difference in the initial position of RBCs upon entering CB11, because the Ca number in CB11 for $Q_2/Q_1 = 9$ to $Q_2/Q_1 = 19$ are designed to be the same ($Ca = 0.1$, see Table 7.1).

7.3.5 Haemo-dilution/concentration in the network

Table 7.3: *(Simulation) Discharge haematocrits H_D measured in the network. The feeding haematocrit at the inlet is fixed as $H_F = 1\%$. For network-level quantification, if any CB has a H_D smaller than the discharge haematocrit in the PB, that branch is defined as haemo-diluted (HD); otherwise, the branch is defined as haemo-concentrated (HC).*

Q_2/Q_1	PB	CB11	CB12	CB21	CB22	CB23	CB24
3	0.972%	0.726%	1.014% (HC)	0.527%	0.831%	1.064% (HC)	0.910%
9	0.971%	0.538%	0.997% (HC)	0.256%	0.658%	1.159% (HC)	0.800%
19	0.966%	0.208%	0.984% (HC)	0	0.267%	1.129% (HC)	0.808
39	0.967%	0	0.973% (HC)	0	0	1.041% (HC)	0.877%

The partitioning behaviour of RBCs at the bifurcations results in highly heterogeneous cell concentration throughout the network. Indeed, distinct density of RBC fluxes can be visually detected from the composite simulation snapshot already (Figure 7.5). To systematically quantify the RBC fluxes within the network and determine the preferential paths for RBCs, the discharge haematocrits H_D are calculated in all branches (Table 7.3). It is important to understand that H_D here is not a conversed quantity at bifurcations (*e.g.,* $H_D^{PB} \neq H_D^{CB11} + H_D^{CB12}$); instead, the RBC flux is (*e.g.,* $Q_{rbc}^{PB} = Q_{rbc}^{CB11} + Q_{rbc}^{CB12}$). One will note that the discharge haematocrit in the PB ($H_D \approx 0.97\%$) is already slightly lower than the feeding haematocrit at the inlet ($H_F = 1\%$).

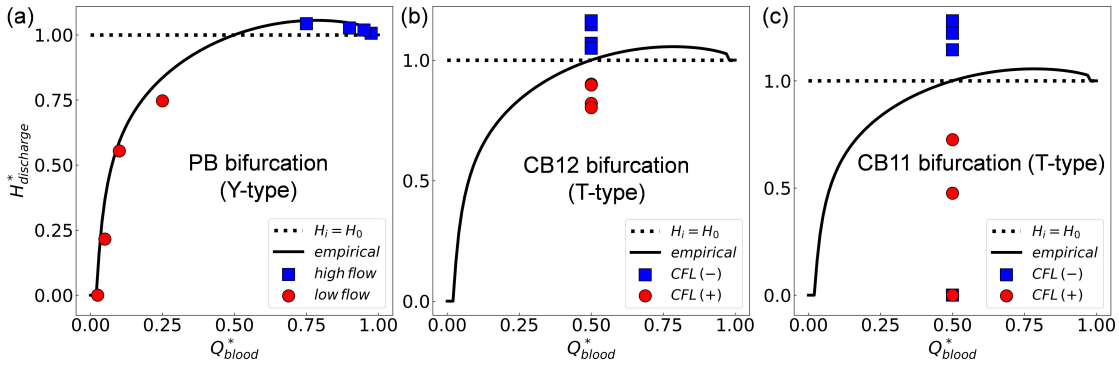

Figure 7.8: *(Simulation) Comparison of the simulated discharge haematocrits against the empirical phase-separation model by Pries* et al. *[242, 244]. (a) PB Y-type bifurcation. (b) CB12 T-type bifurcation. (c) CB11 T-type bifurcation. In (a–c),* $H^*_{discharge}$ *and* Q^*_{blood} *represent the normalised discharge haematocrit and normalised blood flow in a child branch (relative to the parent branch). In (a), the circles and squares represent the relatively lower-flow and higher-flow child branches, respectively. In (b) and (c), the circles and squares represent the CFL-favoured and CFL-unfavoured child branches, respectively. The solid lines in (a–c) describes the empirical predictions.*

This loss of RBC concentration is presumably caused by a cell screening effect at the entrance arising from the geometric transition of the cross-section shape from cylindrical to rectangular. It should be distinguished from the Fåhræus effect which leads to axial migration of cells and causes the dynamic reduction in tube haematocrit (Ht) downstream of a channel while maintaining the absolute cell concentration H_D [9, 283].

When the blood flow encounter the PB-BIF with unequal flow ratios, uneven partitioning of RBCs occurs between CB11 and CB12. As Q_2/Q_1 increases from 3 to 39, the degree of haemodilution in CB11 surges, with H_D dropping down to zero from 0.726%. Interestingly, the haemoconcentration in CB12 is not enhanced but slightly undermined (H_D decreasing from 1.014% to 0.973%). Among the exit branches, CB21 turns out to be the most diluted branch under all investigated flow ratios, whereas CB23 is always most concentrated. The haemo-concentration in CB23 shows a surprising non-monotonic trend against the flow ratio, with a maximum $H_D = 1.159\%$ achieved at $Q_2/Q_1 = 9$.

Further, the H_D of different branches are grouped to evaluate the simulation data separately at the Y-type PB-BIF and T-type CB-BIFs using the empirical model of PSM [242, 244]. Satisfactory agreement is found for the former (Figure 7.8a), whereas poor agreement for the latter

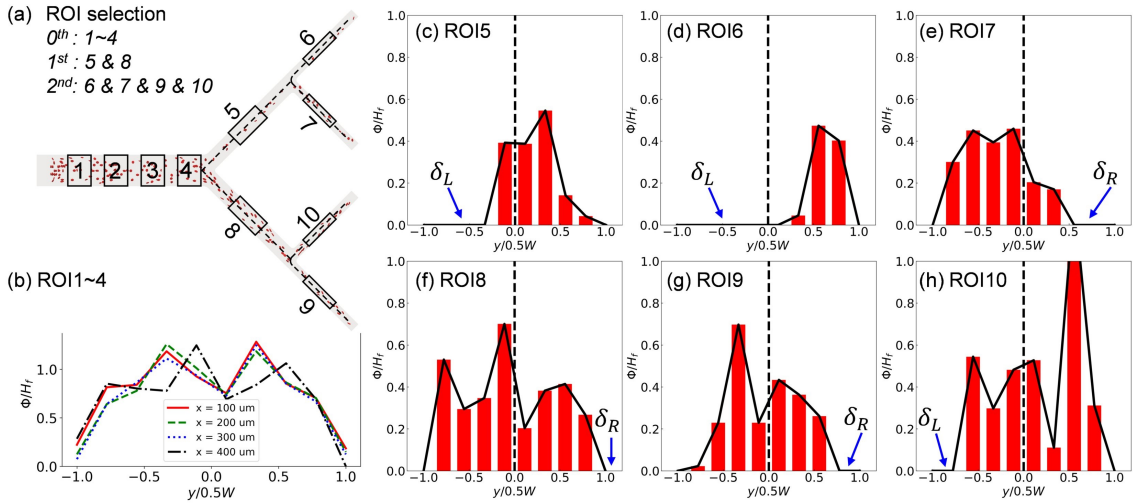

Figure 7.9: *(Simulation) Distribution of RBCs under a moderate flow ratio $Q_2/Q_1 = 9$. (a) ROIs selected from the branches of all generations ($i = 0th, 1st, 2nd$) for haematocrit analysis. (b) Evolution of haematocrit profiles along the PB. (c–e) Histograms of local haematocrits in ROIs located at the upper-half of the network. (f–i) Histograms of local haematocrits in ROIs located at the lower-half of the network.*

(Figure 7.8b–c). However, such results are actually expected as it has been analysed in Sec. 7.3.4 that the partitioning behaviour of RBCs at the Y-bifurcation adheres to the Zweifach-Fung effect, whereas that at the T-bifurcation is substantially biased due to the emerging CFL asymmetry in respective feeding branches. Notably, the haemo-concentration/dilution is much more remarkable downstream of CB11-BIF than CB12-BIF. Such a discrepancy calls for further investigation of the transverse distribution of RBCs in the pertinent branches, particularly the location and thickness of CFLs.

Examination of the haematocrit profiles reveals a rich pattern of transverse RBC distribution (represented by Ht profile) cascading down the bifurcating network (Figure 7.9a). Taking $Q_2/Q_1 = 9$ for example, the haematocrit profile remains symmetric about channel centreline in the PB until approaching the bifurcation region of PB-BIF, where an asymmetry of RBC distribution starts to develop (see $x = 400\,\mu$m in Figure 7.9b).

The asymmetry in the Ht profile is further amplified in CB11 (ROI5), resulting in substantial discrepancy between the CFLs at opposite walls (Figure 7.9c). Due to the low-shear environment in CB11, the CFL asymmetry cannot be removed within the segment length (10 times of CB11

hydraulic diameter), which thus persists till CB11-BIF is meet and causes uneven RBC partitioning under even flow split ($H_D = 0.256\%$ in CB21 versus $H_D = 0.658\%$ in CB22, see Table 7.3). The resultant Ht profile and accompanying CFL in CB21 (ROI6) and CB22 (ROI7) are also highly asymmetric (Figure 7.9d–e). Contrary to CB11, CB12 (ROI8) appears less disturbed after the primary PB-BIF and presents a slight asymmetric Ht profile with the CFL favouring the outer wall (Figure 7.9f). However, the child branches CB24 (ROI9) and CB23 (ROI10) downstream of CB12 still end in much different RBC-concentration (1.159% in CB24 versus 0.800% in CB23, see Table 7.3) and for both the asymmetry in the Ht profile is amplified compared with their parent CB12 (Figure 7.9g–i).

7.4 Discussion

7.4.1 RBC morphology and dynamics

The dynamical RBC morphologies in the present simulation are in line with recent observations of human RBCs under microcirculatory flow conditions where the viscosity contrast $\lambda \geq 5$ between the RBC cytosol and the suspending medium [169, 253]. However, complex RBC shapes such as the polylobed morphology are successfully reproduced in the present simulations ($\lambda = 1$) without setting up a high viscosity contrast, whereas recently attempted RBC simulations in square microchannels adopting $\lambda = 5$ failed to generate the polylobed shape [253]. This is counterintuitive because a high viscosity contrast (other than 1) was asserted crucial for the development of the polylobed structures on the membrane [197].

A potential reason behind this disagreement is the confinement denoting the ratio of RBC effective diameter ($\bar{D}_{rbc} = 6.53\,\mu$m) to the channel hydraulic diameter (*i.e.,* $\chi = \bar{D}_{rbc}/D_h$). It is noted that the confinement considered by the rectangular-channel simulations in [253] was between $\chi = 0.4$–0.75 (matching the confinement conditions in the microfluidic experiments), while in the present simulations χ is much lower and ranges between 0.14–0.22. Indeed, previously simulations which have captured the polylobe formation were for simple shear flow configuration with only one-direction confinement involved (*i.e.,* no side walls as in a real channel flow). The fact that lower-level confinement is required for simulated RBC polylobes to occur than their experimental counterpart reveals potentially important factors that have not been included in existing

simulations (either with $\lambda = 1$ or $\lambda \geq 5$), *e.g.,* the membrane viscosity of the RBC membrane, whose presence increases the membrane shear elasticity and may affect the membrane buckling process that triggers the formation of polylobes.

The variety of RBC dynamics observed from the bifurcating network is rich, even for RBCs at nearly unstressed state presenting a biconcave shape. Apart from the commonly reported tumbling (in low shear) and tank-treading (in moderate/high shear) regimes, the intriguing RBC motion of "Frisbee-like" spinning (a transient state between the rolling motion and tank-treading motion of RBCs under increasing shear, first reported by Dupire *et al.* [76]) is also reproduced here. Therefore, the present computational model incorporated with highly-resolved cell membrane is able to capture the subtle behaviour of RBCs circulating in blood flow at the microscale.

7.4.2 CFL development

The simulated CFLs arising from the cross-streamline migration of RBCs in the bifurcating network qualitatively agree with the experimental results, featuring symmetric CFLs (next to opposite walls) in the parent branch and growingly asymmetric CFLs (especially under high flow ratios) in downstream child branches. However, quantitative matching of CFL thickness between simulations and experiments remains challenging due to the numerical treatment of the flow entry region, where geometric contraction in the width direction is deliberately removed to enable the generation of an artificial CFL immediately after the inlet (see Sec. 7.2.2 for the reason behind this particular treatment).

To validate this numerical treatment, the spatial development of the simulated CFLs in the parent branch of the present study is compared against the scaling law derived earlier in Chapter 6 for a straight channel of identical cross-section (Figure 7.10). The same scaling of CFL growth against development length is found in the depthwise direction (including CFLs at the top/bottom walls) under all investigated flow ratios, showing power-law increase with an exponent of 1/3 (Figure 7.10a–d). Contrarily, the widthwise CFLs (*i.e.,* those at the left/right walls) show negligible increase in thickness, indicated by a small growth rate of nearly zero. The heavily slowed down CFL growth in the parent branch of the present network compared to the previous straight channel can be explained by the magnitude of the initial CFL resulting from the numerical treatment,

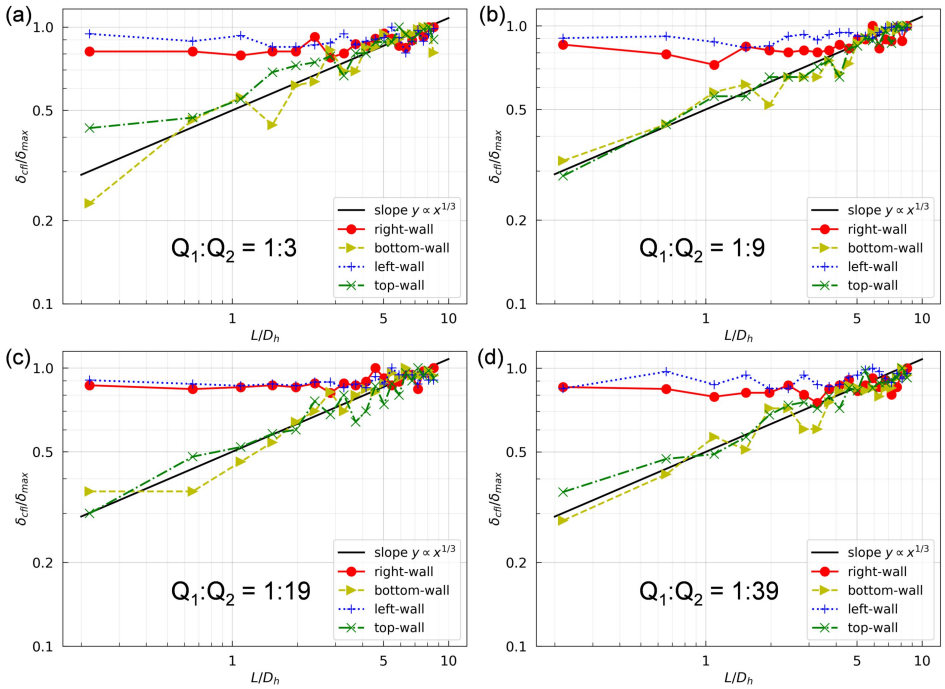

Figure 7.10: *(Simulation) Regression analysis of the simulated CFLs as in Figure 7.4, plotted in log-log scale. The CFL thickness δ_{cfl} is normalised by the maximum CFL value δ_{max} detected within the investigated range ($L \approx 10D_h$). The development length L is normalised by the channel hydraulic diameter D_h.*

i.e., 6-7 μm (see Figure 7.4), which is large enough to substantially alter the scaling law of CFL development according to Equation (6.9) of Chapter 6.

7.4.3 Implications and limitations

The present computational model with highly-resolved RBCs flowing in an artificial vascular network satisfactorily reproduces the phenomenon of biased RBC partitioning observed in the supplementary microfluidic experiments. The simulations elucidate the microscopic behaviour of RBCs at arteriole-level bifurcations (channel hydraulic diameter $D_h = 30$–100 μm) subject to different flow ratio at terminal branches of the network. Furthermore, the findings here suggest the prominent effect of CFL asymmetry on the phase separation process. Such CFL asymmetry arises from upstream disturbances, which can be important even lying more than 10 hydraulic diameters away. Some important implications are:

(I) Artificial vascular network consisting of rectangular microchannels can capture the phase-separation process of RBC suspensions with quantitative accuracy when compared with the established empirical model [242] based on *in vivo* data from microvascular bifurcations (see Figure 7.5), provided that equivalent dimensional description is used (*e.g.,* channel hydraulic diameter versus vessel diameter).

(II) In low Reynolds number flows ($Re \ll 1$) with low-level confinement (small D_{rbc}/D_h), the motion of RBCs in the vicinity of a bifurcation (see Figure 7.6d–f) follow the fluid streamlines and no RBC migration crossing the stagnation streamline occurs. Therefore, neither the obstruction effect proposed by [24] nor the low-flow attraction effect proposed by [74] exists and the partitioning of RBCs obeys the classic Zweifach-Fung effect.

(III) Under high flow ratios, RBCs near the stagnation streamline (separation surface or separatrix in 3D, which divides the fluid layers entering different branches) tend to be drawn towards the lower-flow branch first and linger for a while. They are then pulled away and eventually flow into the higher-flow branch (see Figure 7.6g–i). This observation is in line with the finding of a previous 2D study, where similar behaviour was found for an elastic capsule [310].

(IV) Significant asymmetry in the both CFL and haematocrit profile exists in a vascular network as suggested by [19, 20], owing to the disturbance of upstream bifurcations to the transverse distribution of RBCs (see Figure 7.9). As a consequence, the partitioning of RBCs at successive bifurcations can be substantially biased and would give rise to excessive haemo-dilution in downstream child branches, even under equal flow split (see Figure 7.8).

(V) Last but not least, the lateral migration of RBCs in branches of low flow will be largely suppressed due to the motion regime they undertake under low shear, leading to negligible recovery of CFL symmetry throughout the network.

There are several limitations for the present study: (1) While horse RBCs were used in experiments, the numerical model simulates human RBCs. This may have caused a certain degree of discrepancy between the simulation and experiments. However, the influence on results of the suspension behaviour should be limited to quantitative instead of qualitative differences, according to the previous discussion in Chapter 6. (2) For the sake of tractable computational cost, the simulated RBCs are initialised in a manner that generates considerable initial CFLs at the entry region

of the parent branch. This numerical treatment not only causes difficulty in direct comparison of CFL thickness between simulations and experiments, but also lead to a different critical flow ratio under which complete RBC depletion in certain child branch occurs. For example, CB21 is only nearly depleted under $Q_2/Q_1 = 40$ in experiment, but it is already completely depleted under $Q_2/Q_1 = 19$ in simulation. For quantitative agreement to be achieved, the initialisation strategy needs to be improved in the future, albeit at the price of higher computational cost. (3) So far, only dilute RBC suspensions ($H_F = 1\%$) are considered for a mechanistic understanding of RBC partitioning behaviour in bifurcating microchannels. The performance of the biomimetic microfluidic network in terms of separating RBCs and plasma is subject to scrutiny if the system haematocrit is to be increased to a level when cell-cell interactions become important. This effect remains to be investigated before extension of current findings to biomedical applications, *e.g.,* handling denser RBC suspensions for separation, sorting or purification purposes.

7.5 Concluding remarks

The present chapter studies the partitioning of RBCs in an artificial vascular network designed following biomimetic rules for channel dimensions. The microscopic behaviour of RBCs flowing within are reported in detail, including their morphological variation, motion regime, spatial organisation, interaction with bifurcation and flow-mediated partitioning. Ideal partitioning is found at the primary Y-bifurcation quantitatively agreeing with an established empirical model, but biased partitioning that leads to significant haemo-concentration/dilution in downstream child branches. The latter is attributed to the breakdown of CFL symmetry due to upstream disturbances on RBC distribution and negligible hydrodynamic lift of RBCs that tumble like rigid bodies in low-shear environments.

The qualitative and quantitative agreement demonstrated between simulations and experiments in an arteriole-level artificial vascular network is important to validate the 3D computational model for studying the complex dynamics of cellular blood flow in more realistic microvascular networks. The findings on the partitioning pattern of RBCs within the specially designed bifurcating network may also find applications in manipulating blood samples using microfluidic devices, such as enrichment or sorting of cells.

Chapter 8
Effect of RBC dynamics on vascular patterning during development

Thanks to the rapid development of modern computing facilities, unprecedented large-scale numerical simulations of microcirculatory blood flow in complex vascular networks have become possible and some promising studies emerged in recent years. Combined with advanced *in vivo* imaging and model construction techniques, image-based simulations of the haemodynamics in realistic microvasculature can greatly contribute to a mechanistic understanding of elusive biophysical processes that are otherwise impossible or too expensive to uncover merely relying on state-of-the-art experiments. Among others, the relationship between haemodynamics and cardiovascular development at early stages of life has attracted enormous attention over the past decade.

Vascular remodelling is an essential process for the development of functional networks, achieved through tremendous rearrangements of endothelial cells within the primitive vascular plexus (see earlier introduction in Sec. 2.3.4). Prior work in the literature has uncovered how endothelial cells polarize and migrate responding to flow-induced wall shear stress (WSS), resulting in abundant vessel pruning. However, the shear stresses were evaluated by simplified mathematical models assuming homogeneous blood flow, whereas increasing evidence shows that the discrete presence of red blood cells (RBCs) has a substantial impact on microvascular haemodynamics.

In this chapter, the cellular blood flow in developmental mouse retina is modelled as a suspension of deformable RBCs. The computational results demonstrate highly heterogeneous distribution of RBCs within the primitive vascular network. Furthermore, a remarkable association between vessel regression and RBC depletion is uncovered, the latter of which can be well predicted by a plasma skimming model. Mechanistically, a potential mechanism is proposed for enhancing local WSS differences known to modulate vascular patterning.

This chapter springs from a project in collaboration with my experimental collaborators at Max-Delbrück-Center for Molecular Medicine in the Helmholtz Association (Berlin, Germany). The imaging data in Figure 8.5a (mouse retina plexus) and Figure 8.7a,b,g,h (zebrafish caudal vein plexus) are are provided by T. Perovic and I. Fechner, respectively. Except the above, all contents contained in this chapter are my own work. A preprint [340] has been submitted to bioRxiv [1].

[1] *Zhou, Q* et al., *Association between erythrocyte dynamics and vessel remodelling in developmental vascular networks, bioRxiv:10.1101/2020.05.21.106914*

8.1 Overview

In the current study, the particulate nature of blood is proposed to play a key role in establishing local WSS differences driving vascular remodelling. The problem is approached computationally using developmental mouse retina, a common animal model for the study of vascular patterning. By simulating cellular blood flow in reconstructed vascular networks from images of developing mouse retina, various aspects of the microcirculatory blood flow such as bulk flow rate, RBC dynamics, velocity profile and haematocrit partitioning are systematically studied. Remarkably, a strong association between RBC depletion and vessel regression in the primitive vasculature of mouse retina is uncovered through the simulation and confirmed by subsequent live imaging in a developmental zebrafish model. Furthermore, plasma skimming [88, 160, 247] as described by an established empirical model [242, 244] is identified as the driving mechanism.

It is hypothesised that that plasma skimming enhances local WSS differences within the network, which are known to modulate developmental vascular remodelling [93]. Attributed to the effect of plasma skimming, the distribution of RBCs within the developing retina is highly heterogeneous. Such heterogeneity leads to abundant RBC-rich and RBC-poor (or plasma-only) channels, presumably resulting in augmentation of viscosity contrast and therefore enhancement of local WSS differences between neighbouring branches. Furthermore, it is speculated that vessel pruning driven by the design principle of removing plasma-only channels from the developmental (rather than mature and stabilised) vasculature will lead to a functional network layout that avoids portions of the tissue being vascularised but poorly oxygenated. This constitutes a possible mechanism for optimal design of vascular networks at the development stage, which is highly dynamical and emerging in nature.

This chapter is organised as follows: Sec. 8.2 introduces the experimental and numerical methods. Sec. 8.3.1 presents results of flow rate and cell flux from the simulations in comparison with experimental measurements to validate the present computational model. Secs. 8.3.2–8.3.5 reveal the association between vessel regression and RBC depletion in the developing vascular network, for the latter of which plasma skimming is proposed as the mechanism. Sec. 8.4 discusses the biophysical implications of the present results and potential impact on existing studies of blood flow in microcirculatory networks. Sec. 8.5 concludes the chapter.

Table 8.1: *Key parameters of the whole-plexus simulation using the non-Newtonian Carreau-Yasuda (NNCY) rheology model [30, 34].*

Parameter	Description	Value	Unit	Comment or reference
D_{vessel}	vessel diameter	variable	μm	locally mapped by *PolNet*
Δx	lattice size	0.5	μm	estimated by *PolNet*
Δp	ocular perfusion pressure	55	mmHg	[30]
$\bar{u}$	flow mean velocity	variable	m/s	average over cross-section
Q	volume flow rate	variable	m^3	$Q = \bar{u}\pi D_{vessel}^2/4$
$\dot{\gamma}$	shear rate	variable	1/s	solved by *HemeLB*
$\eta(\dot{\gamma})$	shear-thinning viscosity	variable	mPa s	$\eta(\dot{\gamma}) = \eta_\infty + \frac{(\eta_0-\eta_\infty)}{[1+(\lambda\dot{\gamma})^a]^{(1-n)a}}$
η_0	constant	14.49	mPa s	low-shear viscosity
η_∞	constant	3.265	mPa s	high-shear viscosity
λ	constant	0.1839	s	fitting parameter
n	constant	0.4136	-	fitting parameter
a	constant	2.707	-	fitting parameter

8.2 Model configuration and parameters

8.2.1 Animal model

The vascular plexus for simulation was obtained from postnatal day 5 wild-type mouse retinas, and subsequently stained for Collagen IV matrix sleeves and ICAM2 luminal surface (see experimental details in Sec. 4.3.1). Images of the vascular plexus were then acquired with confocal microscopy. While the ICAM2 mask depicts the remodelled vascular network, the Col.IV mask approximately reflects the network morphology before vascular remodelling if assuming that changes in lumen size immediately after the remodelling process are small. Therefore, by comparing Col.IV and ICAM2, the remodelling events can be tracked.

8.2.2 Numerical simulation

8.2.2.1 Simulation setup

The simulation procedures for the present study have been introduced earlier in Sec. 4.1.2 of Chapter 4. A brief recall is provided here as follows. First, a three-dimensional (3D) full-network geometry of the vessel luminal surface is reconstructed from the binary image of Col.IV mask

Table 8.2: *Boundary conditions for RBC simulations in designated subsets of the retinal network, namely ROI-1, ROI-2 and ROI-3. $\hat{u}$ represents the centreline velocity at the selected cross-section (circular) of a given vessel that serves as the inlet/outlet of the ROI and p is a reference pressure. $\hat{u}$ is set as positive for inlets and negative for outlets.*

ROI	Inlet/Outlet	Boundary type	Value	Unit	D_{vessel} (μm)
1	$\hat{u}_{in1}$	velocity	11.710	mm/s	7.99
	$\hat{u}_{in2}$	velocity	3.756	mm/s	15.68
	$\hat{u}_{out1}$	velocity	-0.774	mm/s	5.39
	$\hat{u}_{out2}$	velocity	-6.164	mm/s	10.58
	$\hat{u}_{out3}$	velocity	-5.209	mm/s	7.13
	$\hat{u}_{out4}$	velocity	-4.829	mm/s	10.41
	p_{out5}	pressure	0	mmHg	14.45
2	$\hat{u}_{in1}$	velocity	4.222	mm/s	19.04
	$\hat{u}_{in2}$	velocity	1.201	mm/s	5.51
	$\hat{u}_{in3}$	velocity	6.367	mm/s	7.80
	$\hat{u}_{out1}$	velocity	-11.658	mm/s	10.33
	$\hat{u}_{out2}$	velocity	-7.182	mm/s	8.62
	$\hat{u}_{out3}$	velocity	-0.514	mm/s	7.33
	$\hat{u}_{out4}$	velocity	-0.113	mm/s	6.83
	p_{out5}	pressure	0	mmHg	8.89
3	$\hat{u}_{in1}$	velocity	1.171	mm/s	7.14
	$\hat{u}_{in2}$	velocity	10.277	mm/s	13.47
	$\hat{u}_{in3}$	velocity	0.049	mm/s	6.89
	$\hat{u}_{in4}$	velocity	0.002	mm/s	2.38
	$\hat{u}_{out1}$	velocity	-14.913	mm/s	8.83
	$\hat{u}_{out2}$	velocity	-30.298	mm/s	4.66
	p_{out3}	pressure	0	mmHg	2.21

of mouse retinal vasculature using the computational tool *PolNet* developed by Bernabeu *et al.* [29] (Figure 4.4a-b). Then, a flow simulation with simplified blood rheology is run for the full-network geometry (see Table 8.1 for key parameters of the whole-plexus simulation.), applying the non-Newtonian Carreau-Yasuda (NNCY) model as in [30]. From this simulation, the velocity field within the vascular plexus (Figure 4.4c) can be obtained under physiological ocular perfusion pressure (OPP, 55 mmHg) to provide information for subsequent simulations of cellular blood flow in designated regions of interest (ROIs, *e.g.,* ROI-1 as in Figure 4.4d). For each ROI subset clipped from the full-network geometry (Figure 4.4e), the boundary conditions (*e.g.,* inflow/outflow and pressure, see Table 8.2) are extracted from the NNCY simulation to initiate a plasma flow simu-

Table 8.3: *Key parameters of the RBC model. The symbol "$\sim$" represents dimensionless simulation units. Please refer to [161] for more details of the RBC model.*

Parameter	Description	Value	Unit	Comment or reference
r_{rbc}	RBC radius	4	μm	[181]
A_{rbc}	RBC surface	140	μm^2	[181]
V_{rbc}	RBC volume	100	μm^3	[181]
η_{plasma}	plasma viscosity	1	mPa s	modelled as liquid water
$\eta_{cytosol}$	artificial cytosol viscosity	1	mPa s	$\eta_{cytosol} = \eta_{plasma}$
$\Gamma_{nominal}$	Föppl-von Kármán number	400	-	$\Gamma_{nominal} = \frac{\kappa_s r_{rbc}^2}{\kappa_b}$
N_f	number of facets	1280	-	$N_f = 20(\frac{r_{rbc}}{\Delta x})^2$
κ_s	strain modulus	50	μN/m	resisting in-plane shearing
κ_b	bending modulus	2×10^{-18}	Nm	resisting off-plane bending
$\tilde{\kappa}_\alpha$	dilation modulus	0.5	-	conserving local area
$\tilde{\kappa}_A$	surface modulus	1	-	conserving RBC surface
$\tilde{\kappa}_V$	volume modulus	1	-	conserving RBC volume

lation, followed by continuous perfusion of RBCs at a fixed haematocrit of 20% from all inlets of the extracted ROI (Figure 4.4f).

8.2.2.2 RBC membrane model

The morphological deformation of an RBC in small vessels or channels are known to be dominated by the strain modulus κ_s and the bending modulus κ_b, both of which have been extensively measured for healthy human RBCs using diverse experimental techniques. The reported values from different experiments somehow converge and present $\kappa_s = 5.5 \pm 3.3\,\mu$N/m and $\kappa_b = 1.15 \pm 0.9 \times 10^{-19}$ Nm, respectively (see reviews [181] and [299]). However, because these measurements all rely on certain deformation protocols that do not necessarily reflect the complex microcirculatory conditions, the obtained values may not apply to RBCs travelling in capillary networks of the mouse retina. Indeed, it is found that the κ_s and κ_b required to maintain the integrity of the RBC membrane in the cellular simulations are roughly one order larger in magnitude than the reported values (see the simulation values in Table 8.3). This substantial increase in required κ_s and κ_b for reasonable RBC morphology may also arise from the intrinsic difference in the haemodynamic environment (*e.g.,* magnitude ranges of the shear rate and wall shear stress) of the microcirculation system between mice and humans.

8.2.3 Data analysis

8.2.3.1 Vessel selection and quantification of RBC flow

To investigate the perfusion of RBCs within the vascular network, all divergent bifurcations (consisting of one parent branch and two downstream child branches) are identified for the cellular flow in designated ROIs. Only vessel branches from these bifurcations are selected for statistical analysis to ensure independent representation of systematic RBC partitioning in the network. In total, 3 ROIs, 22 bifurcations and 66 vessel segments are included (Figure 8.1).

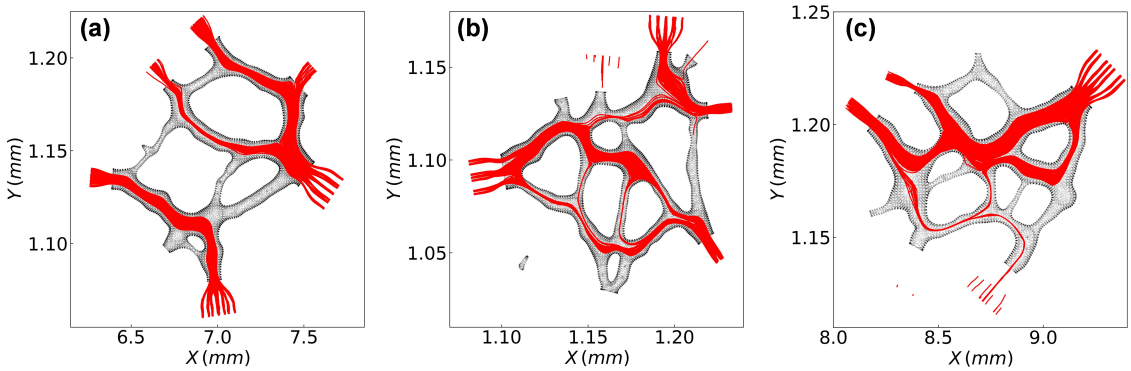

Figure 8.1: *Combined cell trajectories over time in (a) ROI-1, (b) ROI-2 and (c) ROI-3 throughout simulations lasting for 0.33 s each.*

For the quantification of RBC perfusion in any given child branch of the selected bifurcations of interest (BOIs, diverging bifurcations only), two variables are introduced following [242] and [19]: one is Q^*_{blood}, denoting the proportion of blood flow that it receives from its parent branch ($0 \leq Q^*_{blood} \leq 1$); the other is Q^*_{rbc}, denoting the proportion of RBC flux likewise ($0 \leq Q^*_{rbc} \leq 1$). If $Q^*_{rbc} > Q^*_{blood}$, the child branch is receiving more RBCs than linear allocation, and it is defined as a “RBC-enriched" vessel; if $Q^*_{rbc} < Q^*_{blood}$, the child branch is receiving fewer RBCs than linearly allocated, and it is defined as an “RBC-depleted" vessel.

8.2.3.2 Empirical model: the PSM

Several models have been established to describe the phenomenon of plasma skimming [113, 120, 171, 242]. Among others, the most widely applied one is probably the empirical Phase-Separation Model (hereafter referred to as PSM) developed by Pries *et al.* and co-workers based on *in vivo*

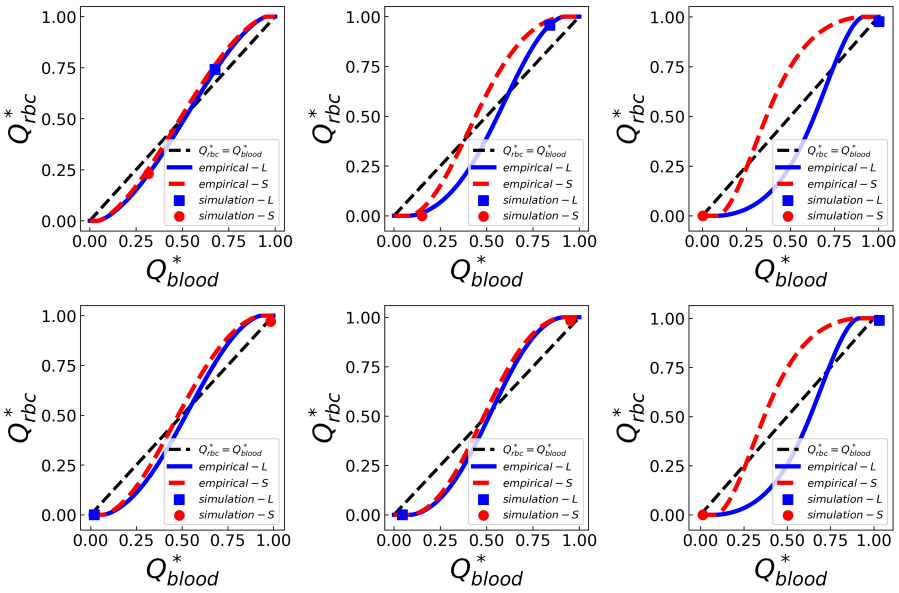

Figure 8.2: *Comparison of simulation data with PSM empirical predictions in the form of fractional RBC flux Q^*_{rbc} against fractional blood flow Q^*_{blood} for all investigated bifurcations in ROI-1 (Figure 8.1a). The simulation data are represented by squares and circles while the PSM predictions are by solid lines. In each bifurcation, the relatively larger child branch is termed "L" (blue squares) and relatively smaller child branch termed "S" (red circles). The black dished line represents a linear hypothesis for Q^*_{rbc} and Q^*_{blood} in the absence of plasma skimming.*

experiments and theoretical modelling [241, 242, 244, 245, 247]. The adopted formulation from PSM has been given in Sec. 7.2.3 of Chapter 7 when studying the RBC partition in a bifurcating microfluidic network, and is therefore not repeated here. Here is a brief recall of key parameters in the PSM: A reflects the size difference of the two child vessels, B reflects the shape of the haematocrit profile in the parent vessel and X_0 is related to the corresponding thickness of cell-depleted layer (or cell-free layer). D_α, D_β and D_F are diameters of the two child branches and the parent branch, respectively. H_D is the discharge haematocrit in the parent branch.

In the present study, With D_α, D_β and D_F measured from the ROI subsets and H_D extracted from the simulation data, A, B, X_0 can be calculated individually for each bifurcation and the empirical curves are plotted in the form of FQ_E versus FQ_B. Equivalently, the simulation data in the form of Q^*_{rbc} versus Q^*_{blood} are plotted for comparison with the empirical predictions. The results for bifurcations in ROI-1, ROI-2 and ROI-3 are listed below in Figures 8.2, 8.3, 8.4.

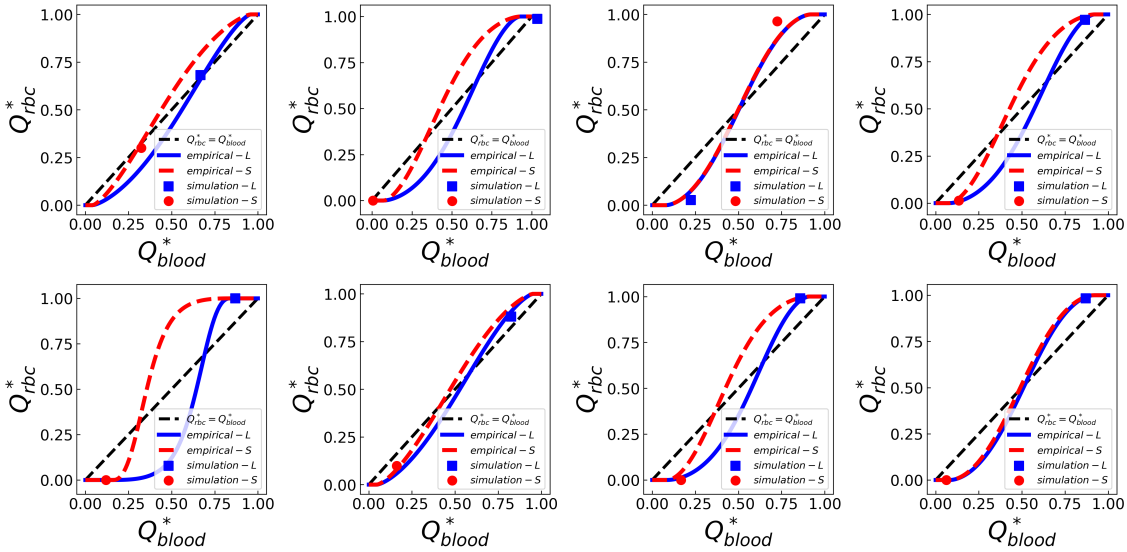

Figure 8.3: *Same caption as Figure 8.2, except for ROI-2 corresponding to Figure 8.1b.*

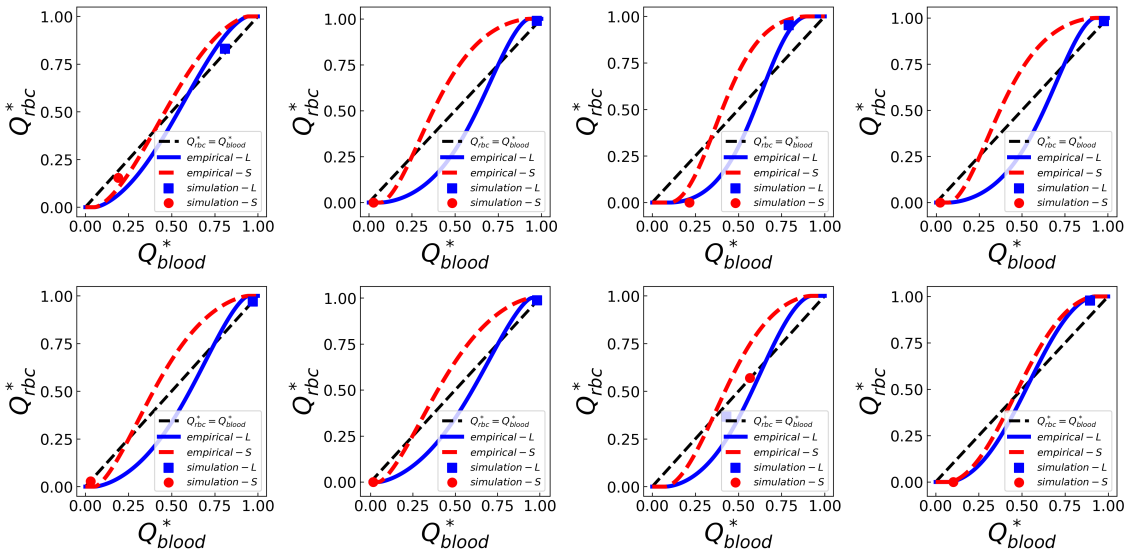

Figure 8.4: *Same caption as Figure 8.2, repeated for ROI-3 corresponding to Figure 8.1c.*

8.3 Results

8.3.1 Validation of simulated blood flow against existing experiments

The superposed image of Col.IV and ICAM2 masks obtained from a postnatal day 5 mouse retina (following the protocol in Sec. 4.3.1) demonstrates a highly primitive vascular plexus (Figure 8.5a), presenting lognormal-like distribution of vessel diameters with a maximum value of 45 μm and a mean of of 11.85 μm (Figure 8.5b). Abundant vessel pruning events are undergoing within the network, represented by three regions of interest (ROIs) from the capillary bed (ROI-1, ROI-2 and ROI-3 in insets of Figure 8.5a). Using a two-step approach described in Figure 4.4 and Sec. 4.1.2, a 3D flow model is reconstructed from the Col.IV binary image and a whole-plexus simulation is run applying generalised non-Newtonian blood rheology, followed by subregional simulations of RBC flow in ROI-1, ROI-2 and ROI-3 with specified inflow/outflow boundary conditions.

For the whole-plexus simulation, an ocular perfusion pressure (OPP) of 55 mmHg was imposed between the artery and veins of the network. The resultant volume flow rates in the artery and veins are 0.36 μL/min and 0.17$\sim$0.19 μl/min, respectively. These flow rates show good agreement with *in vivo* measurements recently achieved for living mouse retina, where the measured values were 0.39$\sim$0.59 μl/min and 0.24 μL/min, respectively [142]. The RBC velocities and fluxes calculated from the simulated ROIs are roughly $0 \sim 12.5$ mm/s (Figure 8.5c) and $0 \sim 1400$ RBC/s (Figure 8.5e), respectively. To validate the simulation RBC data, they are compared with imaging results of single-cell motion captured in living mouse retina, where comprehensive measurements were conducted for capillary vessels of diameter ranging from 3 to 7 μm [118, 142]. Following statistical tests suggest that the RBC velocities from simulations and experiments have no significant difference ($p \gg 0.05$, Figure 8.5d), the median of which being 2.14 mm/s and 1.57 mm/s, respectively. However, the RBC fluxes are significantly different between experiments and simulations ($p < 0.05$, Figure 8.5f), with the median of the former (120 RBC/s) being much higher than the latter (21 RBC/s). The main reason for this much lower median observed in simulations is the presence of a number of vessel segments with zero or negligible RBC fluxes.

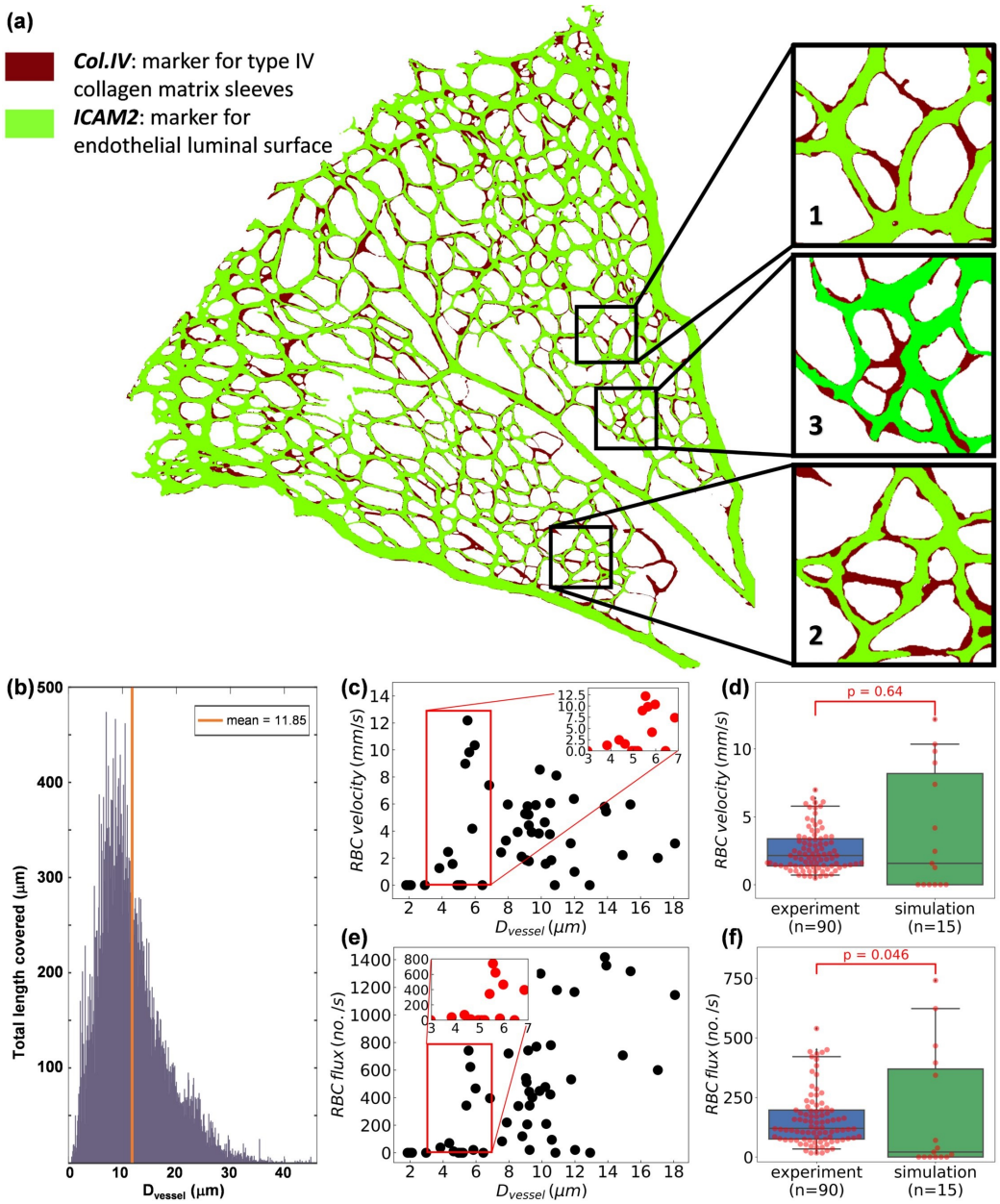

Figure 8.5: *(a) A vascular plexus of postnatal day 5 (P5) mouse retina, with vessel lumina and matrix sleeves labelled by ICAM2 (green) and Col.IV (dark red), respectively. The insets show three regions of interest (ROIs). (b) Network diameter histogram showing the total length covered by vessel segments of a given diameter. (c) Simulation RBC velocities and (d) RBC fluxes measured in divergent bifurcations of the ROIs. The insets of (c–d) highlight results from small vessels within diameter 3∼7 μm. (e–f) Statistical comparison (Mann-Whitney U test) of simulation RBC velocities and RBC fluxes against* in vivo *measurements [118, 142] from capillary vessels with diameter 3∼7 μm.*

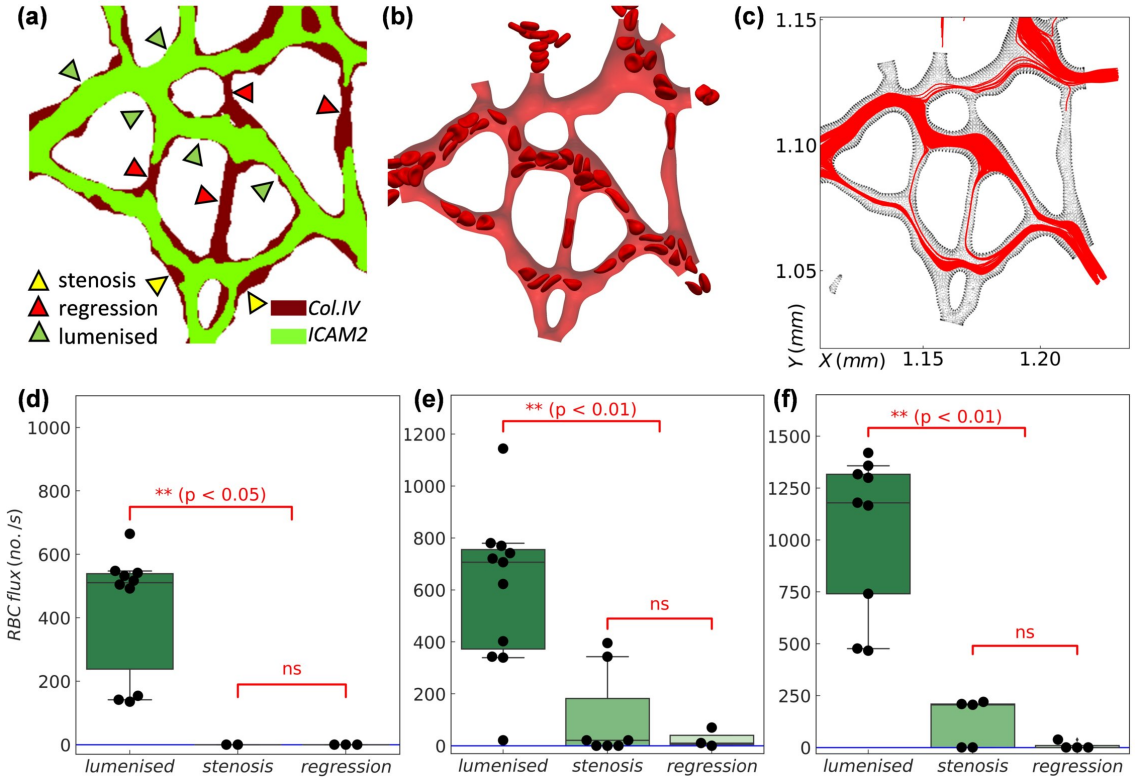

Figure 8.6: *Association between RBC depletion and vessel regression in developmental mouse retina. (a) Characterisation of vessel segments in ROI-2 based on ICAM2 and Col.IV signals. The investigated vessels are divided into three groups, namely lumenised, regression and stenosis. (b) An exemplary simulation of the cellular blood flow in ROI-2. (c) Combined cell trajectories over time in ROI-2 throughout the simulation. (d-f) Quantification (Mann–Whitney U test) of time-average RBC fluxes in ROI-1, ROI-2 and ROI-3, respectively.*

8.3.2 Association between RBC depletion and vessel regression in mouse retina

The vessel segments of the ROIs are categorised into three groups, hereby demonstrating ROI-2 as an example (Figure 8.6a): the “lumenised" group shows positive (+) signals in both Col.IV and ICAM2, featuring open lumina; the “stenosis" group shows positive (+) signal in Col.IV and partial-positive/partial-negative (+/-) signal in ICAM2, featuring vessel stenosis (recognised as a pre-regression process); the “regression" group shows positive (+) signal in Col.IV and negative (-) signal in ICAM2, featuring vessel regression.

For a mechanistic understanding of the blood flow in the developing vascular network, flow mod-

els are constructed from the selected ROIs, which simulate the blood within as suspensions of deformable RBCs (Figure 8.6b). Examination of the cellular flow simulations reveals that most RBC-depleted vessels in the simulation coincide with the regressed vessels observed in the superposed Col.IV/ICAM2 image, suggesting a potential association. To quantitatively verify whether such an association exists, the trajectories of all RBCs within the ROI throughout the simulation are recorded and their density across the network are studied (Figure 8.6c). In general, a vessel segment with denser trajectories represents good RBC perfusion, whereas those with rare existence of trajectories indicate poor RBC perfusion, or RBC depletion. Subsequently, the time-average RBC flux within each vessel segment is calculated and assigned to the three groups accordingly (Figure 8.6d-f). Evidently, vessel segments in the lumenised group have significantly higher RBC fluxes than those in the stenosis group and the regression group ($p < 0.05$ for ROI-1 and $p < 0.01$ for ROI-2 and ROI-3, Figure 8.6d-f). Meanwhile, the difference in RBC flux between the stenosis group and the regression group is insignificant ($p \gg 0.05$ for all ROIs, Figure 8.6d-f). Therefore, there is indeed a strong association between the RBC depletion observed in simulations and the vessel regression observed in experiments.

8.3.3 *in vivo* validation of the RBC depletion-vessel regression association in developmental zebrafish

To provide experimental confirmation of the association between RBC depletion and vessel regression predicted by the computational model, the zebrafish model of vascular development, where simultaneous live imaging of vessel remodelling and RBC dynamics becomes possible, is used. The caudal vein plexus (CVP) is chosen for observation 48–72 hours post fertilisation (hpf), a period during which gradual remodelling of the plexus down to a single, well-defined vascular tube begins [138]. Comparison is made between control (ctl) morpholino oligomer (MO) fish with normal RBC perfusion (Figure 8.7a) and gata1 MO fish not carrying RBCs in their bloodstream (Figure 8.7b, see Sec. 4.3.2 for experimental details). Time-lapse imaging of the CVP in ctl MO fish captures heterogeneous RBC perfusion (Figure 8.7c) leading to multiple findings of intermittent and complete RBC depletion in vessel segments (Figure 8.7d) followed by vessel stenosis (Figure 8.7e) and eventual regression (Figure 8.7f). These *in vivo* findings therefore confirm the computational predictions in Sec. 8.3.2.

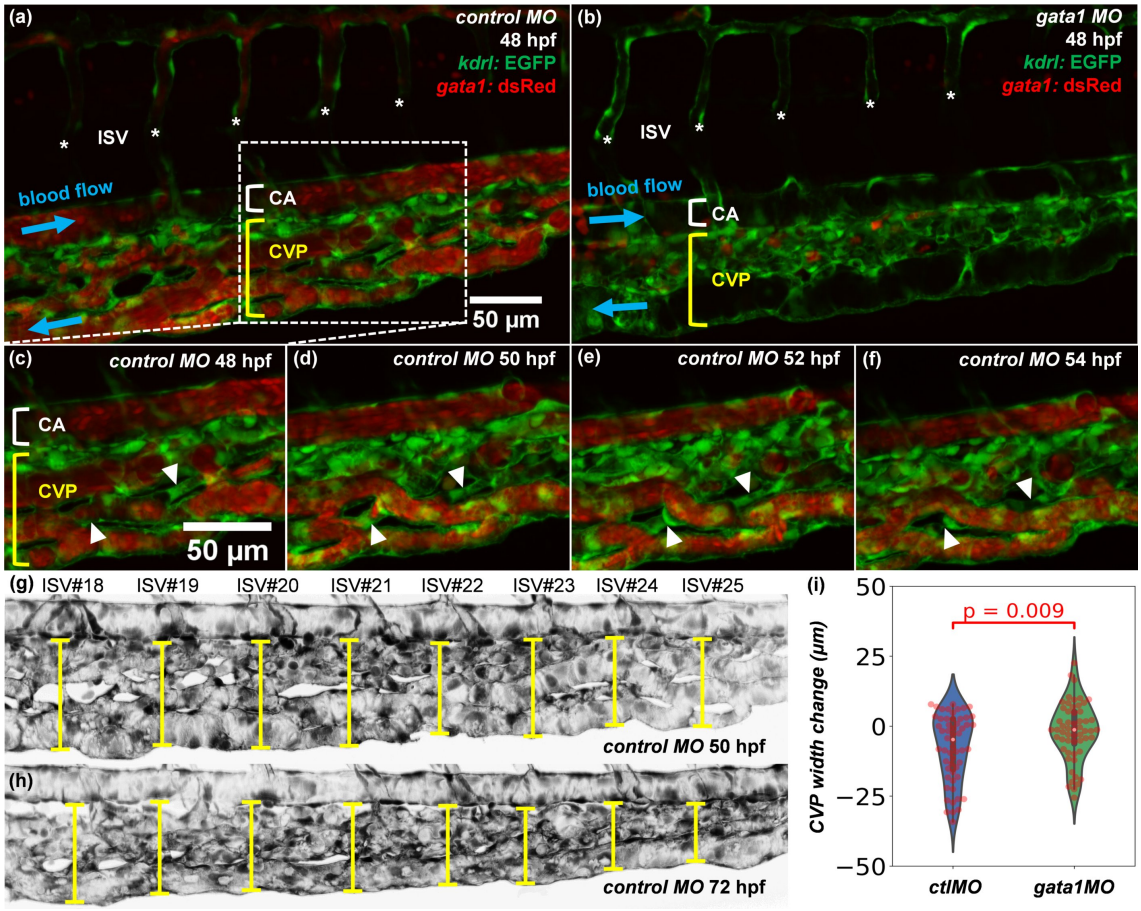

Figure 8.7: *Two caudal vein plexus (CVPs) from (a) a 48 hpf ctl MO embryo (with RBC perfusion) and (b) a 48 hpf gata1 MO embryo (Tg(GATA-1:eGFP), without RBC perfusion). The intersegmental vessels (ISVs) are marked with asterisks, and the caudal artery (CA) by a square bracket. Note that the RBC precursors in (b) are located outside the vasculature and not circulating within the blood stream. (c–f) Time sequence showing vessel regression events observed in a region of interest extracted from the CVP of the zebrafish embryo in panel (a), where two vessel segments marked by white triangles are pruned over time (t = 48 hpf, 50 hpf, 52 hpf, 54 hpf). (g,h) Measurement of CVP widths at t = 50 hpf and t = 72 hpf along the anterior-posterior axis of a ctl MO embryo (Z-projection images) at positions given by eight consecutive ISVs (ISV 18–ISV 25). (i) Variation of the CVP widths between t = 50 hpf and t = 72 hpf calculated from measurements of the ctl MO and gata1 MO groups (Welch's T test, each group containing 7 embryos).*

Next, how RBC deletion in gata1 MO fish impacts CVP remodelling at a network level is investigated.The CVP widths are measured at standardised locations along the anterior-posterior fish axis given by the position of eight consecutive intersegmental vessels (ISV) beginning at ISV 18, for both the ctl MO and gata1 MO groups ($n = 7$ each group) at 50 hpf and 72 hpf (see Figure 8.7g–h for an example fish from the ctl MO group). During this period of time, substantial remodelling leading to narrowing of the plexus is observed in the wild type (agreeing with [138]). Furthermore, significantly larger reduction of CVP width in the ctl MO group is found in comparison to the gata1 MO group, with mean reductions 7.64 μm and 2.01 μm, respectively ($p < 0.01$, Figure 8.7i). This several-fold difference implies that the presence of RBCs is necessary for normal CVP remodelling 50–72 hpf, and therefore the heterogeneity in RBC perfusion described in Figure 8.7c–f does play a role in orchestrating network-level remodelling.

8.3.4 RBC depletion in the network: unpredictable by vessel diameter

The absence of RBCs in some vessel segments from the simulated ROIs poses a crucial question about cellular flow in the vascular network: what is the governing mechanism that determines which vessels to be perfused with cells and which to be devoid of? One may notice the existence of multiple small capillaries in the ROIs and is tempting to speculate that the depletion of RBCs within the network is merely a size-exclusion effect; namely, certain vessel segments are just too narrow to allow cell to pass through. However, albeit with certain effects, the vessel diameters encountered in the present simulations (about 2–16 μm) are unlikely to be the dominant factor affecting RBC transit, since the material model adopted for RBC membrane allows a deformable cell to squeeze through exceedingly small passages as narrow as 1 μm (see Sec. 5.2 for a benchmark test). Furthermore, by examining the cell trajectories in all simulated ROIs (see Figure 8.1), counter-examples can be easily identified: a few tiny vessels are actually well-perfused, whereas some relatively larger ones are RBC-depleted.

The degree of RBC depletion is evaluated by examining $\Delta Q^* = Q^*_{rbc} - Q^*_{blood}$ (see the definitions in Sec. 8.2.3.1) against vessel diameter D_{vessel} for all child branches (44 in total, Figure 8.8a). It is clear that RBC depletion occurs throughout the whole range of vessel sizes investigated ($D_{vessel} \in [2, 16]\,\mu$m). Notably, for one child branch with $D_{vessel} > 9\,\mu$m (larger than the physiological RBC diameter), ΔQ^* is negative and the magnitude is as large as 0.2, indicating 20% fewer

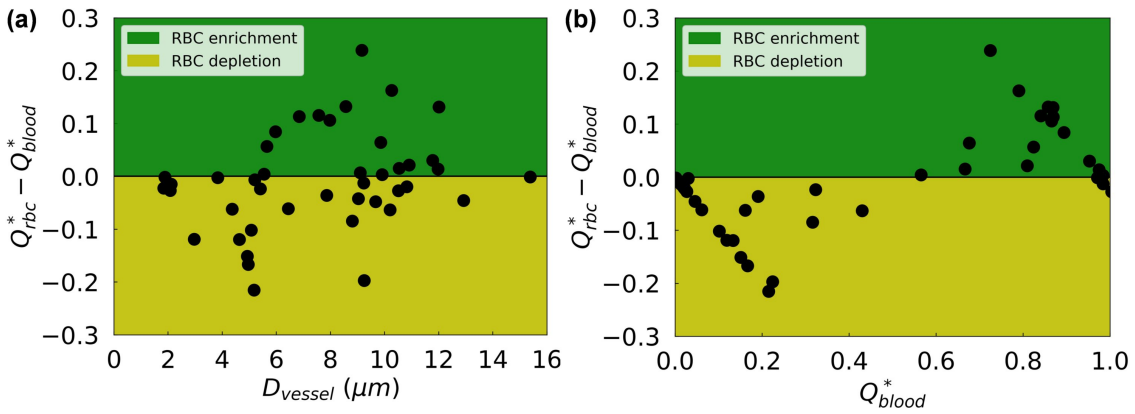

Figure 8.8: *Quantification of RBC depletion in the developing retinal network. Q^*_{rbc} and Q^*_{blood} represent the normalised RBC flux and normalised blood flow in a given child vessel (with diameter D_{vessel}) relative to those in its parent vessel, respectively. The variable $\Delta Q^* = Q^*_{rbc} - Q^*_{blood}$ serves as a disproportionality index of flow-mediated RBC partitioning, based on the sign of which the vessels are classified as "RBC-depletion" (negative ΔQ^*, yellow patch) and "RBC-enrichment" (positive ΔQ^*, green patch). The disproportionality indices for all investigated vessel segments are sorted against (a) vessel diameter D_{vessel} and (b) normalised blood flow Q^*_{blood}, respectively. The analysed vessel segments in this plot are extracted from the three ROIs in Figure 8.5.*

RBCs allocated to it than what would be expected under the assumption of linear correlation. Based on these findings, the RBC depletion observed is not a size-exclusion effect because vessel diameter alone simply cannot predict the location of RBC-depleted vessel segments in the network. Meanwhile, it is found that RBC enrichment happens only in medium/large vessels ($D_{vessel} > 5\,\mu$m). Within the intermediate diameter range 5–12 μm, the vessels have nearly equal possibilities to be RBC-enriched or RBC-depleted..

8.3.5 Mechanism for RBC depletion in the primitive vasculature

Having demonstrated that size-exclusion effect alone is not sufficient to explain the RBC depletion observed within the microvascular network, let us turn our attention to more complex haemorheological mechanisms described by empirical models such as the widely employed PSM (see introduction in Sec. 8.2.3.2). First proposed by Pries and co-workers [242, 244], the PSM actually predicted the phenomenon of RBC-depletion for certain flow split scenarios and may be capable of describing the simulation results. Indeed, a preliminary characterisation of $\Delta Q^* = Q^*_{rbc} - Q^*_{blood}$

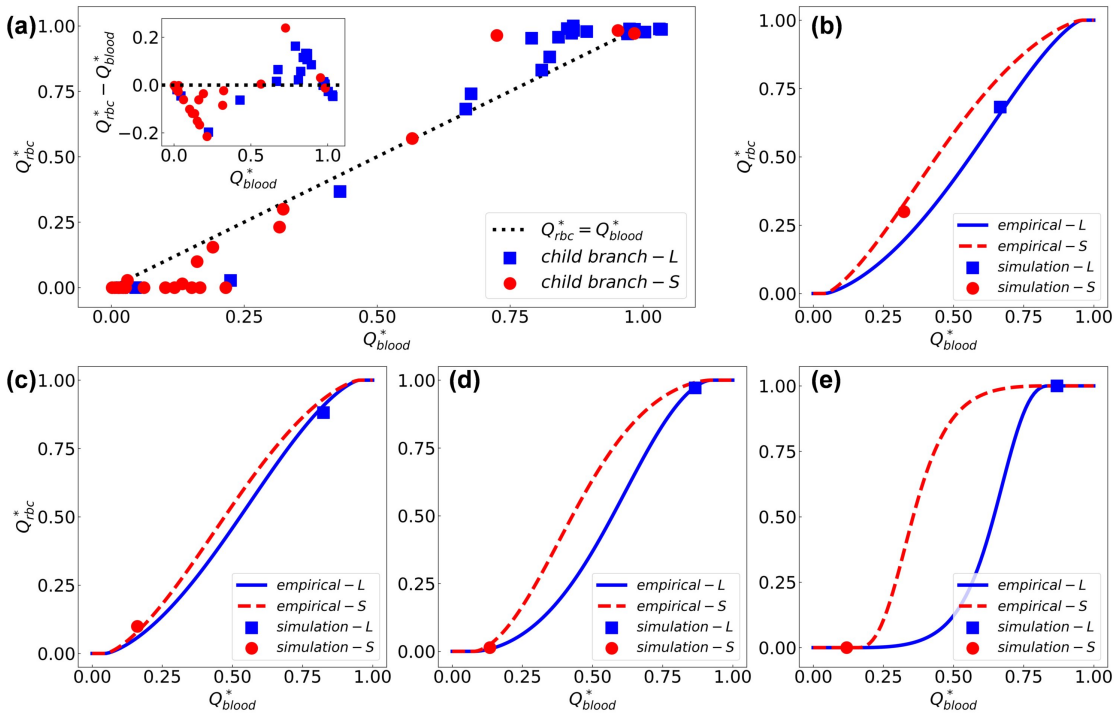

Figure 8.9: *Comparison of simulation data with empirical predictions by the empirical model [242, 244]. (a) Simulation data of fractional RBC flux Q^*_{rbc} against fractional blood flow Q^*_{blood} in the relatively larger child branch "L" (blue squares) and smaller child branch "S" (red circles) from all investigated bifurcations. The inset shows similar results as in Figure 8.8b (characterising the disproportionality index $\Delta Q^* = Q^*_{rbc} - Q^*_{blood}$ against Q^*_{blood}), but with additional information of relative vessel size for child branches in each bifurcation. The black dished line represents a linear hypothesis for Q^*_{rbc} and Q^*_{blood} in the absence of plasma skimming. (b-e) Four exemplary bifurcations in which the simulation data (squares and circles) agree well with PSM predictions (solid lines) for both the "L" and "S" child branches.*

against a naive haemodynamic indicator Q^*_{blood} instead of the geometrical indicator D_{vessel} does satisfactorily separate the RBC-depletion zone and the RBC-enrichment zone (Figure 8.8b).

8.3.5.1 Quantitative agreement with the phase separation model

To probe the simulation data with the empirical model, fractional RBC fluxes in individual child branches (44 in total) are evaluated against their fractional blood flow (Figure 8.9a). Upon initial inspection, this distribution is indeed reminiscent of the sigmoidal relationship between RBC par-

Table 8.4: *Errors of empirical prediction by the phase separation model [242, 244] in comparison to the simulation data. "ROI" represents region of interest; "BOI" represents bifurcation of interest; "CB" represents child branch. "L" and "S" refer to the relatively larger and smaller child branch within each bifurcation, respectively.*

ROI	CB	BOI-1	BOI-2	BOI-3	BOI-4	BOI-5	BOI-6	NA	NA
1	L	0.44%	0.22%	2.38%	0.0%	0.0%	1.12%	NA	NA
1	S	2.26%	3.47%	0.0%	2.89%	1.7%	0.0%	NA	NA
ROI	CB	BOI-7	BOI-8	BOI-9	BOI-10	BOI-11	BOI-12	BOI-13	BOI-14
2	L	2.32%	1.35%	4.74%	0.28%	0.0%	2.5%	1.21%	0.72%
2	S	2.68%	0.0%	9.19%	1.08%	0.0%	1.97%	4.29%	0.0%
ROI	CB	BOI-15	BOI-16	BOI-17	BOI-18	BOI-19	BOI-20	BOI-21	BOI-22
3	L	6.78%	1.16%	3.49%	1.64%	3.03%	1.3%	11.86%	1.58%
3	S	5.28%	0.0%	9.02%	0.0%	2.78%	0.0%	17.62%	0.44%

titioning and flow separation delineated by the PSM: for a child branch, if the fractional blood flow within is higher/smaller than certain thresholds, it receives all/none RBCs from its parent branch. Also, albeit exceptions do exist, the relatively smaller child branch in a given bifurcation tends to receive lower blood flow and consequently fewer RBCs, whereas the relatively larger child branch is more likely to have higher blood flow and attract more RBCs (inset of Figure 8.9a).

Further, the simulation data are compared with empirical predictions made by the PSM adopting parameters A, B, X_0 calculated individually for each bifurcation. Resultantly, satisfactory agreement is observed (with errors of empirical prediction for both child branches of a given bifurcation less than 5 % in comparison with simulation data) for 18 out of 22 bifurcations, and slight or significant deviation for only 4 bifurcations (see Figures 8.2–8.4 and Table 8.4 for complete error evaluation). Here, four representative cases are demonstrated where good agreement is achieved between the simulation and the PSM model (Figure 8.9b-e). In the first bifurcation, both child branches have considerable proportions of blood flow (roughly 30% and 70%, respectively) and are well-perfused with RBCs, with the fractional RBC fluxes nicely matching the PSM predictions (Figure 8.9b). In the second bifurcation, most RBCs ($Q^*_{blood} \approx 90\%$) enter the larger child branch as it receives more than 80% of the blood flow from the parent branch (Figure 8.9c). In the third and fourth bifurcations (Figure 8.9d-e), the smaller child branch is nearly devoid of cells as the relatively larger branch attracts almost all RBCs from the feeding vessel owing to its predominantly higher proportion of blood flow ($Q^*_{blood} > 85\%$).

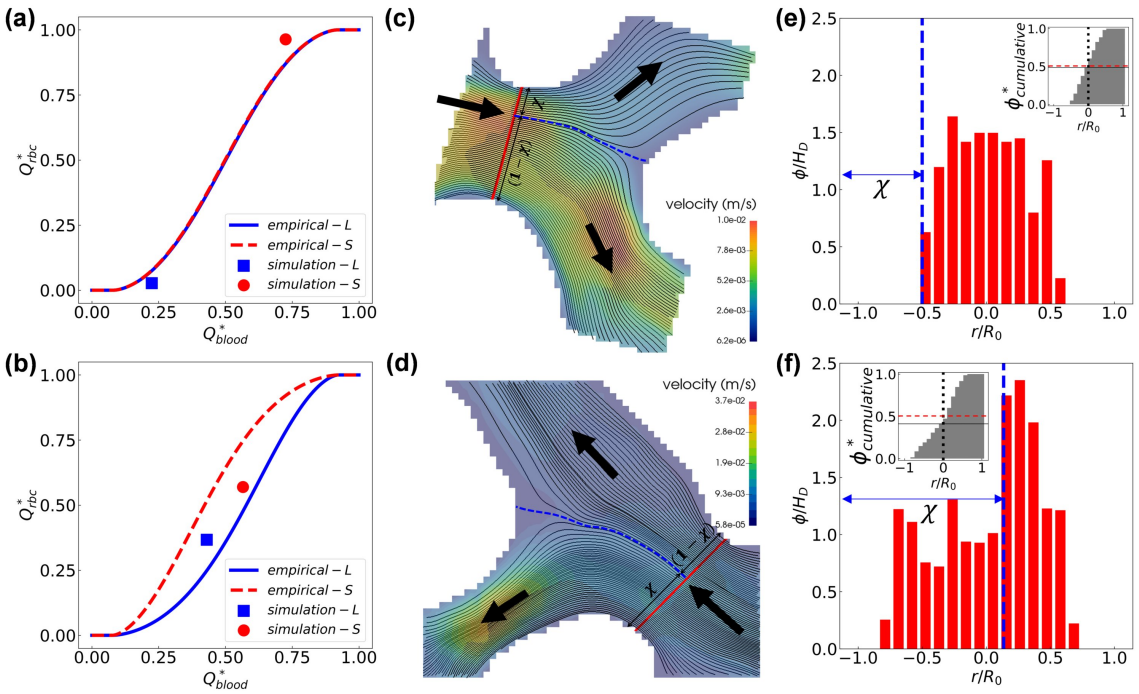

Figure 8.10: *Deviation of simulation data from the empirical model [242, 244] due to the asymmetry of haematocrit profile in the parent branch. (a-b) Two exemplar divergent bifurcations for which the simulation data (circle dots) deviate from PSM predictions (solid lines). (c-d) Visualisation of the flow streamlines separated into the child branches on the mid-plane of the bifurcation (extracted from the 3D simulation). The blue dashed line indicates the location of the separation surface. (e-f) Cross-sectional haematocrit profile in the parent branch, at a position marked by the red solid line in (c-d). The blue dashed line corresponds to the separation surface of flow streamlines as in (c-d). The insets of (e-f) show the cumulative haematocrit distribution corresponding to the haematocrit profile.*

8.3.5.2 Cases of exception to the phase separation model

For a majority of the investigated bifurcations, the agreement between numerical data from the simulations and empirical predictions by the PSM model is excellent as in Figure 8.9b-e. However, disagreement does occur for 4 bifurcations as mentioned earlier in Sec. 8.3.5.1. Shown in Figure 8.10a-b are two cases where the simulated RBC fluxes in the bifurcation deviate from the empirically predicted values. Interestingly, while the RBC flux contrast between the two child branches in case one is slightly underestimated by the PSM model (Figure 8.10a), that in case two is substantially overestimated (Figure 8.10b).

To reveal the reason behind the abnormal RBC partitioning against the PSM model, one needs to understand how the blood flow is split into the child branches from their feeding vessel, or the parent branch. For this purpose, the flow in the mid-plane of the bifurcation is examined and the flow separation line that splits the blood flow into two zones is calculated as in Figure 8.10c-d, where "χ" leads to the left branch and "$1-\chi$" leads to the right branch. Clearly, the higher-flow branch (child branch with larger Q^*_{blood}) in each bifurcation occupies more streamlines, and should ideally receive more RBCs too provided that the cells are axisymmetrically distributed (as assumed by the PSM) in the parent branch and also would flow alongside the streamlines.

Next, whether the axisymmetry assumption by the PSM holds in the simulations is investigated. To this end, the cross-sectional distribution of RBCs in the parent branch is calculated. Surprisingly, the distribution turns out asymmetric rather than axisymmetric, especially for case two (Figure 8.10e-f). In both cases, the haematocrit profile is skewed towards the right-hand side of the bifurcation (based on cumulative haematocrits, see insets of Figure 8.10e-f), making the downstream child branch on this side inherently advantageous for RBC intake (hereafter referred to as "Hct-favoured branch"). In case one, the higher-flow branch coincides with the Hct-favoured branch, resulting in enhanced plasma-skimming effect and enlarged RBC flux difference between the two child branches; whereas in case two, the higher-flow branch contradicts the Hct-favoured branch, thus counterbalancing the plasma-skimming effect and consequently attenuating the RBC flux difference. In this respect, the mismatch of haematocrit-profile alignment with flow split in the parent branch breaks down the predication of the PSM, which was formulated assuming axisymmetric haematocrit profiles. A full description of the mechanism leading to this mismatch, which originates from the interplay between the complex geometry and the emerging RBC behaviour in the microvasculature, is out of the scope of the present study and will be investigated in future work.

8.4 Discussion

8.4.1 Comparison of simulated RBC flow with *in vivo* data

The RBC velocities calculated from the simulated retinal blood flow are similar with *in vivo* measurements made in living mouse retinas [118, 142]. However, a noticeable discrepancy exists between the simulations and experiments in terms of RBC fluxes (Figure 8.5f). This discrepancy

is down to the fact that the capillaries where *in vivo* measurements were made [118, 142] belong to adult mouse retina possessing mature and functional vascular networks, whereas those simulated by us are based on a primitive vascular network of developing mouse retina undergoing progressive vessel regression. The prevalent existence of abundant vessel segments in the simulated network underpins a fundamental structural difference than the experimented ones, leading to a more heterogeneous distribution of RBC fluxes within. It is speculated that as the remodelling process prunes the abundant vessels and the primitive network turns mature, the simulated RBC fluxes will become closer to the *in vivo* measurements from adult mice.

Besides the developmental nature of the simulated retinal network, there are other resources of uncertainty in the present simulations which remain to be quantified if better agreement with *in vivo* measurements are sought. First, to simulate all ROIs in a consistent manner, the feeding haematocrit at inlets are unanimously fixed at 20%. This adopted value is in line with the average haematocrit level reported in the literature ($23\% \pm 14\%$ by [246]), but may not necessarily reflect the haematocrit levels of individual mice experimented in [118, 142]. Second, the flow in realistic microvessels with smaller lumen size than the RBC diameter is generally impeded due to close contact of cells with the endothelial surface layer (ESL, consisting of glycocalyx and/or cilia), whereas in the present in silico model such complex structures are not considered. Such a structural difference is known to cause higher flow resistance values measured *in vivo* than *in vitro* (from glass tubes where the ESL is absent), the former of which was previously reported to be twice as high as the latter [248, 249].

8.4.2 Role of RBC dynamics in vascular remodelling

Earlier studies have extensively researched the effect of blood perfusion on early-stage cardiovascular development and it has now been well-accepted that haemodynamic cues are essential for vascular patterning [48, 156, 189]. Seminal work by Franco *et al.* further established the pivotal role of regional WSS difference, which was found to locally modulate the polarised migration of ECs into high-shear vessel segments and cause the regression of adjacent segments experiencing low shear [93, 94]. The quantification of WSS in all these studies relied on mathematical flow models assuming simplified blood rheology in the absence of RBCs, partially due to the prohibitiveness of modelling RBC flow in realistic networks. However, recent simulations of cel-

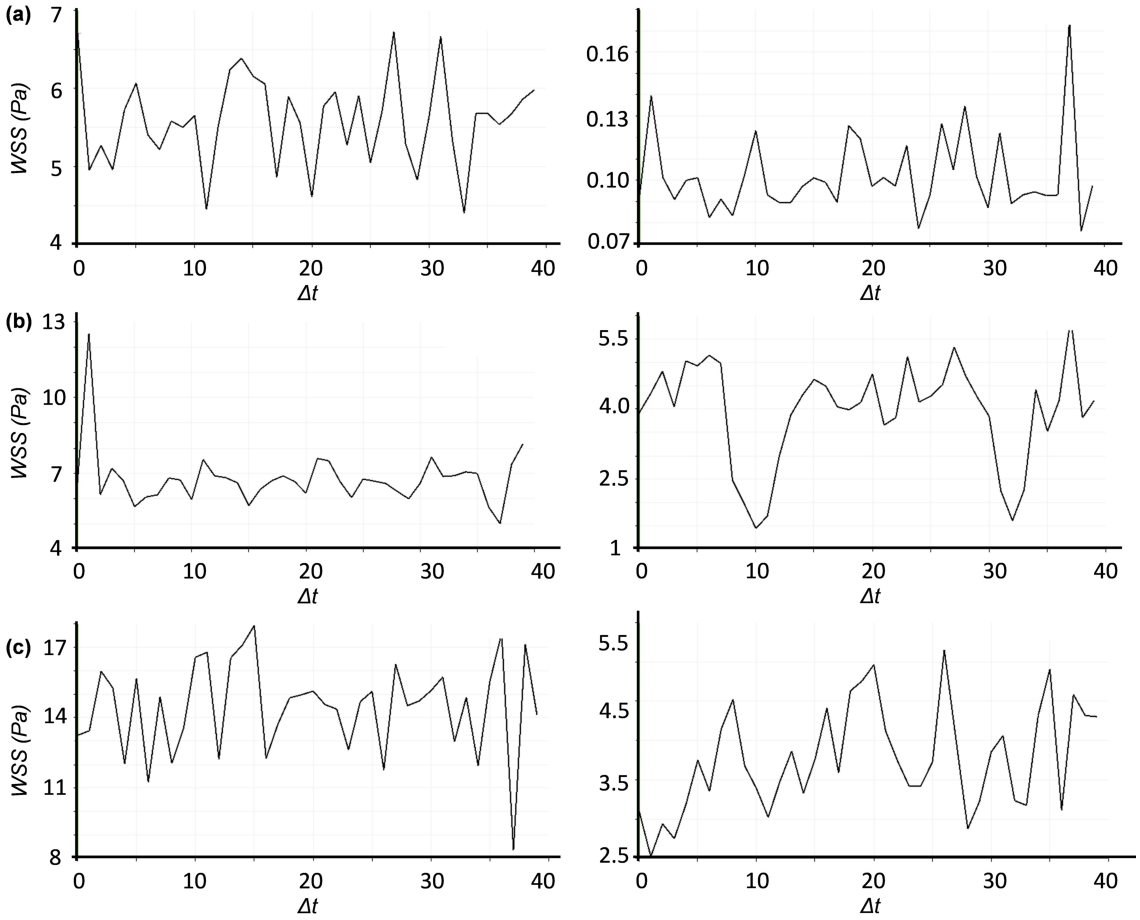

Figure 8.11: *Temporal fluctuation of WSS in three BOIs selected from ROI-2 (see BOI-A, BOI-B and BOI-C marked in Figure 8.12). (a), (b) and (c) represent the first, second and third BOI, respectively. For each BOI, the WSS in its two child branches are tracked over 40 time intervals, with each time interval* $\Delta t = 2.08$ *ms.*

lular blood flow in single microvessels have shown that the transient wall-stress footprint of RBCs can non-trivially modify both the mean and oscillatory components of local WSS, thereby suggesting a salient impact of RBCs on the mechanotransduction of fluid forces during angiogenesis [100, 131, 227]. In the current study, it is hypothesised that RBCs in the developing mouse retina play an active role in the course of vascular patterning towards a functional network via altering WSS spatially and temporally (see Figure 8.11).

The present simulations of cellular blood flow in the developing mouse retina reveals a high-level heterogeneity of RBC perfusion throughout the vascular network, where a number of plasma ves-

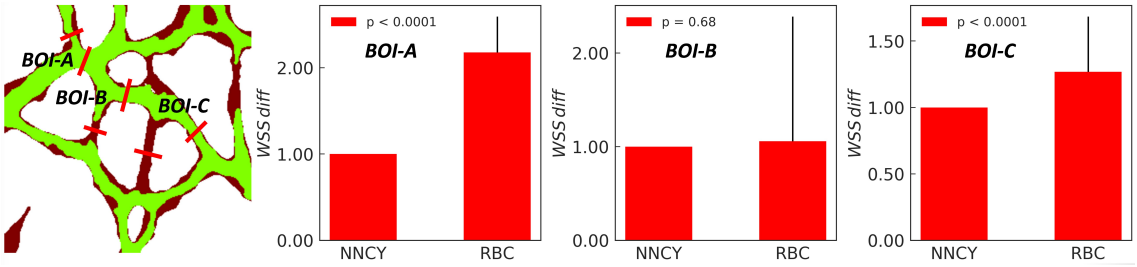

Figure 8.12: *Comparison of the normalised WSS difference (WSS diff) calculated from simulations with and without RBCs for three BOIs selected from ROI-2. The WSS difference for each BOI is defined as* $(\frac{\tau_h - \tau_l}{\tau_l})$*, where* τ_h *and* τ_l *represent the higher WSS and lower WSS measured from the two child branches of each BOI, respectively. "NNCY" (non-Newtonian Carreau-Yasuda) and "RBC" represent results from the flow model adopting simplified blood rheology without RBCs and the cellular blood flow model involving RBCs, respectively. To facilitate visual detection of the enhancement in WSS difference, the values for both "NNCY" and "RBC" are normalised by the WSS difference measured from "NNCY". The error bar in each "RBC" group accounts for temporal WSS fluctuations arising from the transient behaviour of RBCs, hence reflecting the oscillatory part of the WSS difference.*

sels persist with rare RBC transits over time. Given this heterogeneity, the effective viscosity in neighbouring RBC-depleted and RBC-enriched branches can differ substantially. Such viscosity contrast will instantaneously enhance the regional WSS difference between neighbouring branches, which may in turn promote the pruning of the vessel segment depleted of RBCs. Indeed, a preliminary investigation for several BOIs where vessel regression/stenosis takes place reveals a substantially increased mean or oscillatory part of the WSS difference metric for current RBC simulations compared to an equivalent simulation without RBCs applying a non-Newtonian rheology flow model (see Figure 8.12). Further experimental confirmation of these findings in the developmental zebrafish model (amenable to live imaging) is also provided as shown in Figure 8.7. In agreement with Lucitti *et al.* [189], the presence of RBCs is demonstrated necessary for effective remodelling at a whole plexus level. Furthermore, the original conception is extended by the present work in that intermittent and complete RBC depletion selects vessels for regression.

8.4.3 Flow-mediated RBC perfusion in developmental vascular networks

To fully understand the distribution of RBC fluxes within the developing mouse retina, the question below is asked: what is the mechanism for the occurrence of RBC depletion or enrichment in the

vascular network. Subsequent quantification of RBC fluxes against blood flow in the analysed bifurcations negates vessel-size exclusion as the primary factor. Instead, the haemorheological PSM theory explains the uneven partitioning of RBC fluxes satisfactorily in 18 out of 22 cases, implying that the perfusion of RBCs within the developing network is flow-mediated rather than geometry-dominant.

In line with the recently reported *in vivo* data [118, 142], either the flow rate and RBC flux can vary significantly in vessels of similar diameter within the retina network. Note how the data clusters nearby $D = 10\,\mu$m from the simulations span the whole range of flow rates and RBC fluxes (Figure 8.5c,e). These wide variations confirm that vessel diameter alone poorly predicts the haemodynamics in the the microvasculature. The reason behind such variations is the network effect for a microvasculature [244], owing to the fact that the microvessels are interconnected and the flow within any single segment is co-determined by the flow resistance of its own and its upstream/downstream branches.

8.4.4 Asymmetry of haematocrit and velocity profiles

For the 4 cases where the PSM theory does not satisfactorily explain the data, the investigation of RBC flux distribution leads to the finding of significant haematocrit asymmetry in the cross-section of feeding branches, which is against the central assumption of axisymmetrical haematocrit profiles by the PSM formulation. In other words, the emergent behaviour of RBC motion in the network can lead to severely skewed haematocrit profiles in the parent branch of some bifurcations, which may counteract the plasma skimming effect modelled by the PSM on the basis of fractional blood flow. This makes accurate prediction of the RBC perfusion in a given vascular network not possible without knowledge of the cross-sectional cell distributions. The observation of haematocrit-favoured and haematocrit-unfavoured vessel branches at microvascular bifurcations is in line with recent *in vitro* findings of reversion of the classic haematocrit partitioning which otherwise always favours the higher-flow branch [57, 195, 276, 278]. Similar reverse partitioning was reported by simulations of cellular blood flow in microvascular networks with vessel diameters designed based on Horton's law [19].

The asymmetry not only applies to the haematocrit profile, but also the velocity profile. For a

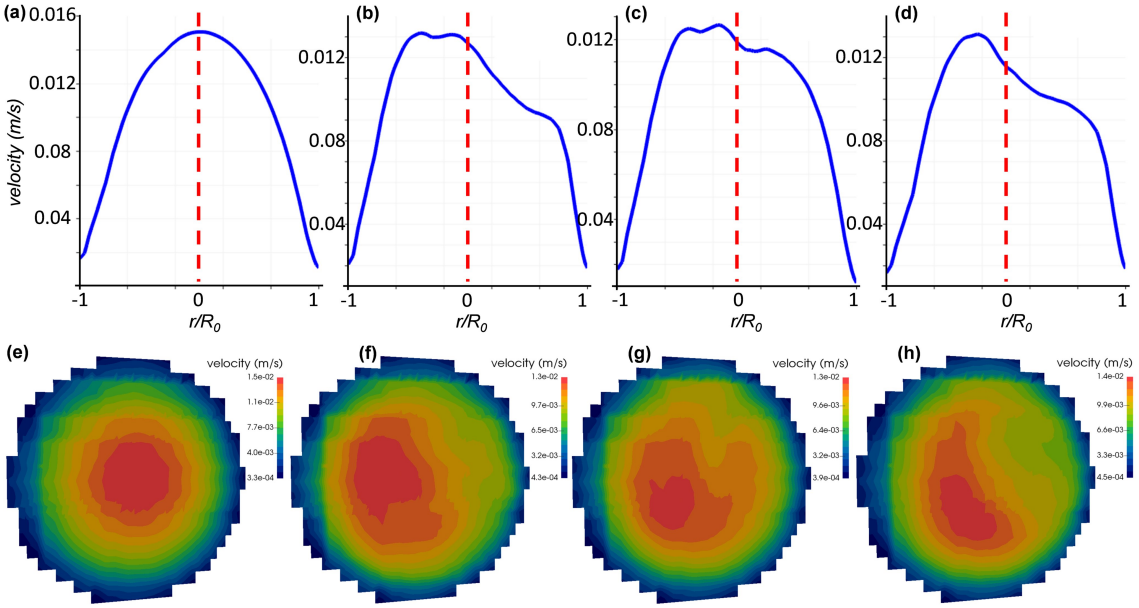

Figure 8.13: *(a-d) Temporal variation of the velocity profile monitored at the red line in Figure 6d. (e-h) Corresponding cross-sectional velocity contours at the same position with warmer colours* (e.g., *red) indicating higher velocity magnitudes. (a) and (e):* t_1 *= 0.042s. (b) and (f):* t_2 *= 0.125s. (c) and (g):* t_3 *= 0.208s. (d) and (h):* t_4 *= 0.291s.*

majority of microcirculatory models, the Poiseuille law has been employed to simplify the blood rheology and reduce computational cost, manifested by parabolic velocity profiles featuring a maximum velocity across the network. Current results counter such a simplification, as the velocity profile in a capillary vessel can significantly deviate from a parabola over time in the presence of travelling RBCs and become skewed towards one side of the vessel wall (Figure 8.13). Similar deviation of velocity profiles has also been confirmed by imaging data from living mouse retina, where a 39% error in flow estimation can happen if a parabolic profile is assumed [118, 142].

The co-existence of asymmetric velocity and haematocrit profiles adds to the complexity of network analysis regarding RBC perfusion, as it turns out unclear whether a general rule holds to determine the preferred child branch when the flow split and cell distribution contradict each other in terms of preference for child branches. This may introduce extra stochastic elements into the development of primitive vasculature towards a functional network, which remains to be investigated. In addition, one should bear in mind the prominence of network effect for a microcirculatory system, which non-trivially modulates the haemodynamics within individual microvessels.

8.5 Concluding remarks

In summary, the present study uncovers a new mechanism for the enhancement of WSS differences driving vascular remodelling in the developmental mouse retina. This is achieved by the uneven distribution of RBCs governed by plasma-skimming at sequential bifurcations that cascade down the whole retina, which yields a high-level heterogeneity of RBC perfusion with the network and contribute to regional viscosity contrasts. Beyond these findings, this study also has important implications for the modelling of microvascular haemodynamics in general. In a network of microvessels, a myriad of effects unable to be explained by continuum flow models (albeit widely employed for modelling blood flow in complex vascular networks by existing studies) occur due to the particulate nature of blood, *i.e.,* essentially a suspension of RBCs. Conventional assumptions such as Poiseuille law, velocity-/haematocrit-profile symmetry, spatial-/time-average accuracy are all subject to scrutiny when quantitatively measuring flow variables such as viscosity and WSS in the microcirculation, especially for vessels with lumen space smaller than the RBC (about 8 μm in diameter at rest).

Part IV

CONCLUSIONS AND OUTLOOK

Measure what can be measured, and make measureable what cannot be measured.

— Galileo Galilei

Chapter 9
Conclusions & future work

Summary This thesis centres around the hypothesis that the cellular character of blood, *i.e.,* essentially a suspension of RBCs, importantly affects the haemodynamics at the microscale and plays a key role in vascular development, potentially *via* the established mechanotransduction link between wall shear stress (WSS) modulation and endothelial cell (EC) migration. The research roadmap designed to verify this hypothesis includes four stages of investigations:

(I) Investigation of single RBC behaviour in biological or biomimetic channels using the proposed computation model (IB-LBM, see Sec. 4.1.1). This serves as validation of the present model and test its suitability for simulating cellular blood flow by examining the deformation, motion and WSS footprint of individual cells.

(II) Investigation of RBC suspensions in microvessels or artificial microchannels. This serves as preliminary study of the spatio-temporal dynamics of RBCs at the microscale, *e.g.,* hydrodynamic lift, cell-free layer development, collective transport pattern, dynamic haematocrit reduction.

(III) Investigation of RBC suspensions in realistic or artificial microvascular networks. This serves as advanced study of microcirculatory haemodynamics within complex geometries, *e.g.,* flow distribution, RBC partitioning, haematocrit heterogeneity, wall shear stress difference.

(IV) Investigation of the relationship between microcirculatory haemodynamics and vascular patterning in developmental animal models. This is where the thesis culminates.

In line with the above roadmap, the research work during my PhD is assigned into four chapters of this thesis that contain original results: Chapter 5 (aligned with Stage I), Chapter 6 (aligned with Stage II), Chapter 7 (aligned with Stage III) and Chapter 8 (aligned with Stage III+IV). All primary research projects presented in the thesis (Chapters 6–8) are highly collaborative in nature, consisting of both computational contributions (by myself) and experimental contributions (by my collaborators). However, it is important to stress that in all concerned chapters, the computer

simulations take the leading role in framing and interpreting the research, whereas experiments either serve as corroborative data or simulation input.

Conclusions Chapter 5 benchmarks a single RBC's behaviour in typical channel flows, including three studies: (1) cell shape and WSS signature in a small cylindrical tube; (2) membrane deformation and cell transit through a narrow spleen slit; (3) motion regime and equilibrium position in a rectangular microchannel. More basic benchmark tests of the fluid flow (*e.g.,* flow compressibility) or RBC properties (*e.g.,* membrane forces) have been performed to validate the IB-LBM model, but only the above three are demonstrated in the thesis because of their close relevance to primary research projects in Chapters 6–8. Benchmark tests 1 and 2 conclude that the present computational model equipped with high-level parallelisation is capable to simulate some of the most numerically challenging cases of RBC flow while showing satisfactory agreement with results of established models. Benchmark test 3 reveals the occurrence of symmetry-breaking by inspecting the angular dynamics of apparently rigid RBCs, which would trigger their cross-streamline migration despite negligible inertia in the channel flow. Such a counterintuitive motion is presumably associated with the shape characteristic and fluid-filled nature of the seemingly "solid" RBC in bounded channel flow, but further research is required to elucidate the exact mechanism.

Chapter 6 addresses the physical effects underlying emerging behaviours in dilute RBC suspensions and examines the validity of common assumptions made by experimentalists about the RBC dynamics within non-circular microchannels. This task is non-trivial at all as a plethora of effects are involved, and it has not been satisfactorily performed in the literature. The cross-validation between simulations and experiments for real-size microchannels (channel length > 1 mm) itself is also challenging as a large number of highly-resolved RBCs need to be modelled. By simulating and analysing the RBC migration and cell-free layer (CFL) development with massively parallel simulations, it is revealed that non-inertial focusing of RBCs within the suspension occurs (resembling the inertial "tubular pinch" effect [271, 272]), which is co-determined by the spatial decay of cell hydrodynamic lift and the global deficiency of cell dispersion in the dilute limit (where the cell concentration is lower than 10%). The development length of CFL within the channel is found exceedingly long compared to earlier findings. In addition, a scaling law is proposed for the CFL growth, which agrees well with both my own simulation data and supplementary experimental

data from my collaborators. This work highlights the importance of transient cell distribution in dilute suspensions even with low or negligible inertia, especially for high-aspect-ratio channels. It cannot therefore be presumed without inspection that cells are regularly distributed and present the commonly reported concentration peak at the channel centre. Also, experimentalists working on dilute suspensions should be careful when designing local channel features, whose disturbances to the particulate flow can take unexpectedly long distances to remove.

Chapter 7 is dedicated to elucidating the microscopic behaviour of RBCs at arteriolar-level bifurcations using a biomimetic vascular network consisting of bifurcating microchannels (channel hydraulic diameter D_h = 30-100 μm). Subject to the terminal flow ratio controlled at the outlets, the artificial vascular network presents ideal partitioning of RBCs at symmetric bifurcations, agreeing with an established empirical model derived for RBC distribution at microvascular bifurcations [242, 244]. This agreement suggests that artificial vascular networks designed using rectangular microchannels can reasonably capture the phase-separation phenomenon and may provide trustworthy approximation of the haemodynamics in realistic microvascular networks, provided that proper biomimetic design rules such as the Murray's law are followed. On the other hand, biased partitioning occurs with the breakdown of CFL symmetry in inter-bifurcation branches, which leads to significant haemo-concentration/dilution in downstream branches. The resultant haematocrit heterogeneity demonstrates the prominent effect of CFL asymmetry on the phase separation process with the presence of upstream disturbances. It is also worth mentioning that, among various RBC shapes and motion regimes found in the present simulation, the intriguing polylobed RBC morphology asserted only for high viscosity-contrast environments (*e.g.,* $\lambda \geq 5$) by recent studies [169, 197] is also captured here, but with a viscosity contrast of unity (*i.e.,* $\lambda = 1$). A detailed discussion is given in the discussion section of Chapter 7.

In Chapter 8, the central chapter of this thesis, an innovative simulation framework is adopted to model microcirculatory blood flow in the vascular networks of developmental mouse retina, which is a complex and sparse structure seldom modelled at the cell-scale by previous works. Through computational quantification and *in vivo* validation, a remarkable association is identified between RBC depletion and vessel regression, as a new mechanism for the enhancement of the WSS differences known to drive vascular remodelling [93]. The enhancing effect arise due to the highly heterogeneous distribution of RBCs within the primitive plexus, which is primarily governed by

plasma skimming [160, 242]. Additionally, it is speculated that vascular remodelling driven by the principle of removing RBC-poor vessels from the primitive vasculature will lead to a network layout that avoids portions of the tissue being vascularised but perfused with poorly oxygenated blood. This RBC-driven process, which is highly dynamical and emerging in nature, can importantly contribute to the optimal patterning of vascular networks during development. Beyond these findings, the work also has wider implications for the mathematical modelling community that studies microvascular haemodynamics. It turns out that in a network of microvessels, multiple effects unable to be explained by continuum flow models occur due to the particulate nature of blood. Conventional assumptions such as Poiseuille law, velocity-/haematocrit-profile symmetry, spatial-/time-average accuracy are all subject to scrutiny when quantitatively measuring flow variables such as effective viscosity and WSS in the microcirculation, especially for vessels with a lumen smaller than the size of an RBC.

Future work The results and methods contained in the present thesis hold the premises to steadily increase our understanding of the intricate microcirculatory haemodynamics. For example, the image-based simulation framework presented in Chapter 8 may be extended to the modelling of cellular blood flow in reconstructed vascular networks based on imaging data of human tissues or organs, so that patient-specific modelling aimed at detecting or predicting haemodynamic disorders becomes possible. As the data of microcirculatory simulations accumulate, we may also make use of these data to inform simplified yet robust reduced-order models that can greatly increase our capability of simulating physiological or pathological microvasculatures. The IB-LBM model equipped with high-level parallelisation, which have been thoroughly applied in the present thesis, justifies itself as reliable simulation tool for practical investigation of microcirculatory blood flow and may see wider applications, such as optimising microfluidic devices. Nevertheless, there are still limitations regarding the model which should be overcome in future work to further increase its applicability and capacity. From a physical perspective, it will be ideal to include more biophysics of the cell, such as the viscosity contrast and membrane viscosity for RBCs (which is currently absent in the model). The deformation and regulatory responses of blood vessels can also be added. From a computational perspective, the load imbalance and communication overhead issues remain to be resolved to enable efficient cellular blood flow simulation in whole-vasculature instead of extracted subsets.

Bibliography

[1] ABAY, A., RECKTENWALD, S. M., JOHN, T., KAESTNER, L., AND WAGNER, C. Cross-sectional focusing of red blood cells in a constricted microfluidic channel. *Soft Matter 16*, 2 (2020), 534–543.

[2] ABKARIAN, M., FAIVRE, M., AND VIALLAT, A. Swinging of Red Blood Cells under Shear Flow. *Physical Review Letters 98*, 18 (2007), 188302.

[3] ABKARIAN, M., LARTIGUE, C., AND VIALLAT, A. Tank Treading and Unbinding of Deformable Vesicles in Shear Flow: Determination of the Lift Force. *Physical Review Letters 88*, 6 (2002).

[4] ABKARIAN, M., AND VIALLAT, A. Vesicles and red blood cells in shear flow. *Soft Matter 4*, 4 (2008), 653–657.

[5] ABREU, D., LEVANT, M., STEINBERG, V., AND SEIFERT, U. Fluid vesicles in flow. *Advances in Colloid and Interface Science 208* (2014), 129–141.

[6] ABULARRAGE, C. J., SIDAWY, A. N., AIDINIAN, G., SINGH, N., WEISWASSER, J. M., AND ARORA, S. Evaluation of the microcirculation in vascular disease. *Journal of Vascular Surgery 42*, 3 (2005), 574–581.

[7] AHMED, F., MEHRABADI, M., LIU, Z., BARABINO, G. A., AND AIDUN, C. K. Internal Viscosity-Dependent Margination of Red Blood Cells in Microfluidic Channels. *Journal of Biomechanical Engineering 140*, 6 (2018), 061013–061013–7.

[8] AIDUN, C. K., AND CLAUSEN, J. R. Lattice-Boltzmann Method for Complex Flows. *Annual Review of Fluid Mechanics 42*, 1 (2010), 439–472.

[9] ALBRECHT, K. H., GAEHTGENS, P., PRIES, A. R., AND HEUSER, M. The Fahraeus effect in narrow capillaries (i.d. 3.3 to 11.0 μm). *Microvascular Research 18*, 1 (1979), 33–47.

[10] ALESTRÖM, P., D'ANGELO, L., MIDTLYNG, P. J., SCHORDERET, D. F., SCHULTE-MERKER, S., SOHM, F., AND WARNER, S. Zebrafish: Housing and husbandry recommendations. *Laboratory Animals* (2019), 0023677219869037.

[11] ALEXEEV, D., AMOUDRUZ, L., LITVINOV, S., AND KOUMOUTSAKOS, P. Mirheo: High-performance mesoscale simulations for microfluidics. *Computer Physics Communications* (2020), 107298, https://doi.org/10.1016/j.cpc.2020.107298.

[12] AMIGO, J. D., ACKERMANN, G. E., COPE, J. J., YU, M., COONEY, J. D., MA, D., LANGER, N. B., SHAFIZADEH, E., SHAW, G. C., HORSELY, W., TREDE, N. S., DAVIDSON, A. J., BARUT, B. A., ZHOU, Y., WOJISKI, S. A., TRAVER, D., MORAN, T. B., KOURKOULIS, G., HSU, K., KANKI, J. P., SHAH, D. I., LIN, H. F., HANDIN, R. I., CANTOR, A. B., AND PAW, B. H. The role and regulation of friend of GATA-1 (FOG-1) during blood development in the zebrafish. *Blood 114*, 21 (2009), 4654–4663.

[13] AOUANE, O., FARUTIN, A., THIÉBAUD, M., BENYOUSSEF, A., WAGNER, C., AND MISBAH, C. Hydrodynamic pairing of soft particles in a confined flow. *Physical Review Fluids 2*, 6 (2017).

[14] ARABGHAHESTANI, M., POOZESH, S., AND AKAFUAH, N. K. Advances in Computational Fluid Mechanics in Cellular Flow Manipulation: A Review. *Applied Sciences 9*, 19 (2019), 4041.

[15] ASMOLOV, E. S. The inertial lift on a spherical particle in a plane Poiseuille flow at large channel Reynolds number. *Journal of Fluid Mechanics 381* (1999), 63–87.

[16] BAEYENS, N., NICOLI, S., COON, B. G., ROSS, T. D., VAN DEN DRIES, K., HAN, J., LAURIDSEN, H. M., MEJEAN, C. O., EICHMANN, A., THOMAS, J.-L., HUMPHREY, J. D., AND SCHWARTZ, M. A. Vascular remodeling is governed by a VEGFR3-dependent fluid shear stress set point. *eLife 4* (2015), e04645.

[17] BAGCHI, P. Mesoscale Simulation of Blood Flow in Small Vessels. *Biophysical Journal 92*, 6 (2007), 1858–1877.

[18] BALOGH, P., AND BAGCHI, P. A computational approach to modeling cellular-scale blood flow in complex geometry. *Journal of Computational Physics 334* (2017), 280–307.

[19] BALOGH, P., AND BAGCHI, P. Analysis of red blood cell partitioning at bifurcations in simulated microvascular networks. *Physics of Fluids 30*, 5 (2018), 051902.

[20] BALOGH, P., AND BAGCHI, P. The cell-free layer in simulated microvascular networks. *Journal of Fluid Mechanics 864* (2019), 768–806.

[21] BARBEE, J. H., AND COKELET, G. R. Prediction of blood flow in tubes with diameters as small as 29 μ. *Microvascular Research 3*, 1 (1971), 17–21.

[22] BARBER, J. O., ALBERDING, J. P., RESTREPO, J. M., AND SECOMB, T. W. Simulated Two-dimensional Red Blood Cell Motion, Deformation, and Partitioning in Microvessel Bifurcations. *Annals of Biomedical Engineering 36*, 10 (2008), 1690–1698.

[23] BARBER, J. O., RESTREPO, J. M., AND SECOMB, T. W. Simulated Red Blood Cell Motion in Microvessel Bifurcations: Effects of Cell–Cell Interactions on Cell Partitioning. *Cardiovascular Engineering and Technology 2*, 4 (2011), 349–360.

[24] BARBER, R. W., AND EMERSON, D. R. Optimal design of microfluidic networks using biologically inspired principles. *Microfluidics and Nanofluidics 4*, 3 (2008), 179–191.

[25] BARTHÈS-BIESEL, D. *Microhydrodynamics and Complex Fluids*. CRC Press, 2012.

[26] BARTHÈS-BIESEL, D. Motion and Deformation of Elastic Capsules and Vesicles in Flow. *Annual Review of Fluid Mechanics 48*, 1 (2016), 25–52.

[27] BASKURT, O. K., FARLEY, R. A., AND MEISELMAN, H. J. Erythrocyte aggregation tendency and cellular properties in horse, human, and rat: a comparative study. *American Journal of Physiology - Heart and Circulatory Physiology 273*, 6 (1997), H2604–H2612.

[28] BAZAZ, S. R., MASHHADIAN, A., EHSANI, A., CHANDRA SAHA, S., KRÜGER, T., AND WARKIANI, M. E. Computational inertial microfluidics: a review. *Lab on a Chip* (2020).

[29] BERNABEU, M. O., JONES, M. L., NASH, R. W., PEZZAROSSA, A., COVENEY, P. V., GERHARDT, H., AND FRANCO, C. A. PolNet: A Tool to Quantify Network-Level Cell Polarity and Blood Flow in Vascular Remodeling. *Biophysical Journal 114*, 9 (2018), 2052–2058.

[30] BERNABEU, M. O., JONES, M. L., NIELSEN, J. H., KRÜGER, T., NASH, R. W., GROEN, D., SCHMIESCHEK, S., HETHERINGTON, J., GERHARDT, H., FRANCO, C. A., AND COVENEY, P. V. Computer simulations reveal complex distribution of haemodynamic forces in a mouse retina model of angiogenesis. *Journal of The Royal Society Interface 11*, 99 (2014), 20140543.

[31] BHATNAGAR, P. L., GROSS, E. P., AND KROOK, M. A Model for Collision Processes in Gases. I. Small Amplitude Processes in Charged and Neutral One-Component Systems. *Physical Review 94*, 3 (1954), 511–525.

[32] BLUMERS, A. L., TANG, Y.-H., LI, Z., LI, X., AND KARNIADAKIS, G. E. GPU-accelerated red blood cells simulations with transport dissipative particle dynamics. *Computer Physics Communications 217* (2017), 171–179.

[33] BOUZIDI, M., FIRDAOUSS, M., AND LALLEMAND, P. Momentum transfer of a Boltzmann-lattice fluid with boundaries. *Physics of Fluids 13*, 11 (2001), 3452–3459.

[34] BOYD, J., BUICK, J. M., AND GREEN, S. Analysis of the Casson and Carreau-Yasuda non-Newtonian blood models in steady and oscillatory flows using the lattice Boltzmann method. *Physics of Fluids 19*, 9 (2007), 093103.

[35] BRETHERTON, F. P. The motion of rigid particles in a shear flow at low Reynolds number. *Journal of Fluid Mechanics 14*, 02 (1962), 284.

[36] BRUST, M., SCHAEFER, C., DOERR, R., PAN, L., GARCIA, M., ARRATIA, P. E., AND WAGNER, C. Rheology of Human Blood Plasma: Viscoelastic Versus Newtonian Behavior. *Physical Review Letters 110*, 7 (2013), 078305.

[37] BRUUS, H. *Theoretical Microfluidics*. Oxford Master Series in Physics. OUP Oxford, 2008.

[38] BRYNGELSON, S. H., GUÉNIAT, F., AND FREUND, J. B. Irregular dynamics of cellular blood flow in a model microvessel. *Physical Review E 100*, 1 (2019), 012203.

[39] BUSSMANN, J., WOLFE, S. A., AND SIEKMANN, A. F. Arterial-venous network formation during brain vascularization involves hemodynamic regulation of chemokine signaling. *Development 138*, 9 (2011), 1717–1726.

[40] BÄCHER, C., KIHM, A., SCHRACK, L., KAESTNER, L., LASCHKE, M. W., WAGNER, C., AND GEKLE, S. Antimargination of Microparticles and Platelets in the Vicinity of Branching Vessels. *Biophysical Journal 115*, 2 (2018), 411–425.

[41] CALLENS, N., MINETTI, C., COUPIER, G., MADER, M.-A., DUBOIS, F., MISBAH, C., AND PODGORSKI, T. Hydrodynamic lift of vesicles under shear flow in microgravity. *EPL (Europhysics Letters) 83*, 2 (2008), 24002.

[42] CANTAT, I., AND MISBAH, C. Lift Force and Dynamical Unbinding of Adhering Vesicles under Shear Flow. *Physical Review Letters 83*, 4 (1999), 880–883.

[43] CARMELIET, P. Mechanisms of angiogenesis and arteriogenesis. *Nature Medicine 6*, 4 (2000), 389–395.

[44] CARR, R. T., AND WICKHAM, L. L. Influence of vessel diameter on red cell distribution at microvascular bifurcations. *Microvascular Research 41*, 2 (1991), 184–196.

[45] CHANG, A. H., RAFTREY, B. C., D'AMATO, G., SURYA, V. N., PODURI, A., CHEN, H. I., GOLDSTONE, A. B., WOO, J., FULLER, G. G., DUNN, A. R., AND RED-HORSE, K. DACH1 stimulates shear stress-guided endothelial cell migration and coronary artery growth through the CXCL12–CXCR4 signaling axis. *Genes & Development* (2017).

[46] CHAPMAN, S., AND COWLING, T. G. The mathematical theory of non-uniform gases. an account of the kinetic theory of viscosity, thermal conduction and diffusion in gases. *Cambridge: University Press, 1970, 3rd ed.* (1970).

[47] CHEN, M., AND BOYLE, F. J. An Enhanced Spring-Particle Model for Red Blood Cell Structural Mechanics: Application to the Stomatocyte–Discocyte–Echinocyte Transformation. *Journal of Biomechanical Engineering 139*, 12 (2017).

[48] CHEN, Q., JIANG, L., LI, C., HU, D., BU, J.-W., CAI, D., AND DU, J.-L. Haemodynamics-Driven Developmental Pruning of Brain Vasculature in Zebrafish. *PLoS Biol 10*, 8 (2012), e1001374.

[49] CHEN, S., AND DOOLEN, G. D. Lattice Boltzmann Method for Fluid Flows. *Annual Review of Fluid Mechanics 30*, 1 (1998), 329–364.

[50] CHIEN, S. Shear Dependence of Effective Cell Volume as a Determinant of Blood Viscosity. *Science 168*, 3934 (1970), 977–979.

[51] CHIEN, S., KING, R. G., SKALAK, R., USAMI, S., AND COPLEY, A. L. Viscoelastic properties of human blood and red cell suspensions. *Biorheology 12*, 6 (1975), 341–346.

[52] CHIEN, S., SUNG, K. L., SKALAK, R., USAMI, S., AND TÖZEREN, A. Theoretical and experimental studies on viscoelastic properties of erythrocyte membrane. *Biophysical Journal 24*, 2 (1978), 463–487.

[53] CHIEN, S., USAMI, S., DELLENBACK, R. J., GREGERSEN, M. I., NANNINGA, L. B., AND GUEST, M. M. Blood Viscosity: Influence of Erythrocyte Aggregation. *Science 157*, 3790 (1967), 829–831.

[54] CHIEN, W., GOMPPER, G., AND FEDOSOV, D. A. Effect of cytosol viscosity on the flow behavior of red blood cell suspensions in microvessels. *arXiv:2003.09217* (2020).

[55] CHUANG, C.-H., KIKUCHI, K., UENO, H., NUMAYAMA-TSURUTA, K., YAMAGUCHI, T., AND ISHIKAWA, T. Collective spreading of red blood cells flowing in a microchannel. *Journal of Biomechanics 69* (2018), 64–69.

[56] CHWANG, A. T. Hydromechanics of low-Reynolds-number flow. Part 3. Motion of a spheroidal particle in quadratic flows. *Journal of Fluid Mechanics 72*, 1 (1975), 17–34.

[57] CLAVICA, F., HOMSY, A., JEANDUPEUX, L., AND OBRIST, D. Red blood cell phase separation in symmetric and asymmetric microchannel networks: effect of capillary dilation and inflow velocity. *Scientific Reports 6* (2016), srep36763.

[58] COKELET, G. R., AND GOLDSMITH, H. L. Decreased hydrodynamic resistance in the two-phase flow of blood through small vertical tubes at low flow rates. *Circulation Research 68*, 1 (1991), 1–17.

[59] CORDASCO, D., AND BAGCHI, P. Orbital drift of capsules and red blood cells in shear flow. *Physics of Fluids 25*, 9 (2013), 091902.

[60] CORDASCO, D., AND BAGCHI, P. On the shape memory of red blood cells. *Physics of Fluids 29*, 4 (2017), 041901.

[61] CORTI, P., YOUNG, S., CHEN, C.-Y., PATRICK, M. J., ROCHON, E. R., PEKKAN, K., AND ROMAN, B. L. Interaction between alk1 and blood flow in the development of arteriovenous malformations. *Development 138*, 8 (2011), 1573–1582.

[62] COULTAS, L., CHAWENGSAKSOPHAK, K., AND ROSSANT, J. Endothelial cells and VEGF in vascular development. *Nature 438*, 7070 (2005), 937.

[63] COUPIER, G., FARUTIN, A., MINETTI, C., PODGORSKI, T., AND MISBAH, C. Shape Diagram of Vesicles in Poiseuille Flow. *Physical Review Letters 108*, 17 (2012).

[64] COUPIER, G., KAOUI, B., PODGORSKI, T., AND MISBAH, C. Noninertial lateral migration of vesicles in bounded Poiseuille flow. *Physics of Fluids 20*, 11 (2008), 111702.

[65] CZAJA, B., GUTIERREZ, M., ZÁVODSZKY, G., KANTER, D. D., HOEKSTRA, A., AND ENIOLA-ADEFESO, O. The influence of red blood cell deformability on hematocrit profiles and platelet margination. *PLOS Computational Biology 16*, 3 (2020), e1007716.

[66] DANKER, G., AND MISBAH, C. Rheology of a Dilute Suspension of Vesicles. *Physical Review Letters 98*, 8 (2007).

[67] DANKER, G., VLAHOVSKA, P. M., AND MISBAH, C. Vesicles in Poiseuille Flow. *Physical Review Letters 102*, 14 (2009), 148102.

[68] DE HAAN, M., ZAVODSZKY, G., AZIZI, V., AND HOEKSTRA, A. G. Numerical Investigation of the Effects of Red Blood Cell Cytoplasmic Viscosity Contrasts on Single Cell and Bulk Transport Behaviour. *Applied Sciences 8*, 9 (2018), 1616.

[69] DESCHAMPS, J., KANTSLER, V., AND STEINBERG, V. Phase Diagram of Single Vesicle Dynamical States in Shear Flow. *Physical Review Letters 102*, 11 (2009).

[70] DIMITRAKOPOULOS, P. Interfacial dynamics in Stokes flow via a three-dimensional fully-implicit interfacial spectral boundary element algorithm. *Journal of Computational Physics 225*, 1 (2007), 408–426.

[71] DODDABALLAPUR, A., MICHALIK, K. M., MANAVSKI, Y., LUCAS, T., HOUTKOOPER, R. H., YOU, X., CHEN, W., ZEIHER, A. M., POTENTE, M., DIMMELER, S., AND BOON, R. A. Laminar Shear Stress Inhibits Endothelial Cell Metabolism via KLF2-Mediated Repression of PFKFB3Significance. *Arteriosclerosis, Thrombosis, and Vascular Biology 35*, 1 (2015), 137–145.

[72] DODDI, S. K., AND BAGCHI, P. Lateral migration of a capsule in a plane Poiseuille flow in a channel. *International Journal of Multiphase Flow 34*, 10 (2008), 966–986.

[73] DODDI, S. K., AND BAGCHI, P. Three-dimensional computational modeling of multiple deformable cells flowing in microvessels. *Physical Review E 79*, 4 (2009), 046318.

[74] DOYEUX, V., PODGORSKI, T., PEPONAS, S., ISMAIL, M., AND COUPIER, G. Spheres in the vicinity of a bifurcation: elucidating the Zweifach–Fung effect. *Journal of Fluid Mechanics 674* (2011), 359–388.

[75] DUPIN, M. M., HALLIDAY, I., CARE, C. M., ALBOUL, L., AND MUNN, L. L. Modeling the flow of dense suspensions of deformable particles in three dimensions. *Physical Review E 75*, 6 (2007), 066707.

[76] DUPIRE, J., SOCOL, M., AND VIALLAT, A. Full dynamics of a red blood cell in shear flow. *Proceedings of the National Academy of Sciences 109*, 51 (2012), 20808–20813.

[77] DUVERNOY, H. M., DELON, S., AND VANNSON, J. L. Cortical blood vessels of the human brain. *Brain Research Bulletin 7*, 5 (1981), 519–579.

[78] ENDEN, G., AND POPEL, A. S. A Numerical Study of Plasma Skimming in Small Vascular Bifurcations. *Journal of Biomechanical Engineering 116*, 1 (1994), 79–88.

[79] ESPAÑOL, P., AND REVENGA, M. Smoothed dissipative particle dynamics. *Physical Review E 67*, 2 (2003), 026705.

[80] FANG, J. S., COON, B. G., GILLIS, N., CHEN, Z., QIU, J., CHITTENDEN, T. W., BURT, J. M., SCHWARTZ, M. A., AND HIRSCHI, K. K. Shear-induced Notch-Cx37-p27 axis arrests endothelial cell cycle to enable arterial specification. *Nature Communications 8*, 1 (2017), 2149.

[81] FARUTIN, A., AND MISBAH, C. Analytical and Numerical Study of Three Main Migration Laws for Vesicles Under Flow. *Physical Review Letters 110*, 10 (2013), 108104.

[82] FEDOSOV, D. A., CASWELL, B., AND KARNIADAKIS, G. E. A Multiscale Red Blood Cell Model with Accurate Mechanics, Rheology, and Dynamics. *Biophysical Journal 98*, 10 (2010), 2215–2225.

[83] FEDOSOV, D. A., CASWELL, B., POPEL, A. S., AND KARNIADAKIS, G. E. Blood Flow and Cell-Free Layer in Microvessels. *Microcirculation 17*, 8 (2010), 615–628.

[84] FEDOSOV, D. A., LEI, H., CASWELL, B., SURESH, S., AND KARNIADAKIS, G. E. Multiscale Modeling of Red Blood Cell Mechanics and Blood Flow in Malaria. *PLOS Computational Biology 7*, 12 (2011), e1002270.

[85] FEDOSOV, D. A., NOGUCHI, H., AND GOMPPER, G. Multiscale modeling of blood flow: from single cells to blood rheology. *Biomechanics and Modeling in Mechanobiology 13*, 2 (2013), 239–258.

[86] FEDOSOV, D. A., PELTOMÄKI, M., AND GOMPPER, G. Deformation and dynamics of red blood cells in flow through cylindrical microchannels. *Soft Matter 10*, 24 (2014), 4258–4267.

[87] FELDSCHUH J, AND ENSON Y. Prediction of the normal blood volume. Relation of blood volume to body habitus. *Circulation 56*, 4 (1977), 605–612.

[88] FENTON, B. M., CARR, R. T., AND COKELET, G. R. Nonuniform red cell distribution in 20 to 100 μm bifurcations. *Microvascular Research 29*, 1 (1985), 103–126.

[89] FISCHER, T., HAEST, C., STÖHR-LIESEN, M., SCHMID-SCHÖNBEIN, H., AND SKALAK, R. The stress-free shape of the red blood cell membrane. *Biophysical Journal 34*, 3 (1981), 409–422.

[90] FISCHER, T. M. Shape Memory of Human Red Blood Cells. *Biophysical Journal 86*, 5 (2004), 3304–3313.

[91] FISCHER, T. M., STOHR-LISSEN, M., AND SCHMID-SCHONBEIN, H. The red cell as a fluid droplet: tank tread-like motion of the human erythrocyte membrane in shear flow. *Science 202*, 4370 (1978), 894–896.

[92] FRANCO, C. A., BLANC, J., PARLAKIAN, A., BLANCO, R., ASPALTER, I. M., KAZAKOVA, N., DIGUET, N., MYLONAS, E., GAO-LI, J., VAAHTOKARI, A., PENARD-LACRONIQUE, V., FRUTTIGER, M., ROSEWELL, I., MERICSKAY, M., GERHARDT, H., AND LI, Z. SRF selectively controls tip cell invasive behavior in angiogenesis. *Development 140*, 11 (2013), 2321–2333.

[93] FRANCO, C. A., JONES, M. L., BERNABEU, M. O., GEUDENS, I., MATHIVET, T., ROSA, A., LOPES, F. M., LIMA, A. P., RAGAB, A., COLLINS, R. T., PHNG, L.-K., COVENEY, P. V., AND GERHARDT, H. Dynamic Endothelial Cell Rearrangements Drive Developmental Vessel Regression. *PLoS Biol 13*, 4 (2015), e1002125.

[94] FRANCO, C. A., JONES, M. L., BERNABEU, M. O., VION, A.-C., BARBACENA, P., FAN, J., MATHIVET, T., FONSECA, C. G., RAGAB, A., YAMAGUCHI, T. P., COVENEY, P. V., LANG, R. A., AND GERHARDT, H. Non-canonical Wnt signalling modulates the endothelial shear stress flow sensor in vascular remodelling. *eLife 5* (2016), e07727.

[95] FREUND, J. Numerical Simulation of Flowing Blood Cells. *Annual Review of Fluid Mechanics 46*, 1 (2014), 67–95.

[96] FREUND, J. B. Leukocyte margination in a model microvessel. *Physics of Fluids 19*, 2 (2007), 023301.

[97] FREUND, J. B. The flow of red blood cells through a narrow spleen-like slit. *Physics of Fluids 25*, 11 (2013), 110807.

[98] FREUND, J. B. A Critical Assessment of Resolution for Red-Blood-Cell Simulation. *Procedia IUTAM 16* (2015), 99–105.

[99] FREUND, J. B., AND ORESCANIN, M. M. Cellular flow in a small blood vessel. *Journal of Fluid Mechanics 671* (2011), 466–490.

[100] FREUND, J. B., AND VERMOT, J. The Wall-stress Footprint of Blood Cells Flowing in Microvessels. *Biophysical Journal 106*, 3 (2014), 752–762.

[101] FRISCH, U., HASSLACHER, B., AND POMEAU, Y. Lattice-Gas Automata for the Navier-Stokes Equation. *Physical Review Letters 56*, 14 (1986), 1505–1508.

[102] FUNG, Y.-C. Stochastic flow in capillary blood vessels. *Microvascular Research 5*, 1 (1973), 34–48.

[103] FÅHRAEUS, R. The Suspension Stability of the Blood. *Physiological Reviews 9*, 2 (1929), 241–274.

[104] FÅHRÆUS, R., AND LINDQVIST, T. The viscosity of the blood in narrow capillary tubes. *American Journal of Physiology-Legacy Content 96*, 3 (1931), 562–568.

[105] GAEHTGENS, P. Flow of blood through narrow capillaries: Rheological mechanisms determining capillary hematocrit and apparent viscosity. *Biorheology 17*, 1-2 (1980), 183–189.

[106] GEISLINGER, T. M., AND FRANKE, T. Hydrodynamic lift of vesicles and red blood cells in flow — from Fåhræus & Lindqvist to microfluidic cell sorting. *Advances in Colloid and Interface Science 208* (2014), 161–176.

[107] GHIGLIOTTI, G., RAHIMIAN, A., BIROS, G., AND MISBAH, C. Vesicle Migration and Spatial Organization Driven by Flow Line Curvature. *Physical Review Letters 106*, 2 (2011).

[108] GINGOLD, R. A., AND MONAGHAN, J. J. Smoothed particle hydrodynamics: theory and application to non-spherical stars. *Monthly Notices of the Royal Astronomical Society 181*, 3 (1977), 375–389.

[109] GOLDSMITH, H. L., COKELET, G. R., AND GAEHTGENS, P. Robin Fahraeus: evolution of his concepts in cardiovascular physiology. *American Journal of Physiology-Heart and Circulatory Physiology 257*, 3 (1989), H1005–H1015.

[110] GOLDSMITH, H. L., MARLOW, J., AND MACINTOSH, F. C. Flow behaviour of erythrocytes - I. Rotation and deformation in dilute suspensions. *Proceedings of the Royal Society of London. Series B. Biological Sciences 182*, 1068 (1972), 351–384.

[111] GOLDSMITH, H. L., AND MASON, S. G. Axial Migration of Particles in Poiseuille Flow. *Nature 190*, 4781 (1961), 1095–1096.

[112] GOLDSMITH, H. L., AND MASON, S. G. The flow of suspensions through tubes. I. Single spheres, rods, and discs. *Journal of Colloid Science 17*, 5 (1962), 448–476.

[113] GOULD, I. G., AND LINNINGER, A. A. Hematocrit Distribution and Tissue Oxygenation in Large Microcirculatory Networks. *Microcirculation 22*, 1 (2015), 1–18.

[114] GRANDCHAMP, X., COUPIER, G., SRIVASTAV, A., MINETTI, C., AND PODGORSKI, T. Lift and Down-Gradient Shear-Induced Diffusion in Red Blood Cell Suspensions. *Physical Review Letters 110*, 10 (2013).

[115] GROSS, M., KRÜGER, T., AND VARNIK, F. Rheology of dense suspensions of elastic capsules: normal stresses, yield stress, jamming and confinement effects. *Soft Matter 10*, 24 (2014), 4360–4372.

[116] GUCKENBERGER, A., AND GEKLE, S. Theory and algorithms to compute Helfrich bending forces: a review. *Journal of Physics: Condensed Matter 29*, 20 (2017), 203001.

[117] GUCKENBERGER, A., KIHM, A., JOHN, T., WAGNER, C., AND GEKLE, S. Numerical-experimental observation of shape bistability of red blood cells flowing in a microchannel. *Soft Matter* (2018).

[118] GUEVARA-TORRES, A., JOSEPH, A., AND SCHALLEK, J. B. Label free measurement of retinal blood cell flux, velocity, hematocrit and capillary width in the living mouse eye. *Biomedical Optics Express 7*, 10 (2016), 4228.

[119] GUGLIETTA, F., BEHR, M., BIFERALE, L., FALCUCCI, G., AND SBRAGAGLIA, M. On the effects of membrane viscosity on transient red blood cell dynamics. *arXiv:2004.04109* (2020).

[120] GUIBERT, R., FONTA, C., AND PLOURABOUÉ, F. A New Approach to Model Confined Suspensions Flows in Complex Networks: Application to Blood Flow. *Transport in Porous Media 83*, 1 (2010), 171–194.

[121] GUIDO, S., AND TOMAIUOLO, G. Microconfined flow behavior of red blood cells in vitro. *Comptes Rendus Physique 10*, 8 (2009), 751–763.

[122] GUO, Z., AND SHU, C. *Lattice Boltzmann Method and Its Applications in Engineering*, vol. 3 of *Advances in Computational Fluid Dynamics*. WORLD SCIENTIFIC, 2013.

[123] GUO, Z., ZHENG, C., AND SHI, B. Discrete lattice effects on the forcing term in the lattice Boltzmann method. *Physical Review E 65*, 4 (2002), 046308.

[124] HAPPEL, J., AND BRENNER, H. *Low Reynolds number hydrodynamics : with special applications to particulate media*. Prentice-Hall International series in physical and chemical engineering sciences. Prentice-Hall, Englewood Cliffs, 1965.

[125] HARDY, J., POMEAU, Y., AND DE PAZZIS, O. Time Evolution of a Two-Dimensional Classical Lattice System. *Physical Review Letters 31*, 5 (1973), 276–279.

[126] HARIPRASAD, D. S., AND SECOMB, T. W. Prediction of noninertial focusing of red blood cells in Poiseuille flow. *Physical Review E 92*, 3 (2015).

[127] HENRÍQUEZ RIVERA, R. G., ZHANG, X., AND GRAHAM, M. D. Mechanistic theory of margination and flow-induced segregation in confined multicomponent suspensions: Simple shear and Poiseuille flows. *Physical Review Fluids 1*, 6 (2016).

[128] HIGUERA, F. J., AND JIMÉNEZ, J. Boltzmann Approach to Lattice Gas Simulations. *EPL (Europhysics Letters) 9*, 7 (1989), 663–668.

[129] HO, B. P., AND LEAL, L. G. Inertial migration of rigid spheres in two-dimensional unidirectional flows. *Journal of Fluid Mechanics 65*, 2 (1974), 365–400.

[130] HOCHMUTH, R. M., AND WAUGH, R. E. Erythrocyte Membrane Elasticity and Viscosity. *Annual Review of Physiology 49*, 1 (1987), 209–219.

[131] HOGAN, B., SHEN, Z., ZHANG, H., MISBAH, C., AND BARAKAT, A. I. Shear stress in the microvasculature: influence of red blood cell morphology and endothelial wall undulation. *Biomechanics and Modeling in Mechanobiology* (2019).

[132] HOGAN, B. M., VERKADE, H., LIESCHKE, G. J., AND HEATH, J. K. Manipulation of Gene Expression During Zebrafish Embryonic Development Using Transient Approaches. In *Wnt Signaling*, E. Vincan, Ed., Methods in Molecular Biology. Humana Press, Totowa, NJ, 2009, pp. 273–300.

[133] HOOGERBRUGGE, P. J., AND KOELMAN, J. M. V. A. Simulating Microscopic Hydrodynamic Phenomena with Dissipative Particle Dynamics. *EPL (Europhysics Letters) 19*, 3 (1992), 155–160.

[134] HOSKINS, P. R. The Microcirculation. In *Cardiovascular Biomechanics*, P. R. Hoskins, P. V. Lawford, and B. J. Doyle, Eds. Springer International Publishing, Cham, 2017, pp. 143–162.

[135] HOSKINS, P. R., AND HARDMAN, D. Blood and Blood Flow. In *Cardiovascular Biomechanics*, P. R. Hoskins, P. V. Lawford, and B. J. Doyle, Eds. Springer International Publishing, Cham, 2017, pp. 37–63.

[136] HYAKUTAKE, T., AND NAGAI, S. Numerical simulation of red blood cell distributions in three-dimensional microvascular bifurcations. *Microvascular Research 97* (2015), 115–123.

[137] IMAI, Y., OMORI, T., SHIMOGONYA, Y., YAMAGUCHI, T., AND ISHIKAWA, T. Numerical methods for simulating blood flow at macro, micro, and multi scales. *Journal of Biomechanics 49*, 11 (2016), 2221–2228.

[138] ISOGAI, S., HORIGUCHI, M., AND WEINSTEIN, B. M. The Vascular Anatomy of the Developing Zebrafish: An Atlas of Embryonic and Early Larval Development. *Developmental Biology 230*, 2 (2001), 278–301.

[139] ISS, C., MIDOU, D., MOREAU, A., HELD, D., CHARRIER, A., MENDEZ, S., VIALLAT, A., AND HELFER, E. Self-organization of red blood cell suspensions under confined 2D flows. *Soft Matter 15*, 14 (2019), 2971–2980.

[140] JAFARI, A., ZAMANKHAN, P., MOUSAVI, S. M., AND KOLARI, P. Numerical investigation of blood flow. Part II: In capillaries. *Communications in Nonlinear Science and Numerical Simulation 14*, 4 (2009), 1396–1402.

[141] JEFFERY, G. B. The Motion of Ellipsoidal Particles Immersed in a Viscous Fluid. *Proceedings of the Royal Society of London A: Mathematical, Physical and Engineering Sciences 102*, 715 (1922), 161–179.

[142] JOSEPH, A., GUEVARA-TORRES, A., AND SCHALLEK, J. Imaging single-cell blood flow in the smallest to largest vessels in the living retina. *eLife 8* (2019), e45077.

[143] JU, M., YE, S. S., NAMGUNG, B., CHO, S., LOW, H. T., LEO, H. L., AND KIM, S. A review of numerical methods for red blood cell flow simulation. *Computer Methods in Biomechanics and Biomedical Engineering 18*, 2 (2015), 130–140.

[144] KANTSLER, V., SEGRE, E., AND STEINBERG, V. Dynamics of interacting vesicles and rheology of vesicle suspension in shear flow. *EPL (Europhysics Letters) 82*, 5 (2008), 58005.

[145] KANTSLER, V., AND STEINBERG, V. Orientation and Dynamics of a Vesicle in Tank-Treading Motion in Shear Flow. *Physical Review Letters 95*, 25 (2005), 258101.

[146] KANTSLER, V., AND STEINBERG, V. Transition to Tumbling and Two Regimes of Tumbling Motion of a Vesicle in Shear Flow. *Physical Review Letters 96*, 3 (2006).

[147] KAOUI, B., BIROS, G., AND MISBAH, C. Why Do Red Blood Cells Have Asymmetric Shapes Even in a Symmetric Flow? *Physical Review Letters 103*, 18 (2009), 188101.

[148] KAOUI, B., HARTING, J., AND MISBAH, C. Two-dimensional vesicle dynamics under shear flow: Effect of confinement. *Physical Review E 83*, 6 (2011), 066319.

[149] KAOUI, B., RISTOW, G. H., CANTAT, I., MISBAH, C., AND ZIMMERMANN, W. Lateral migration of a two-dimensional vesicle in unbounded Poiseuille flow. *Physical Review E 77*, 2 (2008), 021903.

[150] KATANOV, D., GOMPPER, G., AND FEDOSOV, D. A. Microvascular blood flow resistance: Role of red blood cell migration and dispersion. *Microvascular Research 99* (2015), 57–66.

[151] KIM, S., KARRILA, S. J., AND BRENNER, H. *Microhydrodynamics: principles and selected applications*. Newnes, Oxford, 1991.

[152] KIM, S., KONG, R. L., POPEL, A. S., INTAGLIETTA, M., AND JOHNSON, P. C. Temporal and spatial variations of cell-free layer width in arterioles. *American Journal of Physiology - Heart and Circulatory Physiology 293*, 3 (2007), H1526–H1535.

[153] KIM, S., ONG, P. K., YALCIN, O., INTAGLIETTA, M., AND JOHNSON, P. C. The cell-free layer in microvascular blood flow. *Biorheology 46*, 3 (2009), 181–189.

[154] KIMMEL, C. B., BALLARD, W. W., KIMMEL, S. R., ULLMANN, B., AND SCHILLING, T. F. Stages of embryonic development of the zebrafish. *Developmental Dynamics 203*, 3 (1995), 253–310.

[155] KLITZMAN, B., AND JOHNSON, P. C. Capillary network geometry and red cell distribution in hamster cremaster muscle. *American Journal of Physiology-Heart and Circulatory Physiology 242*, 2 (1982), H211–H219.

[156] KOCHHAN, E., LENARD, A., ELLERTSDOTTIR, E., HERWIG, L., AFFOLTER, M., BELTING, H.-G., AND SIEKMANN, A. F. Blood Flow Changes Coincide with Cellular Rearrangements during Blood Vessel Pruning in Zebrafish Embryos. *PLOS ONE 8*, 10 (2013), e75060.

[157] KOSHIZUKA, S., AND OKA, Y. Moving-Particle Semi-Implicit Method for Fragmentation of Incompressible Fluid. *Nuclear Science and Engineering 123*, 3 (1996), 421–434.

[158] KOTSALOS, C., LATT, J., AND CHOPARD, B. Bridging the computational gap between mesoscopic and continuum modeling of red blood cells for fully resolved blood flow. *Journal of Computational Physics 398* (2019), 108905.

[159] KRAUS, M., WINTZ, W., SEIFERT, U., AND LIPOWSKY, R. Fluid Vesicles in Shear Flow. *Physical Review Letters 77*, 17 (1996), 3685–3688.

[160] KROGH, A. Studies on the physiology of capillaries. *The Journal of Physiology 55*, 5-6 (1921), 412–422.

[161] KRÜGER, T. *Computer Simulation Study of Collective Phenomena in Dense Suspensions of Red Blood Cells under Shear*. Vieweg+Teubner Verlag, 2012.

[162] KRÜGER, T., GROSS, M., RAABE, D., AND VARNIK, F. Crossover from tumbling to tank-treading-like motion in dense simulated suspensions of red blood cells. *Soft Matter 9*, 37 (2013), 9008–9015.

[163] KRÜGER, T., KAOUI, B., AND HARTING, J. Interplay of inertia and deformability on rheological properties of a suspension of capsules. *Journal of Fluid Mechanics 751* (2014), 725–745.

[164] KRÜGER, T., KUSUMAATMAJA, H., KUZMIN, A., SHARDT, O., SILVA, G., AND VIGGEN, E. M. *The Lattice Boltzmann Method: Principles and Practice*. Graduate Texts in Physics. Springer International Publishing, 2017.

[165] KRÜGER, T., VARNIK, F., AND RAABE, D. Efficient and accurate simulations of deformable particles immersed in a fluid using a combined immersed boundary lattice Boltzmann finite element method. *Computers & Mathematics with Applications 61*, 12 (2011), 3485–3505.

[166] KUMAR, A., AND GRAHAM, M. D. Mechanism of Margination in Confined Flows of Blood and Other Multicomponent Suspensions. *Physical Review Letters 109*, 10 (2012), 108102.

[167] LADD, A. J. C. Numerical simulations of particulate suspensions via a discretized Boltzmann equation. Part 1. Theoretical foundation. *Journal of Fluid Mechanics 271* (1994), 285–309.

[168] LAN, H., AND KHISMATULLIN, D. B. A numerical study of the lateral migration and deformation of drops and leukocytes in a rectangular microchannel. *International Journal of Multiphase Flow 47* (2012), 73–84.

[169] LANOTTE, L., MAUER, J., MENDEZ, S., FEDOSOV, D. A., FROMENTAL, J.-M., CLAVERIA, V., NICOUD, F., GOMPPER, G., AND ABKARIAN, M. Red cells' dynamic morphologies govern blood shear thinning under microcirculatory flow conditions. *Proceedings of the National Academy of Sciences* (2016), 201608074.

[170] LATT, J., MALASPINAS, O., KONTAXAKIS, D., PARMIGIANI, A., LAGRAVA, D., BROGI, F., BELGACEM, M. B., THORIMBERT, Y., LECLAIRE, S., LI, S., MARSON, F., LEMUS, J., KOTSALOS, C., CONRADIN, R., COREIXAS, C., PETKANTCHIN, R., RAYNAUD, F., BENY, J., AND CHOPARD, B. Palabos: Parallel Lattice Boltzmann Solver. *Computers & Mathematics with Applications* (2020), https://doi.org/10.1016/j.camwa.2020.03.022.

[171] LEE, T.-R., YOO, S. S., AND YANG, J. Generalized plasma skimming model for cells and drug carriers in the microvasculature. *Biomechanics and Modeling in Mechanobiology* (2016), 1–11.

[172] LEI, H., FEDOSOV, D. A., CASWELL, B., AND KARNIADAKIS, G. E. Blood flow in small tubes: quantifying the transition to the non-continuum regime. *Journal of Fluid Mechanics 722* (2013), 214–239.

[173] LEY, K. Chapter 9 - The Microcirculation in Inflammation. In *Microcirculation (Second Edition)*, R. F. Tuma, W. N. Durán, and K. Ley, Eds. Academic Press, San Diego, 2008, pp. 387–448.

[174] LI, G., YE, T., AND LI, X. Parallel modeling of cell suspension flow in complex micro-networks with inflow/outflow boundary conditions. *Journal of Computational Physics 401* (2020), 109031.

[175] LI, G., YE, T., WANG, S., LI, X., AND UI HAQ, R. Numerical design of a highly efficient microfluidic chip for blood plasma separation. *Physics of Fluids 32*, 3 (2020), 031903.

[176] LI, H., LU, L., LI, X., BUFFET, P. A., DAO, M., KARNIADAKIS, G. E., AND SURESH, S. Mechanics of diseased red blood cells in human spleen and consequences for hereditary blood disorders. *Proceedings of the National Academy of Sciences 115*, 38 (2018), 9574–9579.

[177] LI, H., AND LYKOTRAFITIS, G. Erythrocyte Membrane Model with Explicit Description of the Lipid Bilayer and the Spectrin Network. *Biophysical Journal 107*, 3 (2014), 642–653.

[178] LI, J., LYKOTRAFITIS, G., DAO, M., AND SURESH, S. Cytoskeletal dynamics of human erythrocyte. *Proceedings of the National Academy of Sciences 104*, 12 (2007), 4937–4942.

[179] LI, X., POPEL, A. S., AND KARNIADAKIS, G. E. Blood–plasma separation in Y-shaped bifurcating microfluidic channels: a dissipative particle dynamics simulation study. *Physical Biology 9*, 2 (2012), 026010.

[180] LI, Y.-S. J., HAGA, J. H., AND CHIEN, S. Molecular basis of the effects of shear stress on vascular endothelial cells. *Journal of Biomechanics 38*, 10 (2005), 1949–1971.

[181] LIM, G. H. W., WORTIS, M., AND MUKHOPADHYAY, R. Red Blood Cell Shapes and Shape Transformations: Newtonian Mechanics of a Composite Membrane: Sections 2.1–2.4. In *Soft Matter*. John Wiley & Sons, Ltd, 2009, pp. 83–139.

[182] LIMA, R., ISHIKAWA, T., IMAI, Y., TAKEDA, M., WADA, S., AND YAMAGUCHI, T. Radial dispersion of red blood cells in blood flowing through glass capillaries: The role of hematocrit and geometry. *Journal of Biomechanics 41*, 10 (2008), 2188–2196.

[183] LIPOWSKY, H. H. Microvascular Rheology and Hemodynamics. *Microcirculation 12*, 1 (2005), 5–15.

[184] LIU, Y., AND LIU, W. K. Rheology of red blood cell aggregation by computer simulation. *Journal of Computational Physics 220*, 1 (2006), 139–154.

[185] LIU, Y., ZHANG, L., WANG, X., AND LIU, W. K. Coupling of Navier–Stokes equations with protein molecular dynamics and its application to hemodynamics. *International Journal for Numerical Methods in Fluids 46*, 12 (2004), 1237–1252.

[186] LORZ, B., SIMSON, R., NARDI, J., AND SACKMANN, E. Weakly adhering vesicles in shear flow: Tanktreading and anomalous lift force. *EPL (Europhysics Letters) 51*, 4 (2000), 468.

[187] LOSSERAND, S., COUPIER, G., AND PODGORSKI, T. Migration velocity of red blood cells in microchannels. *Microvascular Research 124* (2019), 30–36.

[188] LU, H., AND PENG, Z. Boundary integral simulations of a red blood cell squeezing through a submicron slit under prescribed inlet and outlet pressures. *Physics of Fluids 31*, 3 (2019), 031902.

[189] LUCITTI, J. L., JONES, E. A. V., HUANG, C., CHEN, J., FRASER, S. E., AND DICKINSON, M. E. Vascular remodeling of the mouse yolk sac requires hemodynamic force. *Development 134*, 18 (2007), 3317–3326.

[190] LUCY, L. B. A numerical approach to the testing of the fission hypothesis. *The Astronomical Journal 82* (1977), 1013–1024.

[191] LYKOV, K., LI, X., LEI, H., PIVKIN, I. V., AND KARNIADAKIS, G. E. Inflow/Outflow Boundary Conditions for Particle-Based Blood Flow Simulations: Application to Arterial Bifurcations and Trees. *PLoS Comput Biol 11*, 8 (2015), e1004410.

[192] MACK, J. J., MOSQUEIRO, T. S., ARCHER, B. J., JONES, W. M., SUNSHINE, H., FAAS, G. C., BRIOT, A., ARAGÓN, R. L., SU, T., ROMAY, M. C., MCDONALD, A. I., KUO, C.-H., LIZAMA, C. O., LANE, T. F., ZOVEIN, A. C., FANG, Y., TARLING, E. J., DE AGUIAR VALLIM, T. Q., NAVAB, M., FOGELMAN, A. M., BOUCHARD, L. S., AND IRUELA-ARISPE, M. L. NOTCH1 is a mechanosensor in adult arteries. *Nature Communications 8*, 1 (2017), 1620.

[193] MAGNAUDET, J., TAKAGI, S., AND LEGENDRE, D. Drag, deformation and lateral migration of a buoyant drop moving near a wall. *Journal of Fluid Mechanics 476* (2003), 115–157.

[194] MALEVANETS, A., AND KAPRAL, R. Mesoscopic model for solvent dynamics. *The Journal of Chemical Physics 110*, 17 (1999), 8605–8613.

[195] MANTEGAZZA, A., CLAVICA, F., AND OBRIST, D. In vitro investigations of red blood cell phase separation in a complex microchannel network. *Biomicrofluidics 14*, 1 (2020), 014101.

[196] MARTEL, J. M., AND TONER, M. Inertial Focusing in Microfluidics. *Annual Review of Biomedical Engineering 16*, 1 (2014), 371–396.

[197] MAUER, J., MENDEZ, S., LANOTTE, L., NICOUD, F., ABKARIAN, M., GOMPPER, G., AND FEDOSOV, D. A. Flow-Induced Transitions of Red Blood Cell Shapes under Shear. *Physical Review Letters 121*, 11 (2018).

[198] MAZZEO, M. D., AND COVENEY, P. V. HemeLB: A high performance parallel lattice-Boltzmann code for large scale fluid flow in complex geometries. *Computer Physics Communications 178*, 12 (2008), 894–914.

[199] MCHEDLISHVILI, G., AND VARAZASHVILI, M. Flow conditions of red cells and plasma in microvascular bifurcations. *Biorheology 19*, 5 (1982), 613–620.

[200] MCNAMARA, G. R., AND ZANETTI, G. Use of the Boltzmann Equation to Simulate Lattice-Gas Automata. *Physical Review Letters 61*, 20 (1988), 2332–2335.

[201] MELCHIONNA, S. A Model for Red Blood Cells in Simulations of Large-scale Blood Flows. *Macromolecular Theory and Simulations 20*, 7 (2011), 548–561.

[202] MENDEZ, S., AND ABKARIAN, M. In-plane elasticity controls the full dynamics of red blood cells in shear flow. *Physical Review Fluids 3*, 10 (2018), 101101.

[203] MERRILL, E. W., GILLILAND, E. R., LEE, T. S., AND SALZMAN, E. W. Blood Rheology: Effect of Fibrinogen Deduced by Addition. *Circulation Research 18*, 4 (1966), 437–446.

[204] MESSLINGER, S., SCHMIDT, B., NOGUCHI, H., AND GOMPPER, G. Dynamical regimes and hydrodynamic lift of viscous vesicles under shear. *Physical Review E 80*, 1 (2009).

[205] MISBAH, C. Vacillating Breathing and Tumbling of Vesicles under Shear Flow. *Physical Review Letters 96*, 2 (2006), 028104.

[206] MOHANDAS, N., AND GALLAGHER, P. G. Red cell membrane: past, present, and future. *Blood 112*, 10 (2008), 3939–3948.

[207] MÜLLER, K., FEDOSOV, D. A., AND GOMPPER, G. Understanding particle margination in blood flow – A step toward optimized drug delivery systems. *Medical Engineering & Physics 38*, 1 (2016), 2–10.

[208] NAMGUNG, B., AND KIM, S. Effect of uneven red cell influx on formation of cell-free layer in small venules. *Microvascular Research 92* (2014), 19–24.

[209] NAMGUNG, B., ONG, P. K., JOHNSON, P. C., AND KIM, S. Effect of Cell-Free Layer Variation on Arteriolar Wall Shear Stress. *Annals of Biomedical Engineering 39*, 1 (2010), 359–366.

[210] NEAL, A., NORNES, S., PAYNE, S., WALLACE, M. D., FRITZSCHE, M., LOUPHRASITTHIPHOL, P., WILKINSON, R. N., CHOULIARAS, K. M., LIU, K., PLANT, K., SHOLAPURKAR, R., RATNAYAKA, I., HERZOG, W., BOND, G., CHICO, T., BOU-GHARIOS, G., AND VAL, S. D. Venous identity requires BMP signalling through ALK3. *Nature Communications 10*, 1 (2019), 453.

[211] NG, Y. C., NAMGUNG, B., TIEN, S. L., LEO, H. L., AND KIM, S. Symmetry recovery of cell-free layer after bifurcations of small arterioles in reduced flow conditions: effect of RBC aggregation. *American Journal of Physiology - Heart and Circulatory Physiology 311*, 2 (2016), H487–H497.

[212] NIX, S., IMAI, Y., AND ISHIKAWA, T. Lateral migration of a capsule in a parabolic flow. *Journal of Biomechanics 49*, 11 (2016), 2249–2254.

[213] NOBLE, F. L., MOYON, D., PARDANAUD, L., YUAN, L., DJONOV, V., MATTHIJSEN, R., BRÉANT, C., FLEURY, V., AND EICHMANN, A. Flow regulates arterial-venous differentiation in the chick embryo yolk sac. *Development 131*, 2 (2004), 361–375.

[214] NOGUCHI, H., AND GOMPPER, G. Fluid Vesicles with Viscous Membranes in Shear Flow. *Physical Review Letters 93*, 25 (2004), 258102.

[215] NOGUCHI, H., AND GOMPPER, G. Shape transitions of fluid vesicles and red blood cells in capillary flows. *Proceedings of the National Academy of Sciences of the United States of America 102*, 40 (2005), 14159–14164.

[216] NOGUCHI, H., AND GOMPPER, G. Swinging and Tumbling of Fluid Vesicles in Shear Flow. *Physical Review Letters 98*, 12 (2007).

[217] OBRIST, D., WEBER, B., BUCK, A., AND JENNY, P. Red blood cell distribution in simplified capillary networks. *Philosophical Transactions of the Royal Society A: Mathematical, Physical and Engineering Sciences 368*, 1921 (2010), 2897–2918.

[218] O'CONNOR, J., DAY, P., MANDAL, P., AND REVELL, A. Computational fluid dynamics in the microcirculation and microfluidics: what role can the lattice Boltzmann method play? *Integrative Biology 8*, 5 (2016), 589–602.

[219] OLLA, P. The lift on a tank-treading ellipsoidal cell in a bounded shear flow. *Journal de Physique II 7*, 10 (1997), 1533–1540.

[220] OLLA, P. The role of tank-treading motions in the transverse migration of a spheroidal vesicle in a shear flow. *Journal of Physics A: Mathematical and General 30*, 1 (1997), 317.

[221] OLLA, P. Forces and torques on non-spherical particles in viscous shear flows. *arXiv:chao-dyn/9808022* (1998).

[222] OLLA, P. Simplified Model for Red Cell Dynamics in Small Blood Vessels. *Physical Review Letters 82*, 2 (1999), 453–456.

[223] OLLA, P. The behavior of closed inextensible membranes in linear and quadratic shear flows. *Physica A: Statistical Mechanics and its Applications 278*, 1 (2000), 87–106.

[224] OMORI, T., IMAI, Y., YAMAGUCHI, T., AND ISHIKAWA, T. Reorientation of a Nonspherical Capsule in Creeping Shear Flow. *Physical Review Letters 108*, 13 (2012), 138102.

[225] ONG, P. K., JAIN, S., AND KIM, S. Spatio-temporal variations in cell-free layer formation near bifurcations of small arterioles. *Microvascular Research 83*, 2 (2012), 118–125.

[226] OULAID, O., AND ZHANG, J. Cell-free layer development process in the entrance region of microvessels. *Biomechanics and Modeling in Mechanobiology 14*, 4 (2014), 783–794.

[227] OULAID, O., AND ZHANG, J. Temporal and Spatial Variations of Wall Shear Stress in the Entrance Region of Microvessels. *Journal of Biomechanical Engineering 137*, 6 (2015), 061008.

[228] PAN, W., FEDOSOV, D. A., CASWELL, B., AND KARNIADAKIS, G. E. Predicting dynamics and rheology of blood flow: A comparative study of multiscale and low-dimensional models of red blood cells. *Microvascular Research 82*, 2 (2011), 163–170.

[229] PARK, J.-S., SONG, S.-H., AND JUNG, H.-I. Continuous focusing of microparticles using inertial lift force and vorticity via multi-orifice microfluidic channels. *Lab on a Chip 9*, 7 (2009), 939–948.

[230] PESKIN, C. S. Flow patterns around heart valves: A numerical method. *Journal of Computational Physics 10*, 2 (1972), 252–271.

[231] PESKIN, C. S. The immersed boundary method. *Acta Numerica 11* (2002), 479–517.

[232] PIVKIN, I. V., AND KARNIADAKIS, G. E. Accurate Coarse-Grained Modeling of Red Blood Cells. *Physical Review Letters 101*, 11 (2008), 118105.

[233] PIVKIN, I. V., PENG, Z., KARNIADAKIS, G. E., BUFFET, P. A., DAO, M., AND SURESH, S. Biomechanics of red blood cells in human spleen and consequences for physiology and disease. *Proceedings of the National Academy of Sciences 113*, 28 (2016), 7804–7809.

[234] POPEL, A. S., AND JOHNSON, P. C. Microcirculation and Hemorheology. *Annual Review of Fluid Mechanics 37*, 1 (2005), 43–69.

[235] POTENTE, M., AND CARMELIET, P. The Link Between Angiogenesis and Endothelial Metabolism. *Annual Review of Physiology 79*, 1 (2017), 43–66.

[236] POTENTE, M., GERHARDT, H., AND CARMELIET, P. Basic and Therapeutic Aspects of Angiogenesis. *Cell 146*, 6 (2011), 873–887.

[237] POZRIKIDIS, C. Axisymmetric motion of a file of red blood cells through capillaries. *Physics of Fluids 17*, 3 (2005), 031503.

[238] POZRIKIDIS, C. Orbiting motion of a freely suspended spheroid near a plane wall. *Journal of Fluid Mechanics 541* (2005), 105–114.

[239] PRADO, G., FARUTIN, A., MISBAH, C., AND BUREAU, L. Viscoelastic Transient of Confined Red Blood Cells. *Biophysical Journal 108*, 9 (2015), 2126–2136.

[240] PRETINI, V., KOENEN, M. H., KAESTNER, L., FENS, M. H. A. M., SCHIFFELERS, R. M., BARTELS, M., AND VAN WIJK, R. Red Blood Cells: Chasing Interactions. *Frontiers in Physiology 10* (2019).

[241] PRIES, A. R. Microvascular hemodynamics: System properties. *Biorheology Preprint*, Preprint (2019), 1–13.

[242] PRIES, A. R., LEY, K., CLAASSEN, M., AND GAEHTGENS, P. Red cell distribution at microvascular bifurcations. *Microvascular Research 38*, 1 (1989), 81–101.

[243] PRIES, A. R., NEUHAUS, D., AND GAEHTGENS, P. Blood viscosity in tube flow: dependence on diameter and hematocrit. *American Journal of Physiology - Heart and Circulatory Physiology 263*, 6 (1992), H1770–H1778.

[244] PRIES, A. R., REGLIN, B., AND SECOMB, T. W. Structural response of microcirculatory networks to changes in demand: information transfer by shear stress. *American Journal of Physiology - Heart and Circulatory Physiology 284*, 6 (2003), H2204–H2212.

[245] PRIES, A. R., AND SECOMB, T. W. Microvascular blood viscosity in vivo and the endothelial surface layer. *American Journal of Physiology - Heart and Circulatory Physiology 289*, 6 (2005), H2657–H2664.

[246] PRIES, A. R., AND SECOMB, T. W. Chapter 1 - Blood Flow in Microvascular Networks. In *Microcirculation (Second Edition)*, R. F. Tuma, W. N. Durán, and K. Ley, Eds. Academic Press, San Diego, 2008, pp. 3–36.

[247] PRIES, A. R., SECOMB, T. W., GAEHTGENS, P., AND GROSS, J. F. Blood flow in microvascular networks. Experiments and simulation. *Circulation Research 67*, 4 (1990), 826–834.

[248] PRIES, A. R., SECOMB, T. W., GESSNER, T., SPERANDIO, M. B., GROSS, J. F., AND GAEHTGENS, P. Resistance to blood flow in microvessels in vivo. *Circulation Research 75*, 5 (1994), 904–915.

[249] PRIES, A. R., SECOMB, T. W., JACOBS, H., SPERANDIO, M., OSTERLOH, K., AND GAEHTGENS, P. Microvascular blood flow resistance: role of endothelial surface layer. *American Journal of Physiology - Heart and Circulatory Physiology 273*, 5 (1997), H2272–H2279.

[250] QI, Q. M., AND SHAQFEH, E. S. G. Theory to predict particle migration and margination in the pressure-driven channel flow of blood. *Physical Review Fluids 2*, 9 (2017).

[251] QIAN, Y. H., D'HUMIÈRES, D., AND LALLEMAND, P. Lattice BGK Models for Navier-Stokes Equation. *EPL (Europhysics Letters) 17*, 6 (1992), 479.

[252] RASMUSSEN, P. M., SECOMB, T. W., AND PRIES, A. R. Modeling the hematocrit distribution in microcirculatory networks: A quantitative evaluation of a phase separation model. *Microcirculation 25*, 3 (2018), e12445.

[253] REICHEL, F., MAUER, J., NAWAZ, A. A., GOMPPER, G., GUCK, J., AND FEDOSOV, D. A. High-Throughput Microfluidic Characterization of Erythrocyte Shapes and Mechanical Variability. *Biophysical Journal 117*, 1 (2019), 14–24.

[254] RENEMAN, R. S., ARTS, T., AND HOEKS, A. P. G. Wall Shear Stress – an Important Determinant of Endothelial Cell Function and Structure – in the Arterial System in vivo. *Journal of Vascular Research 43*, 3 (2006), 251–269.

[255] ROBERTSON, A. M., SEQUEIRA, A., AND KAMENEVA, M. V. Hemorheology. In *Hemodynamical Flows*, no. 37 in Oberwolfach Seminars. Birkhäuser Basel, 2008, pp. 63–120.

[256] ROMAN, S., MERLO, A., DURU, P., RISSO, F., AND LORTHOIS, S. Going beyond 20 um-sized channels for studying red blood cell phase separation in microfluidic bifurcations. *Biomicrofluidics 10*, 3 (2016), 034103.

[257] ROSÉN, T. Chaotic rotation of a spheroidal particle in simple shear flow. *Chaos: An Interdisciplinary Journal of Nonlinear Science 27*, 6 (2017), 063112.

[258] ROSÉN, T., EINARSSON, J., NORDMARK, A., AIDUN, C. K., LUNDELL, F., AND MEHLIG, B. Numerical analysis of the angular motion of a neutrally buoyant spheroid in shear flow at small Reynolds numbers. *Physical Review E 92*, 6 (2015).

[259] ROSÉN, T., KOTSUBO, Y., AIDUN, C. K., DO-QUANG, M., AND LUNDELL, F. Orientational dynamics of a triaxial ellipsoid in simple shear flow: Influence of inertia. *Physical Review E 96*, 1 (2017).

[260] SAADAT, A., GUIDO, C. J., AND SHAQFEH, E. S. G. Effect of Cytoplasmic Viscosity on Red Blood Cell Migration in Small Arteriole-level Confinements. *bioRxiv:10.1101/572933* (2019).

[261] SALEHYAR, S., AND ZHU, Q. Deformation and internal stress in a red blood cell as it is driven through a slit by an incoming flow. *Soft Matter 12*, 13 (2016), 3156–3164.

[262] SALEHYAR, S., AND ZHU, Q. Effects of stiffness and volume on the transit time of an erythrocyte through a slit. *Biomechanics and Modeling in Mechanobiology 16*, 3 (2017), 921–931.

[263] SCHAAF, C., AND STARK, H. Inertial migration and axial control of deformable capsules. *Soft Matter 13*, 19 (2017), 3544–3555.

[264] SCHILLER, U. D., KRÜGER, T., AND HENRICH, O. Mesoscopic modelling and simulation of soft matter. *Soft Matter 14*, 1 (2018), 9–26.

[265] SCHMID-SCHÖNBEIN, G. W., SKALAK, R., USAMI, S., AND CHIEN, S. Cell distribution in capillary networks. *Microvascular Research 19*, 1 (1980), 18–44.

[266] SEBASTIAN, B., AND DITTRICH, P. S. Microfluidics to Mimic Blood Flow in Health and Disease. *Annual Review of Fluid Mechanics 50*, 1 (2018), 483–504.

[267] SECOMB, T. W. Flow-dependent rheological properties of blood in capillaries. *Microvascular Research 34*, 1 (1987), 46–58.

[268] SECOMB, T. W. Blood Flow in the Microcirculation. *Annual Review of Fluid Mechanics 49*, 1 (2017), 443–461.

[269] SECOMB, T. W., SKALAK, R., ÖZKAYA, N., AND GROSS, J. F. Flow of axisymmetric red blood cells in narrow capillaries. *Journal of Fluid Mechanics 163* (1986), 405–423.

[270] SECOMB, T. W., STYP-REKOWSKA, B., AND PRIES, A. R. Two-Dimensional Simulation of Red Blood Cell Deformation and Lateral Migration in Microvessels. *Annals of Biomedical Engineering 35*, 5 (2007), 755–765.

[271] SEGRÉ, G., AND SILBERBERG, A. Radial Particle Displacements in Poiseuille Flow of Suspensions. *Nature 189*, 4760 (1961), 209–210.

[272] SEGRÉ, G., AND SILBERBERG, A. Behaviour of macroscopic rigid spheres in Poiseuille flow Part 2. Experimental results and interpretation. *Journal of Fluid Mechanics 14*, 1 (1962), 136–157.

[273] SEIFERT, U. Configurations of fluid membranes and vesicles. *Advances in Physics 46*, 1 (1997), 13–137.

[274] SEIFERT, U. Hydrodynamic Lift on Bound Vesicles. *Physical Review Letters 83*, 4 (1999), 876–879.

[275] SENDER, R., FUCHS, S., AND MILO, R. Revised Estimates for the Number of Human and Bacteria Cells in the Body. *PLOS Biology 14*, 8 (2016), e1002533.

[276] SHEN, Z., COUPIER, G., KAOUI, B., POLACK, B., HARTING, J., MISBAH, C., AND PODGORSKI, T. Inversion of hematocrit partition at microfluidic bifurcations. *Microvascular Research 105* (2016), 40–46.

[277] SHEN, Z., FISCHER, T. M., FARUTIN, A., VLAHOVSKA, P. M., HARTING, J., AND MISBAH, C. Blood Crystal: Emergent Order of Red Blood Cells Under Wall-Confined Shear Flow. *Physical Review Letters 120*, 26 (2018).

[278] SHERWOOD, J. M., HOLMES, D., KALIVIOTIS, E., AND BALABANI, S. Spatial Distributions of Red Blood Cells Significantly Alter Local Haemodynamics. *PLOS ONE 9*, 6 (2014), e100473.

[279] SHI, L., PAN, T.-W., AND GLOWINSKI, R. Lateral migration and equilibrium shape and position of a single red blood cell in bounded Poiseuille flows. *Physical Review E 86*, 5 (2012).

[280] SHI, L., PAN, T.-W., AND GLOWINSKI, R. Three-dimensional numerical simulation of red blood cell motion in Poiseuille flows. *International Journal for Numerical Methods in Fluids 76*, 7 (2014), 397–415.

[281] SIGÜENZA, J., MENDEZ, S., AMBARD, D., DUBOIS, F., JOURDAN, F., MOZUL, R., AND NICOUD, F. Validation of an immersed thick boundary method for simulating fluid–structure interactions of deformable membranes. *Journal of Computational Physics 322* (2016), 723–746.

[282] SINHA, K., AND GRAHAM, M. D. Dynamics of a single red blood cell in simple shear flow. *Physical Review E 92*, 4 (2015).

[283] SKALAK, R., AND CHIEN, S. Capillary Flow: History, experiments and theory. *Biorheology 18*, 3-6 (1981), 307–330.

[284] SKALAK, R., AND CHIEN, S. Rheology of blood cells as soft tissues. *Biorheology 19*, 3 (1982), 453–461.

[285] SKALAK, R., TOZEREN, A., ZARDA, R. P., AND CHIEN, S. Strain Energy Function of Red Blood Cell Membranes. *Biophysical Journal 13*, 3 (1973), 245–264.

[286] SKOTHEIM, J. M., AND SECOMB, T. W. Red Blood Cells and Other Nonspherical Capsules in Shear Flow: Oscillatory Dynamics and the Tank-Treading-to-Tumbling Transition. *Physical Review Letters 98*, 7 (2007).

[287] SMITH, J. E., MOHANDAS, N., AND SHOHET, S. B. Variability in erythrocyte deformability among various mammals. *American Journal of Physiology-Heart and Circulatory Physiology 236*, 5 (1979), H725–H730.

[288] STAPOR, P. C., BOCK, P. K. D., AND CARMELIET, P. P. Essentials of Angiogenesis. In *PanVascular Medicine*, P. Lanzer, Ed. Springer Berlin Heidelberg, 2014, pp. 1–34.

[289] SUCCI, S. *The Lattice Boltzmann Equation: For Fluid Dynamics and Beyond*. Numerical Mathematics and Scientific Computation. Oxford University Press, Oxford, New York, 2001.

[290] SUGIHARA-SEKI, M. The motion of an ellipsoid in tube flow at low Reynolds numbers. *Journal of Fluid Mechanics 324* (1996), 287–308.

[291] SUI, Y., CHEW, Y. T., ROY, P., CHENG, Y. P., AND LOW, H. T. Dynamic motion of red blood cells in simple shear flow. *Physics of Fluids 20*, 11 (2008), 112106.

[292] SUI, Y., CHEW, Y. T., ROY, P., AND LOW, H. T. A hybrid method to study flow-induced deformation of three-dimensional capsules. *Journal of Computational Physics 227*, 12 (2008), 6351–6371.

[293] SUKUMARAN, S., AND SEIFERT, U. Influence of shear flow on vesicles near a wall: A numerical study. *Physical Review E 64*, 1 (2001), 011916.

[294] SUN, C., AND MUNN, L. L. Lattice-Boltzmann simulation of blood flow in digitized vessel networks. *Computers & Mathematics with Applications 55*, 7 (2008), 1594–1600.

[295] SURGENOR, D. M. *The Red Blood Cell: Volume II*. Academic Press, 2013.

[296] SUTERA, S. P., AND SKALAK, R. The History of Poiseuille's Law. *Annual Review of Fluid Mechanics 25*, 1 (1993), 1–20.

[297] SVANES, K., AND ZWEIFACH, B. W. Variations in small blood vessel hematocrits produced in hypothermic rats by micro-occlusion. *Microvascular Research 1*, 2 (1968), 210–220.

[298] TAN, Z., LE, D. V., LIM, K. M., AND KHOO, B. C. An Immersed Interface Method for the Simulation of Inextensible Interfaces in Viscous Fluids. *Communications in Computational Physics 11*, 3 (2012), 925–950.

[299] TOMAIUOLO, G. Biomechanical properties of red blood cells in health and disease towards microfluidics. *Biomicrofluidics 8*, 5 (2014), 051501.

[300] TOMAIUOLO, G., LANOTTE, L., D'APOLITO, R., CASSINESE, A., AND GUIDO, S. Microconfined flow behavior of red blood cells. *Medical Engineering & Physics 38*, 1 (2016), 11–16.

[301] TONER, M., AND IRIMIA, D. Blood-on-a-Chip. *Annual Review of Biomedical Engineering 7*, 1 (2005), 77–103.

[302] TRIPATHI, S., KUMAR, Y. V. B. V., PRABHAKAR, A., JOSHI, S. S., AND AGRAWAL, A. Passive blood plasma separation at the microscale: a review of design principles and microdevices. *Journal of Micromechanics and Microengineering 25*, 8 (2015), 083001.

[303] UDAN, R. S., VADAKKAN, T. J., AND DICKINSON, M. E. Dynamic responses of endothelial cells to changes in blood flow during vascular remodeling of the mouse yolk sac. *Development 140*, 19 (2013), 4041–4050.

[304] VARCHANIS, S., DIMAKOPOULOS, Y., WAGNER, C., AND TSAMOPOULOS, J. How viscoelastic is human blood plasma? *Soft Matter* (2018).

[305] VION, A.-C., ALT, S., KLAUS-BERGMANN, A., SZYMBORSKA, A., ZHENG, T., PEROVIC, T., HAMMOUTENE, A., OLIVEIRA, M. B., BARTELS-KLEIN, E., HOLLFINGER, I., RAUTOU, P.-E., BERNABEU, M. O., AND GERHARDT, H. Primary cilia sensitize endothelial cells to BMP and prevent excessive vascular regression. *J Cell Biol 217*, 5 (2018), 1651–1665.

[306] VLAHOVSKA, P. M., BARTHES-BIESEL, D., AND MISBAH, C. Flow dynamics of red blood cells and their biomimetic counterparts. *Comptes Rendus Physique 14*, 6 (2013), 451–458.

[307] WANG, T., RONGIN, U., AND XING, Z. A micro-scale simulation of red blood cell passage through symmetric and asymmetric bifurcated vessels. *Scientific Reports 6* (2016), 20262.

[308] WANG, Z., SUI, Y., SALSAC, A.-V., BARTHÈS-BIESEL, D., AND WANG, W. Motion of a spherical capsule in branched tube flow with finite inertia. *Journal of Fluid Mechanics 806* (2016), 603–626.

[309] WANG, Z., SUI, Y., SALSAC, A.-V., BARTHÈS-BIESEL, D., AND WANG, W. Path selection of a spherical capsule in a microfluidic branched channel: towards the design of an enrichment device. *Journal of Fluid Mechanics 849* (2018), 136–162.

[310] WOOLFENDEN, H. C., AND BLYTH, M. G. Motion of a two-dimensional elastic capsule in a branching channel flow. *Journal of Fluid Mechanics 669* (2011), 3–31.

[311] XIAO, L. L., LIU, Y., CHEN, S., AND FU, B. M. Numerical simulation of a single cell passing through a narrow slit. *Biomechanics and Modeling in Mechanobiology 15*, 6 (2016), 1655–1667.

[312] XIONG, W., AND ZHANG, J. Shear Stress Variation Induced by Red Blood Cell Motion in Microvessel. *Annals of Biomedical Engineering 38*, 8 (2010), 2649–2659.

[313] XIONG, W., AND ZHANG, J. Two-dimensional lattice Boltzmann study of red blood cell motion through microvascular bifurcation: cell deformability and suspending viscosity effects. *Biomechanics and Modeling in Mechanobiology 11*, 3-4 (2012), 575–583.

[314] XU, D., KALIVIOTIS, E., MUNJIZA, A., AVITAL, E., JI, C., AND WILLIAMS, J. Large scale simulation of red blood cell aggregation in shear flows. *Journal of Biomechanics 46*, 11 (2013), 1810–1817.

[315] YAGINUMA, T., OLIVEIRA, M. S. N., LIMA, R., ISHIKAWA, T., AND YAMAGUCHI, T. Human red blood cell behavior under homogeneous extensional flow in a hyperbolic-shaped microchannel. *Biomicrofluidics 7*, 5 (2013), 054110.

[316] YANG, S., ÜNDAR, A., AND D. ZAHN, J. A microfluidic device for continuous, real time blood plasma separation. *Lab on a Chip 6*, 7 (2006), 871–880.

[317] YASHIRO, K., SHIRATORI, H., AND HAMADA, H. Haemodynamics determined by a genetic programme govern asymmetric development of the aortic arch. *Nature 450*, 7167 (2007), 285–288.

[318] YAZDANI, A., AND BAGCHI, P. Influence of membrane viscosity on capsule dynamics in shear flow. *Journal of Fluid Mechanics 718* (2013), 569–595.

[319] YAZDANI, A., LI, X., AND KARNIADAKIS, G. E. Dynamic and rheological properties of soft biological cell suspensions. *Rheologica Acta 55*, 6 (2016), 433–449.

[320] YAZDANI, A. Z. K., AND BAGCHI, P. Phase diagram and breathing dynamics of a single red blood cell and a biconcave capsule in dilute shear flow. *Physical Review E 84*, 2 (2011), 026314.

[321] YAZDANI, A. Z. K., KALLURI, R. M., AND BAGCHI, P. Tank-treading and tumbling frequencies of capsules and red blood cells. *Physical Review E 83*, 4 (2011).

[322] YE, H., HUANG, H., AND LU, X.-Y. Numerical study on dynamic sorting of a compliant capsule with a thin shell. *Computers & Fluids 114* (2015), 110–120.

[323] YE, S. S., JU, M., AND KIM, S. Recovery of cell-free layer and wall shear stress profile symmetry downstream of an arteriolar bifurcation. *Microvascular Research 106* (2016), 14–23.

[324] YE, T., LI, H., AND LAM, K. Y. Modeling and simulation of microfluid effects on deformation behavior of a red blood cell in a capillary. *Microvascular Research 80*, 3 (2010), 453–463.

[325] YE, T., AND PENG, L. Motion, deformation, and aggregation of multiple red blood cells in three-dimensional microvessel bifurcations. *Physics of Fluids 31*, 2 (2019), 021903.

[326] YE, T., PENG, L., AND LI, G. Red blood cell distribution in a microvascular network with successive bifurcations. *Biomechanics and Modeling in Mechanobiology 18*, 6 (2019), 1821–1835.

[327] YE, T., PENG, L., AND LI, Y. Three-dimensional motion and deformation of a red blood cell in bifurcated microvessels. *Journal of Applied Physics 123*, 6 (2018), 064701.

[328] YE, T., PHAN-THIEN, N., KHOO, B. C., AND LIM, C. T. Dissipative particle dynamics simulations of deformation and aggregation of healthy and diseased red blood cells in a tube flow. *Physics of Fluids 26*, 11 (2014), 111902.

[329] YE, T., PHAN-THIEN, N., AND LIM, C. T. Particle-based simulations of red blood cells—A review. *Journal of Biomechanics 49*, 11 (2016), 2255–2266.

[330] YE, T., PHAN-THIEN, N., LIM, C. T., PENG, L., AND SHI, H. Hybrid smoothed dissipative particle dynamics and immersed boundary method for simulation of red blood cells in flows. *Physical Review E 95*, 6 (2017), 063314.

[331] YE, T., SHI, H., PHAN-THIEN, N., LIM, C. T., AND LI, Y. Relationship between transit time and mechanical properties of a cell through a stenosed microchannel. *Soft Matter* (2017).

[332] YIN, X., THOMAS, T., AND ZHANG, J. Multiple red blood cell flows through microvascular bifurcations: Cell free layer, cell trajectory, and hematocrit separation. *Microvascular Research 89* (2013), 47–56.

[333] YIN, X., AND ZHANG, J. Cell-free layer and wall shear stress variation in microvessels. *Biorheology 49*, 4 (2012), 261–270.

[334] ZHANG, J. Effect of Suspending Viscosity on Red Blood Cell Dynamics and Blood Flows in Microvessels. *Microcirculation 18*, 7 (2011), 562–573.

[335] ZHANG, J., JOHNSON, P. C., AND POPEL, A. S. An immersed boundary lattice Boltzmann approach to simulate deformable liquid capsules and its application to microscopic blood flows. *Physical Biology 4*, 4 (2007), 285.

[336] ZHANG, P., GAO, C., ZHANG, N., SLEPIAN, M. J., DENG, Y., AND BLUESTEIN, D. Multiscale Particle-Based Modeling of Flowing Platelets in Blood Plasma Using Dissipative Particle Dynamics and Coarse Grained Molecular Dynamics. *Cellular and Molecular Bioengineering 7*, 4 (2014), 552–574.

[337] ZHAO, H., ISFAHANI, A. H. G., OLSON, L. N., AND FREUND, J. B. A spectral boundary integral method for flowing blood cells. *Journal of Computational Physics 229*, 10 (2010), 3726–3744.

[338] ZHOU, J., AND PAPAUTSKY, I. Fundamentals of inertial focusing in microchannels. *Lab on a Chip 13*, 6 (2013), 1121–1132.

[339] ZHOU, Q., FIDALGO, J., CALVI, L., BERNABEU, M. O., HOSKINS, P. R., OLIVEIRA, M. S. N., AND KRÜGER, T. Spatiotemporal Dynamics of Dilute Red Blood Cell Suspensions in Low-Inertia Microchannel Flow. *Biophysical Journal 118*, 10 (2020), 2561–2573.

[340] ZHOU, Q., PEROVIC, T., FECHNER, I., EDGAR, L. T., HOSKINS, P. R., GERHARDT, H., KRÜGER, T., AND BERNABEU, M. O. Association between erythrocyte dynamics and vessel remodelling in developmental vascular networks. *bioRxiv:10.1101/2020.05.21.106914* (2020).

[341] ZOGRAFOS, K., BARBER, R. W., EMERSON, D. R., AND OLIVEIRA, M. S. N. A design rule for constant depth microfluidic networks for power-law fluids. *Microfluidics and Nanofluidics 19*, 3 (2015), 737–749.

[342] ZÁVODSZKY, G., VAN ROOIJ, B., AZIZI, V., ALOWAYYED, S., AND HOEKSTRA, A. Hemocell: a high-performance microscopic cellular library. *Procedia Computer Science 108* (2017), 159–165.

[343] ZÁVODSZKY, G., VAN ROOIJ, B., AZIZI, V., AND HOEKSTRA, A. Cellular Level In-silico Modeling of Blood Rheology with An Improved Material Model for Red Blood Cells. *Frontiers in Physiology 8* (2017).